ELSEVIER
SAUNDERS

Radiol Clin N Am 43 (2005) xi

RADIOLOGIC
CLINICS
of North America

Preface

Essentials of Thoracic Imaging

Caroline Chiles, MD
Guest Editor

Diagnostic radiology, like many other medical specialties, does not allow physicians to maintain competence solely on the basis of accumulating experience, but requires a commitment to life–long learning. Keeping pace with new knowledge and new technology competes with clinical demands on a radiologist's time. At the 2002 annual meeting in Chicago, the Radiological Society of North America initiated a series of continuing medical education lectures called "The Essentials." Attendance and audience feedback surpassed all expectations. Surveys of radiologists attending "The Essentials" lectures showed an equal mix of general radiologists, and radiologists who practice subspecialties outside the lecture topic. The participants were seeking practical information that would impact their daily radiology work—applying new technologies to diseases that are encountered every day.

My goal for this issue of *Radiologic Clinics of North America* is to condense the overwhelming amount of current literature in thoracic radiology to the application of new technologies to bread-and-butter cases. Thank you to my colleagues who have shared their expertise in the basics of thoracic imaging: lung cancer, metastatic disease, the solitary pulmonary nodule, pneumonia, cardiovascular disease, and high resolution CT. Thank you as well to Ron Zagoria, who included me in the initial Radiological Society of North America Essentials faculty, and to Barton Dudlick, who saw this project through from start to finish.

Caroline Chiles, MD
Division of Radiological Sciences
Department of Radiology
Wake Forest University School of Medicine
Medical Center Boulevard
Winston-Salem, NC 27157-1088, USA
E-mail address: cchiles@wfubmc.edu

0033-8389/05/$ – see front matter © 2005 Elsevier Inc. All rights reserved.
doi:10.1016/j.rcl.2005.03.001

ELSEVIER
SAUNDERS

Radiol Clin N Am 43 (2005) 467 – 480

RADIOLOGIC
CLINICS
of North America

Imaging of Non–Small Cell Lung Cancer

Reginald F. Munden, MD, DMD*, John Bruzzi, MD

Division of Diagnostic Imaging, Department of Radiology, The University of Texas MD Anderson Cancer Center, 1515 Holcombe Boulevard, Houston, TX 77030, USA

Lung cancer is the most common type of cancer and the leading cause of cancer deaths in the United States for both men and women. It was estimated that 173,770 new cases and 160,440 deaths from lung cancer would occur in 2004 [1]. More Americans die of lung cancer than of colorectal, breast, and prostate cancers combined, which are the second through fourth leading causes of cancer mortality, respectively. Even though major efforts at improving survival have occurred over the years, the overall 5-year survival of lung cancer remains dismal at 14% for all stages (clinical staging), 61% for stage IA, 38% for stage IB, 34% for stage IIA, 24% for stage IIB, 13% for stage IIIA, 5% for stage IIIB, and 1% for stage IV [2].

Once lung cancer has been established, the International System for Staging Lung Cancer is used to stage newly diagnosed non–small cell lung cancer (NSCLC). This system describes the extent of NSCLC in terms of the size, location, and extent of the primary tumor (T descriptor); the presence and location of lymph node involvement (N descriptor); and the presence or absence of distant metastatic disease (M descriptor) [2]. Radiologic evaluation is an important component of the clinical staging evaluation and can greatly influence whether the patient is treated with surgical resection, radiation therapy, chemotherapy, or a combination of these modalities [3]. In addition to staging, the radiologic evaluation of the patient undergoing treatment and subsequent follow-up is important to the clinician for assessing treatment effects and complications. This article discusses the imaging in patients with NSCLC and its use in caring for these patients.

Importance of staging lung cancer

Because surgical resection of lung cancer offers the best chance of cure, accurate staging is important to determine if patients are surgical candidates. In general, clinical stage I, II, and some stage IIIA patients are considered to have disease that is resectable, whereas more extensive disease as in some patients with stage IIIA and most with stage IIIB and IV is treated with radiation therapy, chemotherapy, or a combination of both [4]. More than 60% of patients with lung cancer receive radiotherapy at some point in their disease, 17% of which is for palliation [5]. Patients with early stage disease (stage I–II) who are not surgical candidates because of medical comorbidities or who refuse surgery may undergo radiotherapy with curative intent [6]. Radiotherapy may also be used as preoperative concurrent chemoradiotherapy in locally advanced lung cancer to ''downstage'' the patient to a lower stage and make them a candidate for surgical cure. Preliminary studies suggest this technique may have a role in treating NSCLC, but remains controversial [7]. For locally advanced and inoperable lung cancer, chemotherapy is used in conjunction with radiation therapy to improve survival [8–10]. Chemotherapy alone is used in stage III and IV NSCLC patients who are not candidates for surgery or chemoradiation.

Because the determination of disease extent is often based on clinical staging, imaging studies and the radiologist's interpretation are very important

* Corresponding author.
E-mail address: rmunden@mdanderson.org (R.F. Munden).

0033-8389/05/$ – see front matter © 2005 Elsevier Inc. All rights reserved.
doi:10.1016/j.rcl.2005.01.009

aspects of the treatment plan decision between surgery, radiation therapy, chemotherapy, or a combination of treatments. Common imaging modalities for staging lung cancer are chest radiographs, CT, MR imaging, positron-emission tomography (PET), and fused PET-CT. Although a common method of detecting lung cancer, chest radiographs are of limited value in staging lung cancer. The most common radiologic examination in the lung cancer patient is chest CT [11] because of its ability to provide anatomic information regarding the primary tumor and evaluate the extent of intrathoracic and regional extrathoracic disease. Whole-body PET using fluorine-18–fluorodeoxyglucose (^{18}F-FDG) has become a very useful tool in staging lung cancer; fused PET–CT imaging is a newer technique that has further improved staging [3,12,13].

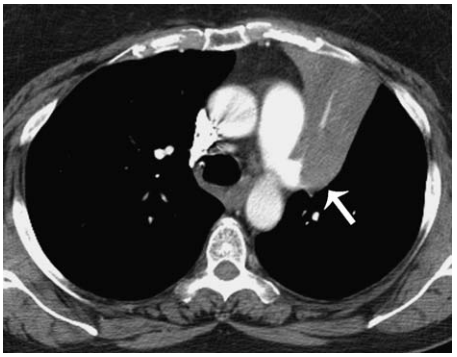

Fig. 1. A 60-year-old man with T2 non–small cell lung cancer. Axial image from a contrast-enhanced CT scan shows that the primary tumor is located centrally (*arrow*), causing distal postobstructive atelectasis. Note the difficulty of differentiating tumor from collapsed lung parenchyma.

Staging

The radiologic evaluation of the primary tumor (T descriptor) should describe the size, location, margins, and relationship to adjacent structures for the surgeon, radiation oncologist, or medical oncologist to determine an appropriate treatment plan. T1 tumors are technically the easiest to resect because they are smaller (< 3 cm) and are limited to the lung parenchyma. T1 tumors are surrounded by lung parenchyma but may reside near other structures that are important to note. As an example, tumors adjacent to pulmonary vessels may require a change in surgical technique or radiotherapy treatment plan.

T2 tumors are larger (≥ 3 cm), but should not be closer than 2 cm to the carina and may have associated atelectasis or pneumonitis that does not include the entire lobe (Fig. 1). As with T1 tumors, the anatomic relationship of the tumor to nearby structures may influence the treatment plan and should be reported. For instance, if the lobar bronchus or main bronchus is involved by tumor, a sleeve resection or pneumonectomy may be required [14]. Associated atelectasis is important because it may require an alteration in the radiotherapy treatment plan.

T3 tumors can be any size; invade the chest wall, diaphragm, mediastinal pleura, parietal pericardium, or be within 2 cm of the carina; or have associated atelectasis or pneumonitis of the entire lobe. Appropriate description of location is important because if the tumor is less than 2 cm from the carina, a carinal pneumonectomy needs to be performed [15]. The extent of chest wall invasion is also important to convey because more extensive surgical techniques or larger radiotherapy treatment plans are required. The sensitivity and specificity of CT in determining chest wall invasion is reported to vary from 38% to 87% and 40% to 90%, respectively [16]. Glazer et al [17] reported CT to have 87% sensitivity, 59% specificity, and 68% accuracy for assessing chest wall invasion; however, local chest pain was more specific (94%) and accurate (85%). MR imaging sensitivity and specificity (63%–90% and 84%–86%, respectively) in diagnosing chest wall invasion are similar to those of CT [16,18,19]. Even though radiologic evaluation for chest wall invasion is somewhat limited, at times definite invasion can be determined, and important to note for treatment planning. Likewise, if invasion is not definite, this uncertainty should also be noted.

Invasion of the primary tumor into the mediastinum is also important to assess. As in chest wall invasion, CT and MR imaging can be accurate (56%–89% and 50%–93%, respectively) for confirming gross invasion of the mediastinum [20–22], but have limited accuracy when invasion is subtle. Definite invasion, however, should be reported. Improvement in determining the extent of chest wall or mediastinal invasion by the primary tumor using PET and PET–CT has not been reported.

T4 tumors involve the mediastinum, heart, great vessels, trachea, esophagus, vertebral body, carina, or have a malignant pleural or pericardial effusion (Fig. 2). If the patients have no other contraindication to surgery, some of these tumors represent the one subset within clinical stage IIIB patients who remain good candidates for surgery [23]. Surgical resection of selected tumors involving the left atrium, great vessels, superior vena cava, vertebral body, trachea, and esophagus in selected patients has been shown to

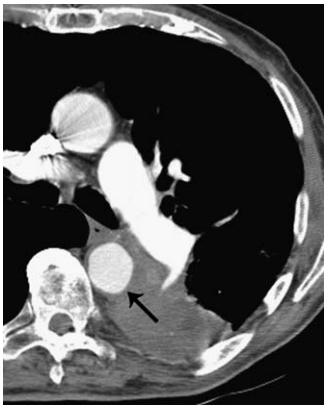

Fig. 2. An 83-year-old man with adenocarcinoma of the left lower lobe that invaded the descending thoracic aorta (*arrow*) and left main pulmonary artery, depicted by contrast-enhanced CT. The invasion of these structures results in classification of the tumor as a T4 lesion.

have an improved survival [24]. Also of note, the most recent version of the International Staging System states that primary tumors of any size associated with satellite nodules in the same lobe are also classified as T4 (Fig. 3), whereas nodules in other lobes are classified as metastatic (M1) [2]. Classification of primary tumors with satellite nodules as T4 may imply a worse prognosis than is warranted, and some authors advocate that patients with satellite nodules undergo definitive resection if no other contraindications to surgery exist [25,26]. Malignant pleural effusion can be difficult to diagnose because cytologic evaluation is positive in only approximately 66% of patients [27]. In the absence of cytology-positive fluid, a clinical T4 staging is assigned if there is clinical suspicion of a malignant effusion, which may be raised because of the radiologic appearance [2,28]. PET imaging with ^{18}F-FDG may aid in characterizing pleural disease [29–32]. It is important for the radiologist to indicate the presence of pleural disease in the radiologic report and to correlate CT and PET images when available.

The goal of radiotherapy is to treat the tumor adequately with minimal damage to the surrounding normal tissues. As with surgeons, radiation oncologists need to understand the size and location of the primary tumor and proximity of tumor to critical structures, particularly the spinal cord, esophagus, and heart where radiation tolerance imposes dose-volume constraints. Even though current imaging techniques cannot determine the true microscopic limits of tumors, radiologic definition of tumor margins is critical for radiotherapy treatment planning. Radiation oncologists take into consideration imaging limitation of defining tumor margin. Accordingly, the International Commission of Radiation Units and Measurements [33,34] has defined the gross tumor volume as tumor that is visible by any imaging modality; clinical target volume as the volume that is likely to contain microscopic disease based on reported patterns of recurrence; and planning target volume (the area to be irradiated) as the clinical tumor volume with an added margin to account for daily setup error and target motion. Assessment of gross tumor volume is becoming more important in radiotherapy with an increasing use of conformal radiation therapy, which is a technique that uses multiple radiation beams that conform tightly to target volumes and limit damage to surrounding normal structures. As the area around the tumor to be treated is decreased, accurate determination of tumor margin becomes more critical. Underestimation of tumor extent can lead to high local recurrence rates and overestimation can lead to destruction of normal tissue and complications. Accurate description of tumor margins is needed and at times diagnostic radiologists may assist in delineating gross tumor margins.

For those patients treated by medical oncologists, determination of tumor location is important if the patient is at potential risk for a significant complication or potentially life-threatening event, such as invasion into a vascular structure that may lead to exsanguination. The most important radiologic information for medical oncologists is the assessment of the effectiveness of treatment (whether the disease is stable, improved, or progressed). Determination of disease response is generally done by assessing the

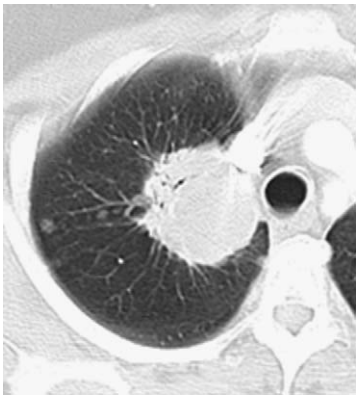

Fig. 3. A 72-year-old woman with mucinous adenocarcinoma of the right upper lobe. Axial CT demonstrates a spiculated right upper lobe mass and satellite nodules in the same lobe. The presence of satellite nodules results in classification of the tumor as a T4 lesion.

primary tumor and metastatic disease for a change in size. To standardize the methods of determining effectiveness of treatment, uniform criteria for reporting response, recurrence, disease-free interval, and toxicity were adopted at a meeting in 1979 on the Standardization of Reporting Results of Cancer Treatment [35,36]. These criteria, known as the ''World Health Organization criteria,'' are based largely on tumor measurements in two dimensions (bidimensional), which are obtained by multiplying the longest diameter of the tumor by the greatest perpendicular diameter in the axial plane. This product is the tumor size, and if there are multiple evaluable tumors, then the sum of the products is obtained to determine the total tumor size. Treatment response is defined as complete response (no evidence of tumor); partial response (decrease in tumor size by 50%); stable disease (no change in tumor size); or progressive disease (increase in tumor size by 25%) [36].

In 1994, the WHO criteria were revised and guidelines known as the ''Response Evaluation Criteria in Solid Tumors'' (RECIST) were proposed, whereby tumor measurements are performed with a single measurement (unidimensional), obtained by measuring the longest diameter of the tumor in the axial plane. This measurement is the tumor size, and if there are multiple tumors used, then the sum of the diameters is used to calculate total tumor size. Using RECIST criteria, treatment response is defined as complete response (no evidence of tumor); partial response (decrease in tumor size by 30%); stable disease (no change in tumor size); and progressive disease (increase in tumor size by 20%). RECIST is now the preferred method of assessing response [37]. Regardless of which criteria are used, new metastatic disease is also indicative of progressive disease and needs to be emphasized. It is important for the radiologist to be aware of these criteria and identify the primary tumor, if present, and any metastatic disease that can serve as measurable disease.

Nodal disease

The presence and location of regional lymph node metastases (N descriptor) is another important component of radiologic staging. Accurate assessment of lymph nodes of the mediastinum is essential in selecting the appropriate treatment plan for patients with NSCLC [38]. To standardize the description of nodal metastases, the American Thoracic Society defined nodal stations in relation to anatomic structures or boundaries that can be identified before and during thoracotomy. Although the American Thoracic Society description of nodal stations is the most commonly used system, others, such as that proposed by Naruke et al [39], are also in use, but this article uses the American Thoracic Society system.

The presence of nodes within the ipsilateral peribronchial region or hilum indicates N1 disease. N1 lymph nodes can usually be resected at surgery,

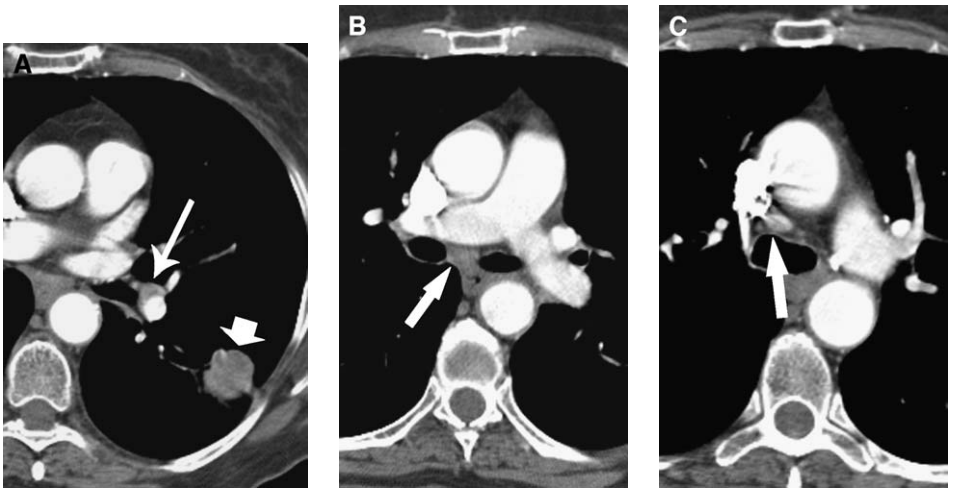

Fig. 4. A 73-year-old woman with non–small cell lung cancer of the left lower lobe and N1, N2, and N3 disease. (*A*) Axial image from a contrast-enhanced CT scan reveals a left lower lobe mass (*short arrow*) and ipsilateral hilar adenopathy (*long arrow*) indicating N1 disease. (*B*) Image more cephalad reveals subcarinal adenopathy (*arrow*) indicating N2 disease. (*C*) More superiorly, an image demonstrates right lower paratracheal adenopathy (*arrow*) consistent with N3 disease.

but technically are more difficult to remove if they involve the pulmonary artery.

Ipsilateral mediastinal or subcarinal adenopathy constitute N2 disease and may be resectable. In contrast, contralateral mediastinal adenopathy, scalene, or supraclavicular adenopathy constitutes N3 disease, which is considered nonsurgical disease (Fig. 4). Two meta-analyses of staging NSCLC with CT, however, indicate the limitations of CT for staging the mediastinum [40,41]. In one review by Dales et al [40] of 42 studies, there was a combined sensitivity of 83%, a specificity of 82%, and an accuracy of 80%. Dwamena et al [41] reviewed 29 studies and reported a combined sensitivity of 60%, specificity of 77%, and accuracy of 75%. This limitation is primarily because CT only shows the size, shape, and location of mediastinal lymph nodes, not the biologic activity. MR imaging has similar limitations.

PET imaging with FDG, which demonstrates metabolic activity, has been shown to be more accurate (reported accuracy, 81%–96%) than CT and MR imaging in the detection of nodal disease [41–47]. PET is also useful in differentiating hyperplastic nodes from metastatic nodes and for detecting metastases within normal-size nodes [45,46,48]. In one meta-analysis of nodal staging, the sensitivity of PET was 79% and specificity was 91% compared with 60% and 77% for CT [41]. Fused PET–CT imaging provides registration of FDG metabolic activity with anatomic detail of CT and is an exciting new development (Fig. 5). PET–CT has recently been reported to be more accurate than PET or CT alone in staging patients with NSCLC [3,13]. Antoch et al [13] reported that the accuracy for detecting metastatic mediastinal lymph nodes was 63% for CT alone, 89% for PET alone, and 93% for PET–CT, whereas the sensitivity and specificity was 89% and 94% for PET–CT, 89% and 89% PET, and 70% and 59% for CT [13].

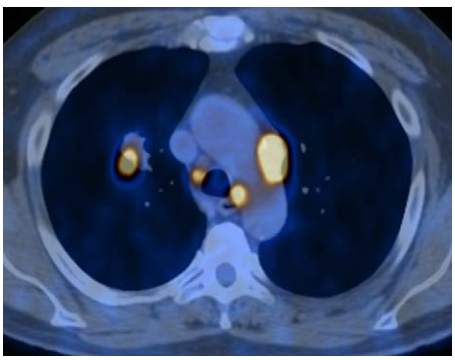

Fig. 5. Fused PET-CT image of a 59-year-old man with non–small cell lung cancer of the right upper lobe. There is FDG activity (yellow areas) within the right upper lobe mass, right and left paratracheal lymph nodes, and aortopulmonary window lymph nodes that indicate metabolically active malignancy.

Even with improvements in resolution and CT techniques, the value of CT in assessing mediastinal lymph nodes in patients with T1 lesions is controversial among thoracic surgeons [49]. If there are no mediastinal lymph nodes detected on CT, some surgeons do not routinely perform mediastinoscopy for peripheral T1 lesions because the prevalence of nodal metastasis associated with T1 tumors is reported to be only 5% to 15% [11], and because they view the procedure as invasive with significant morbidity and mortality [49]. Another report advocates mediastinoscopy be avoided in patients with potentially resectable lung cancer and PET studies showing normal uptake of FDG mediastinal nodes [45]. Other surgeons, however, advocate mediastinoscopy for all patients with T1 lesions [49–51] regardless of CT findings. Seely et al [50] reported a prevalence of up to 21% nodal metastasis in 104 patients with T1 tumors, although CT was reported to be 77% sensitive for ruling out such metastases. Despite this controversy, radiologists should continue to evaluate critically the mediastinum with available imaging techniques and work to improve the ability of these techniques to provide accurate staging of the mediastinum.

Assessment of mediastinal adenopathy for the radiation oncologist is also important because involved nodes are included in their treatment plan. CT done for radiotherapy treatment planning is usually done without contrast, and a good description of nodal disease in the diagnostic examination can assist the radiation oncologist. Furthermore, many of these patients do not undergo mediastinoscopy and an opinion on the presence of metastatic nodal disease is important. Fused PET–CT imaging is another valuable tool in treatment planning for patients who are to undergo radiation therapy. PET–CT is reported to alter the treatment plan in more than 50% of patients with NSCLC when compared with CT alone [52]. Fused imaging can also be used to differentiate suspected metastatic disease from benign lesions and to help differentiate recurrent tumor from radiation fibrosis (Fig. 6).

Metastatic disease

The risk of metastases in NSCLC increases with more advanced local tumor stage and varies accord-

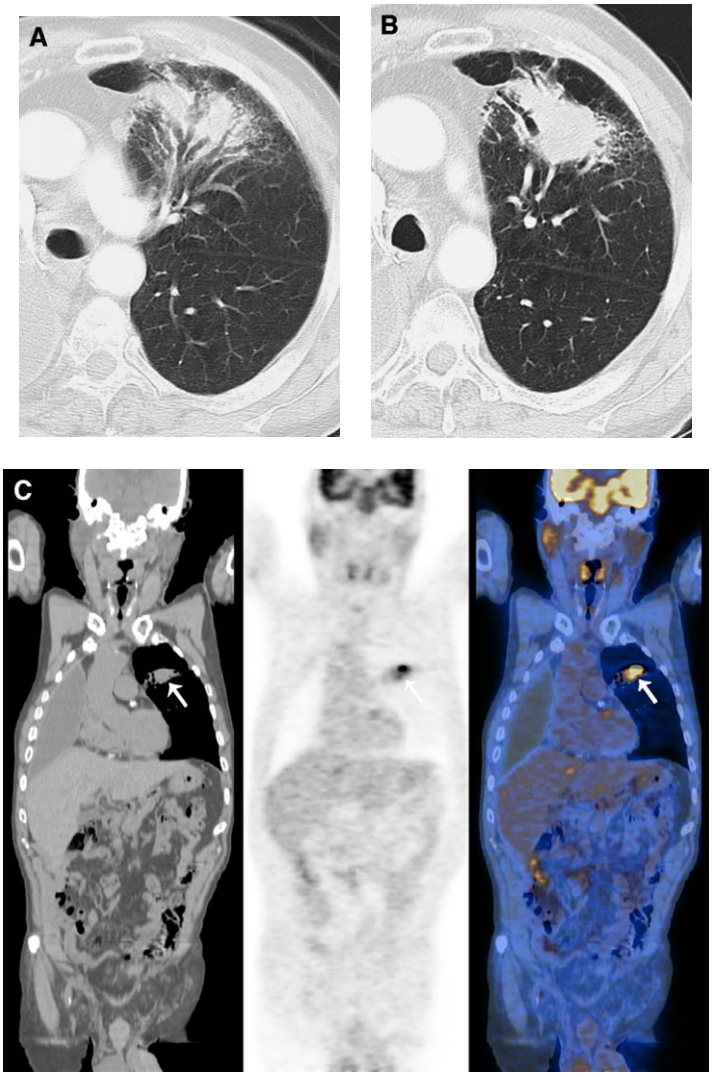

Fig. 6. A 72-year-old man who had undergone right pneumonectomy for squamous cell carcinoma developed a new left upper lobe nodule that was treated with radiation therapy. (*A*) Follow-up CT at 6 months demonstrated signs of evolving radiation fibrosis, manifesting as linear opacities associated with volume loss and traction bronchiectasis. (*B*) Follow-up CT at 14 months demonstrated a new area of mass-like consolidation within the radiation fibrosis. (*C*) Coronal fused PET-CT shows FDG activity within the mass (*arrow*) consistent with recurrent disease.

ing to tumor cell type. Sites of spread include the adrenal glands, bones, brain, liver, and more distant lymph nodes. Systemic metastases are reported to occur more commonly with adenocarcinoma than with squamous cell carcinoma [53]. The presence of distant metastatic spread implies stage IV lung cancer and generally indicates inoperable disease, although resection of isolated metastases can sometimes improve survival. Conventional methods to evaluate for metastases include a combination of biochemical markers (alkaline phosphatase, liver function tests); bone scintigraphy; and imaging of the brain with CT or MR imaging. The decision to search for metastatic disease, however, is not uniform. The risk of occult metastases in patients with early stage (T1 or 2, N0) lung cancer is less than 1% and routine evaluation for metastases in these patients is not advocated [68,69]. Tumor staging in some institutions may be limited to a chest CT and laboratory tests in patients with early stage disease and without extrathoracic symptoms or signs. Other centers may use a more complex range of imaging examinations in asymptomatic patients

with early stage lung cancer [54,55]. One of the commonest sites for metastatic disease is the adrenal gland, occurring in up to 20% of patients with NSCLC at initial presentation [56–59]. Staging thoracic CT examinations are normally extended caudally to include an assessment of the adrenal glands. Benign adrenal adenomas are present in 2% to 10% of the population [4], however, and the detection of an adrenal nodule by CT in the course of lung cancer staging often requires further evaluation. On a non–contrast-enhanced CT scan, an average Hounsfield unit density reading of less than 10 HU in an adrenal nodule indicates a benign adenoma with a high degree of confidence, whereas a density of greater than 20 HU is associated with a high probability of malignancy [60,61]. Unfortunately, most staging CT examinations are performed with intravenous contrast. In such cases, adrenal nodules can undergo further evaluation by delayed CT examination (a decrease in attenuation of at least 50% 10 minutes following intravenous contrast injection indicating benign disease), chemical-shift MR imaging, PET, or fused PET-CT imaging [60–63]. In cases where metastatic disease cannot be excluded by imaging and where such disease affects clinical management, adrenal nodules should be biopsied. It is important to determine the presence of metastatic disease in the adrenal glands, because resection of isolated adrenal metastases has been reported to improve survival, whether such metastases are synchronous or metachronous [64]; in patients who are not candidates for adrenal surgery, radiofrequency ablation has shown promise as an alternative therapy [65].

Extending the chest CT inferiorly to include the adrenal glands also allows most of the liver to be imaged; however, such images are generally not acquired during the phase of optimal contrast enhancement (the portal venous phase). Suspicious lesions need to undergo further evaluation with multiphasic CT or with MR imaging of the liver. Metastatic disease to the liver is uncommon in early stage disease, and the necessity for dedicated liver imaging is controversial. The liver is included in whole-body staging, which is increasingly being performed with fused PET–CT imaging.

Metastases to the brain may be present in up to 18% of patients with NSCLC at initial presentation [53,66–68], but most patients have suggestive symptoms and signs. Resection of isolated metachronous cerebral metastases can improve survival [69,70]; when disease is synchronous, surgical results are more disappointing [69,70]. In the absence of a clinical suspicion of cerebral metastatic disease, systematic imaging of the brain may not be performed [71,72]. MR imaging is more sensitive than CT imaging in the detection of cerebral metastases [73]. Metastases may also be detected by whole-body PET imaging if the entire brain is included as part of the staging scan [74], but it is not certain whether this technique is as sensitive as dedicated imaging of the brain with brain CT, MR imaging, or PET [75,76].

Bone metastases occur in up to 13% of patients with NSCLC at initial presentation [77]. Occult micrometastases to the bone marrow have been shown to be present in up to 34% of patients, but are not an independent marker of long-term prognosis [78]. In patients with early stage NSCLC, imaging of the skeleton has traditionally been reserved for patients with symptoms or signs to suggest bone involvement [53,72,79–81]. A recent PET–CT study has shown, however, that skeletal metastases can occur with NSCLC in the absence of clinical suspicion [77]. In cases of advanced local disease or where bone metastases are already known to exist, additional unsuspected sites of skeletal metastatic involvement can occur; timely detection of such disease is of major palliative importance where such metastases occur in the spine or weight-bearing bones, to avoid fracture or paralysis. Methods of whole-body imaging for metastases include technetium-99m bone scintigraphy, whole-body MR imaging, and, increasingly, whole-body fused PET–CT [82,83]. There have been no direct comparisons of the diagnostic performances of whole-body MR imaging and FDG–PET or PET–CT, however, in the detection of bone metastases from NSCLC in adults. The optimal method for evaluation of bone metastases and the future role of possible fused PET–MR imaging awaits further research.

Increasing experience with the use of fused PET–CT is changing the understanding of the patterns and incidence of metastatic spread. In patients with NSCLC initially selected for curative resection using standard tumor staging, fused PET–CT has been reported to detect occult metastatic disease in 11% to 14% of patients, and alters patient management in up to 40% of cases [41,43,84]. The addition of PET–CT to conventional NSCLC work-up has been found to change the initial tumor stage in 20% of cases [85], and can reduce the incidence of futile thoracotomies from 41% to 21% [86]. Although there have only been a limited number of randomized, controlled studies on the use of PET–CT as a staging tool for NSCLC [85,86], whole-body PET–CT imaging is being increasingly used as a single staging test for NSCLC in centers where it is available. Despite the fact that PET–CT imaging may increase the need for invasive diagnostic procedures, such as mediastino-

scopy to exclude false-positive disease, its reduction of inappropriate surgery and other imaging tests means that it is a cost-effective tool [87]. Since 2001, PET has been reimbursed through Medicare for the diagnosis, staging, and restaging of NSCLC [88]. One caveat to the effectiveness of PET–CT imaging applies to bronchoalveolar carcinoma, which is associated with false-negative findings at PET–CT in up to 40% of cases [89].

Follow-up imaging in lung cancer

Conventional surveillance of tumor response to chemotherapy or radiotherapy and of tumor recurrence after surgery has been based on anatomic changes depicted by CT imaging. Complications of therapy must be identified, and signs of recurrent or metastatic tumor must be differentiated from the range of normal CT appearances in the thorax following surgery and radiotherapy.

The optimal interval for performing surveillance CT scans has not been determined, and follow-up imaging schedules are often based on local preferences, ranging from every month to every 6 months. In individual cases, clinical suspicion of complications or disease recurrence may lead to earlier scan requests, which may heighten the radiologist's suspicion of significant disease.

Following surgery, adequate interpretation of follow-up scans depends on an understanding of the different surgical interventions used. In patients who have undergone pneumonectomy, recurrent tumor may be suggested by an enlarging hydrothorax or the appearance of a new air-fluid level within the hydrothorax. Following lobectomy or sleeve resection, distortion of the normal bronchial anatomy can make CT interpretation difficult: the interval appearance of pulmonary nodules, subtle changes in soft tissue at the hilum, the appearance of new bronchial stenosis, or enlarging hilar or mediastinal lymph nodes may suggest disease recurrence. Some surgeons may use muscle flaps from the latissimus dorsi, serratus anterior, or intercostal muscles to wrap around the sites of anastomosis to reduce the risk of ischemia or bronchial air leaks (Fig. 7), particularly following radiation therapy [90]; the normal appearances of such myoplasties must be recognized and not be confused with recurrent tumor [91].

The range of appearances of radiation injury of the lung following radiotherapy has been well described and occurs in an acute phase, termed "pneumonitis," and a chronic phase, termed "fibrosis." Pneumonitis presents as ground glass opacities within the first 3 months following completion of therapy, but also may be intermixed with irregular or poorly marginated nodules (Fig. 8) [92,93]. Radiation fibrosis presents with volume loss associated with bronchiectasis and consolidation that conforms to the site of irradiation [92,93]. Radiation fibrosis usually evolves from pneumonitis and is well established by 1 to 2 years. Such findings must be differentiated from infection, recurrent tumor, and lymphangitis. Detec-

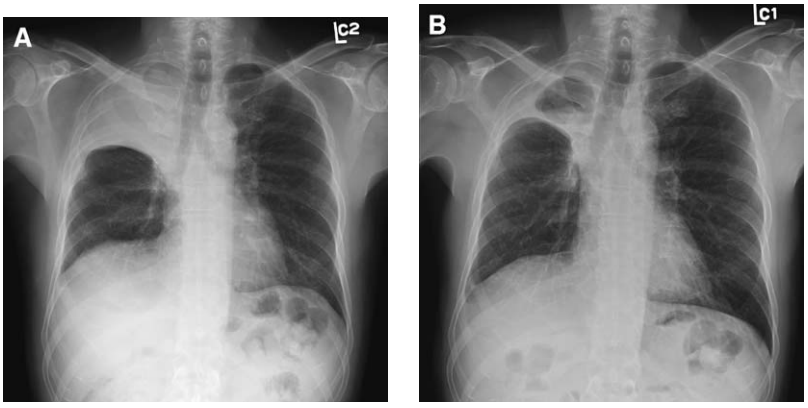

Fig. 7. Bronchopleural fistula in a 57-year-old man who underwent right upper lobectomy for poorly differentiated non–small cell lung cancer. (*A*) Posteroanterior chest radiograph 3 months after surgery demonstrates diffuse opacification of the residual apical pleural space in the right hemithorax consistent with prior surgery. (*B*) Posteroanterior chest radiograph 9 months after surgery demonstrates the presence of a gas collection within the previously opacified pleural space, which was secondary to the development of a bronchopleural fistula. The fistula resolved after treatment incorporating pleural drainage.

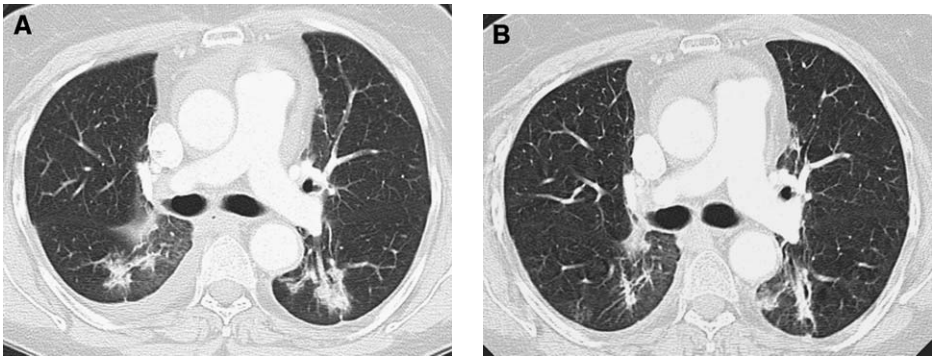

Fig. 8. Surveillance by CT of a 57-year-old woman who underwent radiation therapy for a right upper lobe bronchoalveolar cell carcinoma with metastatic mediastinal adenopathy. (*A*) Axial image 4 months after completion of radiation therapy demonstrates ground glass opacities with a nodular component that is consistent with radiation pneumonitis. (*B*) Axial image 12 months after completion of radiation therapy shows organization of the ground glass opacities and nodules into fibrosis, indicated by volume loss, bronchiectasis, and consolidation.

tion of tumor recurrence within areas of radiation pneumonitis can be difficult but may be suggested by filling in of air bronchograms or by an area of enlarging consolidation within a region of established fibrosis [94]. Complications of radiation therapy also need to be recognized, such as pericarditis, myocarditis, cardiomyopathies, and pleural and pericardial effusions [95–99], which may require aspiration to exclude the possibility of malignant disease. Pleural effusions usually develop within 6 months after completion of therapy [95,98]; if they develop after 6 months, continue to increase in size, or present as large effusions, then a thoracentesis to differentiate benign from malignant disease may be required. The development of pericardial effusions usually occurs within 6 to 9 months after completion of therapy [96,97,99].

Typically, areas of radiation pneumonitis conform to a two-dimensional field of irradiation, exhibiting relatively sharp interfaces with normal nonirradiated lung, do not conform to normal segmental or lobar anatomy, and may cross fissures [92,93]. More recently, three-dimensional conformal therapy has been developed to limit damage to normal tissue, using multiple irradiation planes to concentrate most of the radiation energy at the tumor site with relative sparing of normal adjacent tissue. This has been reported to result in improved local tumor control [100–103], although the impact on long-term survival is not yet clear [104]. These newer techniques result in CT appearances that differ from the more typical findings of radiation pneumonitis, being more centripetal in configuration with edges that are less well defined [105–107]. The resultant lung consolidation may appear more mass-like. Awareness of the method of radiotherapy in individual patients and knowledge of the range of possible CT appearances can help interpretation.

Treatment with radiotherapy, chemotherapy, or a combination, either concurrently or sequentially, increases the risk of toxic side effects. An important aspect of the radiologist's role in treating the patient with NSCLC is the detection of complications from chemotherapy. The most common complications are infections and drug toxicity and radiologists can aid in early detection. Both can present with fever, malaise, and cough. The lung is the most common site of serious infections in cancer patients and etiologies include bacterial, fungal, or viral sources, all of which can be detected with imaging.

Because drug toxicity can mimic infections, pneumonitis, or tumor, a high index of suspicion is needed for detection [108]. Drug toxicity presents radiologically as ground glass opacities, interstitial opacities, or fibrosis. The most common histopathologic patterns include noncardiogenic pulmonary edema; diffuse alveolar damage; nonspecific interstitial pneumonia; cryptogenic organizing pneumonia (bronchiolitis obliterans organizing pneumonia); pulmonary hemorrhage; or fibrosis [108]. Although traditionally associated with chemotherapeutic drugs, such as bleomycin, busulfan, carmustine, methotrexate, cyclophosphamide, and Ara-C, newer therapeutic agents commonly used in lung cancer, such as gemcitabine [109], etoposide [110], and paclitaxel [111], have been reported to cause lung injury. Another example is the new agent gefitinib (Iressa), a new antiepidermal growth factor useful in the

treatment of NSCLC, which has been reported to cause pulmonary fibrosis in a small percentage of patients [112], a complication that should be recognized by radiologists.

Fused PET–CT can differentiate between viable tumor and scar tissue resulting from surgery, radiotherapy, and chemotherapy, and is becoming increasingly important in the follow-up surveillance of patients with NSCLC [113–116]. It is useful both for assessing tumor response to therapy and for detecting recurrent tumor. A baseline PET–CT study is of particular importance for monitoring tumor response to chemotherapy: a reduction in maximum standard uptake value (SUV) of greater than 50% on follow-up PET–CT has been shown to be a better predictor of survival than conventional anatomic imaging criteria [113]. Weber et al [114] have demonstrated improved survival of 44% for patients who had a 20% fall in maximum SUV after one cycle of chemotherapy, compared with only 10% for patients who did not respond. Because SUV values vary according to methods of image acquisition, follow-up of patients with PET–CT should be performed on the same scanner.

In the surveillance for recurrent tumor, fused PET–CT imaging is useful for its ability to identify viable metabolically active tissue located within areas of radiation fibrosis or postoperative scarring, and for the early detection of unsuspected metastatic disease. Nevertheless, the specificity of PET–CT for discriminating recurrent tumor from radiation fibrosis is somewhat limited, because radiation fibrosis itself can display FDG avidity [116].

Radiologists' role in cancer care

There are many aspects of imaging and treating patients with NSCLC that have involved the radiologist in caring for these patients. Improvements in imaging techniques, in particular the development of fused PET-CT imaging, are changing the understanding of tumor behavior and patterns of spread. Metastatic disease is being detected earlier, as is previously unsuspected and undetected disease that may influence the patient's prognosis, and limitations of conventional methods of tumor staging are being recognized. In addition, tumor response can now be monitored more closely using functional assessments, which may influence the decision to continue or change therapy at an earlier stage. Improvements in treatment, such as the emergence of newer, tumor-specific chemotherapeutic agents, development of three-dimensional conformal radiation therapy, combination treatment regiments of chemotherapy and radiotherapy to maximize tumor sensitivity and treat systemic disease [117,118], and deployment of more aggressive interventional techniques, such as isolated metastasis resection and radiofrequency ablation, have influenced the use of imaging. Optimization of all of this new information depends on a multidisciplinary approach that combines input from all professionals involved in the care of the lung cancer patient, and will necessarily change the way in which lung cancer is staged, treated, and surveilled.

Summary

The radiologist serves a critical role in the initial assessment and future follow-up of NSCLC. Accurate diagnosis and staging of the primary tumor requires an understanding of the different treatment options available, particularly where therapy involves a multidisciplinary approach involving surgeons, radiation oncologists, and medical oncologists. New developments in imaging and in treatment require greater collaboration between the different medical disciplines and are changing the understanding of tumor biology.

References

[1] Jemal A, Tiwari RC, Murray T, et al. Cancer statistics, 2004. CA Cancer J Clin 2004;54:8–29.
[2] Mountain CF. Revisions in the international system for staging lung cancer. Chest 1997;111:1710–7.
[3] Lardinois D, Weder W, Hany TF, et al. Staging of non-small-cell lung cancer with integrated positron-emission tomography and computed tomography. N Engl J Med 2003;348:2500–7.
[4] Clinical practice guidelines for the treatment of unresectable non-small-cell lung cancer. Adopted on May 16, 1997 by the American Society of Clinical Oncology. J Clin Oncol 1997;15:2996–3018.
[5] Tyldesley S, Boyd C, Schulze K, et al. Estimating the need for radiotherapy for lung cancer: an evidence-based, epidemiologic approach. Int J Radiat Oncol Biol Phys 2001;49:973–85.
[6] Zimmermann FB, Bamberg M, Molls M, et al. Radiation therapy alone in early stage non-small cell lung cancer. Semin Surg Oncol 2003;21:91–7.
[7] Eberhardt W, Stuschke M, Stamatis G. Preoperative chemoradiation approaches to locally advanced non-small-cell lung cancer: one man's pride, another man's burden? Ann Oncol 2004;15:365–7.

[8] Bhatnagar A, Flickinger JC, Bahri S, et al. Update on results of multifield conformal radiation therapy of non-small-cell lung cancer using multileaf collimated beams. Clin Lung Cancer 2002;3:259–64.
[9] Curran Jr WJ. Evolving chemoradiation treatment strategies for locally advanced non-small-cell lung cancer. Oncology (Huntingt) 2003;17:7–14.
[10] MacRae R, Choy H. Concurrent chemoradiotherapy for inoperable stage III non-small-cell lung cancer. Curr Oncol Rep 2003;5:313–7.
[11] Pretreatment evaluation of non-small-cell lung cancer. The American Thoracic Society and The European Respiratory Society. [This official statement of the American Thoracic Society and the European Respiratory Society was adopted by the ATS Board of Directors, March 1997, and by the ERS Executive Committee, April 1997, and endorsed by the American College of Chest Physicians Board of Regents]. Am J Respir Crit Care Med 1997;156:320–32.
[12] Vansteenkiste JF, Stroobants SG. Positron emission tomography in the management of non-small cell lung cancer. Hematol Oncol Clin North Am 2004;18: 269–88.
[13] Antoch G, Stattaus J, Nemat AT, et al. Non-small cell lung cancer: dual-modality PET/CT in preoperative staging. Radiology 2003;229:526–33.
[14] Deslauriers J, Gregoire J, Jacques LF, et al. Sleeve lobectomy versus pneumonectomy for lung cancer: a comparative analysis of survival and sites or recurrences. Ann Thorac Surg 2004;77:1152–6 [discussion: 1156].
[15] Mitchell JD, Mathisen DJ, Wright CD, et al. Resection for bronchogenic carcinoma involving the carina: long-term results and effect of nodal status on outcome. J Thorac Cardiovasc Surg 2001;121: 465–71.
[16] Quint LE, Francis IR. Radiologic staging of lung cancer. J Thorac Imaging 1999;14:235–46.
[17] Glazer GM, Gross BH, Quint LE, et al. Normal mediastinal lymph nodes: number and size according to American Thoracic Society Mapping. AJR Am J Roentgenol 1985;144:261–5.
[18] Webb WR, Gatsonis C, Zerhouni EA, et al. CT and MR imaging in staging non-small cell bronchogenic carcinoma: report of the Radiologic Diagnostic Oncology Group. Radiology 1991;178:705–13.
[19] Padovani B, Mouroux J, Seksik L, et al. Chest wall invasion by bronchogenic carcinoma: evaluation with MR imaging. Radiology 1993;187:33–8.
[20] Martini N, Heelan R, Westcott J, et al. Comparative merits of conventional, computed tomographic, and magnetic resonance imaging in assessing mediastinal involvement in surgically confirmed lung carcinoma. J Thorac Cardiovasc Surg 1985;90:639–48.
[21] McLoud TC. CT of bronchogenic carcinoma: indeterminate mediastinal invasion. Radiology 1989;173: 15–6.
[22] Muller NL, Miller RR. Neuroendocrine carcinomas of the lung. Semin Roentgenol 1990;25:96–104.
[23] Jett JR, Scott WJ, Rivera MP, et al. Guidelines on treatment of stage IIIB non-small cell lung cancer. Chest 2003;123:221S–5S.
[24] Grunenwald DH. Surgery for advanced stage lung cancer. Semin Surg Oncol 2000;18:137–42.
[25] Burnett RJ, Wood DE. The new lung cancer staging system: What does it mean? Surg Oncol Clin N Am 1999;8:231–44.
[26] Leong SS, Lima CMR, Sherman CA, et al. The 1997 international staging system for non-small cell lung cancer. Chest 1999;115:242–8.
[27] Society AC. Cancer facts and figures—1997. Racial and ethnic patterns. Atlanta: American Cancer Society; 1997.
[28] Mountain CF. Prognostic implications of the International Staging System for Lung Cancer. Semin Oncol 1988;15:236–45.
[29] Erasmus JJ, McAdams HP, Rossi SE, et al. FDG PET of pleural effusions in patients with non-small cell lung cancer. AJR Am J Roentgenol 2000;175: 245–9.
[30] Bury T, Paulus P, Dowlati A, et al. Evaluation of pleural diseases with FDG-PET imaging: preliminary report. Thorax 1997;52:187–9.
[31] Carretta A, Landoni C, Melloni G, et al. 18-FDG positron emission tomography in the evaluation of malignant pleural diseases - a pilot study. Eur J Cardiothorac Surg 2000;17:377–83.
[32] Schaffler GJ, Wolf G, Schoellnast H, et al. Non-small cell lung cancer: evaluation of pleural abnormalities on CT scans with 18F FDG PET. Radiology 2004; 231:858–65.
[33] Chavaudra J, Bridier A. Definition of volumes in external radiotherapy: ICRU reports 50 and 62. Cancer Radiother 2001;5:472–8.
[34] Purdy JA. Current ICRU definitions of volumes: limitations and future directions. Semin Radiat Oncol 2004;14:27–40.
[35] WHO handbook for reporting results of cancer treatment. Offset Publication No. 48. Geneva: World Health Organization; 1979.
[36] Miller AB, Hoogstraten B, Staquet M, et al. Reporting results of cancer treatment. Cancer 1981;47: 207–14.
[37] Therasse P, Arbuck SG, Eisenhauer EA, et al. New guidelines to evaluate the response to treatment in solid tumors. European Organization for Research and Treatment of Cancer, National Cancer Institute of the United States, National Cancer Institute of Canada. J Natl Cancer Inst 2000;92:205–16.
[38] Mountain CF, Dresler CM. Regional lymph node classification for lung cancer staging. Chest 1997; 111:1718–23.
[39] Naruke T, Suemasu K, Ishikawa S. Lymph node mapping and curability at various levels of metastasis in resected lung cancer. J Thorac Cardiovasc Surg 1978;76:832–9.
[40] Dales RE, Stark RM, Raman S. Computed tomography to stage lung cancer: approaching a contro-

versy using meta-analysis. Am Rev Respir Dis 1990; 141:1096–101.

[41] Dwamena BA, Sonnad S, Angobaldo S, et al. Metastases from non-small cell lung cancer. Mediastinal staging in the 1990's: meta-analytic comparison of PET and CT. Radiology 1999;213:530–6.

[42] Kalff V, Hicks RJ, MacManus MP, et al. Clinical impact of (18)F fluorodeoxyglucose positron emission tomography in patients with non-small-cell lung cancer: a prospective study. J Clin Oncol 2001;19: 111–8.

[43] Dietlein M, Weber K, Gandjour A, et al. Cost-effectiveness of FDG-PET for the management of solitary pulmonary nodules: a decision analysis based on cost reimbursement in Germany. Eur J Nucl Med 2000;27:1441–56.

[44] Patz Jr EF, Lowe VJ, Goodman PC, et al. Thoracic nodal staging with PET imaging with 18FDG in patients with bronchogenic carcinoma. Chest 1995; 108:1617–21.

[45] Steinert H, Hauser M, Allenman F, et al. Non-small cell lung cancer: nodal staging with FDG PET versus CT with correlative lymph node mapping and sampling. Radiology 1997;202:441–6.

[46] Wahl RL, Quint LE, Greenough RL, et al. Staging of mediastinal non-small cell lung cancer with FDG PET, CT, and fusion images: preliminary prospective evaluation. Radiology 1994;191:371–7.

[47] von Haag DW, Follette DM, Roberts PF, et al. Advantages of positron emission tomography over computed tomography in mediastinal staging of non-small cell lung cancer. J Surg Res 2002;103: 160–4.

[48] Vansteenkiste JF, Stroobants SG, De Leyn PR, et al. Lymph node staging in non-small-cell lung cancer with FDG-PET scan: a prospective study on 690 lymph node stations from 68 patients. J Clin Oncol 1998;16:2142–9.

[49] Tahara RW, Lackner RP, Graver LM. Is there a role for routine mediastinoscopy in patients with peripheral T1 lung cancers? Am J Surg 2000;180:488–91 [discussion: 491].

[50] Seely JM, Mayo JR, Miller RR, et al. T1 Lung cancer: prevalence of mediastinal nodal metastases and diagnostic accuracy of CT. Radiology 1993;186: 129–32.

[51] Choi YS, Shim YM, Kim J, et al. Mediastinoscopy in patients with clinical stage I non-small cell lung cancer. Ann Thorac Surg 2003;75:364–6.

[52] Bradley J, Thorstad WL, Mutic S, et al. Impact of FDG-PET on radiation therapy volume delineation in non-small-cell lung cancer. Int J Radiat Oncol Biol Phys 2004;59:78–86.

[53] Salvatierra A, Baamonde C, Llamas JM, et al. Extrathoracic staging of bronchogenic carcinoma. Chest 1990;97:1052–8.

[54] Chemotherapy in non-small cell lung cancer: a meta-analysis using updated data on individual patients from 52 randomised clinical trials. Non-small Cell Lung Cancer Collaborative Group. BMJ 1995;311: 899–909.

[55] Wong J, Haramati LB, Rozenshtein A, et al. Non-small-cell lung cancer: practice patterns of extrathoracic imaging. Acad Radiol 1999;6:211–5.

[56] Nielsen MEJ, Heaston DK, Dunnick NR, et al. Preoperative CT evaluation of adrenal glands in non-small cell bronchogenic carcinoma. AJR Am J Roentgenol 1982;139:317–20.

[57] Oliver TWJ, Bernardino ME, Miller JI, et al. Isolated adrenal masses in non-small-cell bronchogenic carcinoma. Radiology 1984;153:217–8.

[58] Pagani JJ. Normal adrenal glands in small cell lung carcinoma: CT-guided biopsy. AJR Am J Roentgenol 1983;140:949–51.

[59] Pagani JJ. Non-small cell lung carcinoma adrenal metastases. Cancer 1984;53:1058–60.

[60] Mayo-Smith WW, Boland GW, Noto RB, et al. State-of-the-art adrenal imaging. Radiographics 2001;21: 995–1012.

[61] Boland GW, Lee MJ, Gazelle GS, et al. Characterization of adrenal masses using unenhanced CT: an analysis of the CT literature. AJR Am J Roentgenol 1998;171:201–4.

[62] Gupta NC, Graeber GM, Tamim WJ, et al. Clinical utility of PET-FDG imaging in differentiation of benign from malignant adrenal masses in lung cancer. Clin Lung Cancer 2001;3:59–64.

[63] Erasmus JJ, Patz EF, McAdams HP, et al. Evaluation of adrenal masses in patients with bronchogenic carcinoma by using 18F-fluorodeoxyglucose positron emission tomography. AJR Am J Roentgenol 1997; 168:1357–60.

[64] Porte H, Siat J, Guibert B, et al. Resection of adrenal metastases from non-small cell lung cancer: a multicenter study. Ann Thorac Surg 2001;71:981–5.

[65] Mayo-Smith WW, Dupuy DE. Adrenal neoplasms: CT-guided radiofrequency ablation–preliminary results. Radiology 2004;231:225–30.

[66] Hooper RG, Tenholder MF, Underwood GH, et al. Computed tomographic scanning of the brain in initial staging of bronchogenic carcinoma. Chest 1984; 85:774–6.

[67] Mintz BJ, Tuhrim S, Alexander S, et al. Intracranial metastases in the initial staging of bronchogenic carcinoma. Chest 1984;86:850–3.

[68] Newman SJ, Hansen HH. Proceedings: Frequency, diagnosis, and treatment of brain metastases in 247 consecutive patients with bronchogenic carcinoma. Cancer 1974;33:492–6.

[69] Billing PS, Miller DL, Allen MS, et al. Surgical treatment of primary lung cancer with synchronous brain metastases. J Thorac Cardiovasc Surg 2001; 122:548–53.

[70] Burt M, Wronski M, Arbit E, et al. Resection of brain metastases from non-small-cell lung carcinoma. Results of therapy. Memorial Sloan-Kettering Cancer Center Thoracic Surgical Staff. J Thorac Cardiovasc Surg 1992;103:399–410 [discussion: 391–410].

[71] Colice GL, Birkmeyer JD, Black WC, et al. Cost-effectiveness of head CT in patients with lung cancer without clinical evidence of metastases. Chest 1995;108:1264–71.
[72] Silvestri GA, Littenberg B, Colice GL. The clinical evaluation for detecting metastatic lung cancer. Am J Respir Crit Care Med 1995;152:225–30.
[73] Yokoi K, Kamiya N, Matsuguma H, et al. Detection of brain metastasis in potentially operable non-small cell lung cancer: a comparison of CT and MRI. Chest 1999;115:714–9.
[74] Marom EM, McAdams HP, Erasmus JJ, et al. Staging non-small cell lung cancer with whole body positron emission tomography. Radiology 1999;212: 803–9.
[75] Brink I, Schumacher T, Mix M, et al. Impact of [(18)F]FDG-PET on the primary staging of small-cell lung cancer. Eur J Nucl Med Mol Imaging 2004; 31:1614–20.
[76] Larcos G, Maisey MN. FDG-PET screening for cerebral metastases in patients with suspected malignancy. Nucl Med Commun 1996;17:197–8.
[77] Bury T, Barreto A, Daenen F, et al. Fluorine-18 deoxyglucose positron emission tomography for the detection of bone metastases in patients with non-small cell lung cancer. Eur J Nucl Med 1998;25: 1244–7.
[78] Hsu CP, Shai SE, Hsia JY, et al. Clinical significance of bone marrow microinvolvement in non-small cell lung carcinoma. Cancer 2004;100:794–800.
[79] Little AG, Stitik FP. Clinical staging of patients with non-small cell lung cancer. Chest 1990;97:1431–8.
[80] Michel F, Soler M, Imhof E, et al. Initial staging of non-small cell lung cancer: value of routine radioisotope bone scanning. Thorax 1991;46:469–73.
[81] Stitik FP. Staging of lung cancer. Radiol Clin North Am 1990;28:619–30.
[82] Eustace S, Tello R, DeCarvalho V, et al. A comparison of whole-body turboSTIR MR imaging and planar 99mTc-methylene diphosphonate scintigraphy in the examination of patients with suspected skeletal metastases. AJR Am J Roentgenol 1997; 169:1655–61.
[83] Cheran SK, Herndon II JE, Patz Jr EF. Comparison of whole-body FDG-PET to bone scan for detection of bone metastases in patients with a new diagnosis of lung cancer. Lung Cancer 2004;44:317–25.
[84] Valk PE, Pounds TR, Hopkins DM, et al. Staging non-small cell lung cancer by whole-body positron emission tomographic imaging. Ann Thorac Surg 1995;60:1573–82.
[85] Viney RC, Boyer MJ, King MT, et al. Randomized controlled trial of the role of positron emission tomography in the management of stage I and II non-small-cell lung cancer. J Clin Oncol 2004;22: 2357–62.
[86] van Tinteren H, Hoekstra OS, Smit EF, et al. Effectiveness of positron emission tomography in the preoperative assessment of patients with suspected non-small-cell lung cancer: the PLUS multicentre randomised trial. Lancet 2002;359:1388–93.
[87] Verboom P, van Tinteren H, Hoekstra OS, et al. Cost-effectiveness of FDG-PET in staging non-small cell lung cancer: the PLUS study. Eur J Nucl Med Mol Imaging 2003;30:1444–9.
[88] Cave L. HCFA approves Medicare coverage of PET scans. J Natl Cancer Inst 2001;93:177.
[89] Heyneman LE, Patz EF. PET imaging in patients with bronchioloalveolar cell carcinoma. Lung Cancer 2002;38:261–6.
[90] Regnard JF, Icard P, Deneuville M, et al. Lung resection after high doses of mediastinal radiotherapy (sixty grays or more): reinforcement of bronchial healing with thoracic muscle flaps in nine cases. J Thorac Cardiovasc Surg 1994;107:607–10.
[91] Bhalla M, Wain JC, Shepard JA, et al. Surgical flaps in the chest: anatomic considerations, applications, and radiologic appearance. Radiology 1994;192: 825–30.
[92] Libshitz HI, Shuman LS. Radiation-induced pulmonary change: CT findings. J Comput Assist Tomogr 1984;8:15–9.
[93] Choi YW, Munden RF, Erasmus JJ, et al. Effects of radiation therapy on the lung: radiologic appearances and differential diagnosis. Radiographics 2004;24: 985–97 [discussion: 998].
[94] Libshitz HI, Sheppard DG. Filling in of radiation therapy-induced bronchiectatic change: a reliable sign of locally recurrent lung cancer. Radiology 1999;210: 25–7.
[95] Bachman AL, Macken K. Pleural effusions following supervoltage radiation for breast carcinoma. Radiology 1959;72:699–709.
[96] Carmel RJ, Kaplan HS. Mantle irradiation in Hodgkin's disease: an analysis of technique, tumor eradication, and complications. Cancer 1976;37: 2813–25.
[97] Cosset JM, Henry-Amar M, Pellae-Cosset B, et al. Pericarditis and myocardial infarctions after Hodgkin's disease therapy. Int J Radiat Oncol Biol Phys 1991;21:447–9.
[98] Libshitz HI, DuBrow RA, Loyer EM, et al. Radiation change in normal organs: an overview of body imaging. Eur Radiol 1996;6:786–95.
[99] Stewart JR, Fajardo LF, Gillette SM, et al. Radiation injury to the heart. Int J Radiat Oncol Biol Phys 1995;31:1205–11.
[100] Armstrong JG. Three-dimensional conformal radiotherapy: precision treatment of lung cancer. Chest Surg Clin N Am 1994;4:29–43.
[101] Emami B. Three-dimensional conformal radiation therapy in bronchogenic carcinoma. Semin Radiat Oncol 1996;6:92–7.
[102] Graham MV, Matthews JW, Harms Sr WB, et al. Three-dimensional radiation treatment planning study for patients with carcinoma of the lung. Int J Radiat Oncol Biol Phys 1994;29:1105–17.
[103] Marks LB, Sibley G. The rationale and use of three-

dimensional radiation treatment planning for lung cancer. Chest 1999;116:539S–49S.
[104] Metz JM, Glatstein E. Local control versus systemic control: is the cart coming before the oncologic horse? Cancer J 2000;6:66–8.
[105] Koenig TR, Munden RF, Erasmus JJ, et al. Radiation injury of the lung after three-dimensional conformal radiation therapy. AJR Am J Roentgenol 2002;178: 1383–8.
[106] Takeda T, Takeda A, Kunieda E, et al. Radiation injury after hypofractionated stereotactic radiotherapy for peripheral small lung tumors: serial changes on CT. AJR Am J Roentgenol 2004;182:1123–8.
[107] Aoki T, Nagata Y, Negoro Y, et al. Evaluation of lung injury after three-dimensional conformal stereotactic radiation therapy for solitary lung tumors: CT appearance. Radiology 2004;230:101–8.
[108] Erasmus JJ, McAdams HP, Rossi SE. Drug-induced lung injury. Semin Roentgenol 2002;37:72–81.
[109] Boiselle PM, Morrin MM, Huberman MS. Gemcitabine pulmonary toxicity: CT features. J Comput Assist Tomogr 2000;24:977–80.
[110] Gurjal A, An T, Valdivieso M, et al. Etoposide-induced pulmonary toxicity. Lung Cancer 1999;26: 109–12.
[111] Ramanathan RK, Reddy VV, Holbert JM, et al. Pulmonary infiltrates following administration of paclitaxel. Chest 1996;110:289–92.
[112] Cohen MH, Williams GA, Sridhara R, et al. United States Food and Drug Administration Drug approval summary: gefitinib (ZD1839; Iressa) tablets. Clin Cancer Res 2004;10:1212–8.
[113] Vansteenkiste JF, Stroobants SG, De Leyn PR, et al. Potential use of FDG-PET scan after induction chemotherapy in surgically staged IIIa-N2 non-small-cell lung cancer: a prospective pilot study. The Leuven Lung Cancer Group. Ann Oncol 1998;9:1193–8.
[114] Weber WA, Petersen V, Schmidt B, et al. Positron emission tomography in non-small-cell lung cancer: prediction of response to chemotherapy by quantitative assessment of glucose use. J Clin Oncol 2003; 21:2651–7.
[115] Stroobants S, Verschakelen J, Vansteenkiste J. Value of FDG-PET in the management of non-small cell lung cancer. Eur J Radiol 2003;45:49–59.
[116] Ryu JS, Choi NC, Fischman AJ, et al. FDG-PET in staging and restaging non-small cell lung cancer after neoadjuvant chemoradiotherapy: correlation with histopathology. Lung Cancer 2002;35:179–87.
[117] Sause WT, Scott C, Taylor S, et al. Radiation Therapy Oncology Group (RTOG) 88–08 and Eastern Cooperative Oncology Group (ECOG) 4588: preliminary results of a phase III trial in regionally advanced, unresectable non-small-cell lung cancer. J Natl Cancer Inst 1995;87:198–205.
[118] Jeremic B, Shibamoto Y, Acimovic L, et al. Hyperfractionated radiation therapy with or without concurrent low-dose daily carboplatin/etoposide for stage III non-small-cell lung cancer: a randomized study. J Clin Oncol 1996;14:1065–70.

ELSEVIER
SAUNDERS

Radiol Clin N Am 43 (2005) 589 – 599

RADIOLOGIC
CLINICS
of North America

Imaging of Interstitial Lung Disease

Sudhakar Pipavath, MD*, J. David Godwin, MD

Department of Radiology, University of Washington Medical Center, Radiology Box 357115, Seattle, WA 98195-7115, USA

The pulmonary interstitium is affected by a broad group of diseases. Of roughly 150 diseases, only a small subset is encountered regularly. Idiopathic interstitial pneumonias, sarcoidosis, Langerhans cell histiocytosis (LCH), hypersensitivity pneumonitis, and pneumoconiosis are among the most common.

The consensus statement on interstitial pneumonias further classifies interstitial lung diseases into idiopathic interstitial pneumonias, diffuse parenchymal lung disease from known causes (eg, collagen vascular diseases), granulomatous disease (sarcoidosis), and a miscellaneous group that includes lymphangioleiomyomatosis (LAM) and LCH [1].

This article presents the imaging findings in sarcoidosis, silicosis, asbestosis, LAM, LCH, collagen vascular diseases, hypersensitivity pneumonitis, and pulmonary alveolar proteinosis (PAP) (Table 1). The idiopathic interstitial pneumonias are discussed in the second article on imaging of interstitial lung disease.

Plain radiography

Plain chest radiography that uses posteroanterior and lateral chest views is an important part of the initial imaging of diffuse lung disease. The advantages of plain radiographs include low cost, high spatial resolution, and low dose of radiation. In assessing diffuse lung disease, the goals of interpreting the chest radiograph are to: (1) determine the pattern of the lung disease; (2) recognize any abnormality of lung volume; (3) note any accompanying abnormalities, such as lymphadenopathy, pleural effusion, pleural thickening, cardiomegaly, bone or joint disease, and soft-tissue calcification; and (4) note changes from previous images.

The pattern of abnormality

Common patterns include nodular, reticular, airspace disease, or a combination of these. A reticulonodular pattern is encountered most commonly. A predominantly nodular pattern is found in sarcoidosis, silicosis, coal worker's pneumoconiosis (CWP), miliary tuberculosis or fungal infection, berylliosis, and LCH. A reticular pattern is found in idiopathic pulmonary fibrosis (IPF), asbestosis, collagen vascular disease, and chronic hypersensitivity pneumonitis. Airspace filling is the dominant pattern in cryptogenic organizing pneumonia (COP), eosinophilic pneumonia, alveolar proteinosis, vasculitis, and so-called "alveolar sarcoidosis."

Lung volumes

Upper lung volume loss is found in sarcoidosis, chronic hypersensitivity pneumonitis, silicosis, CWP, ankylosing spondylitis, and radiation pneumonitis. Lower lobe volume loss is found in IPF, asbestosis, and collagen vascular disease. Lung volumes are preserved in LAM and LCH.

Accompanying abnormalities

Associated abnormalities, such as penciling of the clavicles (in rheumatoid arthritis) or dilation of the

This article originally published in *Clinics in Chest Medicine* 2004;25:455 – 65.

* Corresponding author.
E-mail address: snjp@u.washington.edu (S. Pipavath).

0033-8389/05/$ – see front matter © 2005 Elsevier Inc. All rights reserved.
doi:10.1016/j.rcl.2005.03.005

Table 1
Interstitial lung disease: dominant patterns and characteristic HRCT features

Type of interstitial lung disease	HRCT features	Dominant finding	Distribution	Characteristic pattern
Sarcoidosis	Hilar, mediastinal lymphadenopathy, 5–10 mm nodules, conglomerate nodules, and masses	Hilar/mediastinal nodes and pulmonary nodules	Upper and mid lung Perilymphatic distribution (peribronchovascular, subpleural)	Hilar, mediastinal adenopathy ± parenchymal nodules
Silicosis	Hilar, mediastinal lymphadenopathy, 5–10 mm nodules, conglomerate nodules, and masses	Noncalcified and calcified (egg-shell) lymphadenopathy and pulmonary nodules	Upper and mid lung	Hilar, mediastinal lymphadenopathy ± nodules and occupational history
Asbestosis	Interlobular and intralobular septal thickening, honeycombing, ground-glass opacity	Reticular abnormality	Basal and peripheral	Usual interstitial pneumonitis pattern with features (pleural plaques) or history of exposure
LAM	Discrete cysts, pleural effusion, pneumothorax	Cysts	Diffuse	Discrete cysts, preserved lung volume, chylous pleural effusion in a woman of reproductive age
LCH	Small nodules with or without cysts	Nodules in early stages and combined cystic and nodular or purely cystic forms in later stages	Upper and mid lung	Nodules, cysts in upper lungs; preserved lung volume; history of smoking
HP (acute)	Ground-glass opacity and air-trapping	Ground-glass opacity	Upper and mid lung	Ground-glass opacity and air-trapping
HP (subacute)	Fuzzy centrilobular nodules, Ground-glass opacity ± air-trapping	Fuzzy centrilobular nodules	Upper and mid lung	Fuzzy centrilobular nodules and air-trapping
HP (chronic)	Interlobular and intralobular septal thickening, traction bronchiectasis, and honeycombing	Fibrosis and upper lobe volume loss	Upper and mid lung	UIP pattern in upper- and mid-lung distribution
PAP	Ground-glass opacity with superimposed reticular ‘‘crazy-paving’’	Ground-glass opacity	Often central and symmetric; may have ‘‘geographic’’ margination by septa of spared lobules	Ground-glass opacity

esophagus (in progressive systemic sclerosis [PSS] or calcinous cutis, raynaud phenomenon, esophageal dysmotility, sclerodactyly, telangiectasia [CREST] syndrome) can help in diagnosis. Similarly, soft tissue calcification may be a clue to dermatomyositis, CREST syndrome, or PSS. Mediastinal lymphadenopathy can occur with sarcoidosis or PSS. Pleural effusion points to rheumatoid disease, lupus erythematosus, or LAM. Pleural plaques indicate asbestos exposure and the possibility that basal fibrosis could represent asbestosis.

Comparison with old radiographs can help to distinguish interstitial diseases—which typically run a subacute or chronic course—from acute diseases, such as infection or edema. Comparison helps in assessing progression and response to treatment.

The limitations of plain radiographs are well-known. They include obscured or hidden lung zones; limited contrast resolution, which impairs sensitivity to subtle alterations in lung density (eg, ground-glass opacity or emphysema); and overlap and superimposition of the interstitial opacities within the lung which makes it difficult to characterize their shape and distribution. These difficulties in plain radiographic interpretation of interstitial disease were demonstrated by McLoud et al [2]. They found that the correct histologic diagnosis was predicted by the first two differential diagnoses based on plain radiography in only 50% of cases. Furthermore, there was only 70% interobserver agreement in classifying the opacities and in grading severity.

High-resolution CT

The main difference between HRCT and conventional CT is the thickness of the slice, although there also are differences in image reconstruction. Conventional CT uses a slice thickness between 5 mm and 10 mm, whereas HRCT uses a thickness of 0.5 mm to 2 mm (typically 1 mm or 1.25 mm). The problem with thick slices is that all of the structures therein are imaged as if they were in a single plane. Thus, anatomic resolution is compromised and the density measurements are unreliable because the apparent density is an average made over the whole slice thickness. This degradation of density discrimination makes it difficult to detect subtle alterations of lung density, such as emphysema and ground-glass opacity.

HRCT images usually are not contiguous, but are spaced at intervals to sample different parts of the lung. The lack of contiguous images means that important findings, such as tumor nodules, can be missed. Thus, HRCT is intended for sampling of diffuse disease, rather than for scrutinizing every bit of lung; HRCT is not appropriate for all imaging tasks. Furthermore, HRCT images have to be acquired separately from conventional CT images and thus entail additional radiation dose, although low-dose HRCT can be effective. HRCT images that are acquired at 20 mA yield anatomic information that is equivalent to that obtained with 200-mA scans in most patients, without losing spatial resolution and creating streak artifacts [3]. The patient's ability to hold his breath is more critical in HRCT than conventional CT. Motion artifacts that are caused by breathing or cardiac contraction can create false positive findings, especially ground-glass opacity, pseudobronchiectasis, and double images of fissures and vessels.

A standard HRCT imaging protocol for evaluation of diffuse interstitial lung diseases includes supine and prone images in full inspiration and supine images in full expiration. Prone images are helpful in differentiating dependent atelectasis from actual lung disease. Expiratory images are useful in detecting air-trapping, which is a sign of dysfunction of small airways.

Two recent studies compared the high-resolution spiral CT scans that were obtained from a multi-slice CT scanner and sequential HRCT scans that were obtained on a single slice CT scanner [4,5]. These studies concluded that a comprehensive diagnosis is feasible in patients who have suspected focal and diffuse lung disease by obtaining a single scan (multislice scanner) instead of a two-step process. The investigators acknowledged, however, that the massive amount of data that is generated by this technology puts significant strain on any image analysis and archiving system. Until new modalities for data transfer, data archiving, and image interpretation are devised, multi-slice helical CT will remain underused.

The radiologist needs to have good clinical information to formulate a proper differential diagnosis. CT interpretation in interstitial lung disease depends on assessing the morphology and density of the lung abnormalities (eg, nodular, reticular, cystic, ground-glass) and their distribution in relationship to the secondary pulmonary lobule. HRCT is much better than conventional CT at these tasks.

A glossary of terms that is used in HRCT interpretation is provided in the article "*Standardized terms for high resolution computed tomography of the lung: a proposed glossary*" in the Journal of Thoracic Imaging [6].

The principal terms that we use in reporting HRCT scans include:

Air-trapping. Abnormal retention of gas within a lung or lung units following expiration.

Conglomerate mass. A large opacity that often encompasses bronchi and vessels in the central or parahilar lung.

Consolidation. An increase in lung opacity that results in obscuration of blood vessels.

Cyst. A clearly-marginated lucency with a wall that contains air, and no residual lung tissue. *Emphysema* is another cause of lucency in the lung, but an emphysematous space lacks clear margins and may contain some tissue strands, including blood vessels.

Ground-glass opacity. A hazy increase in lung opacity (compared with the density of normal lung) not associated with obscuration of underlying vessels.

Honeycombing. Cystic spaces ranging from several millimeters to several centimeters in diameter, characterized by thick, clearly definable fibrous walls, which typically are lined by bronchiolar epithelium.

Interlobular interstitial thickening. Abnormal thickening of the interlobular septae.

Intralobular interstitial thickening. Thickening of the intralobular interstitium, resulting in a fine reticular appearance to the lung parenchyma.

Nodule. A discrete, round, small opacity, ranging from 1 mm to 3 cm.

Reticulation. A network of linear strands of thickened interstitium.

Traction bronchiectasis. Bronchial dilation and irregularity occurring in patients who have pulmonary fibrosis, because of traction by fibrous tissue on the bronchial wall. True bronchiectasis is defined as irreversible bronchial dilation as a result of various causes other than fibrosis. Traction bronchiectasis probably does not cause much loss of bronchial function in terms of ciliary motility and bronchial toilet.

Anatomy of the secondary pulmonary lobule

HRCT interpretation depends on understanding the anatomy of the secondary pulmonary lobule (Fig. 1). This building block of the lung is a polyhedron that measures approximately 1 cm to 2.5 cm on a side and contains a few terminal bronchioles, which ultimately supply 3 to 12 acini (a pulmonary acinus is defined as the portion of the lung that is supplied by a first order respiratory bronchiole). Pulmonary arterioles accompany the bronchioles. The lobule is marginated by interlobular septa, which contain connective tissue, venules, and lymphatics.

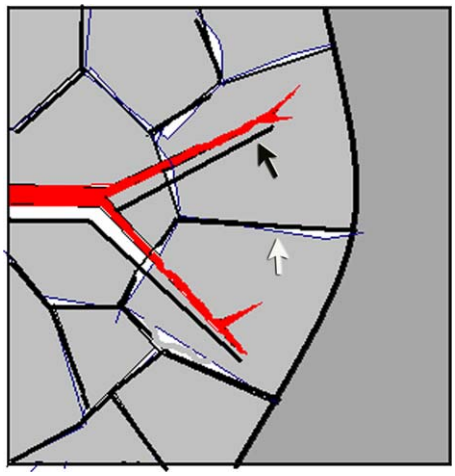

Fig. 1. Line diagram of a secondary pulmonary lobule. Note the bronchiole and pulmonary arteriole (*black arrow*) in the center and the lymphatics and venous structures (*white arrow*) in the periphery.

Sarcoidosis

Sarcoidosis is a multi-system disease with distinct intrathoracic manifestations. On plain radiographs, this disease is categorized into four stages:

Stage 0: Normal chest radiograph
Stage 1: Mediastinal and hilar lymphadenopathy
Stage 2: Lymphadenopathy with pulmonary parenchymal lesions
Stage 3: Pulmonary parenchymal lesions in the absence of hilar lymphadenopathy
Stage 4: Significant lung fibrosis with architectural distortion or bullae

Untreated patients who have stage 1 disease (Fig. 2) may have resolution of symptoms and radiographic abnormalities in 50% to 90% of cases, compared with 30% to 70% of patients who have stage 2 disease, 10% to 20% of patients who have stage 3 disease, and, as expected, 0% of patients who have stage 4 disease [7]. Many times the radiographic severity may be substantially greater than the clinical manifestations. Thus, treatment is more helpful when

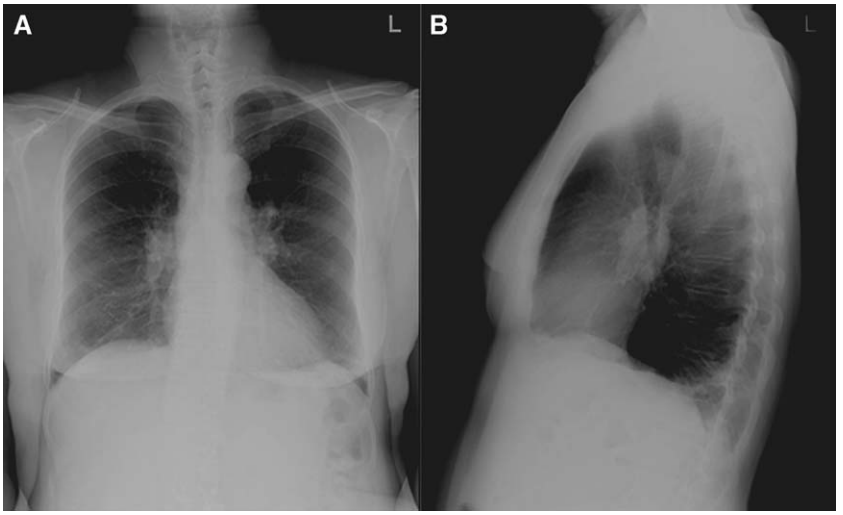

Fig. 2. Sarcoidosis. Chest radiographs (posteroanterior [*A*] and lateral [*B*]) show bilateral hilar lymphadenopathy.

based on clinical symptomatology, rather than on radiographic abnormalities. Radiographic abnormalities may precede clinical symptoms in patients who relapse after a course of treatment [8].

CT findings in sarcoidosis can be classified broadly into typical and atypical features. Typical features include bilateral hilar and mediastinal lymphadenopathy with or without calcification. Sometimes the nodes are calcified at the periphery, creating so-called "egg-shell" calcification. Interstitial abnormalities include smooth or nodular peribronchovascular interstitial thickening and small, well-defined nodules (Fig. 3) in a perilymphatic distribution in relation to the pleural surfaces, interlobular septa, and centrilobular structures. Most nodules are in the range of 5 mm to 10 mm, but miliary nodules (Fig. 4) also occur. Larger nodules and consolidation occur uncommonly. The interstitial abnormalities are concentrated in the mid and upper lungs. In later stages, septal thickening, traction bronchiectasis, and honeycombing (Fig. 5) may occur. In some cases of severe stage 4 disease, conglomerate masses develop near the hila with surrounding paracitricial emphysema. These lesions resemble progressive massive fibrosis in complicated silicosis.

An uncommon pattern of sarcoidosis is the "acinar," "alveolar," or "nummular" (Fig. 6) form. Acinar sarcoid carries a better prognosis than the reticular form. Ipsilateral hilar lymphadenopathy may be associated with this form.

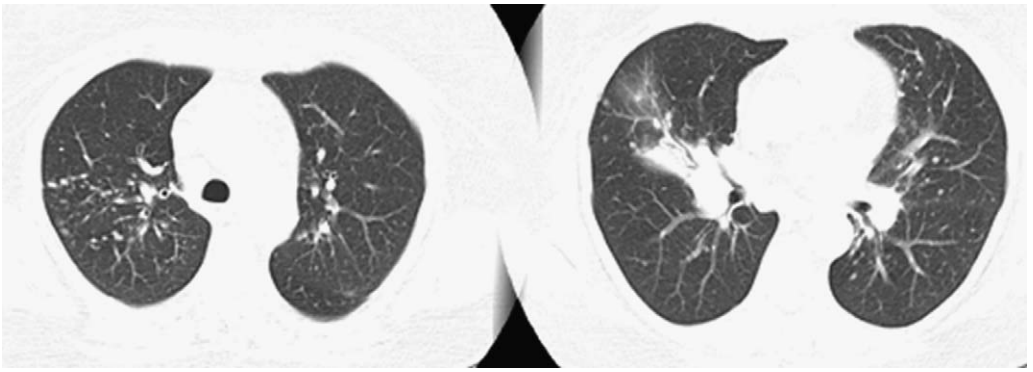

Fig. 3. Sarcoidosis. CT shows 5- to 10-mm nodules in random distribution. Also note endobronchial disease which is responsible for volume loss in the middle lobe.

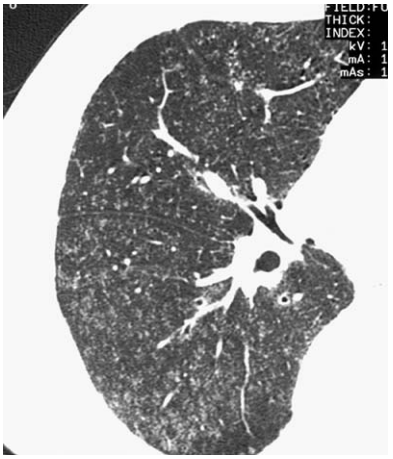

Fig. 4. Sarcoidosis. HRCT shows miliary nodules, an uncommon but distinctive pattern of sarcoidosis. (Courtesy of J. Takasugi, MD, Seattle, WA.)

Solitary pulmonary nodules, multiple lung masses, and cavitary nodules are uncommon manifestations. The presence of cavitary disease should prompt exclusion of other conditions, such as vasculitis, superinfection, and necrotizing sarcoidosis.

Necrotizing sarcoid granulamatosis, first described by Liebow [9], consists of confluent granulomas with or without central necrosis associated with a necrotic granulomatous vasculitis of the pulmonary vessels. It differs from Wegener's granulomatosis in the extensive nature of the sarcoid-like reaction and in its benign clinical course.

Silicosis, CWP, and berylliosis have features that mimic sarcoidosis. Silicosis and CWP tend to be more symmetric than sarcoidosis. Upper lung predominance and conglomerate masses can occur in each of these conditions.

Silicosis

Silicosis is caused by inhalation of dust that contains crystallized silicon dioxide. An appropriate history of exposure, combined with characteristic findings on chest radiographs, often suffices to make the diagnosis.

Simple silicosis

On chest radiographs and on CT scans the characteristic finding is small nodules that range from 3 mm 10 mm. Nodules are concentrated in the upper lungs with a centrilobular and, sometimes, subpleural predilection; this suggests a perilymphatic distribution (Fig. 7) [10]. CT may show a posterior predominance. Hilar or mediastinal lymphadenopathy may occur, with or without calcification; a characteristic feature is egg-shell calcification, as in sarcoidosis.

Complicated silicosis

In complicated silicosis, the individual small nodules have begun to pull together and coalesce because of scarring. The advanced form of this coalescence is progressive massive fibrosis, which consists of dense masses of consolidation (conglomerate masses which form near the hila) on a background of small nodules. Conglomerate masses may develop central necrosis and cavitation, which is unusual in sarcoidosis and CWP. Apical scarring, bullae, and paracicatricial emphysema often accompany silicosis.

CWP and silicosis may be distinct diseases; however, radiographic features are similar. Without appropriate history, distinction by radiographic features is difficult.

Asbestosis

Pleural plaque is the characteristic finding of asbestos exposure (Fig. 8). Diffuse pleural thickening also may occur, but is much less specific for asbestos exposure. Diffuse pleural thickening can result in round atelectasis in the adjacent lung.

Asbestosis is lung fibrosis that results from asbestos exposure. It can be distinguished from other kinds of lung fibrosis if pleural plaques are demonstrated. CT is superior to plain radiography in de-

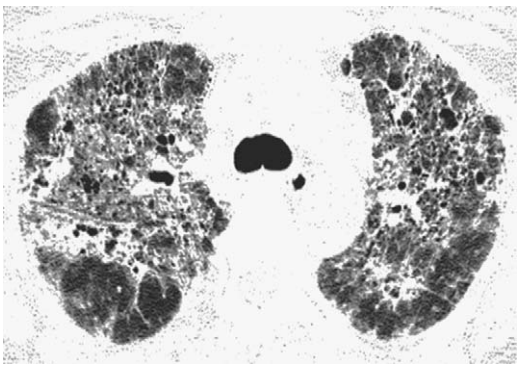

Fig. 5. Sarcoidosis (late, fibrotic stage). HRCT shows fibrosis and honeycombing in the upper lungs on both sides.

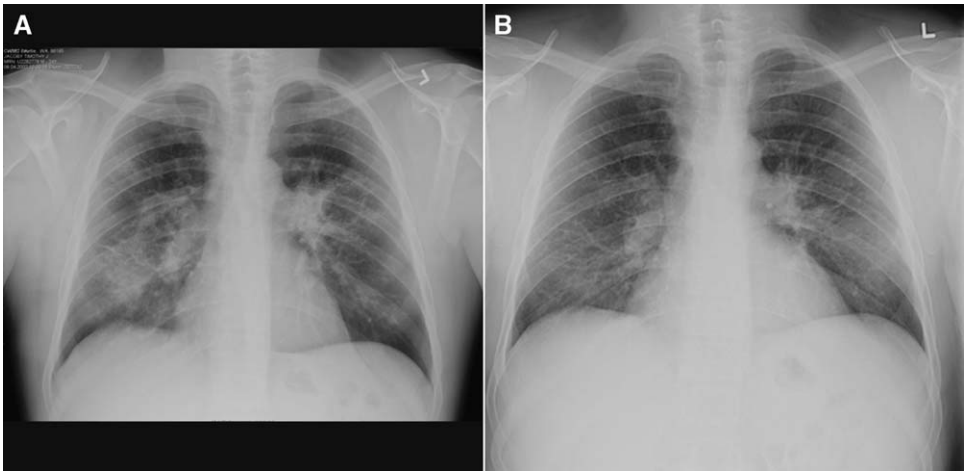

Fig. 6. "Alveolar" sarcoidosis: Pre- (*A*) and posttreatment (*B*) chest radiographs show airspace opacities and bilateral hilar lymphadenopathy. There is significant resolution on the posttreatment radiograph.

tection of pleural and pulmonary manifestations of asbestos exposure, and HRCT is better still [11]. The interstitial abnormalities are concentrated at the bases and periphery and consist of interlobular septal thickening, intralobular interstitial thickening, honeycombing, and parenchymal bands (Fig. 9). Ground-glass opacity was believed to be an early finding that is caused by thickening of alveolar walls; however, ground-glass opacity has many other causes, including simple atelectasis. HRCT is sensitive to early detection of these findings but its specificity is variable. Aberle et al [11] found good correlation between CT scores and pulmonary function impairment.

Lymphangioleiomyomatosis

LAM is a disorder of women of reproductive age (17–50 years) [12]. It is characterized by proliferation of spindle cells in lung tissue. Proliferation around bronchioles leads to development of cysts. Involvement of the lymphatics may cause obstruction and accumulation of chylous pleural effusions.

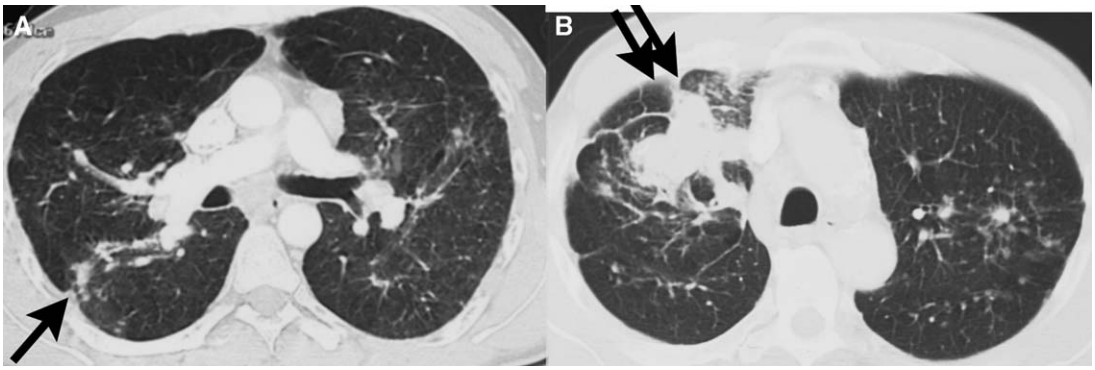

Fig. 7. Silicosis. Simple silicosis with 5- to 10-mm nodules in both upper lungs (*A*). Some of the nodules show early conglomeration (*single arrow*). Advanced silicosis (*B*) with multiple nodules and a large lung cancer in the right upper lobe (*double arrows*).

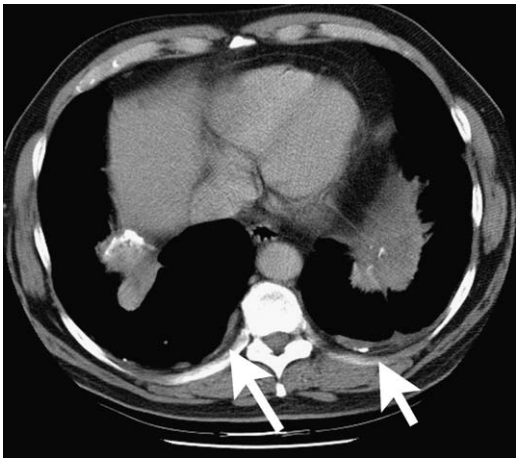

Fig. 8. Asbestos pleural plaque and pleural thickening. There are calcified and noncalcified pleural plaques (*arrows*), including calcified plaque along the right hemidiaphragm.

CT features include thin-walled lung cysts with intervening normal lung tissue (Fig. 10). The cysts occur throughout the lung and lung volume is preserved. The presence of pleural effusion helps to distinguish the cystic lung disease from LCH. Intra-abdominal manifestations include renal angiomyolipomas, lymphangiomatosis, and lymphadenopathy.

Langerhans cell histiocytosis

LCH is an idiopathic disease of young or middle-aged adults, who present with cough and dyspnea. As many as 90% [13] of these patients are cigarette smokers and there is a slight male predominance. Pneumothorax is the presenting manifestation in up to 20% of cases.

Common features on CT include nodules of 1 mm to 5 mm diameter in a peribronchiolar (centrilobular) distribution (Fig. 11). These nodules may cavitate. Thin-walled lung cysts (Fig. 12), which usually are less than 10 mm in diameter, are the other common finding in later stages. Nodules and cysts are concentrated in mid and upper lungs; characteristically, the costophrenic angles are spared on chest radiographs. Many cases resolve if the patient stops smoking. Follow-up CT scans may show regression of nodules, whereas any cysts that have formed are permanent. In cases that do not resolve, scarring may supervene which results in reticulation, thickening of the cyst walls, and architectural distortion with an upper lung concentration. Pulmonary arterial hypertension may develop.

In LCH, cysts tend to spare the basal parts of the lung near the costophrenic angles, whereas in LAM, they occur throughout the lung. In both conditions, lung volumes are preserved and pneumothorax can occur. The presence of pleural effusion helps to distinguish LAM from LCH.

Collagen vascular diseases

Rheumatoid arthritis associated interstitial lung disease, PSS, and CREST syndrome are the principal entities that affect the lung.

Rheumatoid arthritis associated interstitial lung disease

More than 75% of patients who have rheumatoid arthritis have extra-articular manifestations. In the thorax, pleural effusion is the most common: however, lung disease occurs in up to 20% of patients [14,15]. These include interstitial pneumonitis (COP, usual interstitial pneumonia [UIP], nonspecific interstitial pneumonia [NSIP]), pulmonary vascular disease (eg, pulmonary arterial hypertension), bronchiectasis and bronchiolitis (specifically, follicular bronchiolitis), and drug reactions (eg, hypersensitivity pneumonitis from methotrexate).

Necrobiotic nodules in the lung are rare. Typically, they affect men who have advanced joint disease and usually are asymptomatic [16]. They are well-defined

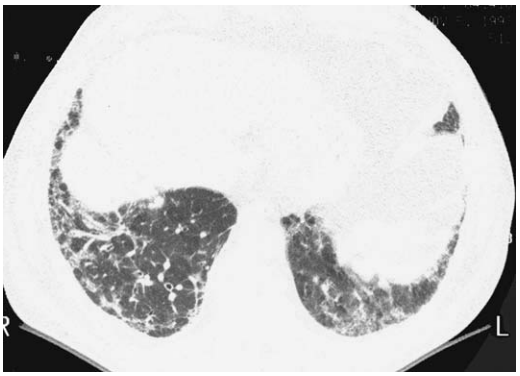

Fig. 9. Asbestosis. Basal and peripheral intralobular and interlobular fibrosis. Pleural plaques are not visible on this lung window.

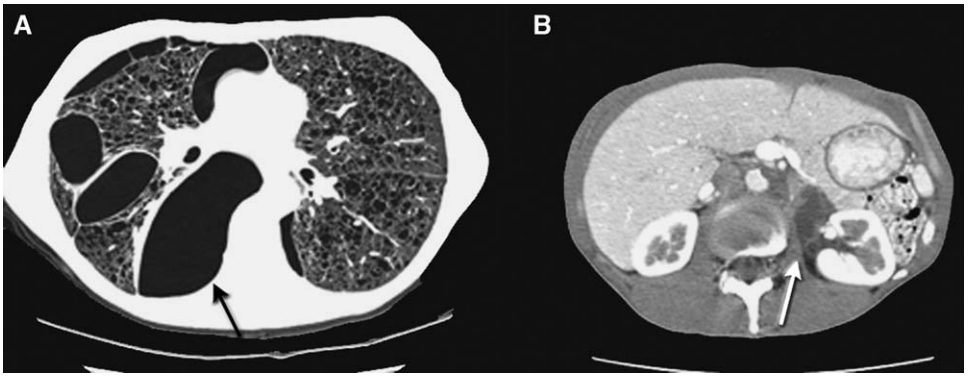

Fig. 10. LAM. HRCT image shows multiple cysts with interspersed normal lung (*A*) and right pneumothorax (*black arrow*). CT of the abdomen (*B*) shows low-attenuation retroperitoneal masses caused by lymphangiomas (*white arrow*).

and may cavitate. Caplan's syndrome is a syndrome of multiple necrobiotic nodules in coal miners who have rheumatoid arthritis.

Progressive systemic sclerosis and CREST syndrome

HRCT shows some degree of interstitial disease in a substantial number of these patients and may be used for monitoring the disease over time [17]. The most common abnormalities that are seen on CT are peripheral and basal ground-glass opacities and fibrosis, pleural or pericardial effusion, esophageal dilation, mediastinal lymphadenopathy, and, sometimes, pulmonary arterial dilation that reflects pulmonary hypertension.

Hypersensitivity pneumonitis

Hypersensitivity pneumonitis (HP) is caused by exposure to various occupational and environmental antigens [18]. Its diagnosis is based on clinical radiographic, cytologic, and histopathalogic findings. Clinical and radiographic features often are characteristic enough to make the diagnosis.

In the acute and subacute stages, the predominant abnormalities on HRCT are ground-glass opacities (Fig. 13) and ill-defined centrilobular nodules (reflecting inflammation around small airways) (Fig. 14). The ground-glass opacities may be concentrated in the centers of the secondary pulmonary lobules with sparing of the periphery. Small airway dysfunction

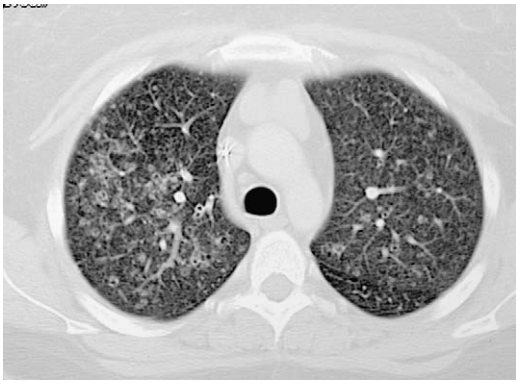

Fig. 11. LCH. CT image shows noncavitary and cavitary nodules in both upper lungs.

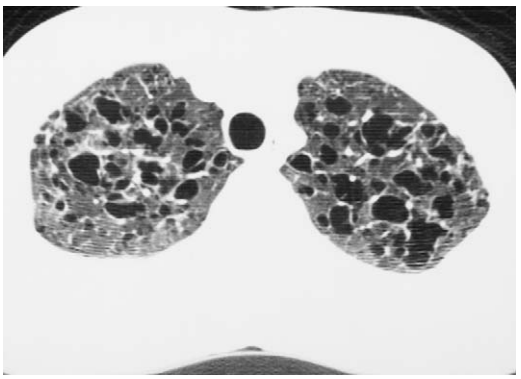

Fig. 12. LCH. CT shows multiple cysts of variable sizes in both upper lungs, a late and irreversible finding.

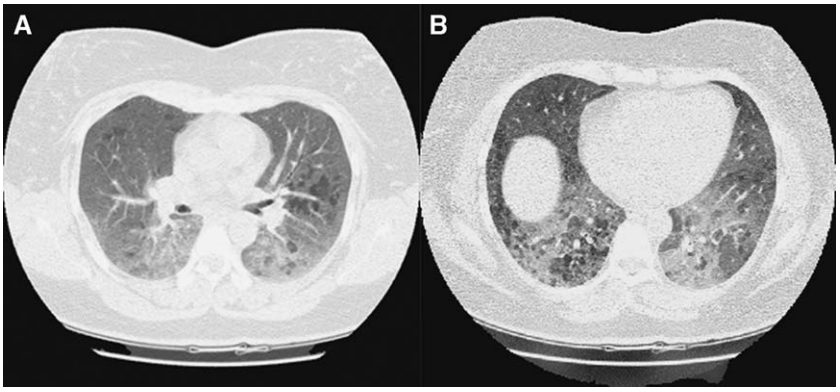

Fig. 13. Acute HP. HRCT images (inspiratory and expiratory) show ground-glass opacity (*A*) with interspersed low-attenuation regions indicating air-trapping (*B*).

can lead to air trapping that becomes visible on expiratory HRCT scans as a mosaic pattern (see Fig. 13). In late stages, fibrosis and emphysema may develop.

Plain films often show no definite abnormality in HP, despite dramatic findings on HRCT. For this reason, the physician should have a low threshold for ordering HRCT when HP is a consideration.

Pulmonary alveolar proteinosis

In PAP, a proteinaceous material accumulates in the alveolar air spaces and causes hypoxemia, restrictive lung disease, and dramatic abnormalities on chest radiographs. Complications are unusual, but of the ones that do occur, infection (particularly with nocardia asteroids) and fibrosis are the most common. Varying combinations of air-space and interstitial patterns may be seen [19]. The CT appearance is of bilateral, symmetric alveolar consolidation or ground-glass opacity, particularly in a perihilar or hilar distribution. Typically, HRCT shows diffuse ground-glass attenuation with superimposed intra- and interlobular septal thickening, often in polygonal shapes (Fig. 15) that are known as "crazy-paving" [20]. Some lobules are spared and the sharp margination of the ground-glass opacity by the interlobular septa of the spared lobules is called "geographic" distribution, because it resembles continents that are marginated by oceans on a map.

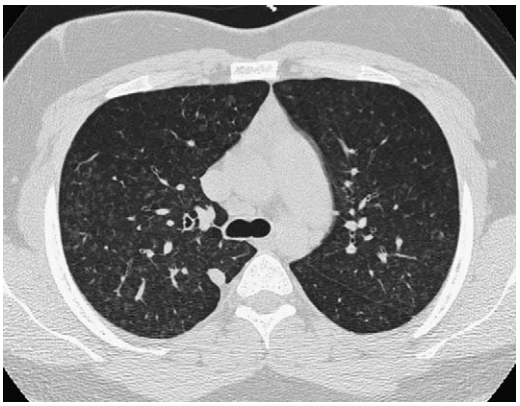

Fig. 14. Subacute HP. Ill-defined centrilobular ground-glass opacities in upper lungs, in combination with the right clinical presentation, suggest subacute HP.

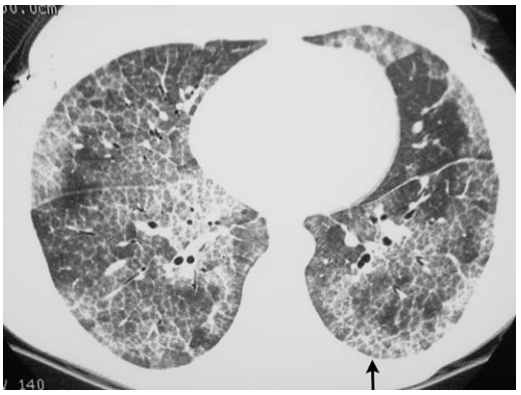

Fig. 15. PAP. HRCT image shows typical ground-glass opacity with superimposed "crazy-paving" pattern (*arrow*). Crazy-paving is the meshwork of lines that represent reversible intralobular and interlobular interstitial thickening by edema and cells.

References

[1] American Thoracic Society/European Respiratory Society International Multidisciplinary Consensus Classification of the Idiopathic Interstitial Pneumonias. Am J Respir Crit Care Med 2002;165:277–304.

[2] McLoud TC, Carrington CB, Gaensler EA. Diffuse infiltrative lung disease: a new scheme for description. Radiology 1983;149:353–63.

[3] Zwirewich CV, Mayo JR, Muller NL. Low-dose high-resolution CT of lung parenchyma. Radiology 1991; 180:413–7.

[4] Mehnert F, Pereira PL, Dammann F, et al. High resolution multislice CT of the lung: comparison with sequential HRCT slices. Rofo Fortschr Geb Rontgenstr Neuen Bildgeb Verfahr 2000;172(12):972–7.

[5] Schoep UJ, Bruening RD, Hong C, et al. Multislice helical CT of focal and diffuse lung disease: comprehensive diagnosis with reconstruction of contiguous and high-resolution CT sections from a single thin-collimation can. AJR Am J Roentgenol 2001;177(1): 179–84.

[6] Webb WR, Muller NL, Naidich DP. Standardized terms for high-resolution computed tomography of the lung: a proposed glossary. J Thorac Imaging 1993;8:167–75.

[7] Lynch JP, Kazerooni EA, Gay SE. Pulmonary sarcoidosis. Clin Chest Med 1997;18:755–85.

[8] Baumann MH, Strange C, Sahn SA. Do chest radiographic findings reflect the clinical course of patients with sarcoidosis during the corticosteroid withdrawal? AJR 1990;154:481–5.

[9] Liebow A. Pulmonary angiitis and granulomatosis. Am Rev Respir Dis 1973;108:1–18.

[10] Begin R, Ostiguy G, Fillion R, et al. Computed tomography scan in the early detection of silicosis. Am Rev Respir Dis 1991;144:697–705.

[11] Aberle DR, Gamsu G, Ray CS, et al. Asbestos related pleural and parenchymal fibrosis: detection with high resolution CT. Radiology 1988;166:729–34.

[12] Sullivan E. Lymphangiomyomatosis: a review. Chest 1998;114:1689–703.

[13] Desai SR, Ryan SM, Colby TV. Smoking-related interstitial lung diseases: histopathological and imaging perspectives. Clin Radiol 2003;58:259–68.

[14] Gabbay E, Tarala R, Will R, et al. Interstitial lung disease in recent onset rheumatoid arthritis. Am J Respir Crit Care Med 1997;156:528–35.

[15] Hurd ER. Extra-articular manifestations of rheumatoid arthritis. Semin Arthritis Rheum 1979;8:151–76.

[16] Ellman P, Ball R. Rheumatoid disease with joint and pulmonary manifestations. Br Med J 1948;2(8):16–9.

[17] Remy-Jardin M, Remy J, Wallert B, et al. Pulmonary involvement in progressive systemic sclerosis: sequential evaluation with CT, pulmonary functions and bronchoalveolar lavage. Radiology 1993;189: 499–506.

[18] Glazer CS, Rose CS, Lynch DA. Clinical and radiologic manifestations of hypersensitivity pneumonitis. J Thorac Imaging 2002;17:261–72.

[19] Godwin JD, Muller NL, Takasugi JE. Pulmonary alveolar proteinosis: CT findings. Radiology 1988;169: 609–13.

[20] Rossi SE, Erasmus JJ, Volpacchio M, et al. Crazy-paving" pattern at thin-section CT of the lungs: radiologic-pathologic overview. Radiographics 2003; 23:1509–19.

ELSEVIER
SAUNDERS

Radiol Clin N Am 43 (2005) 601 – 610

RADIOLOGIC
CLINICS
of North America

Chest Imaging in Iatrogenic Respiratory Disease

Rebecca M. Lindell, MD, Thomas E. Hartman, MD*

Department of Radiology, Mayo Clinic, 200 First Street Southwest, Rochester, MN 55905, USA

Iatrogenic respiratory disease is an important cause of patient morbidity and mortality. Clinical and radiologic findings are nonspecific and diagnosis can be difficult. Therefore, it is important for physicians to be familiar with the iatrogenic diseases for which their patients are at risk, as well as their common radiologic appearances. Causes of iatrogenic respiratory disease include drugs, transplantation, radiation, transfusion, or other miscellaneous therapies.

Drug-induced lung disease

Radiologic manifestations of drug-induced respiratory disease correspond to the underling histologic findings and include nonspecific interstitial pneumonia (NSIP), usual interstitial pneumonia (UIP), hypersensitivity lung disease, pulmonary edema with or without diffuse alveolar damage (DAD), bronchiolitis obliterans, bronchiolitis obliterans organizing pneumonia (BOOP), and diffuse pulmonary hemorrhage. Drug agents that cause respiratory disease can be divided into cytotoxic agents, specifically chemotherapeutic agents, and noncytotoxic agents, such as antibiotics, anti-inflammatory agents and antiarrhythmics.

Nonspecific interstitial pneumonia

All forms of interstitial pneumonitis can be seen with drug therapy, but the most commonly occurring form is NSIP [1]. On chest radiography, NSIP can appear as bilateral ground-glass opacities, consolidation, or interstitial infiltrates. Typically, these are most prominent in the lower lungs [2]. High-resolution CT (HRCT) most often shows patchy ground-glass opacities or consolidation and irregular reticular opacities [3]. These typically have a peripheral and basilar predominance [2]. Honeycombing is uncommon in NSIP, which helps to distinguish it from UIP [4]. Fibrosis and extent of disease increases with severity of drug-induced damage.

Several drugs can cause NSIP. It is the most commonly encountered drug-induced lung disease caused by amiodarone, methotrexate, and carmustine (Fig. 1) [5–8]. Amiodarone toxicity also may cause characteristic high-attenuation areas in the lung parenchyma (Fig. 2) that result from incorporation of amiodarone breakdown products into hyperplastic type II pneumocytes [1,9]. High attenuation in the liver and spleen also may be seen with amiodarone use [5,10,11].

Usual interstitial pneumonitis

Cytotoxic chemotherapeutic agents, such as bleomycin and methotrexate, are the most common cause of UIP. Plain radiographs show bilateral irregular linear opacities that form a reticular pattern that is most prominent in the lung bases [12–15]. The predominant feature on HRCT is fibrosis that leads to subpleural cystic airspaces with thick walls that is known as "honeycombing" (Fig. 3). There is a lower lung and peripheral predominance [16]. Additional findings of fibrosis include traction bronchiectasis and bronchiolectasis. The presence of prominent honeycombing with a subpleural and basilar predominance on HRCT is diagnostic of UIP [17–19] in the appropriate clinical setting.

This article originally published in *Clinics of Chest Medicine* 2004;25:15–24.

* Corresponding author.
E-mail address: hartman.thomas@mayo.edu (T.E. Hartman).

0033-8389/05/$ – see front matter © 2005 Elsevier Inc. All rights reserved.
doi:10.1016/j.rcl.2005.03.004

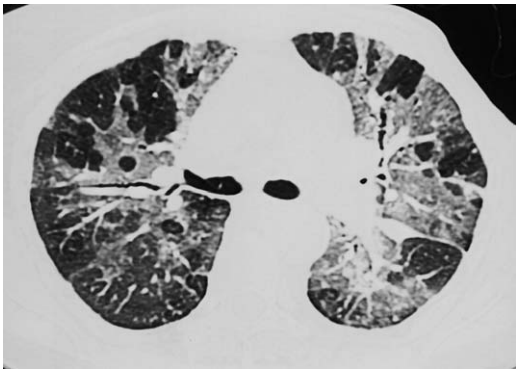

Fig. 1. NSIP in a 75-year-old woman taking cytoxan. HRCT shows bilateral patchy ground-glass opacities and absence of honeycombing.

Hypersensitivity lung disease

Several drugs can result in a hypersensitivity reaction in the lungs. Among the more common causes are methotrexate, bleomycin, penicillamine, cyclophosphamide, nitrofurantoin, procarbazine, carmustine (BCNU), sulfonamides, and nonsteroidal anti-inflammatory drugs (NSAIDs) [7,10,20,21]. Chest radiographs may be normal or may show nonspecific ground-glass opacities with or without small areas of consolidation. The HRCT appearance is similar to that seen in hypersensitivity pneumonitis that is due to other causes. Bilateral patchy ground-glass opacities are the most common HRCT finding (Fig. 4A). Ground-glass centrilobular nodules and air trapping may also be seen on HRCT (Fig. 4B) [22–25].

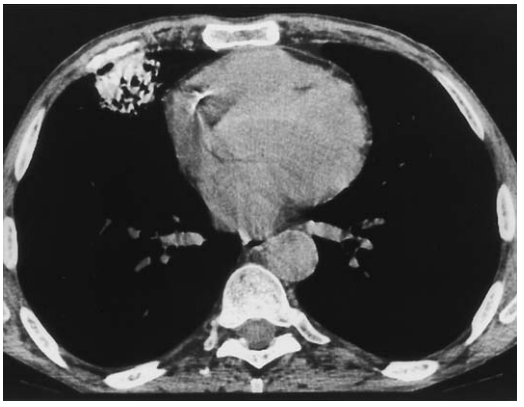

Fig. 2. Amiodarone toxicity in a 69-year-old man. Noncontrast axial CT shows a focal area of high attenuation consolidation in the anterior right midlung, consistent with amiodarone.

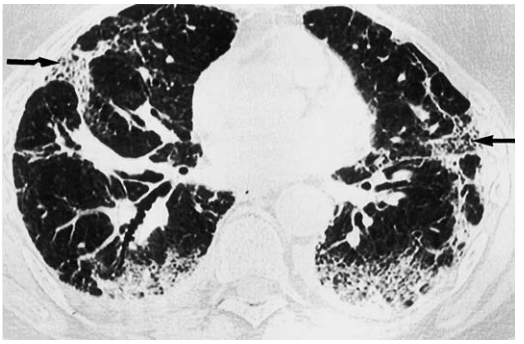

Fig. 3. UIP in a 57-year-old woman taking bleomycin. HRCT image shows subpleural fibrosis with honeycombing (*arrows*) and traction bronchiectasis. This pattern was most prominent in the lung bases.

Bronchiolitis obliterans

Bronchiolitis obliterans primarily has been described in association with penicillamine use in patients who have rheumatoid arthritis (RA). Penicillamine's role is controversial because bronchiolitis obliterans also can be seen in patients who have RA who do not use penicillamine [26] Sulfasalazine may also cause bronchiolitis obliterans [7]. Chest radiographs often are normal. Hyperinflation with decreased peripheral vascularity is the most common abnormality that is seen on chest radiographs [27]. Bronchial dilatation and wall thickening also may be seen. HRCT findings include hyperinflation, decreased vascularity, bronchiectasis, bronchial wall thickening, mosaic perfusion, and air trapping on expiratory images [28,29].

Bronchiolitis obliterans with organizing pneumonia

Many drugs can result in BOOP, including bleomycin, nitrofurantoin, cyclophosphamide, methotrexate, amiodarone, and gold salts [30]. Chest radiographs typically show bilateral patchy opacities or consolidation in a peripheral distribution (Fig. 5) [31]. HRCT findings include bilateral patchy consolidations or ground-glass opacities (Fig. 6). These are predominantly peripheral and also may be seen in a peribronchovascular distribution [31,32]. Nodular consolidation also may be seen in a similar distribution, and, on rare occasions, may mimic pulmonary nodules (Fig. 7) [33].

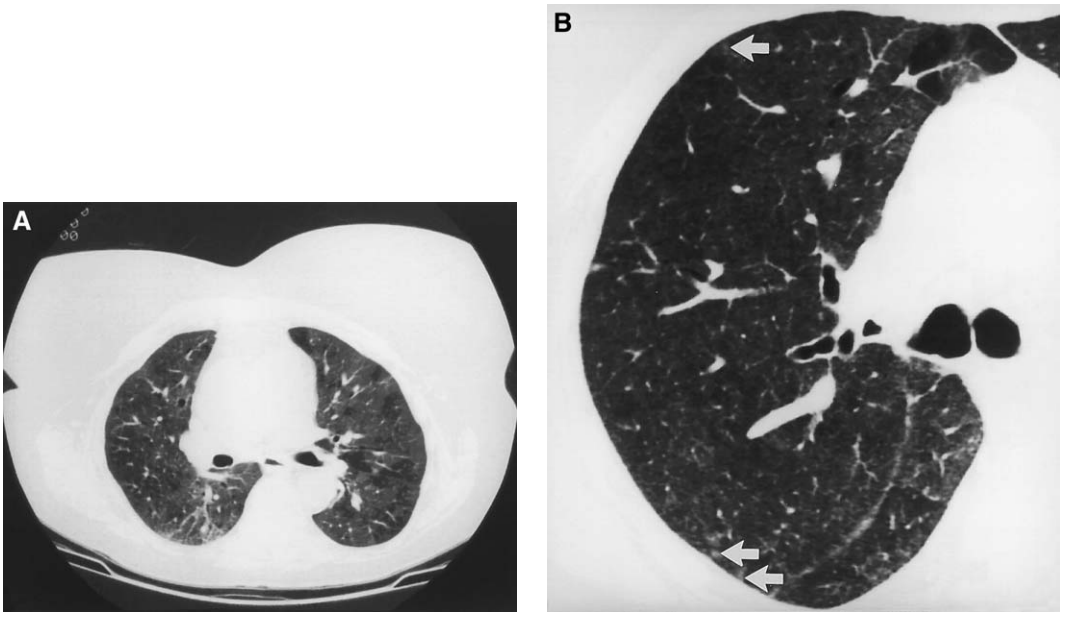

Fig. 4. Hypersensitivity lung reaction secondary to methotrexate in two patients. (*A*) HRCT image of a 42-year-old woman shows patchy areas of ground-glass opacities in both lungs. (*B*) HRCT image of a 46-year-old man shows ground-glass nodules in the right lung (*arrows*).

Pulmonary edema with or without diffuse alveolar damage

Noncardiogenic pulmonary edema with or without DAD may occur with a variety of drugs. It most commonly occurs with cytotoxic agents, such as bleomycin, cytosine arabinoside (Ara-C), methotrexate, and cyclophosphamide [7,34,35]. Other agents include aspirin, NSAIDs, tricyclic antidepressants, and narcotics, either prescription or illicit [20,36]. The onset is usually acute; symptoms occur within days of drug initiation. The probable mechanism of edema is an increase in capillary permeability. With DAD, capillary epithelial damage also has occurred.

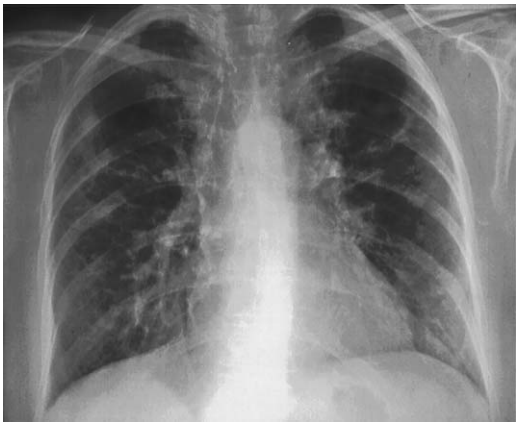

Fig. 5. A 70-year-old woman with drug-induced BOOP. Chest radiograph shows bilateral patchy opacities/consolidation in a peripheral distribution.

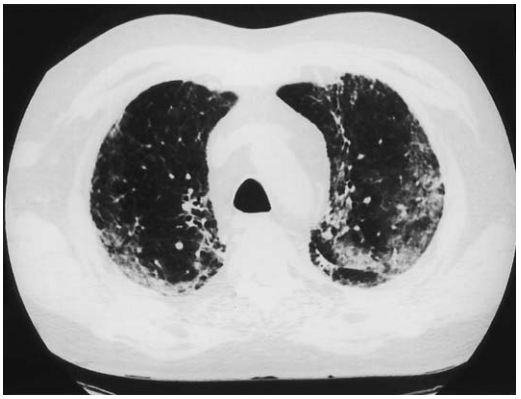

Fig. 6. BOOP in a 68-year-old man on promace cytabom for non-Hodgkin's lymphoma. HRCT image at the level of the aortic arch shows bilateral peripheral patchy ground-glass opacities and small areas of consolidation.

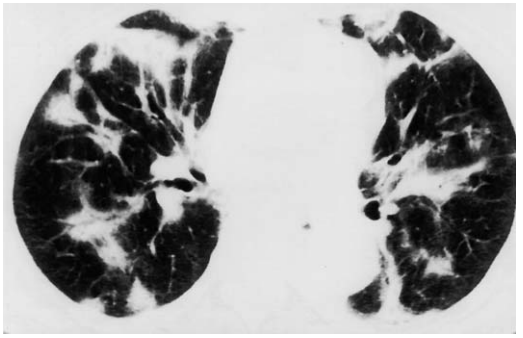

Fig. 7. Nodular appearance of BOOP in a 72-year-old woman on nitrofurantoin. HRCT findings include bilateral patchy areas of consolidation, many of which appear nodular. Distribution is primarily peripheral with some in a peribronchovascular distribution.

Chest radiographs of pulmonary edema without DAD show findings similar to hydrostatic pulmonary edema, including bilateral interstitial thickening and scattered or diffuse alveolar infiltrates (Fig. 8) [37]. HRCT shows interlobular septal thickening with or without alveolar ground-glass opacities [38]. Pleural effusions may be seen on radiographs or CT. When DAD is present, infiltrates are more extensive and consolidative (Fig. 9). On HRCT there are patchy or diffuse bilateral ground-glass opacities or consolidation with predominance of findings in the dependent regions of the lungs (Fig. 10) [10]. This often results in a gradient of attenuation with more normal lung attenuation anteriorly which progresses to dense consolidation posteriorly.

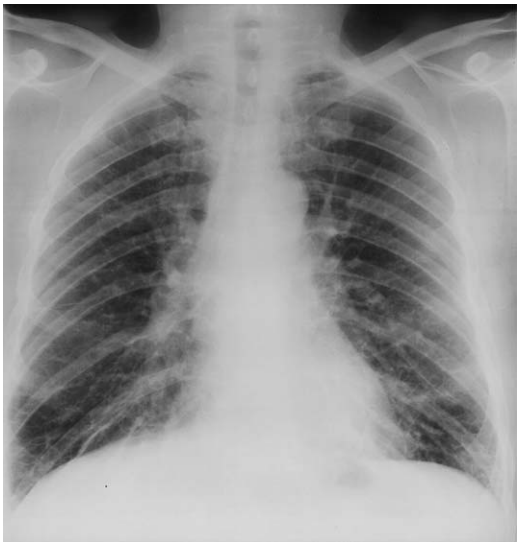

Fig. 8. Pulmonary edema in a 55-year-old man taking nitrofurantoin. Chest radiograph shows interstitial infiltrates with Kerley B lines that are consistent with edema.

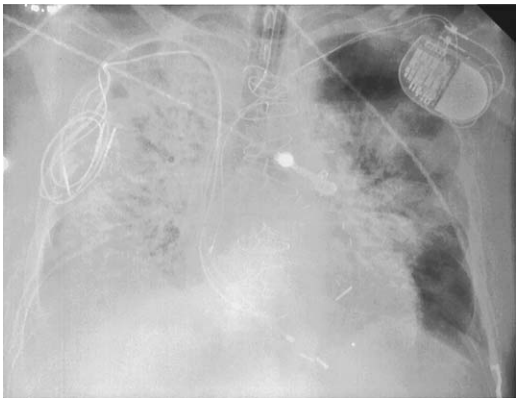

Fig. 9. A 65-year-old man who has pulmonary edema and DAD secondary to amiodarone. Portable chest radiograph shows alveolar infiltrates and consolidation involving the right lung diffusely and the left in a perihilar distribution.

Pulmonary hemorrhage

Pulmonary hemorrhage is an unusual drug-induced lung disease that has occurred with agents, such as anticoagulants, amphotericin B, Ara-C, mitomycin, penicillamine, and high-dose cyclophosphamide [7,20,30]. It also can be seen as a complication of bone marrow transplant. Ground-glass opacities or consolidations are seen scattered or diffusely in both

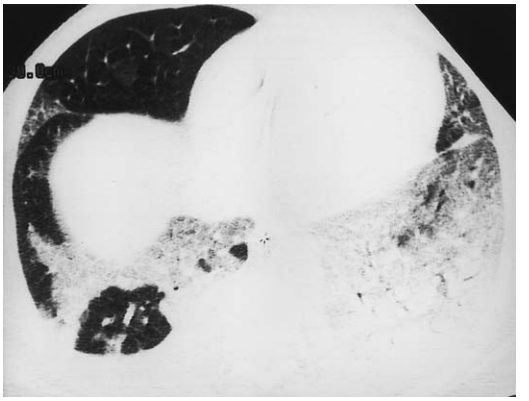

Fig. 10. A 68-year-old man who has pulmonary edema and DAD. HRCT shows extensive left base and patchy right base consolidations with predominance of findings in the dependent regions of the lungs.

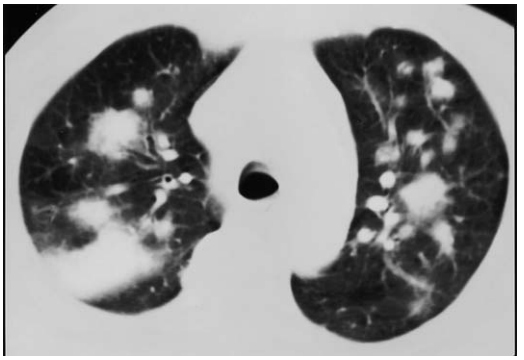

Fig. 11. A 70-year-old patient who received a kidney transplant who has invasive pulmonary aspergillosis. CT scan through the upper lungs shows bilateral pulmonary nodules, some with halos of ground-glass attenuation. There also is focal consolidation of the posterior right upper lobe.

lungs on chest radiograph or CT [39]. A predominance of ill-defined centrilobular nodules is a less common CT appearance. Crazy-paving (intralobular and interlobular septal thickening superimposed on ground-glass opacities) may develop on HRCT within days after the acute episode as hemosiderin-laden macrophages accumulate within the interstitium.

Transplant-related lung diseases

Transplant related lung diseases include infection, lymphoproliferative disorders, and graft versus host disease (GVHD) [40,41]. Familiarity with the radiologic findings of these diseases is important in the care of a transplant recipient.

Infection

Infection is a common and serious transplantation complication. Several fungi, bacteria, and viruses are known to infect transplant recipients. Knowledge of the common infecting organisms and possible imaging appearances can be helpful in diagnosis.

Fungal pneumonia is a significant transplant complication that may increase patient morbidity and mortality. A notable example is *Aspergillus*. During the first 30 days after a bone marrow transplant, *Aspergillus* is the most common pulmonary infection [41,42]. Because the patients are severely neutropenic, the angio-invasive form of *Aspergillus* is commonly seen. As with other fungal infections, single or multiple nodules or areas of focal consolidation may be seen on chest radiograph and CT [43]. On HRCT, the nodule may have a halo of ground-glass attenuation that is characteristic of, although not specific for, angio-invasive *Aspergillus* infection (Fig. 11) [41,44]. An air-crescent sign may appear within the nodule as the patient's neutropenia improves [41].

Another common infectious agent in transplant patients is cytomegalovirus (CMV). In patients who have undergone bone marrow transplant, CMV pneumonitis most commonly occurs 2 to 6 months after transplantation [45]. A variety of findings are possible on chest radiographs, including consolidation, reticulation, or a nodular pattern [44]. Likewise, HRCT findings of CMV pneumonitis also vary. Patchy areas of ground-glass opacification or consolidation may be seen (Fig. 12). Other possible

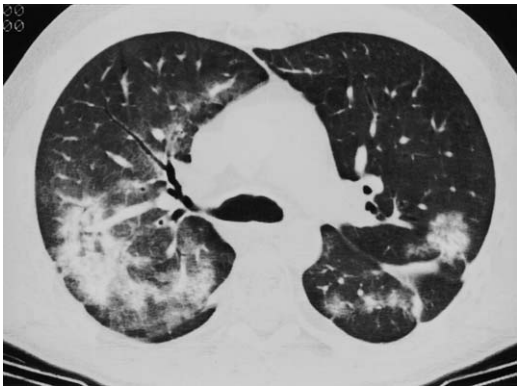

Fig. 12. CMV pneumonitis in a 44-year-old man after bone marrow transplant. HRCT image through the upper lobes shows patchy areas of ground-glass attenuation and consolidation in both lungs, greater on the right.

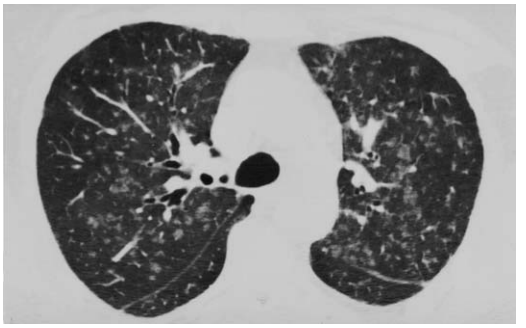

Fig. 13. A 56-year-old woman who has CMV pneumonitis status post bone marrow transplantation. HRCT image through the upper lobes shows small nodular ground-glass opacities scattered in both lungs.

HRCT patterns include scattered bilateral small nodules or reticulation (Fig. 13) [46]. Findings tend to be bilateral and symmetric. The nodules tend to involve the lungs diffusely, whereas consolidation tends to predominate in the lower lungs [46].

Posttransplant lymphoproliferative disorder

Posttransplant lymphoproliferative disorder occurs most commonly within 2 years of bone marrow or solid organ transplantation, but may occur at any time [47]. It affects approximately 2% of patients who receive transplants, most commonly lung transplant recipients. Epstein-Barr virus is a major causative factor [40]. Histology may vary from plasmacytic hyperplasia to malignant lymphoma. Chest radiographs most commonly show single or multiple pulmonary nodules with or without hilar and mediastinal lymphadenopathy [48]. On HRCT, these nodules may be well- or ill-defined and may have a halo of ground-glass attenuation. The nodules may show a peribronchial distribution and may be diffuse or subpleural (Figs. 14, 15) [40].

Graft versus host disease

The imaging findings of chronic GVHD are those of bronchiolitis obliterans [49]. Chest radiographs may be normal or show hyperinflation, bronchial dilatation, and wall thickening. Bronchiectasis, bronchial wall thickening, decreased vascularity, mosaic perfusion, and expiratory air trapping may be seen on HRCT [28,29]. Pulmonary findings in acute GVHD are minimal, but, if present, often appear as noncardiogenic edema [41].

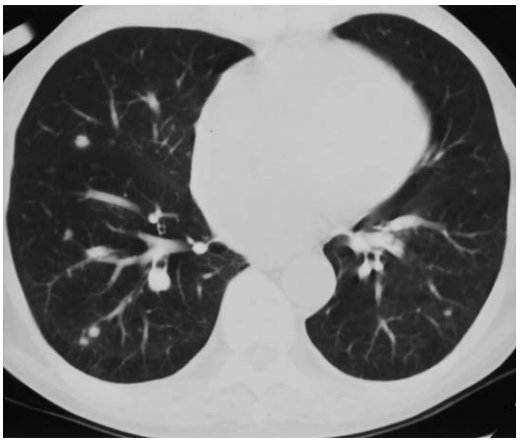

Fig. 14. A 62-year-old man 1 year status post heart and liver transplant for amyloidosis. CT scan shows bilateral pulmonary nodules. Biopsy of the right lower lobe showed posttransplant lymphoproliferative disorder with features of large cell lymphoma.

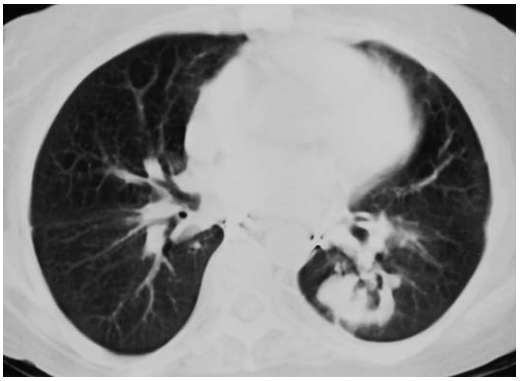

Fig. 15. A 45-year-old woman status post heart, lung, and liver transplantation for primary biliary cirrhosis and pulmonary hypertension. CT scan shows a mass in the left lower lobe that contains dilated bronchi. Biopsy of the mass showed malignant lymphoma consistent with posttransplant lymphoproliferative disorder.

Radiation-induced lung disease

Radiologic manifestations of radiation-induced lung injury can be divided into two stages; radiation

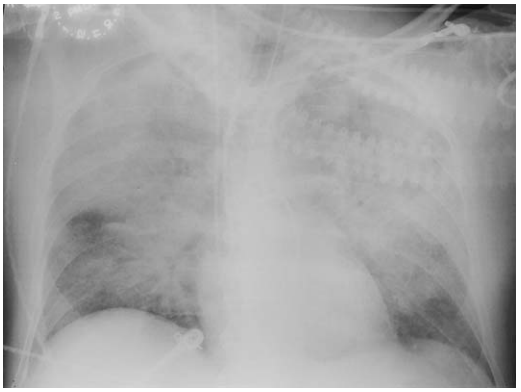

Fig. 16. A 67-year-old man who has TRALI after receiving blood transfusion products during surgery. Portable chest radiographs shows diffuse alveolar infiltrates bilaterally, with near "white-out" of the upper lungs.

pneumonitis and radiation fibrosis. Radiation pneumonitis occurs first, within 1 to 3 months after radiation therapy and peaks in intensity at 3 to 4 months [50,51]. CT shows patchy or homogeneous ground-glass attenuation or consolidation in a characteristic distribution of the radiation port. The involved area crosses segmental and lobar boundaries [51,52]. Radiographic abnormalities include a diffuse hazy infiltrate or a more dense consolidation in the same characteristic distribution. Air bronchograms are common [51]. Pleural effusions are uncommon but should resolve with the radiation pneumonitis. Abnormalities may be seen infrequently outside the radiation port and may be due to edema, hypersensitivity reaction, BOOP or even DAD [52,53].

Radiation pneumonitis may lead to radiation fibrosis, which typically occurs 6 to 12 months after radiation therapy [54,55]. Radiographs and CT show development of reticular opacities, volume loss, progressive consolidation, traction bronchiectasis, and pleural thickening in the area of the radiation port [51,56]. The involved area is usually well-demarcated. These findings typically stabilize 2 years after radiation therapy. Radiation injury also may cause calcified lymph nodes, pericardial effusions, and thymic cysts that also may be seen on radiographs or CT [52].

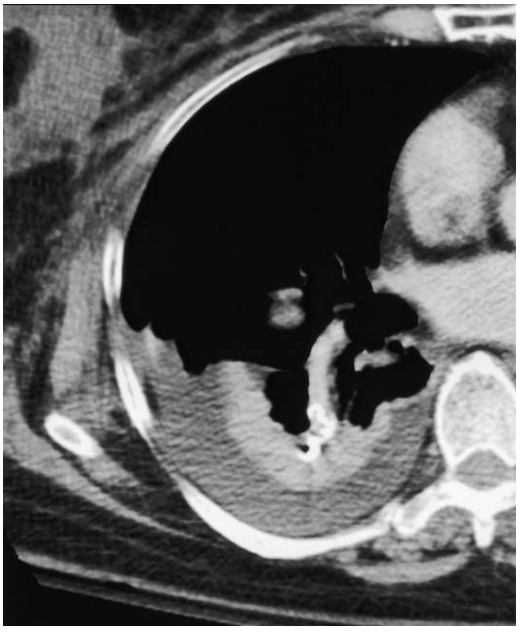

Fig. 17. A 66-year-old woman status post neurointerventional coil embolization of a large occipital lobe arteriovenous malformation. Chest CT scan shows that one coil unintentionally embolized to a right lower lobe subsegmental pulmonary artery.

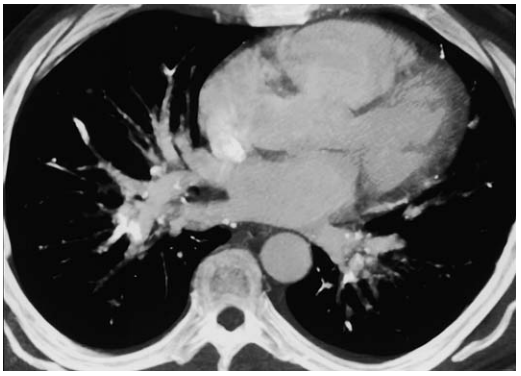

Fig. 18. A 55-year-old man with cirrhosis status post–endoscopic injection sclerotherapy of a gastric varix using a mixture of acrylic glue (n-butyl-2-cyanoacrylate) and lipiodol (iodized oil). Maximum intensity projection images from a contrast-enhanced CT shows areas of increased attenuation in multiple segmental and subsegmental pulmonary arteries, consistent with embolization of the acrylic glue mixture. The iodized oil allows for radiographic visualization.

Miscellaneous

A variety of additional iatrogenic respiratory diseases are worth mentioning. These include trans-

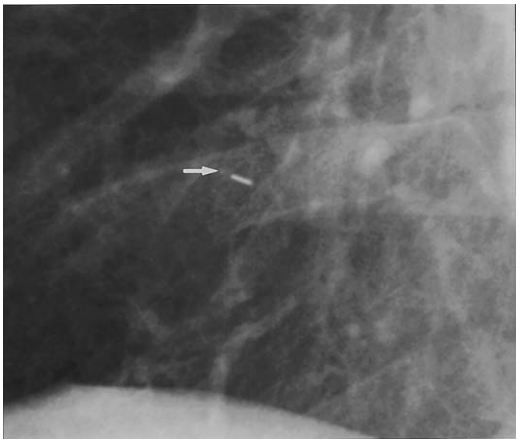

Fig. 19. Chest radiograph shows a tiny linear metallic density in the right lung base (*arrow*). The loop at the tip of the metallic density identifies it as a brachiotherapy seed. This seed has embolized to the right lung in this 74-year-old man undergoing bronchiotherapy for prostate cancer.

fusion-related lung injury (TRALI); embolism of iatrogenic materials, such as sclerotherapy materials and prostate brachytherapy seeds; and transbronchial biopsy-induced lung injury.

Transfusion-related lung injury

TRALI is believed to be secondary to an immune-mediated event [57]. It usually occurs within 2 hours of a transfusion, but may be seen up to 6 hours after transfusion. In the early stages, chest radiographs show signs of pulmonary edema with a distribution in the dependent portions of the lungs [57]. With time, the interstitial and alveolar infiltrates progress and may become so extensive that there is a complete "white-out" of the lungs (Fig. 16) [57]. TRALI should be distinguished clinically from transfusion-associated circulatory overload, which also presents as pulmonary edema [57].

Iatrogenic embolization

Several therapeutic interventions can result in material embolization to the pulmonary arteries. Among these are prostate brachytherapy seeds [58], vascular embolization coils (Fig. 17), vascular catheters, and materials that are used in sclerotherapy (Fig. 18) and vertebroplasty procedures [59]. Nag et al [58] reviewed 107 patients who had radioactive prostate seeds and found that 18% had embolization of one or more seeds to the lung (Fig. 19). Fortunately, all of the seed emboli were asymptomatic.

Transbronchial-induced lung injury

Patients who undergo lung transplants may develop solid or cavitary nodules as a result of direct transbronchial biopsy injury (Fig. 20) [60,61]. These typically resolve but can be seen up to 1 month

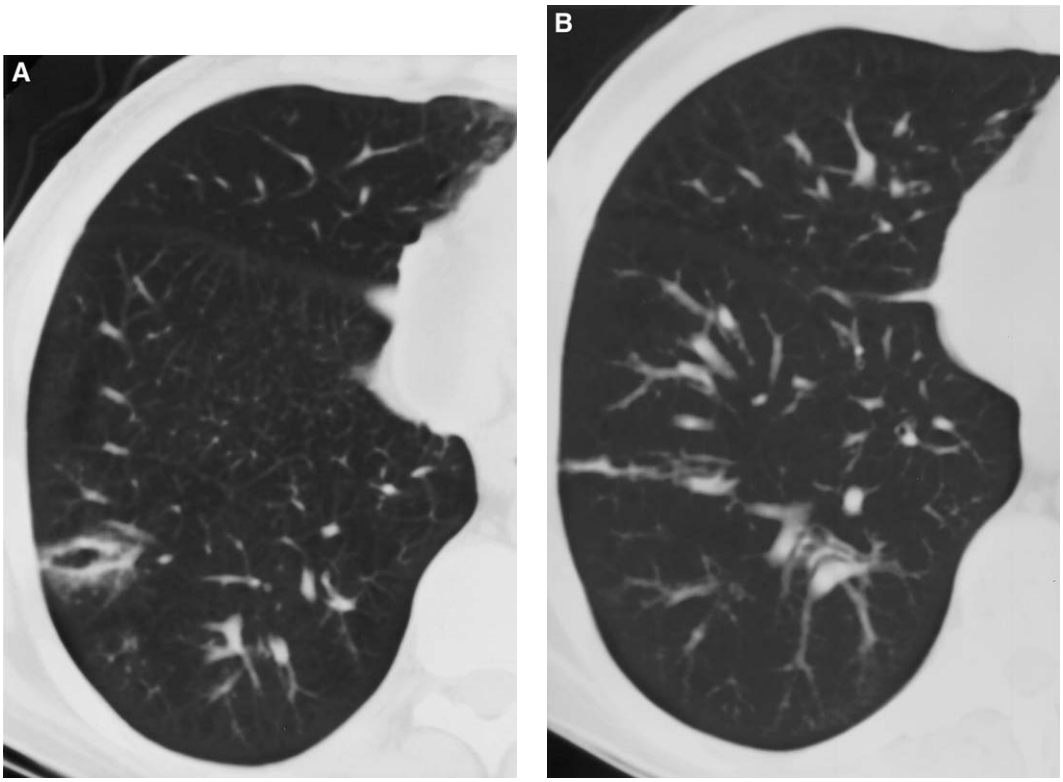

Fig. 20. Transbronchial biopsy lung injury that mimics a cavitary lesion. (*A*) CT image immediately following the transbronchial biopsy shows a new cavitary lesion in the right lung that corresponds with the biopsy site as well as areas of ground glass attenuation that could be due to hemorrhage from the biopsy or lavage fluid. (*B*) The cavitary lesion and areas of ground glass attenuation have resolved on this CT taken 14 days later.

following biopsy [61]. Diagnosis is supported by correlation with biopsy site and resolution on follow-up imaging.

References

[1] Rossi SE, Erasmus JJ, McAdams HP, et al. Pulmonary drug toxicity: radiologic and pathologic manifestations. Radiographics 2000;20:1245–59.

[2] Park JS, Lee KS, Kim JS, et al. Nonspecific interstitial pneumonia with fibrosis: radiographic and CT findings in seven patients. Radiology 1995;195(3):645–8.

[3] Nishiyama O, Kondoh Y, Taniguchi H, et al. Serial high resolution CT findings in nonspecific interstitial pneumonia/fibrosis. J Comput Assist Tomogr 2000; 24(1):41–6.

[4] Johkoh T, Muller NL, Cartier Y, et al. Idiopathic interstitial pneumonias: diagnostic accuracy of thin-section CT in 129 patients. Radiology 1999;211:555–60.

[5] Kuhlman JE, Teigen C, Ren H, et al. Amiodarone pulmonary toxicity: CT findings in symptomatic patients. Radiology 1990;177(1):121–5.

[6] Holoye PY, Jenkins DE, Greenberg SD. Pulmonary toxicity in long-term administration of BCNU. Cancer Treat Rep 1976;60(11):1691–4.

[7] Cooper Jr JA, White DA, Matthay RA. Drug-induced pulmonary disease. Part 1: cytotoxic drugs. Am Rev Respir Dis 1986;133(2):321–40.

[8] Smith GJ. The histopathology of pulmonary reactions to drugs. Clin Chest Med 1990;11(1):95–117.

[9] Bedrossian CW, Warren CJ, Ohar J, et al. Amiodarone pulmonary toxicity: cytopathology, ultrastructure, and immunocytochemistry. Ann Diagn Pathol 1997;1(1): 47–56.

[10] Padley SP, Adler B, Hansell DM, et al. High-resolution computed tomography of drug-induced lung disease. Clin Radiol Oct 1992;46(4):232–6.

[11] Kuhlman JE. The role of chest computed tomography in the diagnosis of drug-related reactions. J Thorac Imaging 1991;6(1):52–61.

[12] Carrington CB, Gaensler EA, Coutu RE, et al. Natural history and treated course of usual and desquamative interstitial pneumonia. N Engl J Med 1978;298(15): 801–9.

[13] McLoud TC, Carrington CB, Gaensler EA. Diffuse infiltrative lung disease: a new scheme for description. Radiology 1983;149(2):353–63.

[14] Grenier P, Chevret S, Beigelman C, et al. Chronic diffuse infiltrative lung disease: determination of the diagnostic value of clinical data, chest radiography, and CT and Bayesian analysis. Radiology 1994;191(2):383–90.

[15] Muller NL, Guerry-Force ML, Staples CA, et al. Differential diagnosis of bronchiolitis obliterans with organizing pneumonia and usual interstitial pneumonia: clinical, functional, and radiologic findings. Radiology 1987;162(1 Pt 1):151–6.

[16] Muller NL, Miller RR, Webb WR, et al. Fibrosing alveolitis: CT-pathologic correlation. Radiology 1986; 160(3):585–8.

[17] Tung KT, Wells AU, Rubens MB, et al. Accuracy of the typical computed tomographic appearances of fibrosing alveolitis. Thorax 1993;48(4):334–8.

[18] Primack SL, Hartman TE, Hansell DM, et al. End-stage lung disease: CT findings in 61 patients. Radiology 1993;189(3):681–6.

[19] al-Jarad N, Strickland B, Pearson MC, et al. High resolution computed tomographic assessment of asbestosis and cryptogenic fibrosing alveolitis: a comparative study. Thorax 1992;47(8):645–50.

[20] Cooper Jr JA, White DA, Matthay RA. Drug-induced pulmonary disease. Part 2: noncytotoxic drugs. Am Rev Respir Dis 1986;133(3):488–505.

[21] Searles G, McKendry RJ. Methotrexate pneumonitis in rheumatoid arthritis: potential risk factors. Four case reports and a review of the literature. J Rheumatol 1987;14(6):1164–71.

[22] Hansell DM, Moskovic E. High-resolution computed tomography in extrinsic allergic alveolitis. Clin Radiol 1991;43(1):8–12.

[23] Remy-Jardin M, Remy J, Wallaert B, et al. Subacute and chronic bird breeder hypersensitivity pneumonitis: sequential evaluation with CT and correlation with lung function tests and bronchoalveolar lavage. Radiology 1993;189(1):111–8.

[24] Hansell DM, Wells AU, Padley SP, et al. Hypersensitivity pneumonitis: correlation of individual CT patterns with functional abnormalities. Radiology 1996;199(1):123–8.

[25] Small JH, Flower CD, Traill ZC, et al. Air-trapping in extrinsic allergic alveolitis on computed tomography. Clin Radiol 1996;51(10):684–8.

[26] Aquino SL, Webb WR, Golden J. Bronchiolitis obliterans associated with rheumatoid arthritis: findings on HRCT and dynamic expiratory CT. J Comput Assist Tomogr 1994;18(4):555–8.

[27] McLoud TC, Epler GR, Colby TV, et al. Bronchiolitis obliterans. Radiology 1986;159(1):1–8.

[28] Arakawa H, Webb WR. Air trapping on expiratory high-resolution CT scans in the absence of inspiratory scan abnormalities: correlation with pulmonary function tests and differential diagnosis. AJR Am J Roentgenol 1998;170(5):1349–53.

[29] Garg K, Lynch DA, Newell JD, et al. Proliferative and constrictive bronchiolitis: classification and radiologic features. AJR Am J Roentgenol 1994;162(4): 803–8.

[30] Rosenow III EC, Myers JL, Swensen SJ, et al. Drug-induced pulmonary disease. An update. Chest 1992; 102(1):239–50.

[31] McAdams HP, Rosado-de-Christenson ML, Wehunt WD, et al. The alphabet soup revisited: the chronic interstitial pneumonias in the 1990s. Radiographics 1996;16(5):1009–33.

[32] Muller NL, Staples CA, Miller RR. Bronchiolitis obliterans organizing pneumonia: CT features in 14 patients. AJR Am J Roentgenol 1990;154(5):983–7.

[33] Akira M, Yamamoto S, Sakatani M. Bronchiolitis obliterans organizing pneumonia manifesting as multiple large nodules or masses. AJR Am J Roentgenol 1998;170(2):291–5.
[34] Wesselius LJ. Pulmonary complications of cancer therapy. Compr Ther 1999;25(5):272–7.
[35] Haupt HM, Hutchins GM, Moore GW. Ara-C lung: noncardiogenic pulmonary edema complicating cytosine arabinoside therapy of leukemia. Am J Med 1981; 70(2):256–61.
[36] Reed CR, Glauser FL. Drug-induced noncardiogenic pulmonary edema. Chest 1991;100(4):1120–4.
[37] Gluecker T, Capasso P, Schnyder P, et al. Clinical and radiologic features of pulmonary edema. Radiographics 1999;19(6):1507–31.
[38] Storto ML, Kee ST, Golden JA, et al. Hydrostatic pulmonary edema: high-resolution CT findings. AJR Am J Roentgenol 1995;165(4):817–20.
[39] Primack SL, Miller RR, Muller NL. Diffuse pulmonary hemorrhage: clinical, pathologic, and imaging features. AJR Am J Roentgenol 1995;164(2):295–300.
[40] Collins J, Muller NL, Leung AN, et al. Epstein-Barr-virus-associated lymphoproliferative disease of the lung: CT and histologic findings. Radiology 1998; 208(3):749–59.
[41] Worthy SA, Flint JD, Muller NL. Pulmonary complications after bone marrow transplantation: high-resolution CT and pathologic findings. Radiographics 1997;17(6):1359–71.
[42] Cunningham I. Pulmonary infections after bone marrow transplant. Semin Respir Infect 1992;7(2): 132–8.
[43] Mori M, Galvin JR, Barloon TJ, et al. Fungal pulmonary infections after bone marrow transplantation: evaluation with radiography and CT. Radiology 1991;178(3):721–6.
[44] Primack SL, Muller NL. High-resolution computed tomography in acute diffuse lung disease in the immunocompromised patient. Radiol Clin North Am 1994;32(4):731–44.
[45] Winer-Muram HT, Gurney JW, Bozeman PM, et al. Pulmonary complications after bone marrow transplantation. Radiol Clin North Am 1996;34(1):97–117.
[46] Kang EY, Patz Jr EF, Muller NL. Cytomegalovirus pneumonia in transplant patients: CT findings. J Comput Assist Tomogr 1996;20(2):295–9.
[47] Nalesnik MA. Clinicopathologic characteristics of post-transplant lymphoproliferative disorders. Recent Results Cancer Res 2002;159:9–18.
[48] Dodd III GD, Greenler DP, Confer SR. Thoracic and abdominal manifestations of lymphoma occurring in the immunocompromised patient. Radiol Clin North Am 1992;30(3):597–610.
[49] Soubani AO, Miller KB, Hassoun PM. Pulmonary complications of bone marrow transplantation. Chest 1996;109(4):1066–77.
[50] Davis SD, Yankelevitz DF, Henschke CI. Radiation effects on the lung: clinical features, pathology, and imaging findings. AJR Am J Roentgenol 1992;159(6): 1157–64.
[51] Libshitz HI. Radiation changes in the lung. Semin Roentgenol 1993;28(4):303–20.
[52] Logan PM. Thoracic manifestations of external beam radiotherapy. AJR Am J Roentgenol 1998;171(3): 569–77.
[53] Ikezoe J, Takashima S, Morimoto S, et al. CT appearance of acute radiation-induced injury in the lung. AJR Am J Roentgenol 1988;150(4):765–70.
[54] Movsas B, Raffin TA, Epstein AH, et al. Pulmonary radiation injury. Chest 1997;111(4):1061–76.
[55] Gross NJ. The pathogenesis of radiation-induced lung damage. Lung 1981;159(3):115–25.
[56] Libshitz HI, Shuman LS. Radiation-induced pulmonary change: CT findings. J Comput Assist Tomogr 1984;8(1):15–9.
[57] Popovsky MA. Transfusion and lung injury. Transfus Clin Biol 2001;8(3):272–7.
[58] Nag S, Vivekanandam S, Martinez-Monge R. Pulmonary embolization of permanently implanted radioactive palladium-103 seeds for carcinoma of the prostate. Int J Radiat Oncol Biol Phys 1997;39(3): 667–70.
[59] Padovani B, Kasriel O, Brunner P, et al. Pulmonary embolism caused by acrylic cement: a rare complication of percutaneous vertebroplasty. AJNR 1999;20(3): 375–7.
[60] Root JD, Molina PL, Anderson DJ, et al. Pulmonary nodular opacities after transbronchial biopsy in patients with lung transplants. Radiology 1992;184(2):435–6.
[61] Kazerooni EA, Cascade PN, Gross BH. Transplanted lungs: nodules following transbronchial biopsy. Radiology 1995;194(1):209–12.

ELSEVIER
SAUNDERS

Radiol Clin N Am 43 (2005) 543 – 569

RADIOLOGIC
CLINICS
of North America

Vascular Diseases of the Thorax: Evaluation with Multidetector CT

Caroline Chiles, MD*, J. Jeffrey Carr, MD

Division of Radiological Sciences, Department of Radiology, Wake Forest University School of Medicine, Medical Center Boulevard, Winston-Salem, NC 27157, USA

The list of vascular diseases in the thorax has been narrowed to three, which are considered essential information for radiologists interpreting CT scans of the thorax: (1) aortic dissection and its variants, intramural hematoma (IMH) and penetrating atherosclerotic ulcer; (2) acute pulmonary embolism (PE); and (3) coronary artery disease. The spatial resolution of multidetector CT (MDCT) is such that CT has become the imaging modality of choice for aortic dissection and PE. This move away from angiography has transpired over the last decade; perhaps the next decade will see the same occur for evaluation of coronary artery disease.

Aortic dissection and its variants

An aortic dissection is characterized by an entrance tear within the intima and media of the aorta, which allows blood flow to create a false lumen within the medial layers of the aortic wall. The media separates in a course parallel to that of the flow of blood. The false lumen lies within the outer half of the media, so that the outer wall of the false lumen is very thin, usually only about one quarter as thick as the original aortic wall [1]. The intimal flap consists of the intima, and one half of the media, so that it is about three times as thick as the outer wall of the false lumen, and about three quarters as thick as the original aortic wall. The thinness of the outer wall of the false lumen explains its tendency to rupture.

In autopsy series, the entrance tear is located in the ascending aorta in 70% of patients, in the aortic arch in 10%, in the descending thoracic aorta in 20%, and rarely within the abdominal aorta [1]. This contrasts with surgical or radiologic studies, in which dissections in the descending aorta are more common, because these studies include the survivors of aortic dissection. From the entrance tear, the dissection of the media occurs in a predominantly anterograde direction, although retrograde dissection is also seen. Re-entrance tears are found less frequently, and in some cases a single tear may be present so that flow within the false channel is bidirectional. Re-entrance tears are most commonly found in the descending thoracic aorta, abdominal aorta, and iliac artery.

In dissections involving the ascending aorta, the entrance tear is typically in the right lateral aortic wall, and the dissection extends in an antegrade fashion along the greater curvature of the ascending, transverse, and descending thoracic aorta (Fig. 1). The arch arteries arise from this portion of the aorta, so that dissection into the right brachiocephalic, left common carotid, and left subclavian arteries is common [1]. The dissection extends along the aorta until it encounters sufficient atherosclerotic plaque or scarring to interrupt its course. At that point, the dissection either stops or rejoins the aortic lumen through the second, re-entrance, tear.

The most frequent cause of death in patients who have aortic dissection is aortic rupture. The rupture site is typically near the original entrance tear. In patients who have entrance tears in the ascending aorta, blood from a ruptured ascending aorta collects in the pericardial sac. Massive hemopericardium is often

* Corresponding author.
E-mail address: cchiles@wfubmc.edu (C. Chiles).

0033-8389/05/$ – see front matter © 2005 Elsevier Inc. All rights reserved.
doi:10.1016/j.rcl.2005.02.010

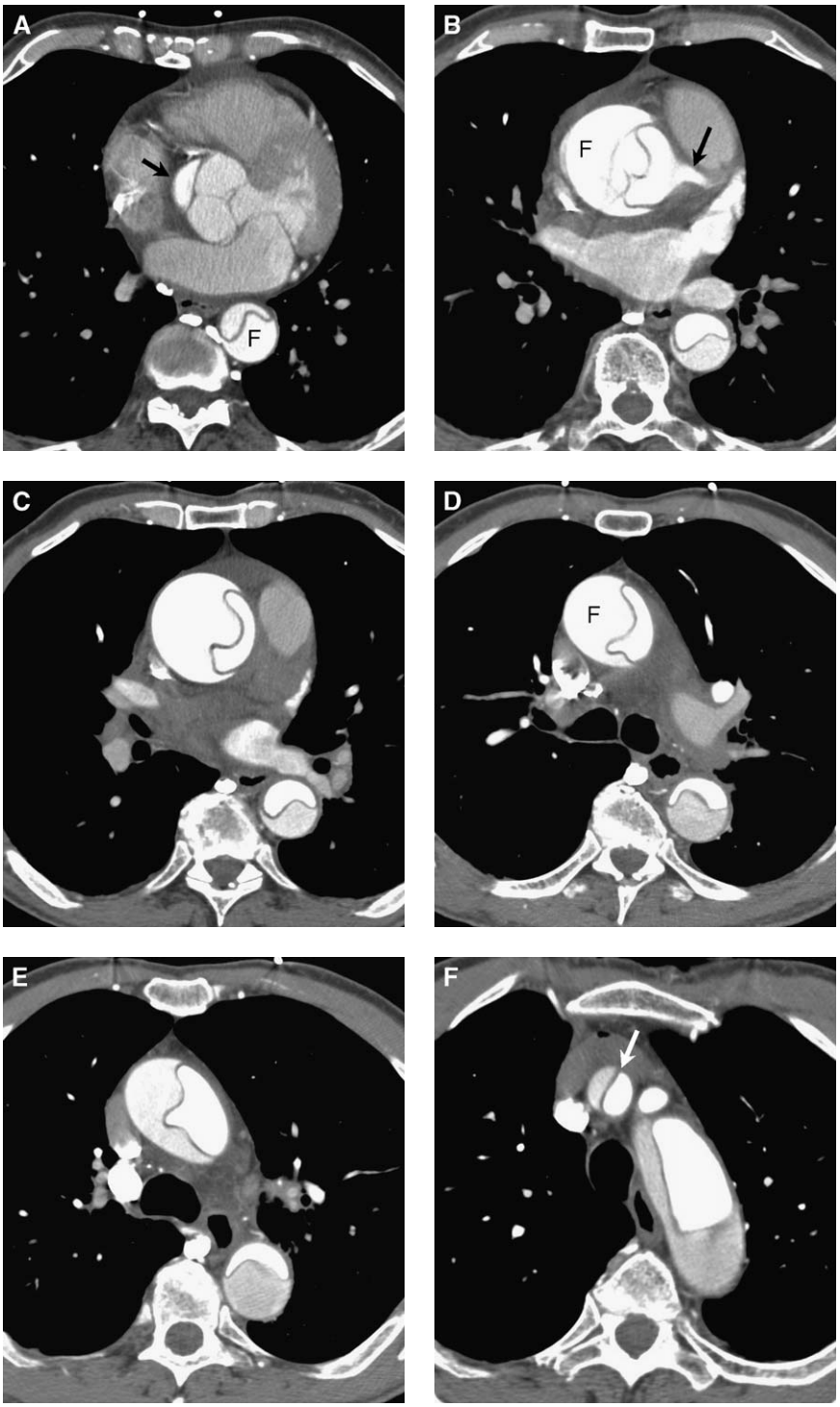
A
F
B
F
C
D
F
E
F

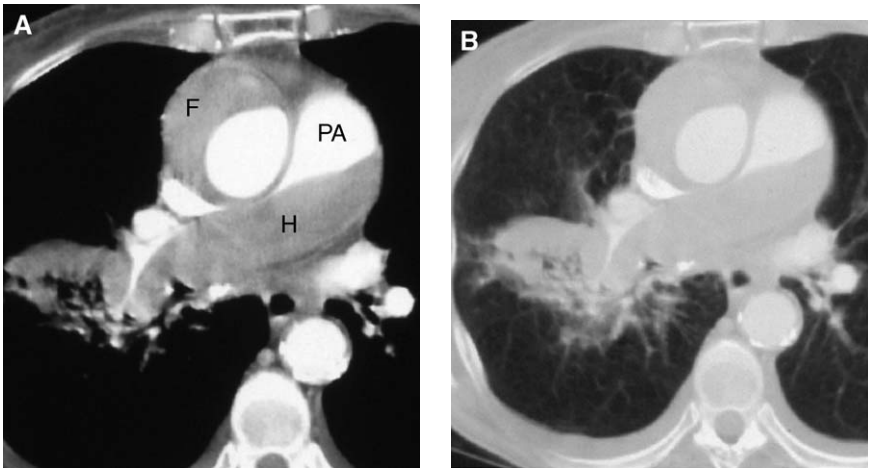

Fig. 2. Dissection of the ascending aorta with mediastinal hematoma (H) extending along the right pulmonary artery (PA). (*A, B*) The ascending aorta and pulmonary artery share a common adventitia. Hemorrhage that enters the adventitial layer of the ascending aorta extends along the right pulmonary artery, causing compression of the right pulmonary artery and pulmonary hemorrhage.

rapidly fatal, but some patients remain hemodynamically stable long enough to reach the hospital, where hemopericardium may be seen on imaging studies. Rupture in the ascending aorta may also cause blood to dissect along the adventitia. The ascending aorta and pulmonary trunk have a common adventitia, so that hemorrhage into the adventitia can extend along the pulmonary trunk, causing compression of the lumen of the main pulmonary arteries (Fig. 2). Blood in various anatomic compartments indicates the most likely site of rupture: hemomediastinum is caused by rupture of the aortic arch, left-sided hemothorax may indicate rupture of the descending thoracic aorta, and hemoperitoneum may be caused by rupture of the abdominal aorta (see Fig. 1).

Compromise of aortic branch arteries is a significant contributor to the morbidity and mortality of this disease. The dissection flap may extend into the branch vessel, or the flap may cover the lumen of the vessel, causing ischemia or necrosis of the organ or tissue normally perfused by that vessel (see Fig. 1B and F) [2]. The coronary arteries may be compromised when dissections in the ascending aorta extend retrograde into the aortic sinus. In these patients, the dissection may also cause loss of commissural support of the aortic valve cusps, resulting in aortic regurgitation. When the dissection involves the transverse portion of the aorta, the arch vessels may become compromised, producing ischemia of the brain or arm. In the abdominal aorta, the renal and mesenteric arteries and celiac axis may be involved, so that the patient presents with signs of renal failure or abdominal organ insufficiency.

Although the cause of spontaneous aortic dissection is unknown, most patients have a history of systemic hypertension. Marfan syndrome is also considered a cause of aortic dissection, but patients who have this syndrome and its characteristic medial cystic necrosis are more likely to have fusiform aneurysms of the ascending aorta than dissection. Other

Fig. 1. Stanford type A dissection. (*A*) The true lumen can be recognized by its continuity with the left ventricle. The entrance tear in type A dissection is often in the right anterolateral wall of the ascending aorta, creating the false lumen along the greater curvature of the ascending aorta (*arrow*). In the descending aorta, the false lumen (F) fills with contrast material at a different rate than the true lumen. (*B*) The false lumen (F) is larger than the true lumen in the ascending aorta, and exhibits the beak sign as the hematoma dissects the media of the aortic wall. The left main coronary artery (*arrow*) is seen, arising from the true lumen. (*C, D*) Mediastinal hematoma can be recognized by measuring the attenuation of fluid surrounding the ascending aorta and right ventricular outflow tract. The presence of mediastinal hematoma suggests rupture of the ascending aorta, associated with type A dissection. (*E*) At the level of the carina, the true lumen is filled with a greater concentration of contrast material in this dynamic CT examination. Note the reversal of the contrast attenuation in images obtained a few seconds later (*A*). (*F*) The intimal flap extends into the right brachiocephalic artery (*arrow*). F, false lumen.

entities associated with an increased risk of aortic dissection are bicuspid aortic valves (with or without aortic stenosis); aortic coarctation; and trauma (with aortic transsection). Aortic dissection may also occur as an iatrogenic complication of catheter insertion.

Elefteriades [3] reviewed a Yale database of 1600 patients who had thoracic aortic aneurysms and determined hinge points for the likelihood of rupture or dissection based on aortic diameter. When the ascending aorta was 6 cm in diameter, the likelihood of rupture or dissection was 31%; when the descending aorta reached a diameter of 7 cm, the likelihood of a critical event was 43%. He recommended intervention for the ascending aorta at a diameter of 5.5 cm and for the descending aorta at 6.5 cm. It should be noted, however, that dissections frequently occur in aortas of normal caliber. Aneurysmal dilatation develops only as the false lumen expands after the onset of dissection.

Classification of aortic dissection

Two classifications of aortic dissection are in widespread use. In 1965, DeBakey et al [4] classified dissecting aneurysms into three types, related to anatomic and pathologic features. Types I and II involve the ascending aorta, with type I dissections extending beyond the aortic arch and type II dissections stopping proximal to the brachiocephalic artery. Type III dissections involve only the descending aorta. In 1970, Daily et al [5] reviewed the experience at Stanford and reported a significant difference in the clinical course and prognosis in patients who had dissections involving the ascending aorta as opposed to those in whom the disease did not extend proximal to the left subclavian artery. They suggested further simplification of the classification to two types: type A indicates involvement of the ascending aorta, and type B dissections are limited to the descending aorta. This classification has been known as the ''Shumway classification,'' after the senior author on that paper or, more recently, the Stanford classification. The simplicity and relevance of this classification to the management of the patient with aortic dissection has helped to make this the most widely used classification system.

Clinical presentation

The International Registry of Acute Aortic Dissection (IRAD) is a multicenter registry, which includes consecutive patients who have acute aortic dissection seen at 18 large referral centers since 1996. The objective of the registry is to assess the etiology, presentation, management, and outcomes of patients who have acute aortic dissection. Of 550 patients who have type A aortic dissections entered into the IRAD in the 3-year interval from 1996 to 1999, the mean age was 62 ± 14 years, and 65.5% were men. Of 384 patients who have type B dissections entered into the IRAD in the 4-year interval from 1996 to 2000, the mean age was 65 ± 13 years, and 71.4% were men. The average duration of symptoms from onset to presentation was 2.9 hours in those with type A dissections. A history of hypertension was recorded in 69.2% of those with type A dissections and 79.9% of those with type B dissections [6,7]. The typical clinical presentation was an acute onset of chest pain. A murmur of aortic regurgitation was present in 41.7% of those with type A dissections [6].

Natural history and treatment

Aortic dissection has long been recognized as a serious disease with a rapidly fatal course without treatment. Anagnostopoulos et al [8] in a 1972 meta-analysis reported death within 1 week in 70% of 963 patients, and death within 3 months in 90%. Of the 550 patients who have type A aortic dissections entered into the IRAD from 1996 to 1999, 79.5% were treated with surgical repair [6]. Ascending aortic replacement was performed in 91.4% of those patients. The mortality for patients who have type A dissections treated surgically was 26.7% compared with a 55.9% mortality for those treated medically. In patients who have type B dissections, 73% received medical management; 15% underwent surgery; and 12% were treated with percutaneous interventions, such as stent placement. In-hospital mortality was 32.1% for those treated surgically, 9.6% for those receiving medical therapy, and 6.5% for those undergoing percutaneous intervention [7]. Three risk factors (the deadly triad) predicted in-hospital death in patients who have acute type B aortic dissection: (1) hypotension or shock, (2) lack of chest or back pain at presentation, and (3) branch vessel involvement [7]. Although medical management has long been the standard of care for type B dissections, the 5-year mortality remains high. Of 50 patients followed with chronic aortic dissection, a fatal rupture occurred in 9 patients (18%) [9]. This has to be considered against the considerable mortality and morbidity in surgical series of descending aorta repair.

Endovascular techniques are emerging as an alternative to surgical repair. Placement of a self-expanding stent-graft in patients who have expanding aortic dissections, active bleeding, or suspected imminent rupture of a descending thoracic aortic dis-

section was described in 22 patients by Fattori et al [10]. Criteria for inclusion included 1 cm or more of normal aortic wall distal to the origin of the left subclavian artery, 42 mm or smaller diameter of the aorta proximal and distal to the dilated portion, and 9 mm or larger diameter of the femoral or iliac arteries. Identification of entry and reentry sites, true and false lumina and their relationship to visceral and femoral vessels, and the extent of the dissections were usually obtained with MR imaging and aortography. The patient was excluded from percutaneous stent-graft placement if a reentry site could not be identified in the abdominal aorta and the origin of one or more visceral vessels was from the false lumen. In their series of 22 patients, there was one death from aortic rupture (at 20 days); one patient with subsequent extension of dissection; and one who developed endoleak at the end of the graft. Two patients were converted to surgical repair.

Hansen et al [11] reported endovascular repair of 24 patients who had aortic dissections (16 acute, 8 chronic). Indications for treatment of acute type B dissections included intractable pain, uncontrollable hypertension, progression of dissection, or end-organ ischemia. Six patients had hemothorax as a primary indicator for treatment. Patients who have chronic type B dissections were considered candidates for endovascular repair if there was aneurysmal dilatation of the proximal descending aorta or if the patient developed acute symptoms. Procedure-related mortality was 13%; one death was attributed to rupture caused by endoleak, and two deaths occurred from retrograde dissection of the ascending aorta leading to cardiac tamponade. Overall mortality was 19% in patients who had acute type B dissections and 13% in patients who have chronic type B dissections, at an average follow-up of 2 years.

Choice of imaging modalities

Aortography was long the procedure of choice for the examination of patients who had aortic dissection. That technique has given way to less invasive, less expensive, and more accurate technologies, including CT, transesophageal echocardiography, and MR imaging. A review of the imaging studies performed in patients enrolled in the IRAD from 1996 through 1999 showed that the initial imaging modality choice was CT, followed by transesophageal echocardiography [12]. CT was selected for 63% of patients compared with transesophageal echocardiography in 32%. MR imaging was ordered less frequently, in part because of the greater distance of many MR imaging scanners from emergency rooms, and the greater difficulty in monitoring critically ill patients in the magnetic field. Aortography was ordered infrequently, perhaps because of its greater cost, longer examination time, and inability to detect IMH. A comparison of spiral CT, transesophageal echocardiography, and MR imaging in 49 patients who had clinically suspected aortic dissection showed 100% sensitivity for aortic dissection for all three techniques, specificity of 100% for CT, and 94% for both transesophageal echocardiography and MR imaging. In the diagnosis of aortic arch vessel involvement, CT was clearly superior with sensitivity and specificity of 93% and 97% compared with transesophageal echocardiography (60% and 85%) and MR imaging (67% and 88%) [13]. Yoshida et al [14] found similarly high accuracy in the CT recognition of arch branch vessel involvement. Comparison with surgical findings in 57 patients who had either aortic dissection or IMH showed a sensitivity of 95%, specificity of 100%, and overall accuracy of 98%.

In the IRAD patients, the chest radiograph was abnormal in most cases. The mediastinum appeared widened in 62% of type A and 56% of type B dissections [6,7]. The aortic contour was abnormal in 45% of type A and 49% of type B dissections. A pleural effusion was present in 19% of patients who had type A dissections.

CT scanning technique

Examination of the thoracic aorta using CT angiography is rapid, noninvasive, and allows depiction of the aorta in a number of imaging planes and in three dimensions. The scan should include the base of the neck, so that the proximal aspects of the carotid and vertebral arteries can be evaluated. Inferiorly, the scan should extend to at least the level of the celiac axis, although imaging through the abdomen and pelvis is often indicated. An unenhanced scan is performed initially, using relatively thick (5 mm) collimation. Intravenous contrast material is injected through an 18- to 20-gague catheter inserted in the right antecubital vein. Injection in the left arm may produce more artifacts because of the horizontal course of the left brachiocephalic vein, near the origins of the aortic arch arteries [15]. The bolus of contrast material should be calculated to continue throughout the duration of the CT scan. Typically, a bolus of 80 to 150 mL of nonionic iodinated contrast material at a rate of 4 to 5 mL per second provides adequate opacification. Bolus tracking software provides the optimal scan delay for initiation of the scan, but an empiric scan delay of 30 seconds can be used. The scan should ideally be performed during a

single breathhold, but quiet breathing can be used in the dyspneic patient. The contrast-enhanced scan can be performed at a section thickness of 2.5 to 3 mm, at a pitch of 1.3 to 1.7 for MDCT. A 1.5-mm reconstruction interval, using standard or soft tissue reconstruction algorithm, is created from the scans. Reconstructions that are useful in assessing the thoracic aorta include thin-slab maximum intensity projections in the coronal and sagittal oblique planes, curved planar reformations, volume renderings, and surface-shaded displays [16]. Some authors have used ECG gating for CT angiography, which helps to reduce pulsation artifacts [17,18].

Findings on CT

Unenhanced CT

Unenhanced CT images provide information that can be obscured by intravenous contrast material. On CT scans performed without intravenous contrast material, displacement of intimal calcification from the aortic wall is consistent with a diagnosis of aortic dissection. This can mimic, however, calcification of mural thrombus within an aortic aneurysm. A major role for unenhanced images is the depiction of IMH. In patients who have aortic IMH, a narrow rim of high-attenuation material is present within the aortic wall, either in a crescentic or circumferential pattern (Fig. 3) Prosthetic aortic valves and grafts are easier to recognize on unenhanced CT (see Fig. 3). In patients who had aortic rupture, the high attenuation of acute blood is readily apparent within the mediastinum, pericardial sac, or pleural space on unenhanced CT (Fig. 4).

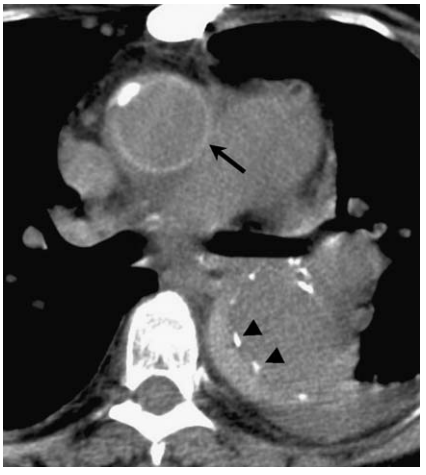

Fig. 3. Aortic intramural hematoma. On an unenhanced CT, intimal calcification (*arrowheads*) is displaced from the wall of the descending aorta by a crescentic area of increased attenuation. This is consistent with acute bleeding into the aortic wall, presumably caused by rupture of the vaso vasorum. The patient has previously undergone graft repair (*arrow*) of the ascending aorta.

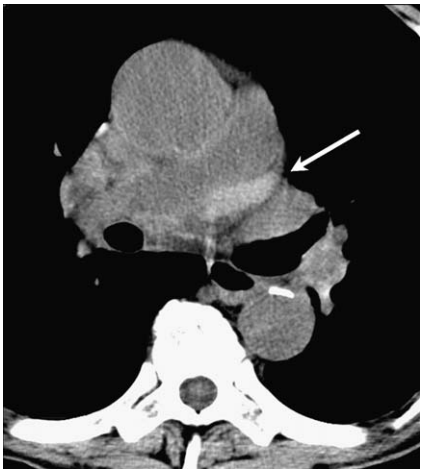

Fig. 4. Mediastinal hematoma. In patients who have aortic rupture, the high attenuation of acute blood (*arrow*) is readily apparent within the mediastinum on unenhanced CT.

Enhanced CT

On enhanced CT, the hallmark of aortic dissection is the intimal flap, separating the true and false lumen (see Fig. 1). The entrance tear is usually at the most proximal extent of the intimal flap. Correlation with surgical findings of entrance tears in 57 patients who had either aortic dissection or IMH showed that CT was 84% accurate in the identification of the entrance tear (sensitivity 82%, specificity of 100%) [14]. False-negative findings were caused by a small entry tear, an aortic pulsation artifact, and artifact caused by catheter or venous enhancement. Correct identification of the entry tear is helpful to surgical planning, because grafts are selected to replace the affected thoracic aorta, including the entrance tear.

Differentiation of true and false lumen

Identification of the true and false lumen in aortic dissection is important in the planning of surgical repair or endovascular graft placement. The origin of major vessels, including coronary, carotid, renal, and mesenteric arteries from either the true or false lumen should be specifically addressed. Arteries arising from the false lumen are at risk of occlusion should the false lumen either spontaneously thrombose or become obliterated during repair. Branch vessels may be obstructed when the dissection flap extends into

the origin of the branch vessel (static obstruction) [2]. Dynamic obstruction occurs when the intimal flap does not directly involve the vessel origin, but is flattened over the vessel origin because of pressure changes in the true lumen.

In most cases, the true lumen can be recognized by continuity with an uninvolved portion of the aorta (see Fig. 1). The true lumen is usually small, containing blood flow traveling at a high velocity, compared with slower blood flow in a larger false lumen. On contrast-enhanced CT, these differing rates of blood flow may be apparent as differing rates of contrast enhancement (see Fig. 1).

On cross-sectional imaging, the junction of the intimal flap and the outer wall of the false lumen forms an acute angle, created as the sharp wedge of the hematoma cleaves the aortic media [19]. On CT, this has been called the ''beak sign'' (see Fig. 1). The space formed by the acute angle can be filled with either high-attenuation contrast-enhanced blood, or low-attenuation hematoma. Another indicator of the false lumen is the presence of aortic cobwebs (Fig. 5). Aortic cobwebs most likely represent strands of fibrous tissue that have been incompletely sheared from the aortic walls during the dissection, and are a hallmark of the false lumen [20]. They range in size from barely noticeable to several millimeters thick, and have been observed within the false lumen in 80% of anatomic specimens in acute dissection, and in 74% of chronic dissections [20]. On CT, cobwebs are thin filling defects, attached at one end to the aortic wall, within the contrast-filled false lumen.

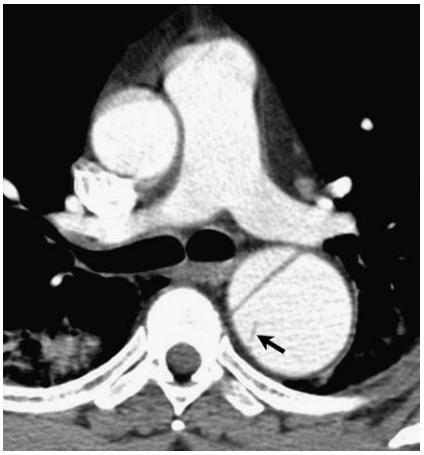

Fig. 5. Aortic cobweb. A thin line of fibrous tissue (*arrow*) is consistent with an aortic cobweb, incompletely sheared from the aortic wall during dissection, and a hallmark of the false lumen.

Atherosclerotic calcification in the outer wall of an aortic lumen indicates the true lumen of an *acute* aortic dissection, and may appear continuous with the calcified intimal flap representing the inner wall of the false lumen. In *chronic* dissection, the outer wall of the false lumen may endothelialize and calcify, so that this sign may not be valid. Displaced calcification on the intimal flap is a hallmark of aortic dissection, and is best seen on unenhanced CT (see Fig. 3). Occasionally, the calcification on the intimal flap is seen to lie eccentrically and, in this situation, faces the true lumen.

LePage et al [21] reviewed the most useful CT indicators of the true and false lumen in 51 patients who had aortic dissection. They found that the most reliable signs of the false lumen were the beak sign and a larger cross-sectional area. The beak sign was seen only in the false lumen, and was present on all CT scans. Aortic cobwebs were also present only in the false lumen, but were seen in only 9% of acute dissections and 17% of chronic dissections. Outer wall calcification was seen in the true lumen in 60% of acute dissections, and never in the false lumen in acute dissection. In chronic dissection, however, outer wall calcification was seen in 17% of false lumens. Intraluminal thrombus was seen in 46% of false lumens and only 6% of true lumens in the acute setting. In chronic dissection, intraluminal thrombus was present in 83% of false lumens, and 4% of true lumens. The false lumen is larger than the true lumen in most cases. The intimal flap may be either curved toward the false lumen, or flat, in acute dissection. In chronic dissections, the intimal flap is flat in 75% and curved toward the false lumen in 25%.

On intravascular ultrasound, the intact outer wall of the true lumen has three visible layers, similar to that of an inverse Oreo cookie [19]. The middle layer is hypoechoic, bordered on each side by a hyperechoic outer layer and hyperechoic inner layer. The outer wall of the false lumen, however, is visible as a single hyperechoic layer, continuous with the hyperechoic outer layer of the true lumen. Aortic cobwebs and thrombus may also be visible within the false lumen on intravascular ultrasound.

Intramural hematoma

IMH, or hemorrhage into the aortic wall, may be an early stage or variant of aortic dissection. It is presumably caused by spontaneous rupture of the vaso vasorum, and is distinguished from aortic dissection by the lack of an intimal flap, and lack of communication with the true lumen. This entity

has been called noncommunicating aortic dissection and aortic dissection without intimal rupture [22]. Bleeding in the media layer of the aorta evolves over a short period of time; the blood may be reabsorbed or progress to aortic dissection or rupture. Current therapy for IMH parallels that for aortic dissection; early surgical repair or endovascular placement of a stent-graft is considered for patients who have IMH involving the ascending aorta [23]. Patients who have IMH involving only the descending aorta are managed medically, with aggressive antihypertensive treatment and frequent follow-up imaging examinations. A minority opinion exists, suggesting that perhaps 50% of patients who have type A IMH can be managed with medical treatment only [24,25]. Moizumi et al [25] suggest that surgery be reserved for patients who have cardiac tamponade, rupture, or impending rupture, and for patients initially managed medically but who experience recurrence of chest or back pain, progression to type A dissection, progressive aortic dilatation to a maximum diameter greater than 6 cm, or progressive enlargement of an ulcerlike projection to greater than 2 cm depth. This conservative approach requires close interval monitoring, because complications forced late surgical intervention in 22% of type A IMH and 26% of type B IMH.

Improved recognition of IMH with cross-sectional imaging has changed the understanding of this entity. IMH was perhaps underdiagnosed for many years, because it is difficult to diagnose with aortography. The mortality of IMH in the first 3 months of evolution is high: 19% in a study of 68 consecutive patients who had IMH [26]. Predictors of early mortality were a maximum aortic diameter greater than 5 cm, and involvement of the ascending aorta. Mortality in those with an aortic diameter greater than 5 cm was 50%. In patients who had involvement of the ascending aorta, early mortality was 8% in those undergoing surgical repair, compared with 55% in those without surgery [26]. Nienaber et al [27] also reported a high mortality in patients who had IMH of the ascending aorta: 80% in those treated medically. In contrast, in patients who had type B IMH, 1-year survival was 80% in the group treated medically and 83% in the group treated surgically.

On unenhanced CT, IMH is visible as a crescent of high-attenuation material within the aortic wall (Figs. 3 and 6). This rim of high attenuation represents acute bleeding into the aortic wall, and occasionally involves the entire circumference of the aorta. Some authors believe that IMH by definition lacks an entrance tear; others believe that the ulcerlike projection sometimes seen within the IMH represents an entrance tear. Ganaha et al [28] suggest that the presence of penetrating atherosclerotic ulcer predicts progression of IMH. Other features that have been reported as predictors that IMH will progress to overt dissection include a greater maximum thickness of the hematoma (a thickness of 16.4 ± 4.4 mm versus 10.5 ± 3.8 mm in the group that did not progress to dissection); flattening of the true lumen so that the short-axis diameter is less than 75% of the long-axis diameter; involvement of the ascending aorta; and the presence of either pericardial or pleural effusion [29]. A hematoma thickness greater than 11 mm was predictive of adverse outcome in a series of 25 patients who had IMH involving the ascending aorta [24]. A normal aortic diameter in the acute phase has also been associated with IMH regression without complications [30].

Differentiation of IMH from intraluminal thrombus on a contrast-enhanced CT may be difficult. Features that suggest IMH are displaced intimal calcifications, and a crescentic or circumferential distribution of the now (relative to contrast) low-attenuating material. Intraluminal thrombus is often localized, and within a dilated aorta, whereas IMH may extend over a longer distance, within a nondilated aorta (see Fig. 6). IMH involved an 8.5 ± 5–cm length of the aorta in a study of 25 patients who had IMH [27]. MR imaging allows detection of the age of the IMH, and may be useful to monitor IMH over time. On sequential T1-weighted images, acute blood is of intermediate signal intensity because of the presence of oxyhemoglobin. Subacute (8–30 days) blood is of high signal intensity because of the presence of methemoglobin in the evolving hematoma [31]. The absence of these characteristic changes in signal intensity may indicate on-going hemorrhage in patients who have recurrent pain. Echocardiographic criteria of IMH include circular or crescentic thickening (>5 mm) of the aortic wall containing an echo-free space, and absence of an intimomedial tear [32].

Follow-up of IMH over time has shown very similar outcomes in two series. Evangelista et al [30] followed 68 consecutive patients, with a mean follow-up of 45 ± 31 months. They found that the most common outcome was progression to aortic aneurysm or pseudoaneurysm. At the end of follow-up, the IMH had evolved to aneurysm in 54% (fusiform aneurysm in 22%, saccular aneurysm in 8%, and pseudoaneurysm in 24%); regressed completely without dilatation in 34%; and progressed to classic dissection in 12%. Sueyoshi et al [33] reported similar findings. A follow-up of 32 patients who have IMH found that all IMH decreased over time, and 34% disappeared almost completely. Aneurysm

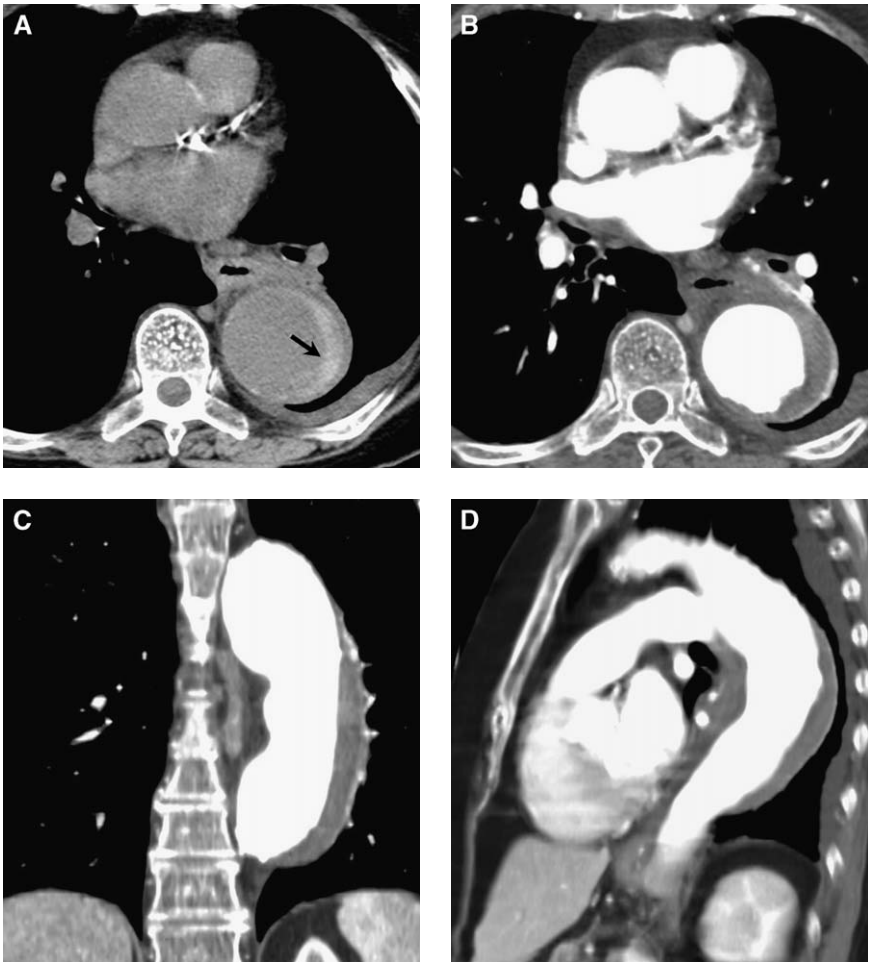

Fig. 6. Aortic intramural hematoma (IMH). (*A*) On unenhanced CT, intramural hematoma is visible as a crescentic area (*arrow*) of increased attenuation in the aortic wall. (*B*) Following intravenous contrast administration, the intramural hematoma may be mistaken for thrombus within an aortic aneurysm. (*C, D*) On coronal and sagittal reformats, the intramural hematoma extends along the posterolateral wall of the descending aorta. IMH typically extends over a long segment of an aorta of normal caliber, whereas thrombus is usually seen along a short segment of a dilated aorta. The diagnosis of IMH requires visualization of displaced intimal calcification or increased attenuation of the aortic wall, both of which may be obscured by intravenous contrast material.

developed in 56% (fusiform in 19%, and saccular aneurysm in 37%). Progression to overt dissection occurred in 6%. Ulcerlike projections were present at the initial study in six patients, and appeared on follow-up studies in 14 patients (Fig. 7). The ulcer-like projections progressed to saccular aneurysm in 12 patients.

Penetrating atherosclerotic ulcer

A penetrating atherosclerotic ulcer forms when an ulcerated atherosclerotic plaque breaks through the intima, resulting in hematoma formation within the media of the aortic wall. Extension of the ulcer beyond the expected margin of the aortic wall and the presence of a hematoma cap over the ulcer helps to differentiate this entity from the more commonly occurring atheromatous ulcer (Fig. 8). It is differentiated from IMH, which has an intact intima, by the ulcer extending beyond the aortic lumen [34]. On unenhanced CT images, acute blood in the aortic wall may be visible as an area of increased attenuation, as in IMH. Contrast-enhanced CT allows recognition of the ulcer and enhancement of the aortic wall [35].

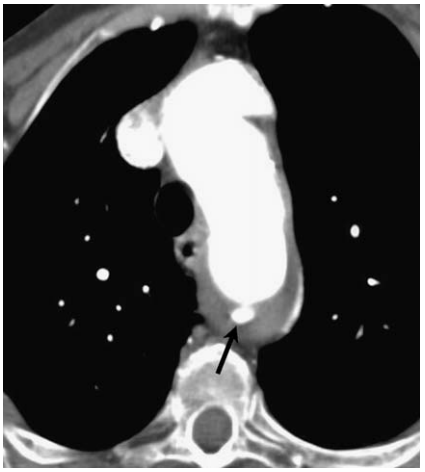

Fig. 7. Aortic intramural hematoma. An ulcerlike projection (*arrow*) may be seen within the intramural hematoma following intravenous contrast administration. This may indicate a greater likelihood of progression to pseudoaneurysm formation.

Similarly with MR imaging, the associated hematoma is well demonstrated on conventional MR imaging, and gadolinium-enhanced MR angiography is better for recognition of the ulcer. The hematoma is also well seen with transesophageal echocardiography, although the ulcer itself is more difficult to identify than with CT or MR imaging.

The clinical presentation of a penetrating atherosclerotic ulcer mimics aortic dissection, with the typical patient elderly, hypertensive, and presenting with symptoms of chest or back pain. Penetrating atherosclerotic ulcer most commonly involves the middle or distal third of the descending thoracic aorta, although any part of the aorta may be involved. In a retrospective review of 105 patients who have penetrating atherosclerotic ulcers by Cho et al [36], a penetrating atherosclerotic ulcer involved the descending aorta in 94% and the ascending aorta in 11% (multiple ulcers were present in 10%).

Over a period of weeks to months, the hematoma associated with a penetrating atherosclerotic ulcer becomes smaller, whereas the ulcer may enlarge. In the series by Cho et al [36], the initial thickness of the hematoma was 10 mm, which decreased or resolved in most patients within 1 month and in all patients within 1 year. The average depth of the ulcer was 11 mm, the width of the mouth of the ulcer was 15 mm, and the length of the ulcer was 16 mm.

The natural history of a penetrating atherosclerotic ulcer is variable. In 33 ulcerlike lesions of the aorta reviewed by Quint et al [37], 21 were stable over a mean follow-up period of 18.4 months. In 10 of 33 lesions, progression over time included an increase in the diameter of the aorta with or without an increase in the size of the ulcer. As the ulcer enlarges and extends through the media, it may be contained by the adventitia, resulting in a saccular pseudo-

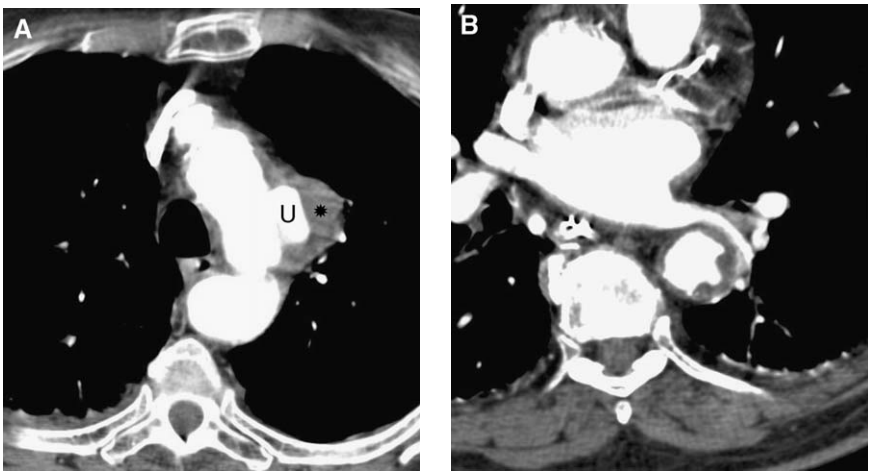

Fig. 8. Penetrating atherosclerotic ulcer versus atheromatous ulcer. (*A, B*) A penetrating atherosclerotic ulcer (PAU) forms when an ulcerated atherosclerotic plaque breaks through the intima, resulting in hematoma formation within the media of the aortic wall. Extension of the ulcer (u) beyond the expected margin of the aortic wall and the presence of a hematoma cap (*) over the ulcer helps to differentiate this entity from the more commonly occurring atheromatous ulcer, seen in *B*.

aneurysm. Among 54 penetrating atherosclerotic ulcer patients who had serial scans, 26 (48%) developed an asymmetric aneurysm [36]. Less commonly, the hematoma associated with the ulcer extends longitudinally, producing a classic aortic dissection. The dissection continues until it reaches sufficient atherosclerotic plaque to halt its progress. Rupture is an infrequent, but often fatal, complication of penetrating atherosclerotic ulcer.

Patients who are hemodynamically stable and in whom penetrating atherosclerotic ulcers are found are generally managed with antihypertensive therapy and close monitoring. Emergent surgery is indicated for patients who are hemodynamically unstable and in those with pseudoaneurysm formation or aortic rupture. Indications for late surgical intervention include persistent or recurrent pain, expanding IMH or pseudoaneurysm, distal embolization, and hemodynamic instability. Operative treatment requires placement of an interposition graft at the site of the ulcer.

Pulmonary embolism

Most cases of PE result from thrombi that become dislodged from their sites of formation in the pelvis or in the deep veins of the legs. There are a number of risk factors for venous thromboembolism, including malignancy, immobilization after surgery or trauma, central venous catheter or pacemaker placement, obesity, oral contraceptive use, and inherited thrombophilia [38,39]. The actual scope of PE is difficult to determine. PE was responsible for 14.6% of all in-hospital deaths in one autopsy series [40]. In 1998, Silverstein et al [41] estimated the incidence of PE to be 69 per 100,000 of population. Most patients develop PE while hospitalized for surgery (24%) or medical illness (22%), or while in a nursing home (13%) [38]. Risk factors are identified in 74% of all cases [38].

Two large prospective studies of PE have provided much of the current understanding of the diagnosis of PE. These studies include the Prospective Investigation of Pulmonary Embolism Diagnosis (PIOPED) in the United States, and the Prospective Investigative Study of Acute Pulmonary Embolism Diagnosis (PISA-PED) in Europe [42,43]. The results from PIOPED II were pending at the time of this writing. The clinical presentation of PE patients in the PIOPED study was dyspnea, tachypnea, or pleuritic chest pain, which were present in 97% of patients. These symptoms were present in non-PE patients, however, in a similar number of patients. The PISA-PED study found that three symptoms (sudden onset of dyspnea, pleuritic chest pain, and fainting) were significant for the presence of PE, particularly when combined with findings on ECG and chest radiography [43]. Sudden onset of dyspnea was the most common symptom, described by 80% of PE patients. One or more of these three symptoms were present in 96% of PE patients, but they were also present in 59% of non-PE patients. Correct classification of patients who had suspected PE was possible in 88%, but only with the use of EKG and chest radiograph findings.

Laboratory tests for PE include the partial pressure of oxygen in arterial blood on room air (PaO_2) and the alveolar-arterial oxygen gradient (PAO_2-PaO_2). PE is usually accompanied by arterial hypoxemia and hypocapnia [43]. These measurements have not proved to be sufficient, however, for the distinction of PE from non-PE patients. The fibrin D-dimer, a degradation product released into the circulation after the breakdown of cross-linked fibrin, is increased in patients who have thrombosis and can be used as a marker for PE. The ELISA method D-dimer has been reported to have a negative predictive value of 99% for PE [44]. A raised level of D-dimer does not imply the presence of PE, because D-dimer levels can be elevated from nonthrombotic conditions. Currently, a negative D-dimer level in a patient with a low or moderate clinical suspicion for PE is considered sufficiently reliable that other diagnoses should be sought for the patient's signs and symptoms [45]. The experienced clinician who accurately assesses a patient's clinical probability for PE can, in combination with the D-dimer assay, significantly reduce the need for imaging.

The value of incorporating the D-dimer assay in a diagnostic algorithm for PE has been supported by many studies. Perrier et al [46] prospectively evaluated 918 consecutive patients presenting to the emergency room with clinically suspected venous thromboembolism. A normal D-dimer concentration (<500 μg/L by a rapid ELISA) ruled out venous thromboembolism in 286 (31%) members of the study cohort. The 3-month thromboembolic risk in patients not given anticoagulants, based on the results of the diagnostic protocol, was 1.8% (95% confidence interval 0.9–3.1). In a separate study, Abacarian et al [47] reported that, in 84 patients who had a negative D-dimer assay, 82 had negative findings on CT pulmonary angiography (CTPA) and the remaining 2 patients had indeterminate CT scans but low-probability ventilation-perfusion scans. Although the ELISA method D-dimer has proven to be an important part of the diagnostic protocol in

outpatients who have clinical suspicion of PE, it has not been shown to be effective in the management of inpatients who have suspected PE [48].

The chest radiograph plays an ancillary role in the evaluation of patients who have clinical suspicion of PE. It is helpful in the diagnosis of diseases that may mimic PE clinically, such as pneumonia. It is also helpful in the interpretation of ventilation-perfusion scintigraphy. The ventilation-perfusion scan was, for many years, the primary test in the patient with clinical suspicion of PE. The PIOPED study was conducted from 1985 to 1986 to develop accurate standards for the interpretation of ventilation-perfusion scans. In the PIOPED population, scans were normal to near-normal in 14%, low probability in 34%, intermediate probability in 39%, and high probability in 13%. When the results of the ventilation-perfusion scan were concordant with the clinical suspicion, the diagnosis was accurate in 96% to 98% of patients. For example, when a high-probability scan occurred in a patient with a high clinical suspicion, 96% of patients had PE [42]. In patients who have a low-probability scan with a low clinical suspicion, the diagnosis of PE was excluded in 96% of patients. Unfortunately, these combinations applied to only 16% of patients. The large percentage of intermediate scans left a need for a more reliable test. Interobserver variability in the interpretation of ventilation-perfusion scans is another limitation of this imaging study. Although interobserver agreement was high in the interpretation of high-probability, very-low-probability, and normal scans, disagreement among observers was 25% and 30%, respectively, for intermediate-probability and low-probability scans in the PIOPED study. The ventilation-perfusion scan is more likely to be diagnostic when the chest radiograph is normal and there is no pre-existing cardiopulmonary disease. When the ventilation-perfusion scan is normal, PE is reliably excluded.

CT pulmonary angiography

Over the last decade, CTPA has become the imaging modality of choice in patients who have clinical suspicion of PE [49,50]. On single-slice CT scans in the 1980s and 1990s, PE was often an incidental finding. With the advent of helical CT, and particularly with MDCT, thromboemboli within the pulmonary arterial system can be directly viewed on high-quality images obtained in a single breathhold with optimal contrast bolus timing. The accuracy of CT in the diagnosis of PE in studies published from 1992 through 1998 ranged from 74% to 100%, but standard CT technique at that time was 5-mm slice thickness on single-detector CT scanners [51–56]. A major concern at that time was the lower accuracy in the detection of emboli within subsegmental arteries, an issue that has been addressed with MDCT scanners. This concern is not new for radiologists. Diffin et al [57] point out that, even with pulmonary angiography, one-third of patients who have isolated subsegmental emboli may be initially misdiagnosed.

The difficulty in evaluating the accuracy of the current generation of MDCT (4-, 8-, 16-, and 64-detector) scanners is that CT may now be more accurate than the gold standard of conventional pulmonary angiography [58]. The high resolution of 1-mm or submillimeter collimation data sets, acquired in a single breathhold, allows evaluation of pulmonary vessels down to the level of sixth-order branches, and increases the rate of detection of segmental and subsegmental emboli [59,60]. Ghaye et al [59] found that 1.25-mm scans reconstructed from data sets obtained on a four-detector CT scanner allowed analysis of 94% of subsegmental arteries, 74% of fifth-order, and 35% of sixth-order arterial branches. In the evaluation of subsegmental emboli, Schoepf et al [60] reported a substantial decrease in the number of indeterminate cases and greater interobserver agreement when 1-mm section thickness images were compared with 3-mm section width.

A review of the diagnosis of PE in 220 consecutive patients using four-detector row helical CT showed consistent interpretation ($\kappa = 0.88$) in two reading sessions, and a small (9%) percentage of nondiagnostic CT studies [61]. Of the 54 PE patients, 8 had only subsegmental PE. The 3-month rate of thromboembolic events after negative CTPA or negative CT venography was 1.8% (95% confidence interval 0.2%–6.4%). Coche et al [62] performed CTPA using a four-detector CT scanner and ventilation-perfusion scans in 94 consecutive patients who had clinical suspicion of acute PE. The interpretations were concordant in 82 patients (58 negative CT per normal or low probability V/Q; 24 positive CT per high probability V/Q). In the remaining 12 patients in whom there was discordance between the CT and the V/Q interpretations, the pulmonary angiogram was concordant with the CT interpretation in 10 of 11 patients; the angiogram was negative in the twelfth patient, in whom CT was indeterminate. The sensitivity and specificity of both the CT and the V/Q scans was high (96% and 86% for CT, 98% and 88% for V/Q). Examinations with CT yielded more conclusive results more often, however, than ventilation-perfusion scintigraphy.

A major advantage of CT over other imaging modalities is that it can provide alternative diagnoses in patients who have other causes for dyspnea and pleuritic chest pain, including pneumonia, malignancy, pleural effusion, esophagitis, pericarditis, and aortic dissection. Helical CT identified an alternative diagnosis in 25% to 46% of patients who had signs and symptoms suggestive of PE [63–65].

Just as in the era before performing dedicated CT to diagnose PE, emboli are occasionally diagnosed in patients referred for routine contrast-enhanced chest CT in whom PE is not clinically suspected. Gosselin et al [66] found a prevalence of PE of 0.6% in outpatients and 5% in inpatients. Of the 12 patients who had unsuspected PE, 10 had an underlying diagnosis of malignancy.

CT technique

CT scanning for suspected PE should include the entire thorax. Many radiologists choose to scan in a craniocaudal direction, so that if the patient cannot maintain the breathhold, the lung bases (the more likely site for PE) are scanned at the beginning of the study, and the upper lobes, which are less susceptible to respiratory motion artifact, are scanned at the end of the study. Optimal bolus timing is achieved with bolus tracking software or, alternatively, with a fixed scan delay of 15 to 20 seconds. A 100 to 150 mL bolus of nonionic iodinated contrast material is injected at a rate of 4 to 5 mL per second, by an 18- to 20-gauge catheter inserted into the right antecubital vein. On a four-detector scanner, the raw data set is obtained with a 4 × 1-mm, or 4 × 1.25-mm, collimation with a pitch of 6 (table feed of 6 mm per 500-millisecond scanner rotation), and reconstructed to 1- or 1.25-mm section thickness. Interpretation of 1.25-mm images, compared with 2.5-mm collimation, significantly improves visualization of segmental and subsegmental pulmonary arteries, with greater interobserver agreement in the diagnosis of PE [67]. Review of the images at a computer workstation is essential, because this allows scrolling through the large number of images obtained and manipulation of the window and level settings, which can improve conspicuity of filling defects within the contrast-enhanced pulmonary arteries.

CT findings

Findings of PE on CTPA are similar to the observations on conventional pulmonary angiography. Most patients have more than one embolus, which on 1.25-mm images are visible on more than one contiguous image. An angiographic study of the anatomic distribution of PE showed that patients who underwent bilateral pulmonary angiography had an average of three emboli (range 1–16), with most (58%) located in the central (segmental or larger) arteries [68]. The Advances in New Technologies Evaluating the Localization of Pulmonary Embolism group reported that the largest pulmonary arterial branch involved in 130 PE patients was central or lobar in 51%, segmental in 27%, and isolated subsegmental in 22% [69]. Sixty percent of the emboli were nonocclusive. Fifty-eight percent of emboli were in the lower lobes.

On CT, a PE is most commonly seen as a filling defect within the lumen of a contrast-filled pulmonary artery (Fig. 9). The thrombi typically originate in the deep veins of the lower extremities, and the long, narrow thrombi straddle the bifurcations of the pulmonary arteries. The largest ones, straddling the bifurcation of the main pulmonary arteries, are called ‘‘saddle emboli,’’ but this same phenomenon also occurs throughout the smaller arteries. The embolus may appear somewhat eccentrically located at the level of the bifurcation, with the two limbs floating in the lumen of the downstream vessels. Because most emboli are longer than 1 to 2 mm, filling defects that are visible on only one 1.25-mm image, and not on contiguous images, are more likely to be artifacts than emboli. The emboli are typically nonocclusive, although complete vessel cutoff may also be seen when the thromboembolus occludes the vessel. When an artery is imaged longitudinally, contrast may be seen coursing along the margins of the filling defect, producing a ‘‘railway track’’ appearance.

PE may rarely be visible on unenhanced CT, as either hyperattenuating or hypoattenuating areas of intraluminal thrombus in the central pulmonary arteries [70,71]. On lung window settings, pulmonary parenchymal abnormalities may also be seen in pe patients. Two signs, linear bands of subsegmental atelectasis and wedge-shaped peripheral areas of parenchymal consolidation, occur more commonly in PE patients than non-PE patients [72]. Pleural effusions, however, are present in similar proportions in PE and non-PE patients [73]. Regions of decreased enhancement within areas of nonaerated lung are seen in 19% of PE patients, but are also nonspecific (Fig. 10) [74].

Massive PE may cause acute right ventricular dysfunction and reduced cardiac output. Right ventricular dilatation may be visible on CT, with displacement of the interventricular septum toward the

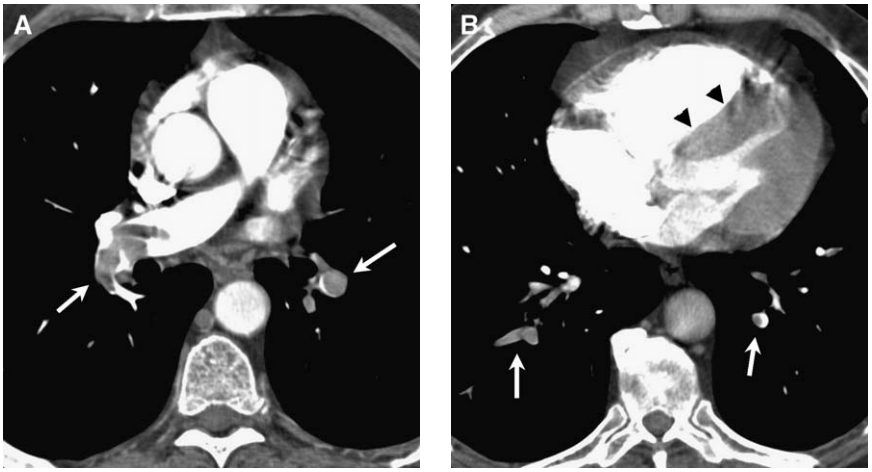

Fig. 9. Pulmonary emboli. (*A*) Filling defects are present bilaterally (*arrows*), in the right pulmonary artery, extending into the right descending pulmonary artery, and in the left descending pulmonary artery. (*B*) Thromboemboli are visible as filling defects (*arrows*) in the segmental and subsegmental pulmonary arteries of both lower lobes. The clot burden caused an increase in right heart pressures, with right ventricular dilatation and bowing of the interventricular septum (*arrowheads*) visible on CT.

left ventricle (Fig. 11) [75]. Reid and Murchison [76] suggest that a ratio of right ventricle:left ventricle short-axis diameter of 1.5:1 or greater indicates severe right ventricular strain. Reflux of contrast material into the inferior vena cava may also be encountered. Quiroz et al [77] measured the ventricular diameters in patients who had CT-confirmed PE on both axial images and a multiplanar axial reconstruction of a four-chamber view. The maximal distance between the ventricular endocardium and the interventricular septum, perpendicular to the long axis, was defined as the chamber diameter. When the right ventricle–left ventricle diameter was greater than 0.9 on the four-chamber view, adverse events, such as 30-day mortality or need for cardiopulmonary resuscitation, embolectomy, or mechanical ventilation, occurred more commonly (80% versus 51%). The measurements from the axial views were not predictive of an adverse outcome.

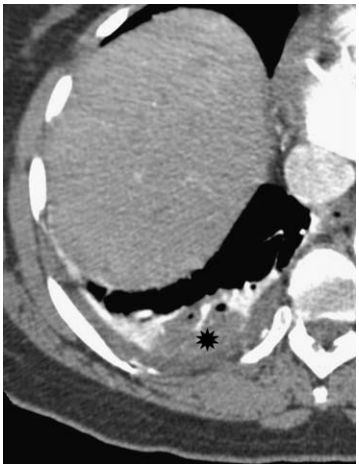

Fig. 10. Pulmonary embolus. Regions of decreased enhancement (*) within areas of nonaerated lung are seen in 19% of patients who have pulmonary embolism, but are nonspecific.

CT measurement of clot burden has also been recommended as a predictor of outcome. Qanadli et al [78] proposed a CT index to quantify arterial obstruction, which was based on the sum of the values of the proximal clot site multiplied by the degree of obstruction (1 = partial, 2 = complete obstruction). Proximal clot in the right or left pulmonary artery was assigned a value of 10, because each artery supplies 10 segmental arteries; values of lobar arteries were based on the number of segmental arteries within the lobe (range 2–5); the segmental and subsegmental arteries were each assigned a value of 1. These sums are divided by 40 (the highest possible score) and multiplied by 100 to develop a percentage value. A CT obstruction value of greater than 40% correlated well with the finding of right ventricular dilatation on echocardiography. Wu et al [79], using this CT index, found that five of six patients who had an index greater than 60% died, whereas 52 of 53 patients who had an index of less than 60% survived.

Pitfalls in the interpretation of PE on CT include a number of patient factors, technical factors, and anatomic features [80]. Respiratory motion can wreak

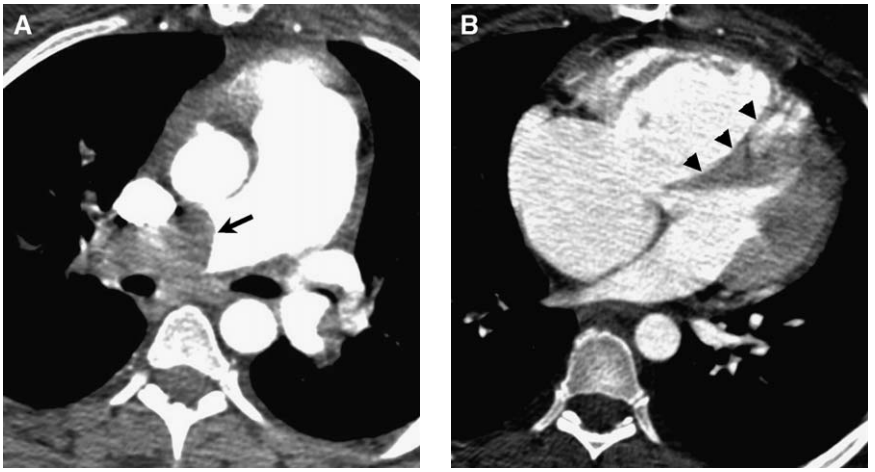

Fig. 11. Massive pulmonary embolism. (*A*) Thromboembolus causes occlusion (*arrow*) of the right pulmonary artery. A clot burden of this magnitude may cause acute right ventricular dysfunction and reduced cardiac output. (*B*) Right ventricular dilatation is visible on CT, with displacement of the interventricular septum (*arrowheads*) toward the left ventricle. A ratio of RV:LV short-axis diameter of 1.5:1 or greater indicates severe right ventricular strain.

havoc on image quality, such that CT may not be indicated in the patient who cannot be expected to maintain the breathhold. CTPA should be performed, when possible, on CT scanners with the fastest acquisition times, to minimize respiratory artifacts. Patient size is also a factor in image quality, because significant noise may be encountered on images of obese patients, despite compensatory increases in kilovolt (peak) and milliamperes.

In a small number of scans, adequate contrast material may be present in the superior vena cava and right heart, and also in the left-sided cardiac chambers and aorta, yet opacification of the pulmonary arteries is inadequate (Fig. 12). This has the appearance of two separate contrast boluses, with an intervening gap. It may be caused by a column of unopacified blood from the inferior vena cava, which transiently interrupts the contrast bolus [81,82]. This flow artifact may be associated with inspiratory effort. Right-to-left shunting across a patent foramen ovale caused by a Valsalva's maneuver during the breathhold has also been postulated [83]. The artifact can be recognized by the symmetric absence of contrast material in both the right and left pulmonary arteries at the same level in the thorax (see Fig. 12).

Anatomic details that may help in the identification of PE include the position of pulmonary arteries relative to bronchi. Segmental and subsegmental pulmonary arteries are part of a bronchoarterial bundle, visible in cross-section as a contrast-filled artery adjacent to an air-filled bronchus of similar diameter. In the upper lobes, the segmental and subsegmental arteries lie anterior and medial to their corresponding bronchi; in the middle and lower lobes, the arteries lie posterior and lateral to their corresponding bronchi. Pulmonary veins occur in isolation, and review of images on "lung windows" may help to differentiate arteries from veins.

A number of normal-sized lymph nodes can be seen, and are most often located between major bronchi and pulmonary arteries [84]. These can mimic eccentric filling defects and cause false-positive interpretations. Knowledge of the normal locations of these lymph nodes and reconstruction of the images in the coronal plane aids in the recognition that these lie outside the vessel lumen.

Venous ultrasound and CT venography

Diagnostic algorithms that have been developed for patients who have suspected venous thromboembolism differ in their recommendations for the use of venous ultrasound. In a patient with clinical suspicion of deep venous thrombosis (DVT), it is reasonable to include leg ultrasound as an initial test. Identification of DVT precludes the need for additional testing because treatment can be instituted. A negative examination is less useful, however, in that one cannot distinguish those in whom thrombus was never present from those in whom the thrombus has completely embolized to the lungs. Some authors recommend venous ultrasound as an initial imaging modality only in patients who have clinical suspicion of DVT, and CTPA as the initial imaging modality in

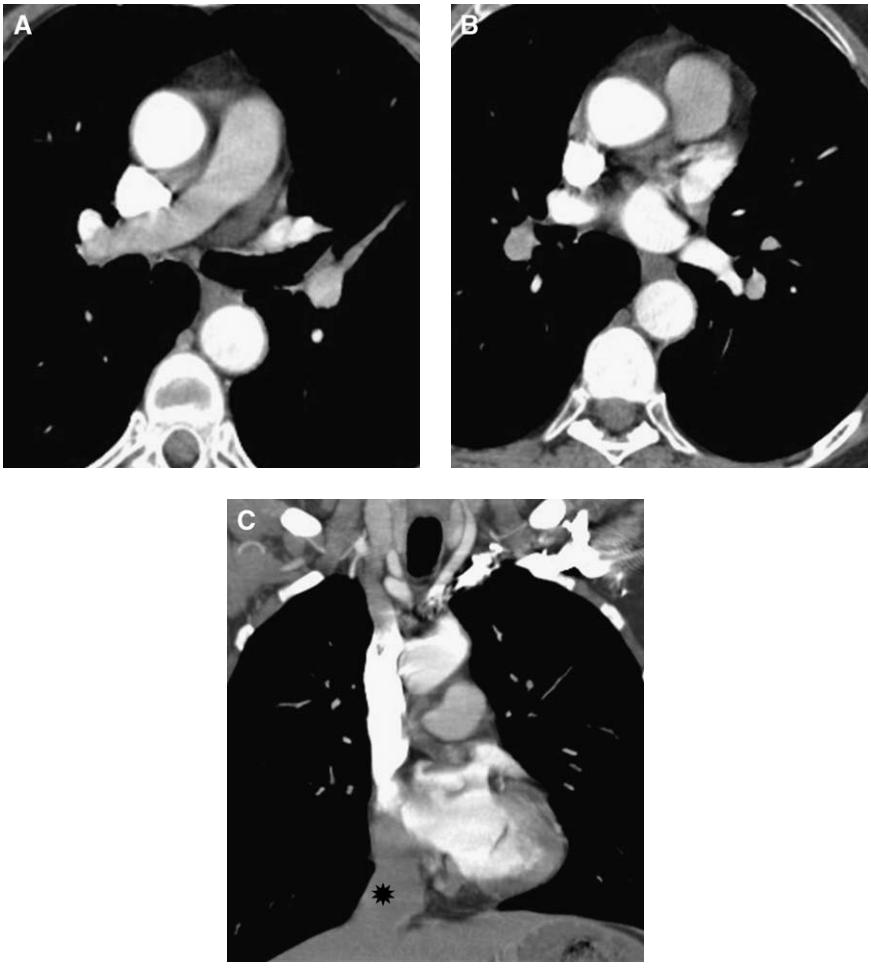

Fig. 12. Artifact caused by unopacified venous return from the inferior vena cava. (*A, B*) Adequate contrast material is present in the superior vena cava and right heart, and also in the left-sided cardiac chambers and aorta, yet opacification of the pulmonary arteries is inadequate. This has the appearance of two separate contrast boluses, with an intervening gap. (*C*) The flow artifact may be caused by a column of unopacified blood from the inferior vena cava (*), which transiently interrupts the contrast bolus. This flow artifact may be associated with inspiratory effort or a Valsalva's maneuver.

patients who have suspected PE but without clinical evidence of DVT [39,49,85]. Other authors recommend venous ultrasound as the initial imaging modality in all inpatients who have suspected PE or DVT, and in all outpatients who have a positive D-dimer [86]. The prevalence of DVT in patients suspected of having PE is 18% [87]. In patents with proved PE, the prevalence is twice that at 36%.

Because DVT and PE are both manifestations of a single disorder, venous thromboembolism, which uniformly requires anticoagulation, combined CTPA and venography has been recommended as an imaging technique capable of identifying both PE and DVT [88,89]. Currently, compression venous ultrasonography is the procedure of choice in patients who have suspected DVT because of its noninvasive nature, portability, wide availability, and low cost. CT venography has been shown to correlate well with lower-extremity venous sonography, but has the advantage of depicting the iliac veins and inferior vena cava [90,91]. The additional cost and radiation dose of CT venography has resulted in limited use of this technique.

The CT venogram is performed in a caudal-cranial direction, with 5-mm-thick slices at 5-cm intervals from the upper calves to either the iliac crest or diaphragm, after a delay of 2 to 3.5 minutes following the CTPA. CT findings of DVT are intraluminal

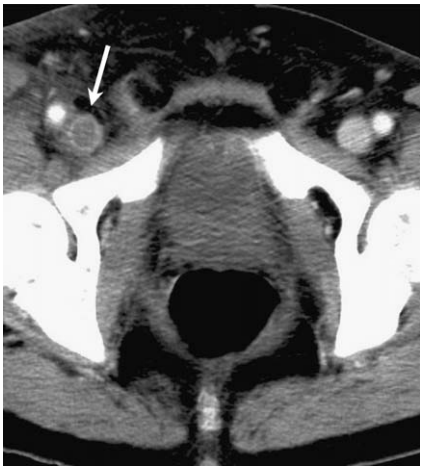

Fig. 13. Deep venous thrombosis. CT findings of deep venous thrombosis are intraluminal filling defects within the popliteal, femoral (*arrow*), iliac veins, or inferior vena cava. The vein is often distended, and the wall may show contrast enhancement. In most patients, an intraluminal filling defect involves multiple venous segments, and is visible on multiple contiguous images.

filling defects within the popliteal, femoral, or iliac veins or inferior vena cava (Fig. 13). In some cases, the vein is distended, and the wall may show contrast enhancement. In most patients, an intraluminal filling defect involves multiple venous segments, and is visible on multiple contiguous images [92]. A pitfall of interpretation of DVT is inadequate contrast enhancement, which can occur with a scan delay that is too short, or in patients who have severe peripheral vascular disease. Beam-hardening artifacts can also occur, caused by adjacent arterial calcification or orthopedic hardware.

Coronary artery disease

Cardiac CT has rapidly evolved in the past decade from, at best, a niche test with minimal impact on clinical medicine to where now it is poised to play a primary role in both the identification and diagnosis of cardiac diseases. The constant beating of the heart results in complex motions of not only the coronary arteries but also the valves and chambers of the heart. Previously, when using CT to image the thorax, the region of the heart located centrally within the thorax was simply a blur of motion unsharpness. The development and clinical introduction of the electron-beam CT scanner in the late 1980s and 1990s demonstrated the capability of CT when coupled with rapid image acquisition times and cardiac gating [93]. The advent of helical CT in the 1990s coupled with improved gantry rotation speeds of under a second provided the temporal and spatial resolution to image not only the pulmonary arteries but to begin to resolve cardiac structures and the coronary arteries. The addition of cardiac gating and multiple detectors from 4 to 8 to 16 to 64 and beyond has allowed cardiac imaging with CT to play a major role in the identification and diagnosis of cardiac-related diseases. Currently, cardiac imaging with CT can be broken into two distinct roles. The first and more established role is using noncontrasted cardiac CT to measure calcified coronary plaque for coronary heart disease risk assessment. The second rapidly evolving role is using cardiac CT with intravenous contrast material in a diagnostic role to evaluate the anatomy, pathology, and function of the coronary arteries, heart chambers, pericardium, and surrounding structures.

Measuring calcified plaque with cardiac CT

Calcified coronary plaque or atheroma is an established component of the atheromatous lesion [94]. Expert consensus statements agree that calcifications of the coronary artery documents the presence of coronary atherosclerosis, and that individuals with calcified coronary plaque are at higher risk for cardiovascular events [95,96]. An individual in whom calcified plaque is identified in the wall of a coronary artery has crossed the threshold from having risk factors to documented subclinical cardiovascular disease (CVD) (Fig. 14). The amount of calcified plaque is highly correlated with total coronary

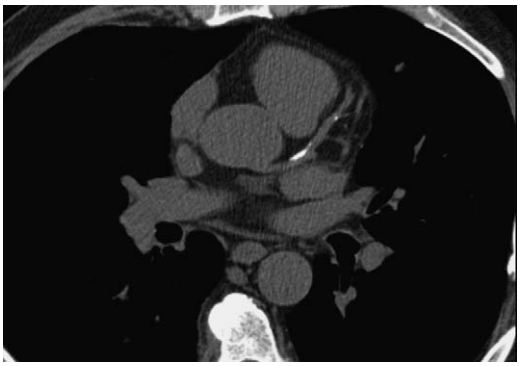

Fig. 14. ECG gated cardiac CT examination without intravascular contrast demonstrating calcified coronary plaque in the wall of the distal left main and proximal left anterior descending (LAD) coronary arteries. A small calcified plaque is present in the distal LAD at the origin of the second diagonal.

atheroma at histology but not correlated with the presence of stenosis [97,98]. Studies correlating measures of atherosclerosis remodeling of coronary vessels with intracoronary ultrasound and CT coronary angiography with MDCT have likewise indicated very high correlations in the ability of cardiac CT to quantify coronary atherosclerosis [99]. The culprit lesion or plaque of acute myocardial infarction seems to be associated with what has been termed a "spotty pattern" of calcified plaque by intracoronary ultrasound and this pattern of calcification can be demonstrated by cardiac CT [100].

The development of the electron-beam CT coupled with cardiac gating provided a means for quantification of the amount of calcified plaque and the development of the Agatston calcium score, which is widely used to report the burden of calcified plaque [101]. The sum of the calcified plaque in each of the main coronary arteries using the Agatston method is often reported as a total calcium score. The score is calculated by defining calcified plaques as lesions meeting a predefined minimum size and measuring greater than 130 HU. Based on the highest pixel within the lesion a discrete weighting factor of 1, 2, 3, or 4 is multiplied by the area of the lesion to determine the lesion score. Numerous alternative methods for measuring calcified plaque have been proposed, including the volume and mass of calcified plaque. In clinical practice the Agatston or Total Calcium Score remains the primary method of communicating results.

The published literature strongly supports that calcified coronary plaque measured by cardiac CT predicts future CVD events and provides significant additional information to traditional CVD risk factors. Support for this is strong historically based on cardiac fluoroscopy studies, which demonstrate that calcified plaque, even when qualitatively assessed, provided significant information about an individual's future risk of a cardiovascular event independent of other risk factors and had significantly greater mortality when compared with those without calcified plaque after adjusting for other factors, such as ejection fraction or percent stenosis [102,103]. The initial studies evaluating the predictive ability of calcified coronary plaque in populations asymptomatic for coronary heart disease indicate increased risk of cardiovascular events in individuals with coronary calcified plaque (relative risk ratios between 2.3 and 20.2) [104–110]. Although these studies have limitations, expert panels, which have reviewed the data from these studies including the two previously mentioned consensus statements and the Preventions V Conference of 2000 by the American Heart Association [111,112], all concluded that the presence of calcified plaque by CT significantly increased the risk for future CVD events. What remained unknown in 2000 was whether the coronary calcium score provided additional information concerning CVD risk when added to traditional risk factors. The value of adding the calcium score to traditional CVD risk factor screen, such as the Framingham Risk Index or the National Cholesterol Education Panels–Adult Treatment Panel III, needed to be determined to justify its implementation as a screening tool. The Prevention V Conference went on to recommend that a physician use the coronary calcium score as a risk assessment tool in those individuals at intermediate risk for CVD in whom the test could be used to guide the physician and patient in determining the most effective prevention strategy [112].

In 2004, the South Bay Heart Study reported results in which they demonstrated that the calcium score added significant risk prediction to traditional CVD risk factors as measured by the Framingham risk score [109] for myocardial infarction and coronary heart disease death. Participants in this study who had a total calcium score greater than 300 (Agatston score) at entry into the study had significantly more events after an average of 7 years of follow-up. This elevated risk of hard coronary heart disease events was present in individuals determined to be at low, intermediate, or high risk by the Framingham risk score, again at entry into the study.

Guidelines for risk assessment for CVD based on calcified coronary plaque need to be specific for gender and likely ethnicity because these factors impact the prevalence of CVD. The National Heart, Lung and Blood Institute's Multi-Ethnic Study of Atherosclerosis (MESA; http://www.mesa-nhlbi.org/) is a population-based cohort study studying risk factors for CVD in 6118 individuals [113]. This cohort study was initiated in 2000 with baseline measurements of coronary calcified plaque by cardiac CT already completed. MESA has demonstrated that measurement of calcified plaque with both electron-beam CT and MDCT can be performed efficiently at clinical centers across the United States [114] and provide the prevalence and incidence of calcified coronary plaque in the United States. MESA will track cardiovascular events and will have good power in determining the predictive ability of the calcium score in men and women in four different ethnic groups. Moreover, the comparative ability of coronary calcium to predict events with other diagnostic tests, such as cholesterol levels, C-reactive protein, and other inflammatory markers, and other imaging

tests, such as cardiac MR imaging and intimal medial thickness by carotid ultrasound, will be available for the first time.

Cardiac CT systems for measuring calcified plaque require temporal resolution and cardiac gating to obtain images of the coronary arteries, which minimize motion unsharpness and compensate for cardiac motion. The specifics and rational of the protocols have been detailed previously [114,115]. The minimum configuration is a 0.5-second gantry, four-slice MDCT or a C-150 electron-beam CT. More recent configurations, such as a 16-, 32-, 40-, or 64-channel MDCT or the newest version of the electron-beam CT termed the "E-Speed," improve the measurement of calcified plaque through enhanced temporal resolution or improved signal to noise. In addition, for the MDCTs the use of an eight-channel or greater system dramatically reduces the breathhold time to less than 15 seconds requiring fewer heartbeats for imaging the entire coronary system.

The basic protocol for acquiring the images for calcium scoring uses a 2.5- to 3-mm slice collimation, cardiac gating, 120 kilovolt (peak), and 50 to 100 milliamperes depending on type of scanner. It is important to note that the various vendors determine and report milliamperes or effective milliamperes in different ways and these values are guidelines that must be modified based on the specific scanner. The calcium scoring protocol uses a low-dose technique with an effective dose for the typical protocol ranging from 0.8 to 1.8 mSv depending on the technique used, the CT system, and individual scanned. Prospective ECG gating or triggering is used to initiate image acquisition at a specific time during the cardiac cycle based on the R-wave of the QRS complex. Traditionally, in the electron-beam CT literature, imaging was in late diastole (70%–80% of the R to R interval) although arguments have been made for imaging earlier in diastole (40%–50% of the R to R interval) [116,117].

Higher resolution imaging of the coronary arteries without contrast using thinner slice collimation and a helical cardiac acquisition are areas of active research; however, at this time the benefits have not been established. The cardiac helical acquisition, in particular, results in a significant increase in dose. At this time there are no data to support that enhanced accuracy, and the measurement of the calcified plaque would significantly improve the risk assessment when compared with the traditional 2.5- to 3-mm slice collimation using the low-dose technique.

The typical examination can be obtained in less than 10 minutes and consists of a scout image followed by a single low-dose scan through the heart requiring 10 to 40 seconds depending on the vintage of the CT system used. Once the scan is completed the axial image data are transferred to a computer work station in which an individual knowledgeable of the coronary artery anatomy reviews the images and in a semiautomated manner identifies calcified plaques related to the coronary arteries. These plaques are then measured and tabulated by coronary vessel into an Agatston score, a volume of calcified plaque and the mass of calcified plaque. The Agatston score was defined for the original electron-beam CT using a 3-mm slice collimation and did not formally take into account the slice width in calculating the score. Subsequent modifications of the Agatston score have been implemented to account for slice collimation resulting in a modification of the original Agatston score. Currently, for clinical purposes the Agatston score is used for decision making; however, there are methodologic reasons that the volume and mass score may be more appropriate metrics and research is ongoing [118].

The application of the calcium score to CVD prevention in the clinical setting remains incompletely defined at this point in time. The identification of calcified plaque documents the presence of coronary atherosclerosis and the presence of subclinical disease. Furthermore, the amount of calcified plaque is tightly correlated with the overall plaque burden seen at histology. The calcium score is a good estimate of total plaque burden. Over the years various strategies for grouping individuals based on their absolute calcified plaque burden or percentile have been proposed. Recently, the results from the South Bay Heart Study indicate that individuals with an Agatston score greater than 300 are at significantly greater risk of having a CVD event, such as a myocardial infarction or a cardiovascular death, than those with lower scores irregardless of their current risks based on traditional cardiovascular risk factors as determined by the Framingham Score [119]. This prospective study using "hard end points" (myocardial infarction and CVD death) provides strong rational for using an Agatston score of 300 as a threshold value for more aggressive CVD prevention strategies.

Cardiac CT with contrast

Electron-beam CT provided the foundation for the types of data one could acquire with the contrast-enhanced CT. These include imaging the coronary arteries, evaluating coronary bypass graft, and performing functional studies of the heart. The advent of the MDCT opened the door for imaging the coronary arteries with higher spatial resolution and the initial

studies using four-channel systems demonstrated the feasibility of coronary CTA and the limitations in comparison studies to conventional coronary angiography. The 16-channel MDCT provided the first near isotropic spatial resolution imaging of the heart with cardiac gating. Images could be obtained with a submillimeter spatial resolution resulting in reasonable image quality of the coronary arteries. The subsequent advances to 32, 40, and 64 improved the robustness of cardiac CT. This enhanced image quality makes it possible to perform high-quality cardiac imaging on most individuals.

The CT scanner for cardiac imaging is faced with a daunting task. It must image rapidly moving coronary arteries at specific phases during the cardiac cycle [116]. To achieve this, the CT system must image at both high spatial resolution and rapid temporal resolution while compensating for the cardiac motion. Currently, to achieve this combination, all MDCT vendors use a helical cardiac gated acquisition. The reconstruction algorithm incorporates the ECG tracing of the cardiac cycle and the relative position of the heart to the various detector channels and with this information reconstructs images of a specific cardiac phase and location [120]. These reconstruction algorithms are vendor specific and are rapidly evolving in conjunction with the evolution of the cardiac CT systems. Simplistically, the cardiac helical acquisition algorithms use a low-pitch scan in which a given location of the heart (eg, the origin of the left main coronary artery) has data acquired throughout the entire cardiac cycle on more than one detector row. This oversampling provides redundant views (or sectors), which can be used to reconstruct a given location at a given time during the cardiac cycle. Furthermore, the images can be assembled from views (or sectors) from multiple channels. By obtaining data from multiple channels, the effective temporal resolution of the images is reduced (or shortened). This method is analogous in many ways to cardiac gating strategies used in cardiac MR imaging or nuclear medicine. The low pitch results in increased radiation exposure, which is reduced in part through a technique termed ''milliampere modulation.'' The primary diagnostic images requiring the highest image quality remain those in diastole. By modulating the tube current (milliampere) based on the ECG waveform dose reductions of 20% to 50% can be achieved during systole while maintaining image quality during diastole. The continued improvement in gantry speed to less than 400 milliseconds with the 64 MDCT system provides better temporal resolution. The shorter imaging times result in higher image quality and a wider range of acceptable heart rates further improving the robustness of cardiac CT.

Cardiac CT, like all of imaging, requires attention to all of the technical aspects to obtain high-quality studies. The delivery of intravenous contrast material and the selection of contrast material are equally important to the CT scanner and require attention to several factors [121]. Significant improvements in image quality can be obtained with a dual-chamber power injector to administer intravenous contrast material followed by saline and is essential for obtaining high-quality studies. The saline allows for a reduction in the amount of contrast used and a reduction in artifact by dramatically lowering the concentration of contrast material in the superior vena cava and right heart, which cause streak artifacts and can obscure portions of the coronary arteries. Experience with CT coronary angiography using 16-channel systems indicates that using 100 mL of contrast material with an injection rate of 4 mL/s followed by a saline chaser with imaging beginning 18 seconds after the injections provides good opacification of the coronary arteries in individuals with normal cardiac function. Circulation timing scans are valuable in those individuals suspected of reduced cardiac output or intravenous access other than an antecubital vein.

Clinical applications of cardiac CT with contrast

Cardiac gating and imaging the heart and attendant vessels with high resolution provides a rapid

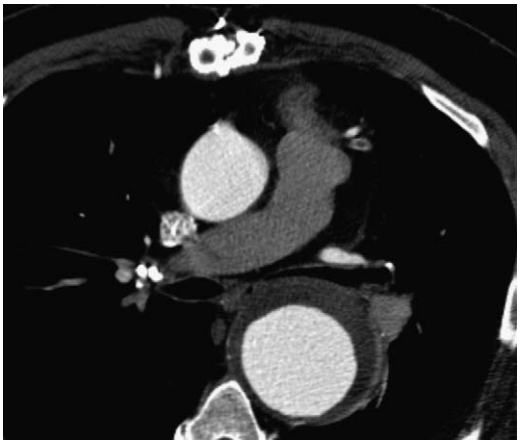

Fig. 15. Thoracic CT angiography (without ECG gating) demonstrating contrast within the patent left internal mammary graft located directly anterior to a thrombosed saphenous vein graft both adjacent to the main pulmonary artery in this individual with a thoracic aortic aneurysm with extensive thrombus.

way of gaining valuable information in numerous clinical scenarios. Cardiac CT and ungated CT angiography of the chest, such as routinely performed for PE evaluation, can provide diagnostic imaging of coronary artery bypass grafts. Saphenous vein grafts originating from the ascending aorta and internal thoracic (internal mammary) arteries are easily identified. Failure for the grafts to enhance with contrast can document graft occlusion (Fig. 15). Congenital anomalies related to the coronary arteries are also well demonstrated thanks to the three-dimensional capability of cardiac CT. Anomalies of the coronary artery determined at catheter-based coronary angiography range from 0.3% to 1%, although the prevalence with CT angiography is likely to be higher. Cardiac CT can clearly identify the course of an anomalous coronary artery and demonstrate or exclude the presence of an interarterial course between the ascending aorta and pulmonary artery, which places the individual at higher risk for sudden death. CT coronary angiography can also document the locations and origins of the coronary arteries from the ascending aorta (Fig. 16). Cardiac masses can also be well demonstrated with cardiac CT with the identification of their location in relationship to the cardiac chambers and other structures (Fig. 17).

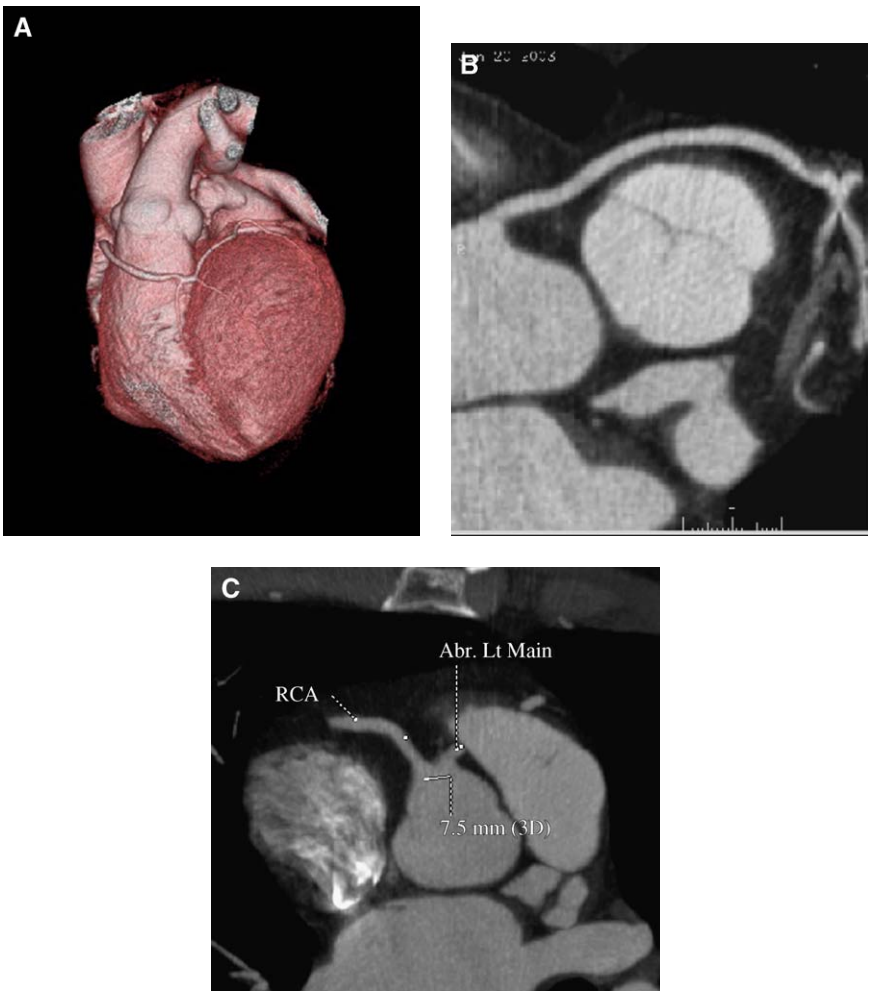

Fig. 16. Anomalous left coronary artery originating from the right sinus of Valsalva. (*A*) Volume-rendered image demonstrating the course anterior to the main pulmonary artery. (*B*) Curved reformat image showing the course of the vessel from the right sinus of the ascending aorta and anterior to the pulmonary artery. (*C*) Thin slab maximum intensity projection image demonstrating the separate ostia of the right and anomalous left coronary arteries.

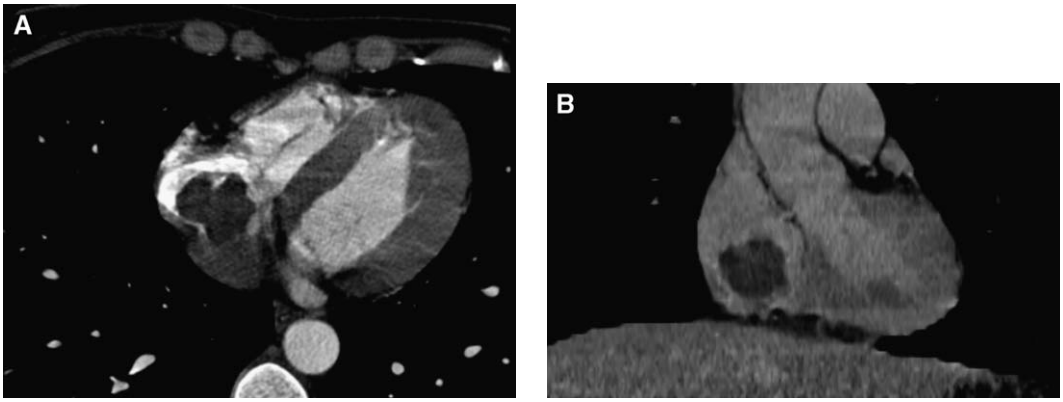

Fig. 17. Low-attenuation mass identified in the inferior right atrium following removal of a dialysis catheter. (*A*) Single slice from a cardiac helical acquisition demonstrating the low-attenuation mass within the right atrium. (*B*) A 3-minute delay image, which equalizes contrast enhancement on the right and left sides of the heart, reformatted in the coronal plane again demonstrating the thrombus in the right atrium, which resolved following therapy.

Cardiac CT is excellent for imaging the pericardium and can identify focal and diffuse involvement of the pericardium.

The three-dimensional anatomic detail possible with cardiac CT has created new applications, such as mapping the pulmonary veins and left atrium in preparation for interventional electrophysiology procedures. The high resolution of CT allows easy identification of the presence of middle pulmonary veins and other anatomic variants and can reduce procedure time (Fig. 18). These three-dimensional models can be exported to the electrophysiology suite and provide an anatomic road map for the cardiologist.

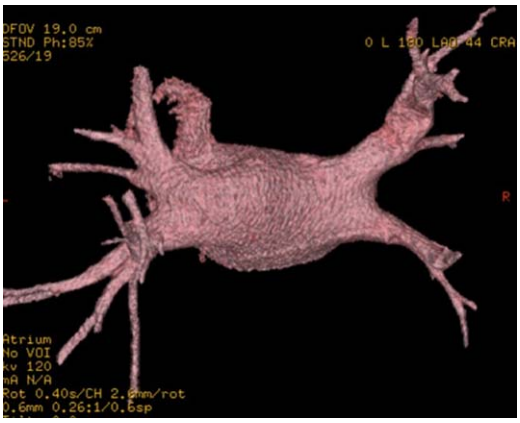

Fig. 18. Volume-rendered image with the left atrium and pulmonary veins segmented into a separate volume. These images can be interactively manipulated on a computer screen and coregistered with electrophysiologic data to provide an anatomic roadmap during the intervention.

Contrast-enhanced CT is also used to evaluate the coronary arteries. Previous studies have documented the sensitivity and specificity of four-channel MDCT [122,123]. Limitations, principally related to motion and other factors, such as calcified plaque, resulted in a significant number of coronary artery segments not being of sufficient quality for diagnosis. The advent of the 16-channel MDCT cardiac systems improved spatial and temporal resolution [124,125]. In both published studies using MDCT 16-channel systems, beta blockade was used to lower the heart rate before the scan. Using these techniques inadequate image quality was present on 7% to 12% of the coronary segments. With 16-slice MDCT, Nieman et al [125] was able to obtain an accuracy of 78% of classifying an individual as having multivessel, single vessel, or no vessel with significant stenosis. At the time of this writing, the improved spatial resolution and temporal resolution possible with the 64-channel systems has been demonstrated but not systematically evaluated. It is clear from the early reports that the improved image quality results in an even more robust test for imaging the coronary arteries. That said, before widespread clinical application, additional comparative studies with coronary angiography are required and the development of new diagnostic and treatment strategies are need to guide patient care.

Given the rapid technologic advance and the demands of clinical practice, how can CT coronary angiography be implemented into clinical practice? The authors' practice uses CT coronary angiography as an integrated tool along with the other cardiac imaging modalities. They tailor the use of cardiac CT based on the clinical scenario. The primary clinical patients who had been referred for coronary CT

angiography have been those individuals with symptoms predicted to be at low risk of coronary artery disease in whom the likelihood of positive findings at coronary angiography are believed to be low. These individuals typically are younger individuals often presenting with atypical chest pain of an undefined origin. The differential may include anomalous coronary artery or other atypical cause of chest pain. The second group of individuals is those with established CVD secondary to prior stent placement or coronary artery bypass graft with recurrent symptoms. In these individuals, there is often complex anatomy with the presence of coronary artery bypass grafts and multiple stents and CT coronary angiography can identify both the cardiac anatomy and the coronary arterial anatomy to aid in the decision process concerning continued conservative management verses reintervention by a catheter-based or surgical approach. Further benefits of the cardiac CT in these situations are imaging the surrounding chest, mediastinum, and lung parenchyma in individuals commonly with multisystem disease.

References

[1] Roberts WC. Aortic dissection: anatomy, consequences, and causes. Am Heart J 1981;101:195–214.

[2] Williams DM, LePage MA, Lee DY. The dissected aorta. Part III. Anatomy and radiologic diagnosis of branch-vessel compromise. Radiology 1997;203: 37–44.

[3] Elefteriades JA. Natural history of thoracic aortic aneurysms: indications for surgery, and surgical versus nonsurgical risks. Ann Thorac Surg 2002;74: S1877–80.

[4] DeBakey ME, McCollum CH, Crawford ES, et al. Dissection and dissecting aneurysms of the aorta: twenty-year follow-up of five hundred twenty-seven patients treated surgically. Surgery 1982;92:1118–34.

[5] Daily PO, Trueblood HW, Stinson EB, et al. Management of acute aortic dissections. Ann Thorac Surg 1970;10:237–47.

[6] Mehta RH, O'Gara PR, Bossone E, et al. Acute type A aortic dissection in the elderly: clinical characteristics, management, and outcomes in the current era. J Am Coll Cardiol 2002;40:685–92.

[7] Suzuki T, Mehta RH, Ince H, et al. Clinical profiles and outcomes of acute type B aortic dissection in the current era: lessons from the International Registry of Aortic Dissection (IRAD). Circulation 2003; 108(Suppl II):II-312–7.

[8] Anagnostopoulos CE, Prabhakar MJS, Kittle CF. Aortic dissections and dissecting aneurysms. Am J Cardiol 1972;30:263–73.

[9] Griepp RB, Ergin MA, Galla JD, et al. Natural history of descending thoracic and thoracoabdominal aneurysms. Ann Thorac Surg 1999;67:1927–30.

[10] Fattori R, Napoli G, Lovato L, et al. Descending thoracic aortic diseases: stent-graft repair. Radiology 2003;229:176–83.

[11] Hansen CJ, Bui H, Donayre CE, et al. Complications of endovascular repair of high-risk and emergent descending thoracic aortic aneurysms and dissections. J Vasc Surg 2004;40:228–34.

[12] Moore AG, Eagle KA, Bruckman D, et al. Choice of computed tomography, transesophageal echocardiography, magnetic resonance imaging, and aortography in acute aortic dissection: international registry of acute aortic dissection (IRAD). Am J Cardiol 2002; 89:1235–8.

[13] Sommer T, Fehske W, Holzknecht N, et al. Aortic dissection: a comparative study of diagnosis with spiral CT, multiplanar transesophageal echocardiography, and MR imaging. Radiology 1996;199:347–52.

[14] Yoshida S, Akiba HG, Tamakawa M, et al. Thoracic involvement of type A aortic dissection and intramural hematoma: diagnostic accuracy—comparison of emergency helical CT and surgical findings. Radiology 2003;228:430–5.

[15] Batra P, Bigoni B, Manning J, et al. Pitfalls in the diagnosis of thoracic aortic dissection at CT angiography. Radiographics 2000;20:309–20.

[16] Quint LE, Francis IR, Williams DM, et al. Evaluation of thoracic aortic disease with the use of helical CT and multiplanar reconstructions: comparison with surgical findings. Radiology 1996;201:37–41.

[17] Roos JE, Willmann JK, Weishaupt D, et al. Thoracic aorta: motion artifact reduction with retrospective and prospective electrocardiography-assisted multidetector row CT. Radiology 2002;222:271–7.

[18] Morgan-Hughes GJ, Owens PE, Marshall AJ, et al. Thoracic aorta at multi-detector row CT: motion artifact with various reconstruction windows. Radiology 2003;228:583–8.

[19] Lee DY, Williams DM, Abrams GD. The dissected aorta. Part II. Differentiation of the true from the false lumen with intravascular US. Radiology 1997;203: 32–6.

[20] Williams DM, Joshi A, Dake MD, et al. Aortic cobwebs: an anatomic marker identifying the false lumen in aortic dissection—imaging and pathologic correlation. Radiology 1994;190:167–74.

[21] LePage MA, Quint LE, Sonnad SS, et al. Aortic dissection: CT features that distinguish true lumen from false lumen. AJR Am J Roentgenol 2001;177: 207–11.

[22] Yamada T, Tada S, Harada J. Aortic dissection without intimal rupture: diagnosis with MR imaging and CT. Radiology 1988;168:347–52.

[23] Dake MD. Aortic intramural haematoma: current therapeutic strategy. Heart 2004;90:375–8.

[24] Song J-M, Kim H-S, Song J-K, et al. Usefulness of the initial noninvasive imaging study to predict the

adverse outcomes in the medical treatment of acute type A aortic intramural hematoma. Circulation 2003; 108(Suppl II):II-324–8.
[25] Moizumi Y, Komatsu T, Motoyoshi N, et al. Clinical features and long-term outcome of type A and type B intramural hematoma of the aorta. J Thorac Cardiovasc Surg 2004;127:421–7.
[26] Evangelista A, Dominguez R, Sebastia C, et al. Prognostic value of clinical and morphologic findings in short-term evolution of aortic intramural haematoma. Eur Heart J 2004;25:81–7.
[27] Nienaber CA, von Kodolitsch Y, Petersen B, et al. Intramural hemorrhage of the thoracic aorta: diagnostic and therapeutic implications. Circulation 1995; 92:1465–72.
[28] Ganaha F, Miller DC, Sugimoto K, et al. Prognosis of aortic intramural hematoma with and without penetrating atherosclerotic ulcer: a clinical and radiological analysis. Circulation 2002;106:342–8.
[29] Choi SH, Choi SJ, Kim JH, et al. Useful CT findings for predicting the progression of aortic intramural hematoma to overt aortic dissection. J Comput Assist Tomogr 2001;25:295–9.
[30] Evangelista A, Dominguez R, Sebastia C, et al. Long-term follow-up of aortic intramural hematoma. Circulation 2003;108:583–9.
[31] Murray JG, Manisali M, Flamm SD, et al. Intramural hematoma of the thoracic aorta: MR image findings and their prognostic implications. Radiology 1997; 204:349–55.
[32] Vilacosta I, San Román JA, Ferreiró J, et al. Natural history and serial morphology of aortic intramural hematoma: a novel variant of aortic dissection. Am Heart J 1997;134:495–507.
[33] Sueyoshi E, Matsuoka Y, Sakamoto I, et al. Fate of intramural hematoma of the aorta: CT evaluation. J Comput Assist Tomogr 1997;21:931–8.
[34] Kazerooni EA, Bree RL, Williams DM. Penetrating atherosclerotic ulcers of the descending thoracic aorta: evaluation with CT and distinction from aortic dissection. Radiology 1992;183:759–65.
[35] Hayashi H, Matsuoka Y, Sakamoto I, et al. Penetrating atherosclerotic ulcer of the aorta: imaging features and disease concept. Radiographics 2000;20: 995–1005.
[36] Cho KR, Stanson AW, Potter DD, et al. Penetrating atherosclerotic ulcer of the descending thoracic aorta and arch. J Thorac Cardiovasc Surg 2004;127: 1393–401.
[37] Quint LE, Williams DM, Francis IR, et al. Ulcerlike lesions of the aorta: imaging features and natural history. Radiology 2001;218:719–23.
[38] Heit JA, O'Fallon M, Petterson TM, et al. Relative impact of risk factors for deep vein thrombosis and pulmonary embolism. Arch Intern Med 2002;162: 1245–8.
[39] Goldhaber SZ. Pulmonary embolism. Lancet 2004; 363:1295–305.
[40] Saeger W, Genzkow M. Venous thromboses and pulmonary embolisms in post-mortem series: probable causes by correlations of clinical data and basic diseases. Pathol Res Pract 1994;190:394–9.
[41] Silverstein MD, Heit JA, Mohr DN, et al. Trends in the incidence of deep vein thrombosis and pulmonary embolism. Arch Intern Med 1998;158:585–93.
[42] The PIOPED Investigators. Value of the ventilation/perfusion scan in acute pulmonary embolism. JAMA 1990;263:2753–9.
[43] Miniati M, Pediletto R, Formichi B, et al. Accuracy of clinical assessment in the diagnosis of pulmonary embolism. Am J Respir Crit Care Med 1999;159: 864–71.
[44] Dunn KL, Wolf JP, Dorfman DM, et al. Normal D-dimer levels in emergency department patients suspected of acute pulmonary embolism. J Am Coll Cardiol 2002;40:1475–8.
[45] Stein PD, Hull RD, Patel KC, et al. D-dimer for the exclusion of acute venous thrombosis and pulmonary embolism. Ann Intern Med 2004;140:589–602.
[46] Perrier A, Desmarais S, Miron MJ, et al. Non-invasive diagnosis of venous thromboembolism in outpatients. Lancet 1999;353:190–5.
[47] Abcarian PW, Sweet JD, Watabe JT, et al. Role of a quantitative D-dimer assay in determining the need for CT angiography of acute pulmonary embolism. AJR Am J Roentgenol 2004;182:1377–81.
[48] Rathbun SW, Whitsett TL, Vesely SK, et al. Clinical utility of D-dimer in patients with suspected pulmonary embolism and nondiagnostic lung scans or negative CT findings. Chest 2004;125:851–5.
[49] British Thoracic Society Standards of Care Committee Pulmonary Embolism Guideline Development Group. British Thoracic Society guidelines for the management of suspected acute pulmonary embolism. Thorax 2003;58:470–84.
[50] Shoepf UJ, Costello P. CT angiography for diagnosis of pulmonary embolism: state of the art. Radiology 2004;230:329–37.
[51] Remy-Jardin M, Remy J, Wattinne L, et al. Central pulmonary thromboembolism: diagnosis with spiral volumetric CT with the single-breath-hold technique—comparison with pulmonary angiography. Radiology 1992;185:381–7.
[52] Blum AG, Delfau F, Grignon B, et al. Spiral-computed tomography versus pulmonary angiography in the diagnosis of acute massive pulmonary embolism. Am J Cardiol 1994;74:96–8.
[53] Goodman LR, Curtin JJ, Mewissen MW, et al. Detection of pulmonary embolism in patients with unresolved clinical and scintigraphic diagnosis: helical CT versus angiography. AJR Am J Roentgenol 1995;164:1369–74.
[54] Remy-Jardin M, Remy J, Deschildre F, et al. Diagnosis of pulmonary embolism with spiral CT: comparison with pulmonary angiography and scintigraphy. Radiology 1996;200:699–706.
[55] Christiansen F. Diagnostic imaging of acute pulmonary embolism. Acta Radiol Suppl 1997;410:1–33.

[56] Drucker EA, Rivitz SM, Shepard JO, et al. Acute pulmonary embolism: assessment of helical CT for diagnosis. Radiology 1998;209:235–41.
[57] Diffin DC, Leyendecker JR, Johnson SP, et al. Effect of anatomic distribution of pulmonary emboli on interobserver pulmonary angiography. AJR Am J Roentgenol 1998;171:1085–9.
[58] Winer-Muram HT, Rydberg J, Johnson MS, et al. Suspected acute pulmonary embolism: evaluation with multi-detector row CT versus digital subtraction pulmonary arteriography. Radiology 2004;233:806–15.
[59] Ghaye B, Szapiro D, Mastora I, et al. Peripheral pulmonary arteries: how far in the lung does multidetector row spiral CT allow analysis? Radiology 2001;219:629–36.
[60] Schoepf UJ, Holzknecht N, Helmberger TK, et al. Subsegmental pulmonary emboli: improved detection with thin-collimation multi-detector row spiral CT. Radiology 2002;222:483–90.
[61] Revel MR, Petrover D, Hernigou A, et al. Diagnosing pulmonary embolism with four-detector row helical CT: prospective evaluation of 216 outpatients and inpatients. Radiology 2005;234:265–73.
[62] Coche E, Verschuren F, Keyeux A, et al. Diagnosis of acute pulmonary embolism in outpatients: comparison of thin-collimation multi-detector row spiral CT and planar ventilation-perfusion scintigraphy. Radiology 2003;229:757–65.
[63] van Strijen MJL, de Monyé W, Schiereck J, et al. Single-detector helical computed tomography as the primary diagnostic test in suspected pulmonary embolism: a multicenter clinical management study of 510 patients. Ann Intern Med 2003;138:307–14.
[64] Van Rossum AB, Pattynama PMT, Mallens WMC, et al. Can helical CT replace scintigraphy in the diagnostic process in suspected pulmonary embolism? A retrolective-prolective cohort study focusing on total diagnostic yield. Eur Radiol 1998;8:90–6.
[65] Remy-Jardin M, Remy J, Baghaie F, et al. Clinical value of thin collimation in the diagnostic workup of pulmonary embolism. AJR Am J Roentgenol 2000; 175:407–11.
[66] Gosselin MV, Rubin GD, Leung AN, et al. Unsuspected pulmonary embolism: prospective detection on routine helical CT scans. Radiology 1998;208:209–15.
[67] Patel S, Kazerooni EA, Cascade PN. Pulmonary embolism: optimization of small pulmonary artery visualization at multi-detector row CT. Radiology 2003; 227:455–60.
[68] Oser RF, Zuckerman DA, Gutierrez FR, et al. Anatomic distribution of pulmonary emboli at pulmonary angiography: implications for cross-sectional imaging. Radiology 1996;199:31–5.
[69] de Monyé W, van Strijen MJ, Huisman MV, et al. Suspected pulmonary embolism: prevalence and anatomic distribution in 487 consecutive patients. Radiology 2000;215:184–8.
[70] Kanne JP, Gotway MB, Thoongsuwan N, et al. Six cases of acute central pulmonary embolism revealed on unenhanced multidetector CT of the chest. AJR Am J Roentgenol 2003;180:1661–4.
[71] Cobelli R, Zompatori M. Visualization of hypoattenuation clots on unenhanced CT of the thorax [letter]. AJR Am J Roentgenol 2004;182:530–1.
[72] Coche EE, Müller NL, Kim KI, et al. Acute pulmonary embolism: ancillary findings at spiral CT. Radiology 1998;207:753–8.
[73] Shah AA, Davis SD, Gamsu G, et al. Parenchymal and pleural findings in patients with and patients without acute pulmonary embolism detected at spiral CT. Radiology 1999;211:147–53.
[74] Johnson PT, Wechsler RJ, Salazar AM, et al. Spiral CT of acute pulmonary thromboembolism: evaluation of pleuroparenchymal abnormalities. J Comput Assist Tomogr 1999;23:369–73.
[75] Oliver TB, Reid JH, Murchison JT. Interventricular septal shift due to massive pulmonary embolism shown by CT pulmonary angiography: an old sign revisited. Thorax 1998;53:1092–4.
[76] Reid JH, Murchison JT. Acute right ventricular dilatation: a new helical CT sign of massive pulmonary embolism. Clin Radiol 1998;53:694–8.
[77] Quiroz R, Kucher N, Schoepf UJ, et al. Right ventricular enlargement on chest computed tomography. Circulation 2004;109:2401–4.
[78] Qanadli SD, Hajjam ME, Vieillard-Baron A, et al. New CT index to quantify arterial obstruction in pulmonary embolism: comparison with angiographic index and echocardiography. AJR Am J Roentgenol 2001;176:1415–20.
[79] Wu AS, Pezzullo JA, Cronan JJ, et al. CT pulmonary angiography: quantification of pulmonary embolus as a predictor of patient outcome: initial experience. Radiology 2004;230:831–5.
[80] Wittram C, Maher MM, Yoo AJ, et al. CT angiography of pulmonary embolism: diagnostic criteria and causes of misdiagnosis. Radiographics 2004;24: 1219–38.
[81] Gosselin MV, Rassner UA, Thieszen SL, et al. Contrast dynamics during CT pulmonary angiogram. J Thorac Imaging 2004;19:1–7.
[82] Wittram C. Pulmonary artery enhancement at CT pulmonary angiography [letter]. Radiology 2003;229:932.
[83] Henk CB, Grampp S, Linnau KF, et al. Suspected pulmonary embolism: enhancement of pulmonary arteries at deep-inspiration CT angiography—influence of patent foramen ovale and atrial-septal defect. Radiology 2003;226:749–55.
[84] Remy-Jardin M, Duyck P, Remy J, et al. Hilar lymph nodes: identification with spiral CT and histologic correlation. Radiology 1995;196:387–94.
[85] Sheiman RG, McArdle CR. Clinically suspected pulmonary embolism: use of bilateral lower extremity US as the initial examination—a prospective study. Radiology 1999;212:75–8.
[86] Perrier A, Roy PM, Aujesky D, et al. Diagnosing pulmonary embolism in outpatients with clinical assessment, D-dimer measurement, venous ultrasound,

and helical computed tomography: a multicenter management study. Am J Med 2004;116:291–9.
[87] Van Rossum AB, Van Houwelingen HC, Kieft GJ, et al. Prevalence of deep vein thrombosis in suspected and proven pulmonary embolism: a meta-analysis. Br J Radiol 1998;71:1260–5.
[88] Loud PA, Grossman ZD, Klippen DL, et al. Combined CT venography and pulmonary angiography: a new diagnostic technique for suspected thromboembolic disease. AJR Am J Roentgenol 1998;170:951–4.
[89] Cham MD, Yankelevitz DF, Shaham D, et al. Deep venous thrombosis: detection by using indirect CT venography. Radiology 2000;216:744–51.
[90] Loud PA, Katz DS, Klippenstein DL, et al. Combined CT venography and pulmonary angiography in suspected thromboembolic disease: diagnostic accuracy for deep venous evaluation. AJR Am J Roentgenol 2000;174:61–5.
[91] Loud PA, Katz DS, Bruce DA, et al. Deep venous thrombosis with suspected pulmonary embolism: detection with combined CT venography and pulmonary angiography. Radiology 2001;219:498–502.
[92] Garg K, Mao J. Deep venous thrombosis: spectrum of findings and pitfalls in interpretation on CT venography. AJR Am J Roentgenol 2001;177:319–23.
[93] Boyd DP, Lipton MJ. Cardiac computed tomography. Proc IEEE 1983;71:298–307.
[94] Stary HC, Chandler AB, Dinsmore RE, et al. A definition of advanced types of atherosclerotic lesions and a histological classification of atherosclerosis: a report from the Committee on Vascular Lesions of the Council on Arteriosclerosis, American Heart Association. Circulation 1995;92:1355–74.
[95] Wexler L, Brundage B, Crouse J, et al. Coronary artery calcification: pathophysiology, epidemiology, imaging methods, and clinical implications: a statement for health professionals from the American Heart Association. Writing Group. Circulation 1996; 94:1175–92.
[96] O'Rourke RA, Brundage BH, Froelicher VF, et al. American College of Cardiology/American Heart Association Expert Consensus Document on Electron-Beam Computed Tomography for the Diagnosis and Prognosis of Coronary Artery Disease. J Am Coll Cardiol 2000;36:236–40.
[97] Rumberger JA, Simons DB, Fitzpatrick LA, et al. Coronary artery calcium area by electron-beam computed tomography and coronary atherosclerotic plaque area: a histopathologic correlative study [see comments]. Circulation 1995;92:2157–62.
[98] Sangiorgi G, Rumberger JA, Severson A, et al. Arterial calcification and not lumen stenosis is highly correlated with atherosclerotic plaque burden in humans: a histologic study of 723 coronary artery segments using nondecalcifying methodology. J Am Coll Cardiol 1998;31:126–33.
[99] Achenbach S, Ropers D, Hoffmann U, et al. Assessment of coronary remodeling in stenotic and nonstenotic coronary atherosclerotic lesions by multidetector spiral computed tomography. J Am Coll Cardiol 2004;43:842–7.
[100] Ehara S, Kobayashi Y, Yoshiyama M, et al. Spotty calcification typifies the culprit plaque in patients with acute myocardial infarction: an intravascular ultrasound study. Circulation 2004;110:3424–9.
[101] Agatston AS, Janowitz WR, Hildner FJ, et al. Quantification of coronary artery calcium using ultrafast computed tomography. J Am Coll Cardiol 1990;15:827–32.
[102] Margolis JR, Chen JT, Kong Y, et al. The diagnostic and prognostic significance of coronary artery calcification: a report of 800 cases. Radiology 1980;137: 609–16.
[103] Detrano RC, Wong ND, Tang W, et al. Prognostic significance of cardiac cinefluoroscopy for coronary calcific deposits in asymptomatic high risk subjects. J Am Coll Cardiol 1994;24:354–8.
[104] Arad Y, Spadaro LA, Goodman K, et al. Prediction of coronary events with electron beam computed tomography. J Am Coll Cardiol 2000;36:1253–60.
[105] Detrano RC, Wong ND, Doherty TM, et al. Coronary calcium does not accurately predict near-term future coronary events in high-risk adults [see comments]. Circulation 1999;99:2633–8.
[106] Raggi P, Callister TQ, Cooil B, et al. Identification of patients at increased risk of first unheralded acute myocardial infarction by electron-beam computed tomography. Circulation 2000;101:850–5.
[107] Wong ND, Hsu JC, Detrano RC, et al. Coronary artery calcium evaluation by electron beam computed tomography and its relation to new cardiovascular events. Am J Cardiol 2000;86:495–8.
[108] Kondos GT, Hoff JA, Sevrukov A, et al. Electron-beam tomography coronary artery calcium and cardiac events: a 37-month follow-up of 5635 initially asymptomatic low- to intermediate-risk adults. Circulation 2003;107:2571–6.
[109] Greenland P, LaBree L, Azen SP, et al. Coronary artery calcium score combined with Framingham score for risk prediction in asymptomatic individuals. JAMA 2004;291:210–5.
[110] Shaw LJ, Raggi P, Schisterman E, et al. Prognostic value of cardiac risk factors and coronary artery calcium screening for all-cause mortality. Radiology 2003;228:826–33.
[111] Smith SC, Amsterdam E, Balady GJ, et al. Prevention Conference V. Beyond Secondary Prevention: Identifying the high-risk patient for primary prevention. Tests for silent and inducible ischemia. Circulation 2000;101:e12–5.
[112] Greenland P, Abrams J, Aurigemma GP, et al. Prevention Conference V. Beyond secondary prevention: identifying the high-risk patient for primary prevention: noninvasive tests of atherosclerotic burden: Writing Group III. Circulation 2000;101:E16–22.
[113] Bild DE, Bluemke DA, Burke GL, et al. Multi-ethnic study of atherosclerosis: objectives and design. Am J Epidemiol 2002;156:871–81.

[114] Carr JJ, Nelson JC, Wong ND, et al. Calcified coronary artery plaque measurement with cardiac CT in population-based studies: standardized protocol of Multi-Ethnic Study of Atherosclerosis (MESA) and Coronary Artery Risk Development in Young Adults (CARDIA) study. Radiology 2005;234:35–43.
[115] Carr JJ. Coronary calcium: the case for helical computed tomography. J Thorac Imaging 2001;16:16–24.
[116] Achenbach S, Ropers D, Holle J, et al. In-plane coronary arterial motion velocity: measurement with electron-beam CT. Radiology 2000;216:457–63.
[117] Mao S, Bakhsheshi H, Lu B, et al. Effect of electrocardiogram triggering on reproducibility of coronary artery calcium scoring. Radiology 2001;220:707–11.
[118] Callister TQ, Cooil B, Raya SP, et al. Coronary artery disease: improved reproducibility of calcium scoring with an electron-beam CT volumetric method [see comments]. Radiology 1998;208:807–14.
[119] Greenland PLL, Azen SP, Doherty TM, et al. Coronary Artery Calcium Score combined with Framingham Score for risk prediction in asymptomatic individuals. JAMA 2004;291:210–5.
[120] Flohr T, Pan T. Image reconstruction for ECG-triggered and ECG-gated multislice CT. In: Schoepf UJ, editor. Contemporary cardiology: CT of the heart. Totowa, NJ: Humana Press; 2005. p. 45–54.
[121] Cademartiri F, Nieman K. Contrast material injection techniques for CT angiography of the coronary arteries. In: Schoepf UJ, editor. Contemporary cardiology: CT of the heart. Totowa, NJ: Humana Press; 2005. p. 237–45.
[122] Nieman K, Oudkerk M, Rensing BJ, et al. Coronary angiography with multi-slice computed tomography. Lancet 2001;357:599–603.
[123] Achenbach S, Giesler T, Ropers D, et al. Detection of coronary artery stenoses by contrast-enhanced, retrospectively electrocardiographically-gated, multislice spiral computed tomography. Circulation 2001;103:2535–8.
[124] Ropers D, Baum U, Pohle K, et al. Detection of coronary artery stenoses with thin-slice multi-detector row spiral computed tomography and multiplanar reconstruction. Circulation 2003;107:664–6.
[125] Nieman K, Cademartiri F, Lemos PA, et al. Reliable noninvasive coronary angiography with fast submillimeter multislice spiral computed tomography. Circulation 2002;106:2051–4.

ELSEVIER
SAUNDERS

Radiol Clin N Am 43 (2005) 513 – 542

RADIOLOGIC
CLINICS
of North America

High-Resolution CT of the Lung: Patterns of Disease and Differential Diagnoses

Michael B. Gotway, MD[a,*], Gautham P. Reddy, MD, MPH[b], W. Richard Webb, MD[b], Brett M. Elicker, MD[b], Jessica W.T. Leung, MD[c]

[a]*Department of Radiology, San Francisco General Hospital, University of California at San Francisco, 1001 Potrero Avenue, Room 1X 55, Box 1325, San Francisco, CA 94110, USA*
[b]*Department of Radiology, University of California at San Francisco, San Francisco, CA 94143, USA*
[c]*Department of Radiology, Medical Center/Mount Zion Campus, University of California at San Francisco, 1600 Divisadero Street, Suite H-2801, San Francisco, CA 94115, USA*

High-resolution CT (HRCT) has become a valuable tool for the evaluation of patients with diffuse pulmonary diseases. HRCT is now widely recognized as more sensitive and specific than chest radiography for the assessment of such patients, and it has been integrated into the diagnostic algorithms for the assessment of a number of diffuse lung processes, most notably the idiopathic interstitial pneumonias, eosinophilic lung diseases, and obstructive lung diseases. Furthermore, HRCT has become a front-line test for the evaluation of patients with a number of very common clinical complaints, including patients with chronic cough and progressive shortness of breath or exertional dyspnea. Because HRCT is a commonly requested imaging technique, familiarity with the basis of interpretation of HRCT images is critical for accurate diagnosis.

In essence, HRCT imaging, by use of narrow collimation and high spatial frequency reconstruction algorithms, seeks to maximize spatial resolution and thereby approach a pathologic representation of a disease process. Maximizing spatial resolution allows HRCT findings frequently to correlate closely with pathologic findings. As stated in the forward to the first edition of *High-Resolution CT of the Lung* by Webb et al [1], "...to the extent that gross pathology can be used to diagnose lung disease, HRCT can as well." In some circumstances, this observation may even be extended to the histopathologic level. For this reason, much of the HRCT literature has focused on radiologic–pathologic correlations for various pulmonary diseases to improve appreciation for disease patterns on imaging. It is clear that detailed knowledge of normal pulmonary anatomy and an understanding of how normal anatomy is altered in disease states are required to appreciate fully HRCT findings in patients with pulmonary disease. With such a foundation, a pattern approach to HRCT interpretation may be used successfully.

Pulmonary anatomy: the requisites for high-resolution CT interpretation

The pulmonary interstitium

A basic understanding of pulmonary anatomy is required for accurate HRCT interpretation. Pulmonary anatomy may be broadly divided into the pulmonary gas exchange units and the pulmonary interstitium. The pulmonary interstitium may be further subdivided into the central peribronchovascular interstitium and the peripheral centrilobular interstitium; these two fiber networks are continuous with one another. The central peribronchovascular inter-

* Corresponding author.
E-mail address: michael.gotway@radiology.ucsf.edu (M.B. Gotway).

0033-8389/05/$ – see front matter © 2005 Elsevier Inc. All rights reserved.
doi:10.1016/j.rcl.2005.01.010

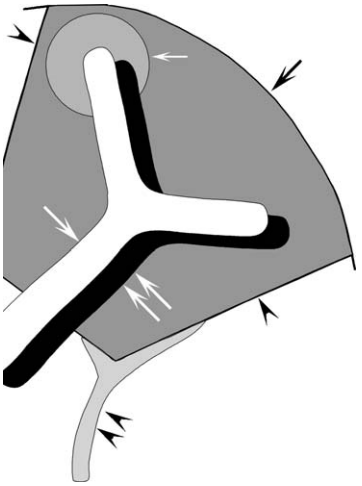

Fig. 1. Secondary pulmonary lobular anatomy. Centrilobular bronchus (*single wide white arrow*) and artery (*double white arrow*, 1-mm size); interlobular septa (*single arrowhead*, 0.1-mm thickness); pulmonary vein (*double arrowheads*, 0.5-mm size); visceral pleura (*single black arrow*, 0.1-mm thickness); and pulmonary acinus (*single thin white arrow*, 5–10 mm size).

stitium invests the larger central bronchi and vessels near the pulmonary hilum and courses peripherally, producing the peripheral centrilobular interstitium, eventually merging with the subpleural interstitial fiber network. The latter is located immediately beneath the visceral pleura and extends into the underlying lung parenchyma at various intervals to produce interlobular septa.

In the peripheral lung, the components of the pulmonary gas exchange units, including the respiratory ducts, alveolar ducts, and alveoli, are suspended from the interlobular septa and the peripheral centrilobular interstitium by the intralobular interstitium. Fibers of the intralobular interstitium consist of a very fine web of connective tissue that is not routinely visible on HRCT studies.

The secondary pulmonary lobule

The secondary pulmonary lobule is defined as the smallest unit of lung function marginated by connective tissue septa; these connective tissue septa are the interlobular septa [1]. Pulmonary veins course within the interlobular septa at the edges of a secondary pulmonary lobule (Fig. 1). Secondary pulmonary lobules vary in size from 1 to 2.5 cm and are usually most easily visible over the upper lobes, the anterior and lateral aspects of the right middle lobe and lingula, and over the diaphragmatic surfaces of the lower lobes, where they are the most well developed. On average, each secondary pulmonary lobule contains 12 or fewer pulmonary acini. Secondary pulmonary lobules are supplied by an artery and bronchus, termed the ‘‘centrilobular artery and bronchus.’’ The centrilobular artery and bronchus branch dichotomously within the secondary pulmonary lobule, successively producing intralobular arteries and bronchi, acinar arteries, and respiratory bronchioles, eventually terminating in pulmonary gas exchange units.

Intralobular anatomy

The centrilobular artery and bronchus are approximately 1 mm in diameter and are located about 5 to 10 mm from the visceral pleural surface [1]. Intralobular arteries are slightly smaller, and smaller still are the acinar arteries, which vary in size from 0.3 to 0.5 mm (see Fig. 1) [1–3]. Acinar arteries may be visible on HRCT scans as a small dot positioned about 3 to 5 mm from interlobular septa or the visceral pleural surface [2,3]. Although very small arteries within the secondary pulmonary lobule are often visible on clinical HRCT scans, the resolution of HRCT for tubular structures, such as bronchi, is considerably less. Bronchi within the secondary pulmonary lobule are not normally visible on HRCT

Table 1
Typical high-resolution CT protocols: techniques and commonly requested indications

	HRCT imaging	
Protocol	Supine	Supine and prone
Technique	1 mm every 10 mm with expiratory HRCT	1 mm every 20 mm with expiratory HRCT
Clinical presentation	Chronic cough	Exertional dyspnea
	Fever in an immunocompromised patient	Progressive or chronic shortness of breath
	Pulmonary hypertension	Suspected idiopathic interstitial pneumonia
Pulmonary function test abnormalities	Obstructive lung patterns	Restrictive lung patterns
	Decreased diffusion capacity of carbon monoxide	

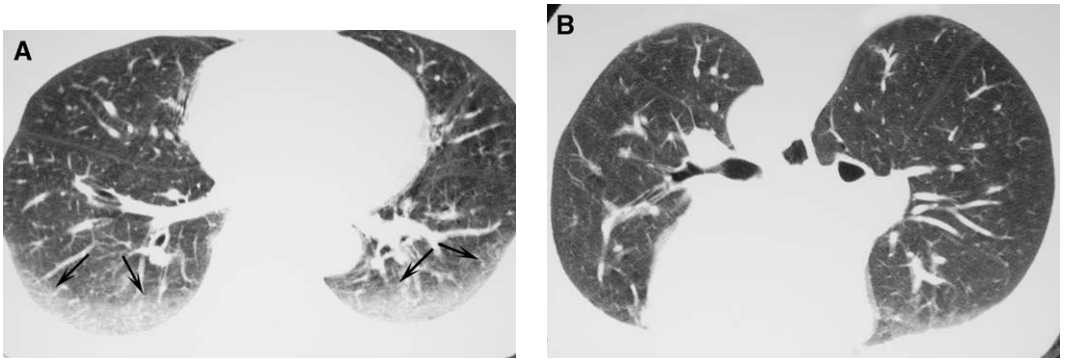

Fig. 2. Value of prone HRCT imaging. (*A*) Axial supine HRCT images shows opacity in the posterior lungs (*arrows*), which could represent either dependent density (atelectasis) or pulmonary inflammation. (*B*) Axial prone HRCT image shows complete resolution of the posterior opacity, indicating that it represented atelectasis.

studies; visibility of intralobular bronchi on HRCT studies usually represents a disease state [1,2].

Within the secondary pulmonary lobule is a series of meshlike connective tissue fibers that suspend the various lobular structures to the interlobular septa marginating the lobule. Collectively, this connective tissue framework is referred to as the ''intralobular interstitium.'' An understanding of this anatomy is quite important. One of the earliest manifestations of fibrotic lung disease on HRCT is abnormal thickening of the intralobular interstitium.

High-resolution CT technique

Narrow collimation and the use of a high spatial frequency reconstruction algorithm are the two most important technical factors that distinguish a thoracic CT examination as an HRCT study. Other technical modifications may be used to enhance the quality of an HRCT examination, such as targeted reconstructions and higher kilovolt (peak) or milliamperage values [4], but these techniques are not required to produce diagnostic-quality HRCT images. In fact, in recent years increasing awareness of the radiation dose attributable to diagnostic imaging, in particular CT, has led a number of investigators to reduce kilovolt (peak) and milliampere to limit patient radiation dose [5–11]. In general, it has been shown that diagnostic-quality HRCT examinations may be obtained with substantially decreased radiation doses compared with standard-dose HRCT examinations [8,11]. Nevertheless, because some subtle abnormalities may be less visible on HRCT examinations performed with reduced-dose technique [5], and because optimal low-dose HRCT techniques likely

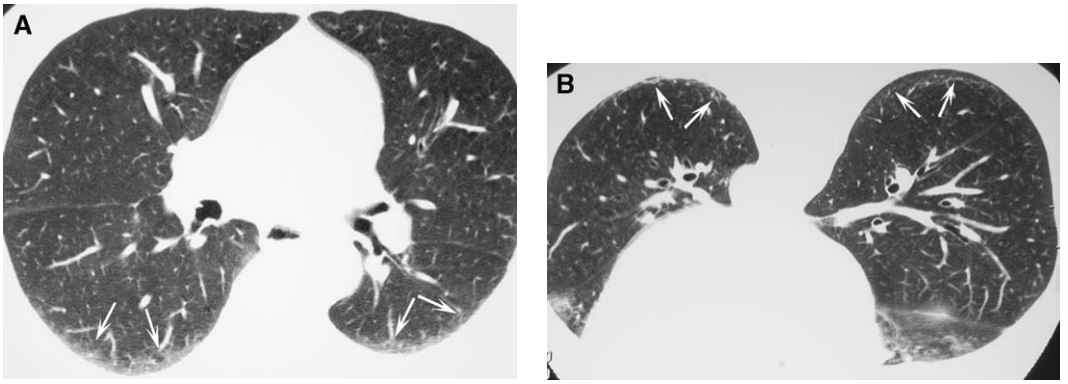

Fig. 3. Value of prone HRCT imaging. (*A*) Axial supine HRCT images shows reticular opacity in the posterior lungs (*arrows*), which could represent either dependent density (atelectasis) or pulmonary inflammation or fibrosis. (*B*) Axial prone HRCT image shows persistence of the posterior reticular opacities (*arrows*), consistent with the presence of pulmonary inflammation or fibrosis.

Table 2
High-resolution CT findings of pulmonary disease: increased and decreased lung opacity

HRCT finding	Further pattern subclassification	Diseases frequently implicated
Increased lung capacity		
Nodules	Centrilobular, perilymphatic, random	Bronchiolitis, sarcoidosis, Hematogenously disseminated infection
Linear abnormalities	Interlobular septal thickening, parenchymal bands, subpleural lines	Pulmonary edema, lymphangitic carcinomatosis
Reticular abnormalities	Coarse or fine reticulation, intralobular interstitial thickening	Idiopathic interstitial pneumonias, pneumoconioses
Ground-glass opacity	Must be based on clinical history and associated scan findings	Opportunistic infection, idiopathic interstitial pneumonia, pulmonary alveolar proteinosis
Consolidation	Must be based on clinical history and associated scan findings	Pneumonia, cryptogenic organizing pneumonia, pulmonary hemorrhage
Decreased lung capacity		
Areas of decreased attenuation with walls (cysts or ccystlike appearance)	Cyst shape, distribution, wall thickness, pattern of organization	Langerhans' cell histiocytosis, lymphangioleiomyomatosis, bronchiectasis, paraseptal emphysema, idiopathic interstitial pneumonias
Areas of decreased attenuation without walls	Emphysema, mosaic perfusion	Centrilobular or panlobular emphysema, diseases affecting small airways

vary among patients and indications and have not yet been established, several investigators have advocated that initial HRCT examinations be performed with standard-dose techniques and that low-dose HRCT be reserved for following patients with known abnormalities or screening large numbers of patients at high risk for a particular disease [1].

Display parameters, especially window width and level, are crucial for accurate HRCT interpretation. In general, window levels ranging from −600 to −700 HU and window widths ranging from 1000 to 1500 HU are appropriate for displaying ''lung windows.'' Window widths below 1000 HU produce too much contrast for optimal viewing, whereas excessive window widths inappropriately decrease the contrast between and adjacent structures and can render fine detail inconspicuous. Once proper display parameters are chosen, the same parameters should be used when evaluating serial studies for a particular patient. Viewing serial imaging using different display parameters makes determination of interval change difficult and can contribute to diagnostic inaccuracy.

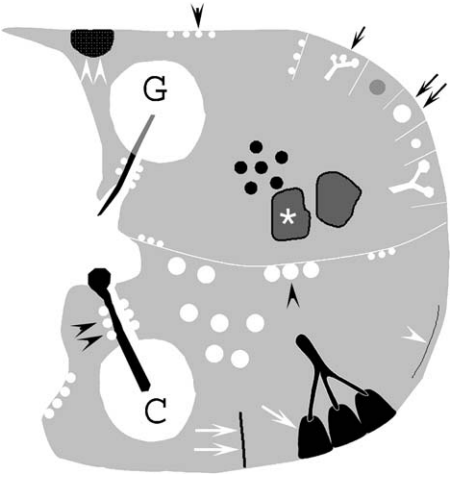

Fig. 4. HRCT findings in patients with diffuse lung disease. Centrilobular nodules with (*small black arrow*) and without (*double small black arrows*) tree-in-bud; perilymphatic nodules (*black arrowhead*); peribronchovascular nodules (*double black arrowheads*); ground-glass opacity (G); consolidation (C); lobular low attenuation representing mosaic perfusion (*white arrow*); parenchymal bands (*white double arrows*); subpleural lines (*white arrowhead*); paraseptal (*double white arrowheads*) and centrilobular emphysema; and lung cysts (*).

Collimation

HRCT imaging requires narrow collimation, usually on the order of 1 mm, to achieve maximal spatial resolution, and is typically performed at full inspiration. Usually, HRCT imaging is performed using

axial technique. The rapid acquisition times provided by multislice CT (MSCT) have allowed the relatively recent development of volumetric HRCT, a technique that is described later.

Typical HRCT protocols (Table 1) use 1- to 1.5-mm collimation every 10 to 20 mm throughout the thorax, which effectively images only approximately 10% of the lung parenchyma. Because HRCT is typically used for the assessment of diffuse lung disease, such a sampling technique provides adequate representation of the disease process while minimizing the radiation dose delivered to the patient.

Supine HRCT protocols, often used for the assessment of patients with suspected obstructive lung diseases (including bronchiectasis, emphysema, and bronchiolitis obliterans), patients with suspected opportunistic infections (eg, *Pneumocystis jiroveci* pneumonia), and patients with suspected cystic lung disease (see Table 1) typically use 10-mm spacing between images (interslice gap). HRCT protocols using both supine and prone imaging often use a 20-mm interslice gap; the radiation dose associated with supine and prone HRCT imaging is nearly equivalent to that delivered by supine HRCT protocol.

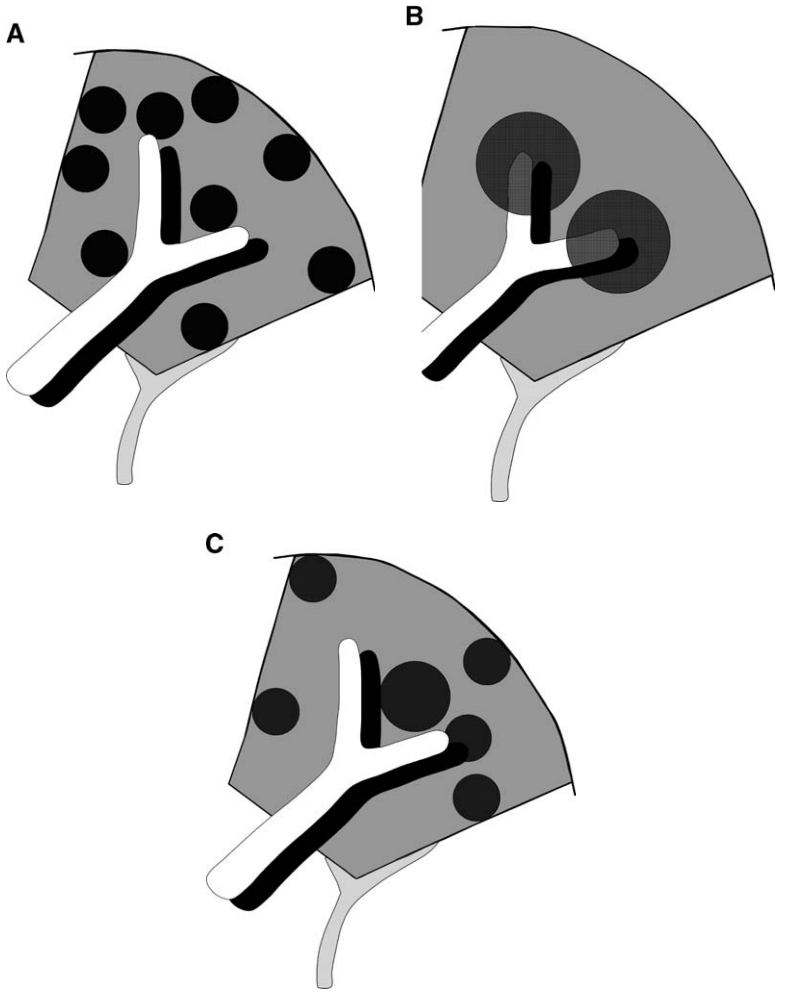

Fig. 5. Nodules on HRCT: distribution within the secondary pulmonary lobule. (*A*) Perilymphatic nodules. Nodules are immediately in contact with interlobular septa and the visceral pleura. (*B*) Centrilobular nodules. Nodules are positioned 5 to 10 mm from costal and visceral pleural surfaces and interlobular septa. Note that peribronchovascular nodules are also often present with pathologic processes that involve the lymphatic tissues, and may be part of the spectrum of perilymphatic nodules. For this reason, centrilobular nodules are seen with processes producing perilymphatic nodules, but they are not the predominant pattern. (*C*) Random nodules. Random nodules show no obvious relationship to any secondary pulmonary lobular structures. They are found in relation to the visceral pleura, interlobular septa, and center of the lobule roughly equally.

Supine and prone HRCT imaging is often used for the evaluation of patients with suspected idiopathic interstitial pneumonias or patients with restrictive patterns on pulmonary function testing (see Table 1). Prone imaging is essential in this context for distinguishing dependent density (atelectasis) from pulmonary inflammation or fibrosis-atelectasis detected on supine imaging resolves with prone imaging (Fig. 2), whereas alveolitis or fibrosis persists on prone imaging (Fig. 3) [12–14]. Furthermore, the relatively small interslice gap used with supine HRCT protocols allows one to track abnormalities more easily sequentially from image to image (eg, ectatic bronchi in patients with bronchiectasis) than do prone protocols that use a wider interslice gap.

Expiratory scanning

Expiratory scanning is a critical component to any HRCT protocol [15]. Expiratory HRCT may be performed using static HRCT methods or dynamic expiratory HRCT (imaging during a forced vital capacity maneuver). Static methods of expiratory scanning image the patient's lungs at or near functional residual capacity, and are performed by imaging after complete exhalation ("take a deep breath in and blow it all out") or using lateral decubitus CT [16]. The latter is particularly useful when expiratory imaging is desired but patient cooperation with specific breathing instructions is not ensured, as is often the case when language barriers are present.

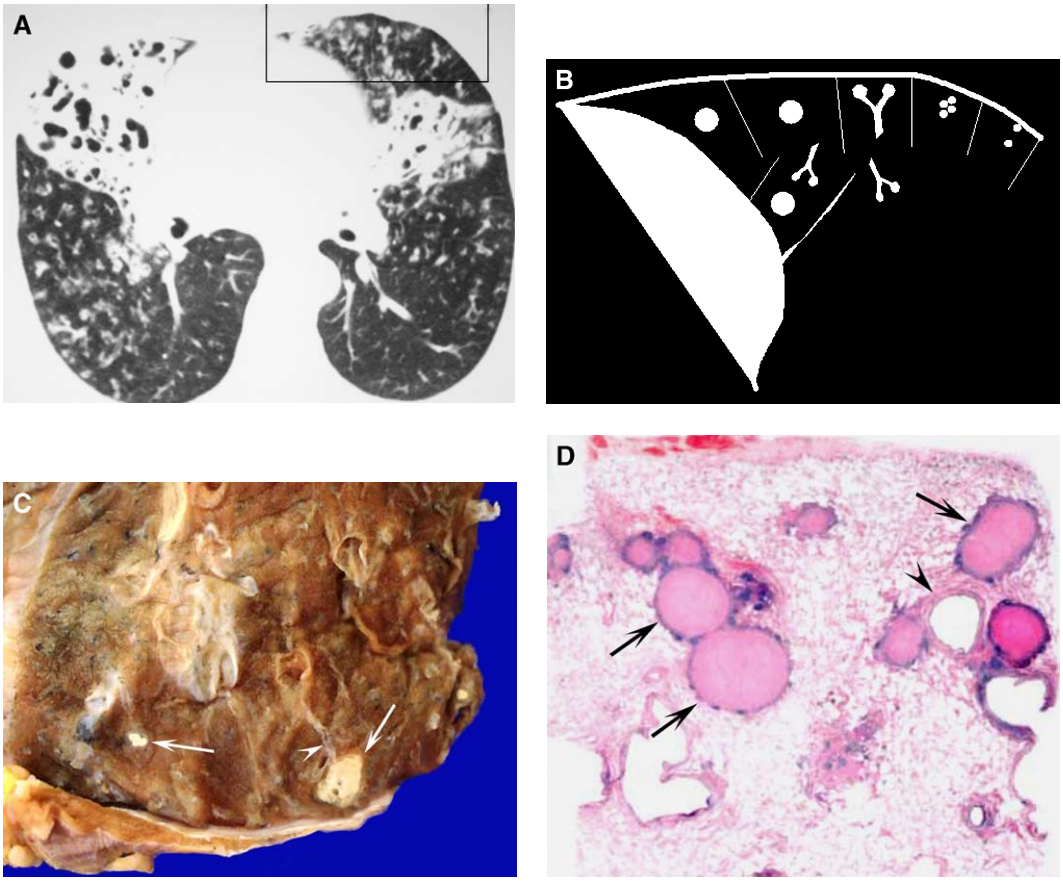

Fig. 6. Centrilobular nodules: *Mycobacterium avium*–complex infection. (*A*) Axial CT shows right middle lobe and lingular predominant bronchiectasis with bronchiolar impaction, representing tree-in-bud. The findings present within the rectangle enclosing part of the lingula are detailed in *B*. (*B*) Schematic view of *A* details the centrilobular nodules. The branching nodules represent bronchiolar impaction (tree-in-bud), with smaller, clustered nodules representing rosettes. (*C*) Gross specimen shows centrilobular nodules (*arrows*). The thin rim of lung peripheral to the nodules is consistent with a centrilobular position. Note ecstatic bronchus (*arrowhead*), confirming airway disease. (*D*) Histopathologic specimen shows centrilobular nodules (*arrows*) and abnormally dilated airway (*arrowhead*). Note position of nodules from visceral pleura at top of image.

Dynamic expiratory HRCT is performed by imaging the patient during a forced vital capacity maneuver, using either a spiral CT scanner or an electron-beam CT scanner [17–19]. Dynamic expiratory HRCT is also performed easily with MSCT scanners. Images are acquired at user-selected levels with imaging performed in cine mode (without table increment), usually for six to eight images per level [17,19]. Dynamic expiratory HRCT provides a greater overall increase in lung attenuation compared with static expiratory methods and may be more sensitive for the detection of subtle or transient air trapping than static expiratory methods. Dynamic expiratory HRCT may be performed using low-dose techniques with no compromise in diagnostic quality [19].

Volumetric (multislice) high-resolution CT

Volumetric HRCT has been performed using several different methods, including clustered axial scans at user-selected levels [20]; single breathhold single-slice CT [21,22]; and, most recently, entire-thorax MSCT-HRCT [23–27]. Although volumetric HRCT of the chest was performed with some success using conventional and single-slice CT methods, until the introduction of MSCT, the difficulty inherent in imaging the entire thorax with these older methods limited their use. MSCT, particularly scanners with 16 detectors or greater, easily allows imaging of the entire thorax using 1-mm collimation within a single breathhold. The volumetric dataset obtained with current MSCT scanners allows near-isotropic imaging, which provides the ability to view the dataset in any desired plane and for the creation of maximum intensity or minimum intensity projected images, also in any desired plane or level. For example, volumetric MSCT-HRCT may provide improved assessment of the distribution of parenchymal lung abnormalities in patients with diffuse lung diseases [24,28], and volumetric MSCT-HRCT may allow for simultaneous assessment of small airway and large airway pathology [28]. The major drawback to the widespread use of volumetric MSCT-HRCT is the increased radiation dose: volumetric MSCT-HRCT studies may deliver more than five times the radiation dose compared with routine axial HRCT techniques [23].

High-resolution CT patterns of disease

An organized approach to HRCT scan findings is critical to successful interpretation. Although simple pattern recognition can often provide the correct diagnosis in a number of cases, a firm understanding of the pathologic presentations of disease on HRCT is far more rewarding in many circumstances.

HRCT scan findings may be broadly classified into findings of increased lung opacity (Table 2) and decreased lung opacity (Table 2 and Fig. 4). HRCT disease patterns, both those manifesting as increased lung opacity and those manifesting as decreased lung opacity, may be further subclassified to facilitate organization and differential diagnosis. Occasionally, findings of increased and decreased opacity may be present on the same imaging study, either reflecting the presence of two or more diseases or, in certain cases, a pathologic process that manifests with both an infiltrative and obstructive process.

High-resolution CT scan findings manifesting as increased lung opacity

HRCT scan findings manifesting as increased lung opacity may be further subclassified into nodular abnormalities, linear abnormalities, reticular ab-

Table 3
Diagnostic utility of nodule distribution relative to the secondary pulmonary lobule

Nodule distribution on HRCT	Relevant secondary pulmonary lobular anatomic structures	Representative diseases
Centrilobular	Centrilobular artery and bronchus	Infectious bronchiolitis, diffuse panbronchiolitis, hypersensitivity pneumonitis, respiratory bronchiolitis, lymphocytic interstitial pneumonia, pulmonary edema, vasculitis, plexogenic lesions of pulmonary hypertension, metastatic neoplasms
Perilymphatic	Interlobular septa, subpleural interstitium, centrilobular bronchus	Sarcoidosis, lymphangitic carcinomatosis, amyloidosis
Random	All structures of the lobule	Hematogenously disseminated infections and neoplasms

normalities, ground-glass opacity, and consolidation (see Table 2).

Nodules

A pulmonary nodule may be broadly defined as any relatively sharply defined, discrete, nearly circular opacity within the lung, ranging in size from 2 to 30 mm. Nodules are usually further characterized with respect to size, border definition, density, number, and location. The term "micronodule" is occasionally used when describing HRCT findings, usually referring to nodules less than 3 to 7 mm in size, but the significance of this designation is uncertain [29].

The diagnostic value of HRCT for the assessment of diffuse nodular diseases relies heavily on the distribution of the nodules relative to the secondary pulmonary lobule, a diagnostic approach that was first recognized as valuable for interpretation of biopsy and surgical histopathologic specimens. HRCT technique allows imagers to extrapolate these pathologic findings to imaging findings [30]. Histopathologically, at least four nodule distributions within the secondary pulmonary lobule are recognized: (1) bronchiolocentric, (2) angiocentric, (3) lymphatic, and (4) random [30]. Nodules that are bronchiolocentric in distribution are related to the centrilobular and lobular bronchi, and angiocentric nodules are related

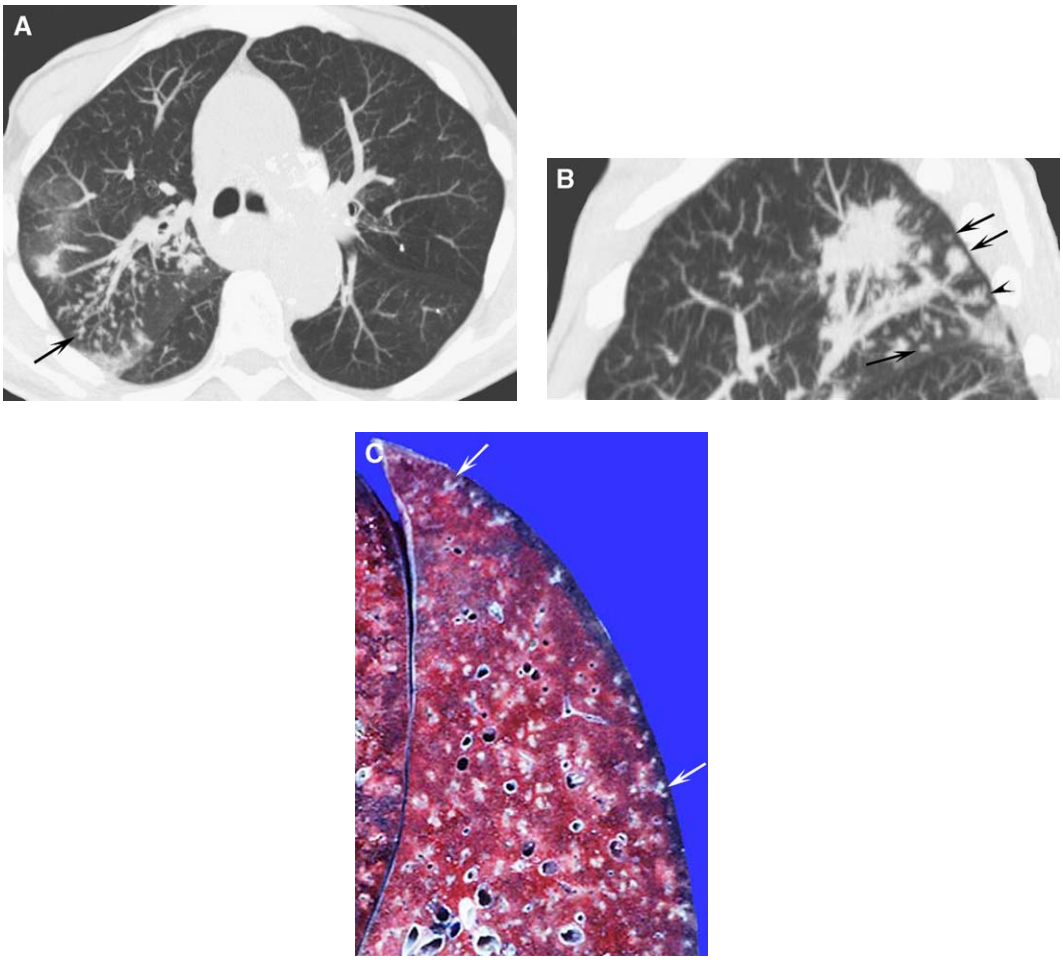

Fig. 7. Centrilobular nodules: *Mycobacterium tuberculosis* infection. (*A*) Axial HRCT image through the upper lobes shows peripheral, branching opacity consistent with bronchiolar impaction (tree-in-bud) (*arrow*). (*B*) Sagittal maximum intensity projected image from Fig. 7A demonstrates centrilobular nodules (*arrows*), some showing tree-in-bud (*arrowhead*). Note that the nodules approach, but do not contact, pleura, consistent with a centrilobular distribution. (*C*) Gross specimen shows tree-in-bud opacity (*arrows*).

to the pulmonary arteries within the secondary pulmonary lobule; because the artery and bronchus are in close proximity to one another, both nodule types are located in or very near the center of the secondary pulmonary lobule. These two distributions are not readily distinguished from one another on HRCT, so bronchiolocentric and angiocentric nodule histopathologic distributions are grouped together as centrilobular nodules, and three distributions of nodules within the secondary pulmonary lobule are recognized on HRCT: (1) centrilobular, (2) perilymphatic, and (3) random (Fig. 5).

Centrilobular nodules. Centrilobular nodules are distributed primarily within the center of the secondary pulmonary lobule (see Figs. 5B and 6). Centrilobular nodules range in size from a few millimeters to slightly greater than 1 cm, and may be well-defined or ill-defined, depending on the underlying disease process. A centrilobular nodular distribution may be recognized when nodules are roughly evenly spaced from one another and approach, but do not contact, visceral pleural surfaces (see Figs. 4, 5B, and 6); the nodules are usually positioned about 5 to 10 mm from the visceral pleural surface. Because the centrilobular artery and bronchus are the structures that predominate in the center of the pulmonary lobule, diseases affecting these two anatomic structures account for most processes that produce centrilobular nodules on HRCT (Table 3).

Centrilobular nodules may be further characterized by the presence or absence of a branching configuration, so-called "tree-in-bud." Tree-in-bud reflects the presence of impaction of the centrilobular bronchus with mucous, pus, or fluid, resulting in dilation of the bronchus, associated with peribronchiolar inflammation (see Figs. 6A, 6B, and 7) [31]. Dilated, impacted bronchi produce Y- or V-shaped structures on HRCT imaging, and have been likened to a budding tree in spring [32,33], hence the term "tree-in-bud." The presence of centrilobular nodules with tree-in-bud morphology is very diagnostically useful, because this finding is almost always seen with pulmonary infections. When centrilobular nodules are present but tree-in-bud morphology is absent, infections remain a consideration, but the differential diagnosis must be expanded (Box 1) to include several noninfectious etiologies and certain vascular lesions. Despite the relatively large and varied differential diagnosis that requires consideration when centrilobular nodules without tree-in-bud are encountered, other features of the nodules themselves may provide useful information. For instance, poorly defined centrilobular nodules distributed evenly from pulmonary apex to base are characteristic of subacute hypersensitivity pneumonitis, whereas well-defined centrilobular nodules in the posterior portions of the upper lobes, associated with nodules in the subpleural region of lung, are suggestive of silicosis (Fig. 8). Additionally, other findings are often present to assist in generating a sensible differential diagnosis. For example, well-defined centrilobular nodules, associated with bizarre-shaped cysts distributed primarily within the upper lobes in a smoker, are characteristic of Langerhans' cell histiocytosis [29,34].

Box 1. Centrilobular nodules *with* or *without* tree-in-bud opacity: diagnostic considerations

With

- Bacterial pneumonia with infectious bronchiolitis
- Typical and atypical mycobacterial infections
- Aspiration
- Allergic bronchopulmonary aspergillosis
- Cystic fibrosis
- Diffuse panbronchiolitis
- Endobronchial neoplasms (particularly bronchioloalveolar carcinoma)

Without

- All causes of centrilobular nodules with tree-in-bud opacity
- Hypersensitivity pneumonitis
- Respiratory bronchiolitis and respiratory bronchiolitis-interstitial lung disease
- Cryptogenic organizing pneumonia
- Pneumoconioses (especially silicosis and coal-worker's pneumoconiosis)
- Langerhans' cell histiocytosis
- Pulmonary edema
- Vasculitis
- Pulmonary hypertension

Perilymphatic nodules. Perilymphatic nodules are seen with diseases that preferentially involve lymphatic structures, such as sarcoidosis, lymphangitic carcinomatosis, lymphoproliferative disorders, and amyloidosis (Box 2). Pulmonary lymphatics are normally found within the visceral pleura, within the interlobular septa, and along the veins and bronchovascular bundles, so diseases involving the lym-

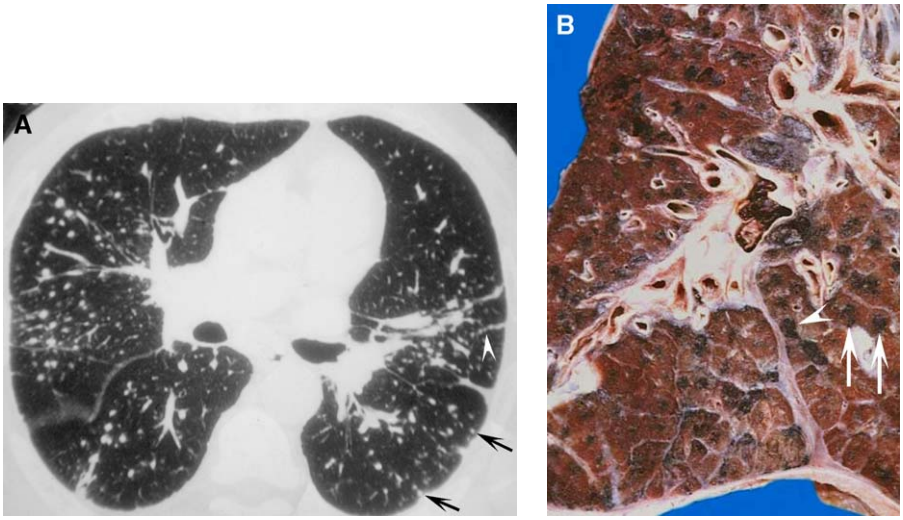

Fig. 8. Centrilobular nodules without tree-in-bud morphology: silicosis. (*A*) Axial HRCT shows numerous small nodules in a somewhat patchy distribution throughout the upper lobes. Some of the nodules approach, but do not contact, visceral pleural surfaces (*arrows*). Consistent with silicosis, nodules are also present along interlobular septa (*arrowhead*). (*B*) Gross specimen in a patient with silicosis shows a combination of centrilobular (*arrows*) and subpleural (*arrowhead*) nodules.

phatics may produce nodules in relation to these structures (see Fig. 5A). Perilymphatic nodules are recognized on HRCT as nodules that abut costal and fissural pleural surfaces, usually in a patchy distribution (Fig. 9). Note that because pulmonary lymphatics are present along bronchovascular bundles, centrilobular nodules are commonly also seen in diseases producing perilymphatic nodules; however, the nodules are predominately found along interlobular septa and the visceral pleura and not within the center of the lobule.

Random nodules. Random nodules show no definable distribution relative to the secondary pulmonary lobule; nodules are seen in the center of the lobule and in contact with interlobular septa and visceral pleural surfaces (see Fig. 5C). The differential diagnosis of randomly distributed nodules on HRCT is listed in Box 3. Random nodules, in contrast to perilymphatic nodules, usually do not show a patchy distribution in the lung parenchyma; rather, random nodules are usually distributed uniformly throughout the lung parenchyma in a bilaterally symmetric distribution (Fig. 10).

Box 2. Perilymphatic nodules: diagnostic considerations

- Sarcoidosis
- Lymphangitic carcinomatosis
- Follicular bronchiolitis and lymphocytic interstitial pneumonia
- Lymphoproliferative disorders
- Amyloidosis

Anatomic nodule localization. Localizing nodules on HRCT begins first with assessing whether or not subpleural nodules are present (nodules in contact with the visceral pleura surfaces, either costal pleura or fissures) (Fig. 11). If subpleural nodules are absent, then the nodules are centrilobular in location (see Figs. 5B and 6–8). Once nodules are identified as centrilobular, one should search for tree-in-bud. The presence of tree-in-bud opacity essentially limits the differential diagnosis to infections (see Box 1).

If subpleural nodules predominate, then either a perilymphatic or random distribution is present. In this case, the overall distribution of nodules, with reference to the upper, mid, and lower lungs, should be assessed. If the nodules are patchy in distribution, a perilymphatic distribution is present (see Fig. 9). If the nodules are scattered rather evenly throughout the upper, mid, and lower lungs, a random distribution is present (see Fig. 10).

When small nodules detected on HRCT are approached using the anatomic localization method just described, HRCT possesses a high diagnostic

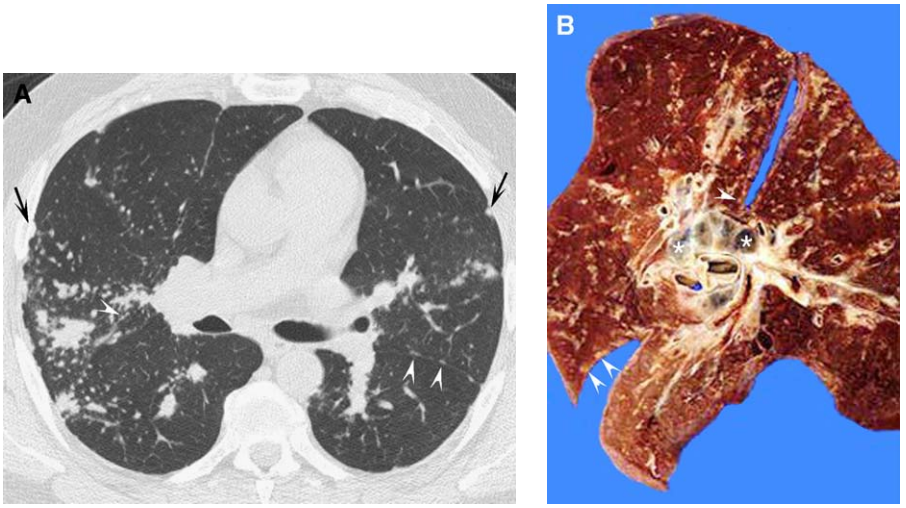

Fig. 9. Perilymphatic nodules: sarcoidosis. (*A*) Axial HRCT image shows multiple nodules, many of which are in contact with the costal (*arrows*) and fissural pleural (*arrowheads*) surfaces, consistent with a perilymphatic nodule distribution. (*B*) Gross specimen in a patient with sarcoidosis shows multiple small nodules predominantly within the upper lobes, some of which are easily appreciated along the fissural pleural surface (*arrowheads*). Hilar lymphadenopathy is also present (*).

accuracy. In a study by Gruden et al [34], anatomic nodule localization using the method described previously allowed the proper classification of the nodule distribution in 94% of cases with high interobserver agreement.

Linear abnormalities

A number of linear abnormalities may be evident on HRCT scans of the thorax, including interlobular septal thickening, parenchymal bands, subpleural lines, and irregular linear opacities. Among these linear findings on HRCT, interlobular septal thickening is the most diagnostically useful.

Interlobular septal thickening. Interlobular septa are normally about 0.1 mm thick and are just at the threshold for detection on HRCT imaging. Visualization of a few interlobular septa, usually anteriorly or along the mediastinal pleural surfaces, is normal, but visualization of numerous septa indicates an abnormal condition. Thickening of interlobular septa may be seen in conditions associated with dilatation of the pulmonary veins; infiltration of the pulmonary lymphatics; or with infiltration of the pulmonary interstitium by cells, fluid, or fibrosis. Thickened septa should be characterized as smooth, nodular, or irregular (Box 4). Smooth interlobular septal thickening is commonly seen with pulmonary edema (Fig. 12) and pulmonary alveolar proteinosis, among other etiologies (see Box 4). Lymphangitic carcinomatosis also often produces smooth interlobular septal thickening, although nodular interlobular septal thickening is more characteristic.

Nodular interlobular septal thickening is typical of diseases that involve the pulmonary lymphatics, particularly lymphangitic carcinomatosis (Fig. 13) and sarcoidosis. Both of these diseases may also produce perilymphatic nodules, but sarcoidosis is often associated with architectural distortion, reflecting underlying pulmonary fibrosis, whereas lymphangitic carcinomatosis is a nonfibrosing process and does not produce architectural distortion.

Irregular interlobular septal thickening is usually seen in fibrosing lung diseases (Fig. 14). Generally, the presence of irregular interlobular septal thickening is of limited diagnostic value and usually other findings are present on HRCT to assist in generating a differential diagnosis.

Box 3. Random nodules: diagnostic considerations

Hematogenous metastases
Miliary tuberculosis
Miliary fungal infection
Disseminated viral infection
Silicosis or coal-worker's pneumoconiosis
Langerhans' cell histiocytosis

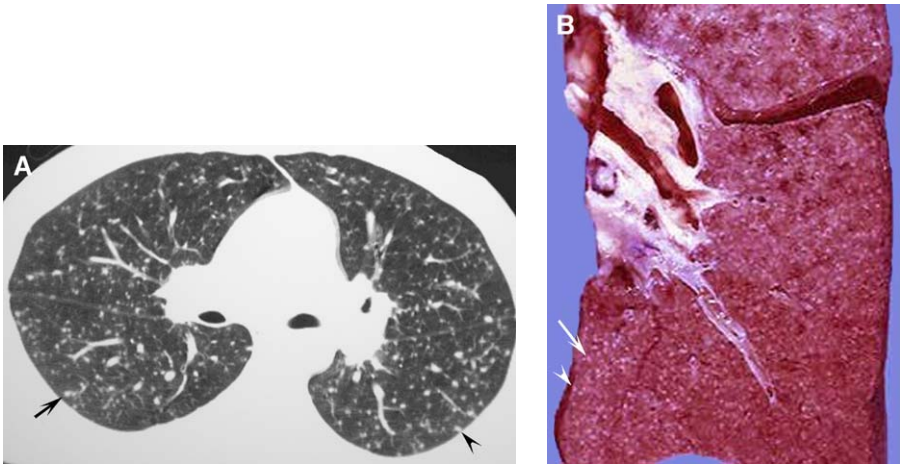

Fig. 10. Random nodules: miliary tuberculosis. (*A*) Axial HRCT image shows multiple nodules scattered uniformly throughout the lung parenchyma. Some nodules show a centrilobular distribution (*arrow*), whereas others are located in the subpleural regions of lung (*arrowhead*) or along interlobular septa, consistent with a random nodule distribution. (*B*) Gross specimen shows numerous, widely scattered small nodules, some of which are centrilobular in location (*arrow*), whereas others are subpleural in location (*arrowhead*), consistent with a random distribution.

Parenchymal bands. The term "parenchymal band" refers to a nontapering linear or reticular opacity ranging from 2 to 5 cm in length, usually perpendicular to and in contact with the pleural surfaces (Fig. 15). Parenchymal bands vary in thickness from

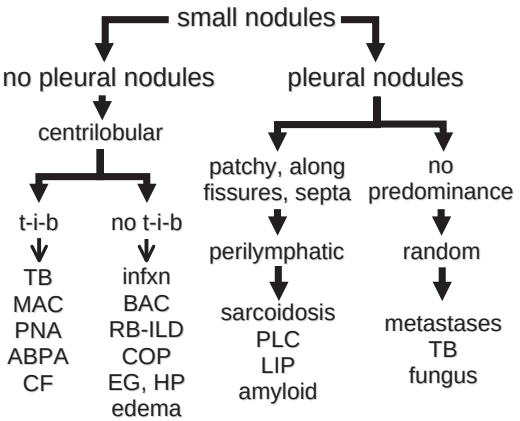

Fig. 11. Anatomic nodule localization on HRCT. ABPA, allergic bronchopulmonary aspergillosis; BAC, bronchioloalveolar carcinoma; CF, cystic fibrosis; COP, cryptogenic organizing pneumonia; EG, Langerhans' cell histiocytosis; HP, hypersensitivity pneumonitis; infxn, infection (bacterial, fungal, or viral); LIP, lymphocytic interstitial pneumonia; MAC, *Mycobacterium-avium*–complex; PLC, pulmonary lymphangitic carcinomatosis; PNA, pneumonia (most commonly bacterial); RB-ILD, respiratory bronchiolitis–interstitial lung disease; TB, *Mycobacterium tuberculosis*; tib, tree-in-bud.

Box 4. Interlobular septal thickening: differential diagnostic considerations

Smooth

Pulmonary edema
Pulmonary alveolar proteinosis
Lymphangitic carcinomatosis
Pulmonary hemorrhage
Lymphoproliferative disease
Infections (especially subacute *Pneumocystis jiroveci* pneumonia)
Amyloidosis

Nodular

Lymphangitic carcinomatosis
Sarcoidosis
Lymphocytic interstitial pneumonia
Amyloidosis
Lymphoproliferative diseases

Irregular

Chronic hypersensitivity pneumonitis
Sarcoidosis
Silicosis/coal worker's pneumoconiosis
Asbestosis
Usual interstitial pneumonia

Fig. 12. Smooth interlobular septal thickening: pulmonary edema. Axial HRCT shows extensive smooth interlobular septal thickening (*arrows*) in the lung bases of a patient with congestive heart failure. Note presence of centrilobular nodules without tree-in-bud opacity.

one to several millimeters and are most commonly encountered in patients with atelectasis or fibrosing lung diseases. Occasionally, a parenchymal band represents several contiguous interlobular septa. Parenchymal bands have been reported to occur frequently in patients with asbestos exposure [13], although they may be encountered in a wide variety of fibrotic lung processes and are ultimately nonspecific.

Subpleural lines. A subpleural line is a curvilinear opacity measuring less than 10 mm in thickness that parallels the pleura (Fig. 16). Subpleural lines are nonspecific, and usually represent atelectasis, fibrosis, or inflammation. Subpleural lines were first described in patients with asbestosis, and are seen more commonly in this disease than other fibrotic lung diseases, but they are not excusive to patients with asbestosis.

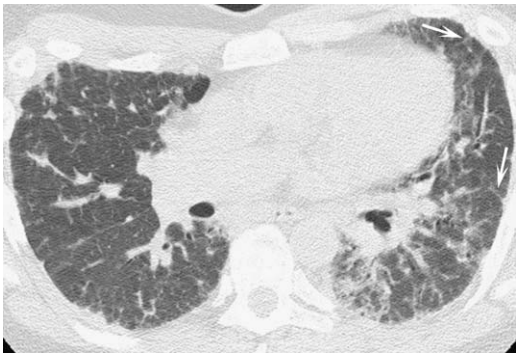

Fig. 14. Irregular interlobular septal thickening in a patient with pulmonary fibrosis of uncertain etiology. Axial HRCT shows peripheral reticulation and irregular linear opacities and several irregularly thickened interlobular septa (*arrows*).

Irregular linear opacities. Irregular linear opacities are nonspecific linear structures that cannot be classified as a parenchyma band, subpleural line, or interlobular septa. They range in thickness from 1 to

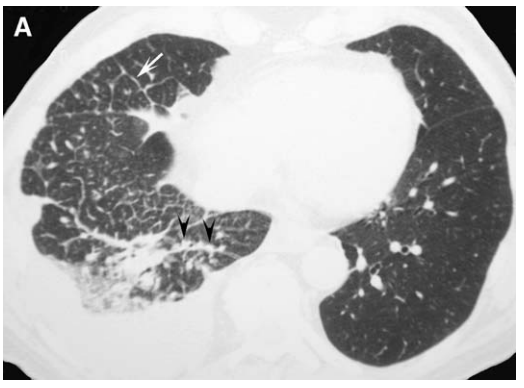

Fig. 13. Nodular interlobular septal thickening: lymphangitic carcinomatosis. (*A*) Axial HRCT image shows smooth interlobular septal thickening (*arrow*) in the anterior right lung (more commonly seen with lymphangitic carcinomatosis), with nodular interlobular septal thickening (*arrowheads*) in the posterior right lung base (more characteristic of lymphangitic carcinomatosis). Note presence of ipsilateral pleural effusion and the marked asymmetry of the process. (*B*) Gross specimen of a patient with lymphangitic carcinomatosis shows nodular interlobular septal thickening (*arrows*).

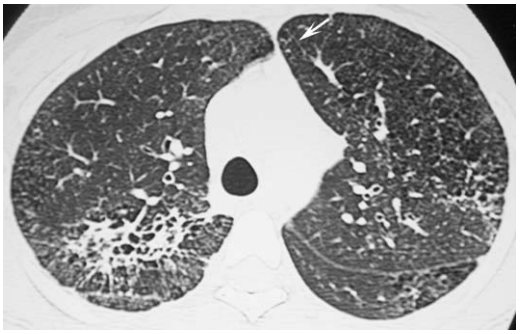

Fig. 15. Parenchymal band in a patient with sarcoidosis. Axial HRCT through the upper lobes shows a thin, linear opacity in the medial left upper lobe (*arrow*), consistent with a parenchymal band. Note presence of traction bronchiectasis secondary to fibrosis related to sarcoidosis.

3 mm and are most commonly encountered in fibrotic lung diseases, and are quite nonspecific.

Reticular abnormalities

Reticular opacities represent linear opacities that intersect one another at various angles, producing a netlike pattern. The most important form of reticular opacity encountered on HRCT imaging is intralobular interstitial thickening. Intralobular interstitial thickening reflects infiltration and thickening of the interstitial framework of the secondary pulmonary lobule and may be caused by pulmonary fibrosis or inflammation in the absence of fibrosis. When underlying fibrosis is present, the reticulation often appears coarse, and traction bronchiolectasis and architectural distortion may also be seen [2,35].

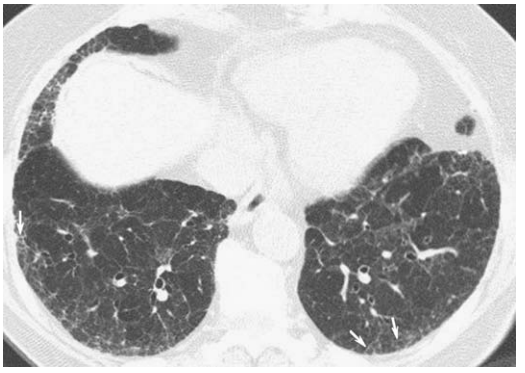

Fig. 17. Intralobular interstitial thickening and reticulation in a patient with usual interstitial pneumonia–idiopathic pulmonary fibrosis. Axial HRCT shows bilateral subpleural coarse reticular opacities (*arrows*) representing a combination of intralobular interstitial thickening and irregular linear opacities. Surgical lung biopsy showed usual interstitial pneumonia.

Intralobular interstitial thickening is a common finding in patients with usual interstitial pneumonia–idiopathic pulmonary fibrosis, and may be the predominant finding before honeycombing is evident (Fig. 17). Intralobular interstitial thickening is also a common finding in patients with nonspecific interstitial pneumonitis and pulmonary disease associated with collagen vascular diseases (Fig. 18) [36–39]. Intralobular interstitial thickening may also be seen in other idiopathic interstitial pneumonias, pulmo-

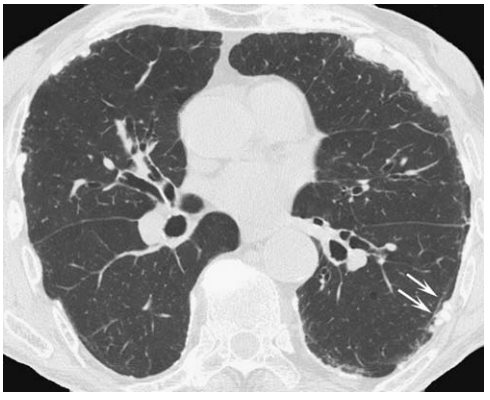

Fig. 16. Subpleural line in a patient with asbestos exposure. Axial HRCT through the lower lobes shows a thin, curvilinear opacity in the left lower lobe (*arrows*), consistent with a subpleural line. Note presence of calcified pleural plaque, consistent with asbestos-related pleural disease.

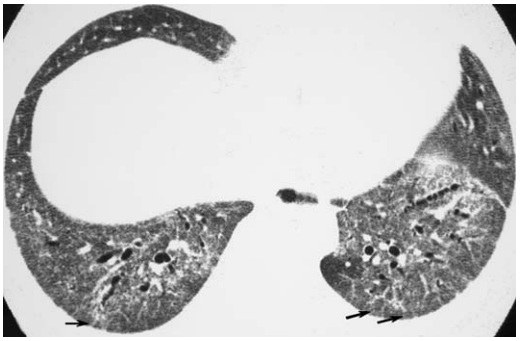

Fig. 18. Intralobular interstitial thickening and reticulation in a patient with nonspecific interstitial pneumonia associated with scleroderma. Axial HRCT shows bilateral subpleural fine reticular opacities (*arrows*) representing intralobular interstitial thickening. Surgical lung biopsy showed nonspecific interstitial pneumonia.

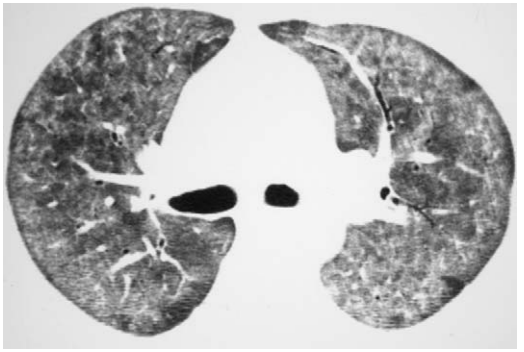

Fig. 19. Ground-glass opacity on HRCT imaging: *Pneumocystis jiroveci* pneumonia. Axial HRCT image shows multifocal bilateral ground-glass opacity in a patient with AIDS, fever, and progressive shortness of breath. Sputum induction recovered *P jiroveci.*

nary infections, pulmonary edema, and lymphangitic carcinomatosis.

Ground-glass opacity

Ground-glass opacity is defined as hazy increased attenuation that does not obscure visibility of the underlying vasculature (see Fig. 4). Ground-glass opacity is a nonspecific finding that may reflect volume averaging of abnormalities that cannot be completely resolved with HRCT technique, a purely interstitial abnormality, a purely alveolar abnormality, or a disease process that involves both the pulmonary interstitium and the air spaces [40,41]. A study by Leung et al [41] of the histopathologic correlates

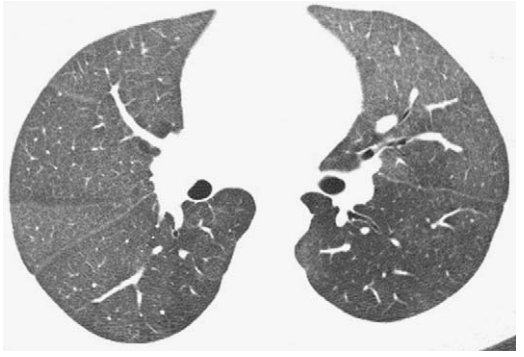

Fig. 20. Ground-glass opacity on HRCT imaging: pulmonary hemorrhage. Axial HRCT image shows multifocal bilateral ground-glass opacity, best appreciated in the right lung, in a patient with hemoptysis and systemic lupus erythematosis.

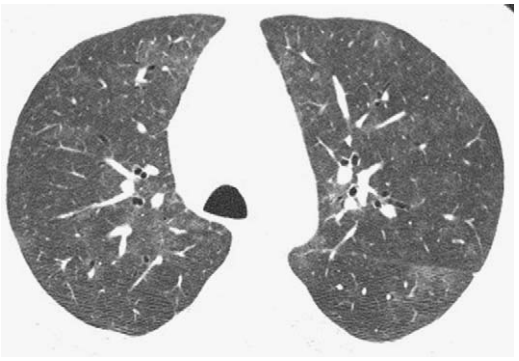

Fig. 21. Ground-glass opacity on HRCT imaging: hypersensitivity pneumonitis. Axial HRCT image shows multifocal bilateral ground-glass opacity in a patient with shortness of breath and exposure to avian antigen. Surgical lung biopsy findings were consistent with hypersensitivity pneumonitis.

of ground-glass opacity on HRCT showed that 54% of patients had a primarily interstitial abnormality, 32% had a mixed interstitial and alveolar process, and 14% of patients had primarily an alveolar process.

The significance of ground-glass opacity depends on the patient's symptoms (acute versus chronic, and the actual presenting symptoms); the distribution of the ground-glass opacity on HRCT; and the presence or absence of other findings on the HRCT study. In severely immunocompromised patients with a clinical presentation suggesting infection, ground-

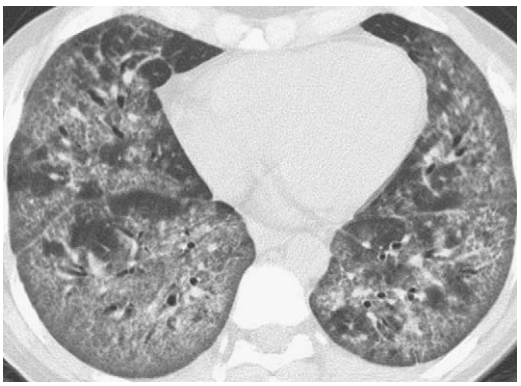

Fig. 22. Ground-glass opacity on HRCT imaging: potentially reversible pulmonary inflammation. Axial HRCT image shows basilar, posterior-predominant ground-glass opacity in a patient with collagen vascular disease. Some traction bronchiectasis and reticulation is present, but the amount of ground-glass opacity is far in excess of the findings suggesting pulmonary fibrosis. Surgical lung biopsy showed nonspecific interstitial pneumonitis.

Box 5. Peripheral and subpleural consolidation on HRCT imaging: differential diagnosis

Cryptogenic organizing pneumonia
Chronic eosinophilic pneumonia
Atypical pulmonary edema
Churg-Strauss syndrome
Drug reactions
Pulmonary contusion
Pulmonary infarct
Sarcoidosis

glass opacity often reflects active infection, such as viral pneumonia or *P jiroveci* pneumonia (Fig. 19). In patients presenting with hemoptysis, falling hematocrit, or pulmonary capillaritis, multifocal ground-glass opacity often reflects pulmonary hemorrhage (Fig. 20). For patients with a suggestive antigen exposure, multifocal ground-glass opacity reflects the histopathologic presence of poorly formed granulomas, cellular bronchiolitis, and interstitial inflammation caused by hypersensitivity pneumonitis (Fig. 21).

The presence of ground-glass opacity in patients with idiopathic interstitial pneumonias often, but not invariably, reflects active pulmonary inflammation and potentially reversible disease. In the study by Leung et al [41] cited previously, 82% of patients with ground-glass opacity on HRCT had reversible disease shown on lung biopsy. Similarly, Remy-Jardin et al [40] showed that ground-glass opacity on HRCT corresponded to active, reversible pulmonary inflammation in 65% of patients undergoing biopsy. In this same study, however, 22% of patients with ground-glass opacity on HRCT had lung biopsies showing more fibrosis than inflammation, and in 13% of patients only fibrosis was found on biopsy. For these latter patients, ground-glass opacity on HRCT represented fibrosis below the limit of HRCT resolution. Ground-glass opacity should be interpreted as active, potentially reversible disease when unaccompanied by other findings suggestive of fibrosis, such as traction bronchiectasis and honeycombing (Fig. 22) [40,42]. In patients with ground-glass opacity in some areas of lung but findings suggesting fibrosis in other areas, biopsy should be directed toward the areas of ground-glass opacity and away from areas more suggestive of fibrosis [40,42].

Consolidation

Consolidation is defined as increased attenuation, which results in obscuration of the underlying vasculature, usually producing air bronchograms (see Fig. 4). The presence of consolidation implies that the air within affected alveoli has been replaced by another substance, such as blood, pus, edema, or cells. When consolidation is evident on a chest radiograph, HRCT does not usually provide additional diagnostically useful information. HRCT may detect consolidation earlier than chest radiography, however, and in certain circumstances may provide useful information regarding the distribution of con-

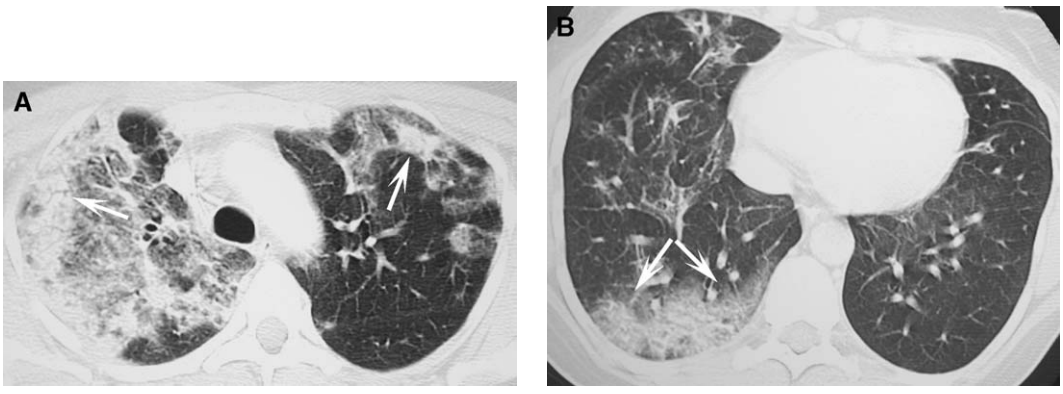

Fig. 23. Consolidation on HRCT imaging: chronic eosinophilic pneumonia. Axial HRCT images through the upper (*A*) and lower (*B*) lungs show multifocal, bilateral, peripheral consolidations (*arrows*) highly suggestive of chronic eosinophilic pneumonia or cryptogenic organizing pneumonia. Recognition of the peripheral nature of these opacities prompted bronchoscopy, which showed pulmonary eosinophilia, confirming the diagnosis of chronic eosinophilic pneumonia. The opacities resolved completely 1 week later following steroid treatment.

Table 4
Causes of bronchiectasis and characteristic disease distribution

Etiology	Characteristic disease distribution	Comment
Postinfectious (bacterial and viral)	Lower lobe	—
AIDS-related airway disease	Lower lobe	—
Cystic fibrosis	Upper lobe	Mucoid impaction
Allergic bronchopulmonary aspergillosis (see Fig. 26)	Central, upper lobe	Mucoid impaction (may be high attenuation)
Williams-Campbell syndrome	Central	—
Mycobacterium avium complex infection (see Fig. 6A)	Right middle lobe, lingula	Older women
Immotile cilia syndromes	Right middle lobe, lingula, lower lobes	May be accompanied by situs invertus in Kartagener's syndrome
Hypogammaglobulinemia	Right middle lobe, lingula	—
Airway obstruction (neoplasm, stricture)	Focal, distal to obstruction	Often shows a lobar distribution

Distribution reflects predominant areas of involvement. Other regions may also be simultaneously involved.

solidation and detect findings diagnostically important but not visible radiographically.

The differential diagnosis of consolidation is extensive, and requires integration of clinical history with other relevant scan findings to become manageable. One circumstance where HRCT is quite valuable in the assessment of consolidation is the determination of the distribution of findings. Although many etiologies of consolidation may often be indistinguishable from one another on HRCT imaging, consolidation in a peripheral or subpleural distribution should evoke a specific differential diagnosis (Box 5). Recognition of this particular distribution of consolidation can be diagnostically quite useful (Fig. 23).

High-resolution CT scan findings manifesting as decreased opacity

Bronchiectasis

Bronchiectasis is defined as localized, irreversible dilation of the bronchial tree. There are numerous

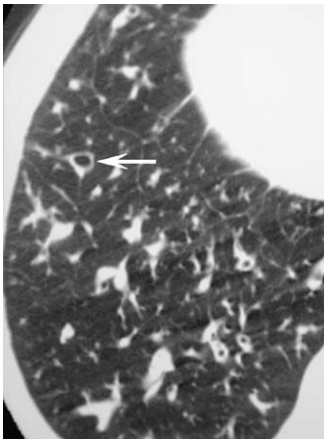

Fig. 24. HRCT assessment of bronchiectasis: the "signet ring" sign. Coned axial HRCT image shows a dilated bronchus (*arrow*) in cross-section. Note that the internal diameter of the bronchus exceeds the diameter of the adjacent pulmonary artery.

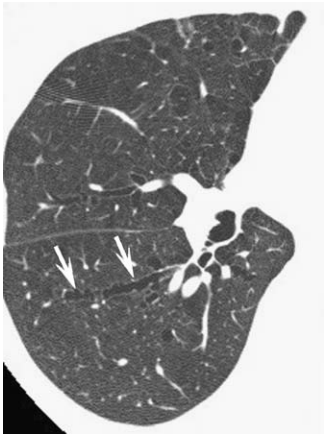

Fig. 25. HRCT assessment of bronchiectasis: lack of bronchial tapering. Coned axial HRCT image shows bronchial dilation with lack of tapering (*arrows*). Bronchial morphology is consistent with varicose bronchiectasis.

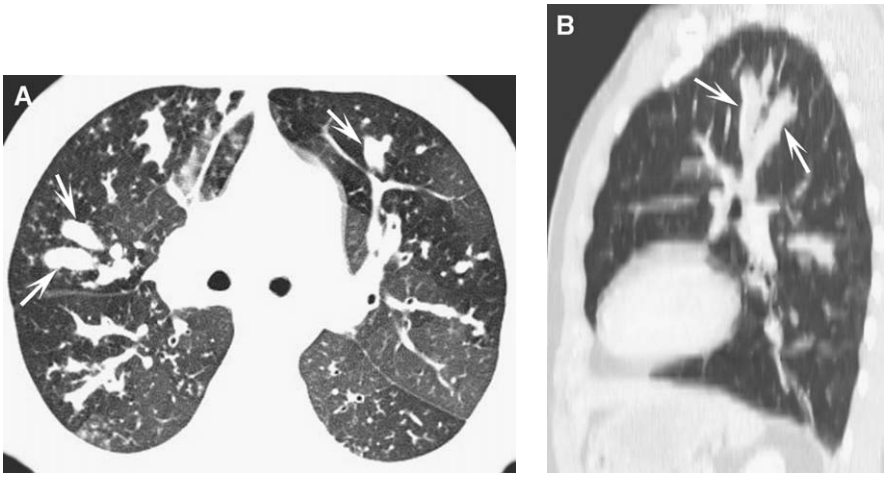

Fig. 26. HRCT assessment of bronchiectasis: mucoid impaction. (*A*) Axial HRCT image shows extensive, bilateral mucoid impaction (*arrows*). Bilateral inhomogeneous lung opacity represents mosaic perfusion caused by large and small airway obstruction. Small centrilobular nodules are visible in the right lower lobe. (*B*) Sagittal maximum intensity projected image shows the mucoid impaction (*arrows*) to advantage; ''finger-in-glove'' appearance is clear.

causes of bronchiectasis. Several of the most common etiologies are listed in Table 4. Bronchography was traditionally performed to confirm the diagnosis of bronchiectasis, but now has been replaced by HRCT. HRCT findings of bronchiectasis include increased bronchoarterial ratios, lack of appropriate airway tapering, bronchial wall thickening and irregularity, mucoid impaction, and mosaic perfusion with air trapping.

Bronchial dilation (increased bronchoarterial ratio). Bronchial dilation is the most specific finding for bronchiectasis. In general, bronchiectasis

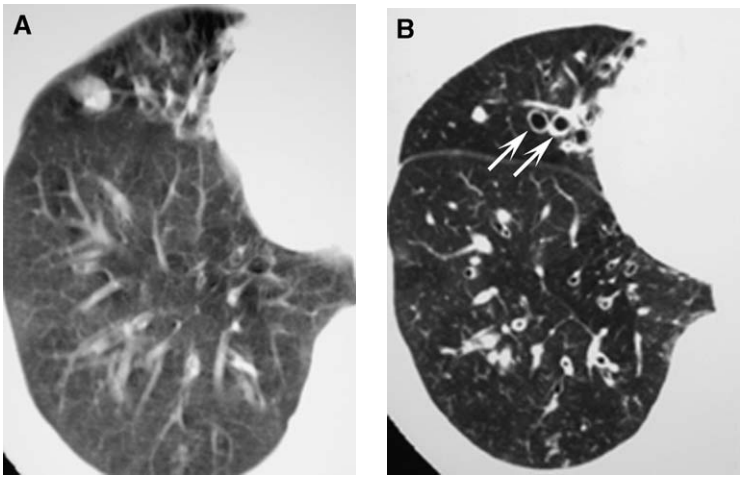

Fig. 27. Pitfalls in the HRCT assessment of bronchiectasis: wide collimation and respiratory motion. (*A*) Coned axial CT image obtained with 7-mm collimation and degraded by respiratory motion fails to demonstrate bronchiectasis clearly. (*B*) Coned axial HRCT image clearly shows bronchiectasis in the right middle lobe (*arrows*) and the right lower lobe.

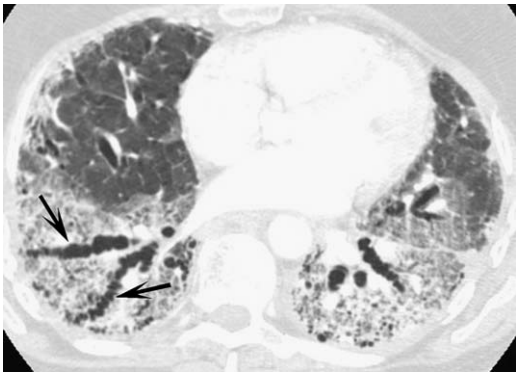

Fig. 28. Pitfalls in the HRCT assessment of bronchiectasis: traction bronchiectasis. Axial HRCT image shows extensive lower lobe bronchial dilation (*arrows*). Note corrugated appearance of bronchi; this morphology is characteristic of traction bronchiectasis. Surrounding architectural distortion, ground-glass opacity, and coarse reticulation are present and suggest presence of fibrotic lung disease. Bronchi are also visible in the immediate subpleural regions of lung. This finding indicates an abnormal condition, and may be seen with traction bronchiectasis or primary large and small airway diseases.

is present when the bronchoarterial ratio (the ratio of the internal diameter of the bronchus to its adjacent pulmonary artery) exceeds 1. When an increased bronchoarterial ratio is seen in cross-section, it has been termed the "signet ring" sign (Fig. 24). This sign is suggestive of bronchiectasis, but it does have limitations. The ratio may not be perceptibly increased in areas of consolidation, and patients who live at altitudes well above sea level or asthmatics often have bronchoarterial ratios greater than 1 [43].

Lack of bronchial tapering. Perhaps the earliest sign of cylindrical bronchiectasis, lack of bronchial tapering, is often subtle, but is important to appreciate. It is probably easiest to see in longitudinal section (Fig. 25). In cross-section, with noncontiguous HRCT images, the finding is difficult to assess. One indication of this finding in cross-section is lack of change in the size of an airway over 2 cm after branching.

Visualization of peripheral airways. Visualization of an airway within 1 cm of the costal pleura is abnormal and indicates potential bronchiectasis. Airways may be seen within 1 cm of the mediastinal pleura, but should never be seen actually to abut the mediastinal pleura.

Mucoid impaction. Fluid- or mucous-filled, dilated bronchi are usually easily appreciated on HRCT. They may be seen as branching structures when imaged in longitudinal section, or as nodules when imaged in cross-section (Fig. 26).

Ancillary findings. Ancillary findings of bronchiectasis include indicators of bronchiolectasis (with mucoid impaction and tree-in-bud); mosaic perfu-

Table 5
Pitfalls in high-resolution CT diagnosis of bronchiectasis

Pitfall	Comment
Inadequate HRCT technique-collimation too wide, large interslice gap (see Fig. 27)	Use narrow collimation; interlslice gap should not exceed 1 cm
Respiratory (see Fig. 27) and cardiac motion	Usually maximal near heart in right middle lobe and lingula. May mimic or obscure (see Fig. 27A) diagnosis of bronchiectasis. Look for motion elsewhere on the scan
Consolidation	Avoid diagnosing bronchiectasis when active infection or significant atelectasis is present; obtain follow up imaging
Cystic lung diseases	Use narrow collimation and narrow interslice gap to facilitate appreciation of airway origin of pulmonary cystic lucency (cystic lung diseases lack tubular morphology). To suggest bronchiectasis, look for constant relationship of cysts to pulmonary arteries and for "cluster of grapes" morphology
Increased bronchoarterial ratios in normal patients	Obtain history of asthma or residence at altitude
Traction bronchiectasis (see Fig. 28)	Look for other findings of fibrosis

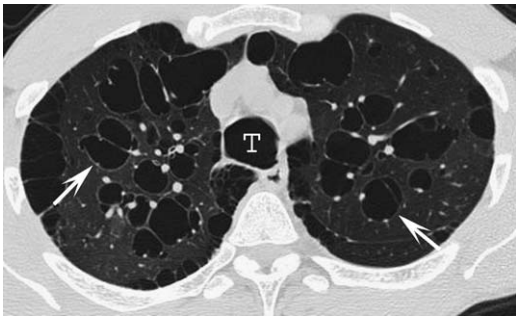

Fig. 29. HRCT assessment of bronchiectasis: cystic bronchiectasis. Axial HRCT imaging shows extensive bilateral cystic bronchiectasis (*arrows*), consistent with the diagnosis of tracheobronchomegaly. Note dilated trachea (T).

sion (discussed later); air trapping; and bronchial wall thickening.

Pitfalls in the high-resolution CT diagnosis of bronchiectasis. Pitfalls in the diagnosis of bronchiectasis (Figs. 27 and 28) are listed in Table 5. Careful attention to technique is essential for avoiding some of these pitfalls. MSCT-HRCT imaging of the thorax may play a role in the evaluation of suspected bronchiectasis because volumetric imaging obtained in a very brief time period avoids several of the pitfalls in bronchiectasis imaging that may occur with routine HRCT technique.

Use of high-resolution CT for the diagnosis of the etiology of bronchiectasis. Bronchiectasis may be classified, in ascending order of severity, as cylindrical (see Fig. 24), varicose (see Fig. 25), and cystic (Fig. 29), although this classification provides little information regarding the etiology of bronchiectasis in individual cases. It is more diagnostically rewarding to approach the assessment of the etiology of bronchiectasis based on the distribution of the bronchiectasis on imaging studies. Some etiologies of bronchiectasis have particular distributions visible on HRCT imaging that may allow a specific diagnosis to be suggested (Table 4), although this approach has met with variable success [44–47]. The likelihood of diagnosing a specific cause of bronchiectasis is enhanced when the imaging studies are interpreted in the presence of specific clinical information [45].

Emphysema

Emphysema is defined as a condition "of the lung characterized by permanent, abnormal enlargement of the airspaces distal to the terminal bronchiole, accompanied by destruction of the air space walls" [48,49]. Emphysema results from an imbalance between proteolytic and antiproteolytic enzymes, and the balance is shifted toward proteolysis by smoking or enzymatic deficiencies, such as α_1-antiprotease deficiency [50].

Classification of emphysema: approach using high-resolution CT. Emphysema may be classified into centrilobular, panlobular, and distal acinar (paraseptal) patterns using both histopathologic techniques and HRCT imaging (Table 6). Centrilobular emphysema (Fig. 30) is found most commonly in the upper lobes and manifests as multiple small areas of low attenuation without a perceptible wall, producing a

Table 6
Emphysema on high-resolution CT imaging: distinguishing features

Pattern	Distribution	Appearance	Comment
Centrilobular	Upper lobe	Rounded low attenuation with minimal or no perceptible wall. May see centrilobular artery within area of low attenuation	Smokers
Panlobular	Generalized or lower lobe	Lobular low attenuation, diffuse low attenuation with simplification of pulmonary architecture	α-1–Antiprotease deficiency. May be difficult to appreciate until moderate or severe
Paraseptal	Upper lobe	Thin-walled cyst in subpleural regions of upper lobes. Spontaneous pneumothorax	Smokers, associated with other forms of emphysema. May be seen in nonsmokers
Irregular air space enlargement	None (more commonly upper lobe)	Irregular low attenuation in proximity to scars or progressive massive fibrosis	Silicosis, sarcoidosis

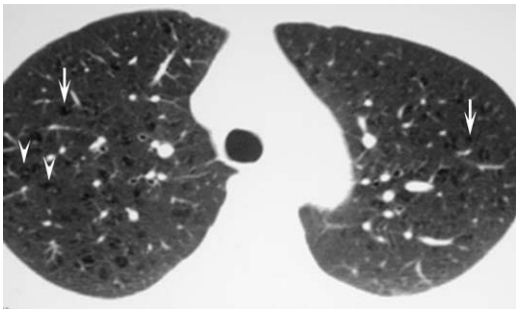

Fig. 30. HRCT assessment of emphysema: centrilobular emphysema. Axial HRCT image through the upper lobes shows numerous scattered low-attenuation foci with minimal or no perceptible walls (*arrows*) consistent with centrilobular emphysema. Some of the lucencies have small dots within them (*arrowheads*), representing the centrilobular artery.

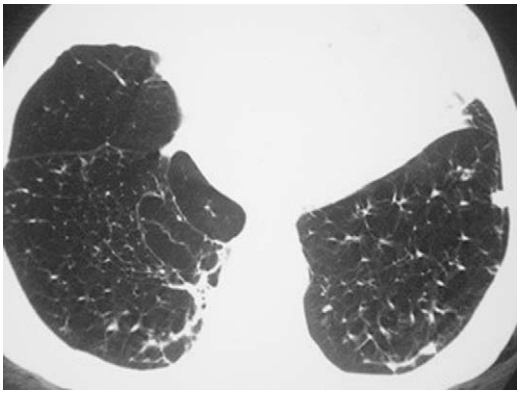

Fig. 32. HRCT assessment of emphysema: panlobular emphysema. Axial HRCT image through the lower lobes shows diffuse low attenuation and simplification of pulmonary architecture. Note how the vasculature in the lower lobes seems stretched and attenuated. Discrete areas of low attenuation are more difficult to appreciate in patients with panlobular emphysema than those with centrilobular emphysema.

punched-out appearance. Often the centrilobular artery is visible within the center of these lucencies. On occasion, a very thin, barely perceptible, wall may be encountered in patients with centrilobular emphysema, probably related to some degree of surrounding fibrosis. When centrilobular emphysema becomes more pronounced, areas of confluent low attenuation become evident. This appearance has been referred to as ''confluent centrilobular emphysema'' (Fig. 31).

In contrast to centrilobular emphysema, panlobular emphysema is histopathologically characterized by complete destruction of the entire pulmonary lobule, and shows either diffuse or lower lobe predominance. This is the pattern of emphysema commonly present in patients with α_1-antiprotease deficiency [50]. On HRCT, panlobular emphysema appears as extensive low attenuation that manifests as diffuse ''simplification'' of pulmonary architecture

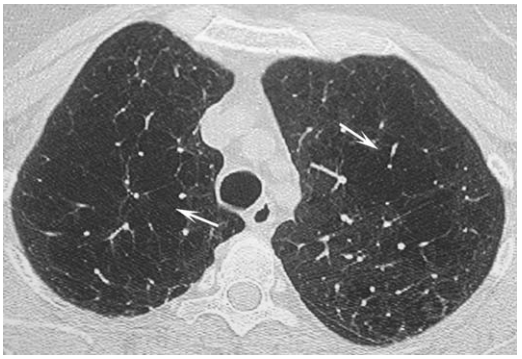

Fig. 31. HRCT assessment of emphysema: confluent centrilobular emphysema. Axial HRCT image through the upper lobes shows large areas of decreased attenuation (*arrows*), representing confluent centrilobular emphysema.

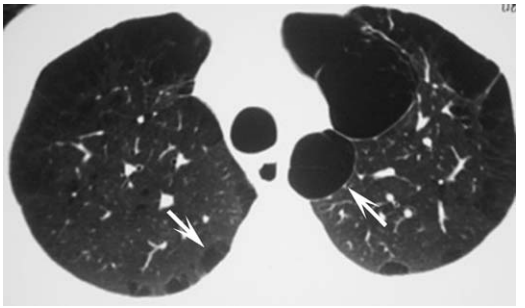

Fig. 33. HRCT assessment of emphysema: distal acinar and paraseptal emphysema. Axial HRCT image through the upper lobes shows subpleural areas of low attenuation with very thin, uniform walls (*arrows*) consistent with paraseptal emphysema. Note how paraseptal emphysema forms a single layer in the subpleural regions of lung.

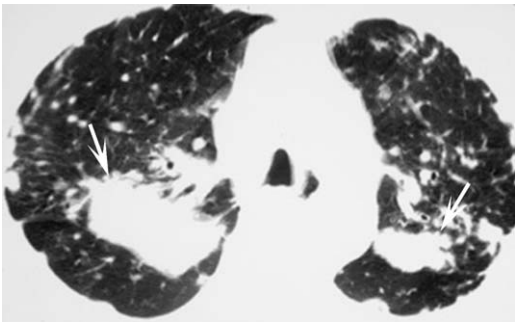

Fig. 34. HRCT assessment of emphysema: irregular air space enlargement (previously referred to as ''cicatricial emphysema''). Axial HRCT image through the upper lobes in a patient with complicated silicosis shows opacities consistent with progressive massive fibrosis (*arrows*), associated with irregular low attenuation in the wake of the upper lobe opacities; the low-attenuation areas represent irregular air space enlargement.

(Fig. 32) [51], and the pulmonary vessels appear stretched and attenuated in the presence of panlobular emphysema. Centrilobular emphysema and paraseptal emphysema are uncommonly associated with panlobular emphysema.

Distal acinar, or paraseptal, emphysema commonly occurs in smokers and shows upper lobe predominance, although paraseptal emphysema may be seen associated with other types of emphysema and even in nonsmokers. Because this pattern of emphysema preferentially destroys the distal portion of the pulmonary acinus, findings on HRCT are characteristically peripheral in distribution (Fig. 33). Paraseptal emphysema appears on HRCT imaging as multiple areas of low attenuation with thin, definable, uniform walls distributed in the subpleural regions of lung, forming a single layer. Spontaneous pneumothorax may occur in association with paraseptal emphysema.

Finally, cicatricial emphysema, now more properly termed ''irregular air space enlargement,'' may be recognized in association with parenchymal scars, especially in the setting of progressive massive fibrosis in patients with pneumoconiosis. Irregular emphysema appears on HRCT as low attenuation in immediate proximity to progressive massive fibrosis or pulmonary scars (Fig. 34).

Honeycomb lung

Honeycomb lung represents the presence of end-stage lung and may occur from a wide variety of insults. Pathologically, honeycomb cysts consists of air-containing spaces with thick walls that are lined with bronchiolar epithelium and fibrous tissue. The HRCT demonstration of honeycomb cysts allows for a confident diagnosis of a fibrosing pulmonary process, and the specific distribution of the honeycomb cysts may be a clue to the etiology of the fibrotic lung disease (Table 7). Note, however, that microscopic honeycomb cysts may be shown on surgical lung biopsy in patients without clear evidence of honeycomb cysts on HRCT.

Table 7
Honeycomb cysts: diagnostic utility of distribution of honeycomb cysts on high-resolution CT imaging

Disease etiology	Distribution	Comment
UIP	Lower lobe	Includes idiopathic pulmonary fibrosis (UIP), asbestosis, aspiration, and connective tissue disorders
NSIP	Lower lobe	Includes fibrotic NSIP, connective tissue disorders
Other idiopathic interstitial pneumonias		
AIP	Variable	Associated with respiratory failure, diffuse ground-glass opacity and consolidation
DIP	Variable	Smokers with multifocal or diffuse ground-glass opacity [61,62]
Hypersensitivity pneumonitis	Mid-lungs	Tends to spare extreme bases, unlike UIP [63]
Sarcoidosis	Upper lobe	May see associated perilymphatic nodules (see Fig. 15)
Radiation injury	Variable	Depends on port; may recognize abrupt margins and nonanatomic distribution
ARDS (postrecovery)	Anterior lung	Posterior atelectasis in ARDS may be protective from oxygen toxicity, allowing preferential damage to anterior lung [64]

Abbreviations: AIP, acute interstitial pneumonia; ARDS, adult respiratory distress syndrome; DIP, desquamative interstitial pneumonia; NSIP, nonspecific interstitial pneumonia; UIP, usual interstitial pneumonia.

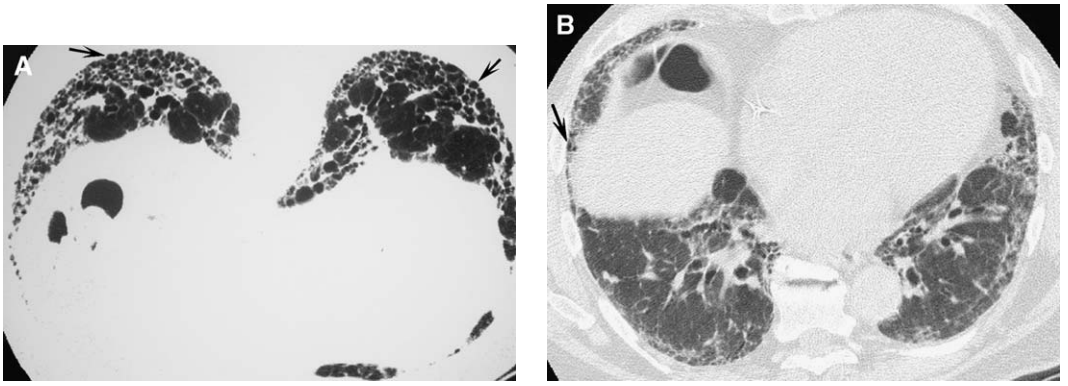

Fig. 35. HRCT demonstration of honeycomb lung in patients with idiopathic pulmonary fibrosis–usual interstitial pneumonia (UIP). (*A*) Axial HRCT image through the lung bases shows multiple cystic structures in the subpleural regions of lung (*arrows*), consistent with honeycomb lung. Note how the cysts stack on themselves in layers and share walls with one another. (*B*) Axial HRCT image through the lung bases shows subpleural reticulation (*arrow*), suggestive of fibrotic lung disease. Several honeycomb cysts are present within the right lower lobe, allowing the diagnosis of UIP to be suggested on the basis of imaging.

Honeycomb cysts on HRCT appear as cystic areas with clearly definable walls, ranging from a few millimeters to several centimeters in size. Honeycomb cysts may form a single layer in the subpleural lung, although when the disease process becomes more advanced, honeycomb cysts stack on one another in several layers (Fig. 35A); this allows them to be readily distinguished from bullae in patients with paraseptal emphysema. Honeycomb cysts usually share walls with one another, and associated findings of fibrosis (architectural distortion, coarse reticulation, intralobular interstitial thickening, and traction bronchiectasis) are also commonly present (Fig. 35).

The determination of the presence or absence of honeycombing on HRCT in patients with idiopathic interstitial pneumonia is of great importance. The confident diagnosis of lower lobe, subpleural honeycombing in such patients strongly suggests usual interstitial pneumonia–idiopathic pulmonary fibrosis, and obviates the need for surgical lung biopsy (see Fig. 35). In a group of patients from multiple centers selected on the basis of the suspicion of idiopathic pulmonary fibrosis, thoracic radiologists confidently diagnosed usual interstitial pneumonia in nearly 60% of patients, with a positive predictive value of 96% [52]. In a subsequent analysis of these data, the presence of either of two HRCT features (upper lobe reticulation and lower lobe honeycombing) was found to increase the probability of a histopathologic diagnosis of usual interstitial pneumonia by fivefold to sixfold [53]. Similarly, in another study of patients suspected of having an idiopathic interstitial pneumonia, the presence of honeycombing on HRCT in at least one lobe had a positive predictive value of 92%

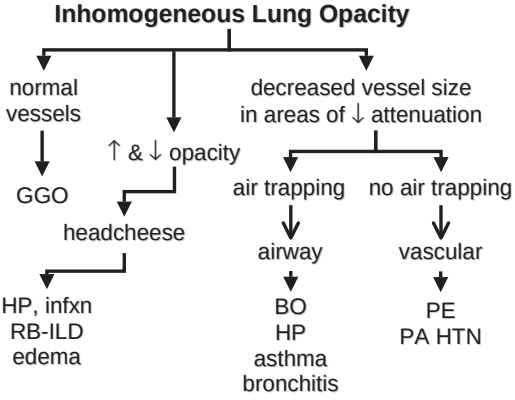

Fig. 36. Inhomogeneous lung opacity: differentiating between infiltrative and obstructive etiologies. BO, bronchiolitis obliterans; GGO, ground-glass opacity; HP, hypersensitivity pneumonitis; infxn, infection (bacterial or viral); PA HTN, pulmonary hypertension; PE, pulmonary embolism; RB-ILD, respiratory bronchiolitis–interstitial lung disease.

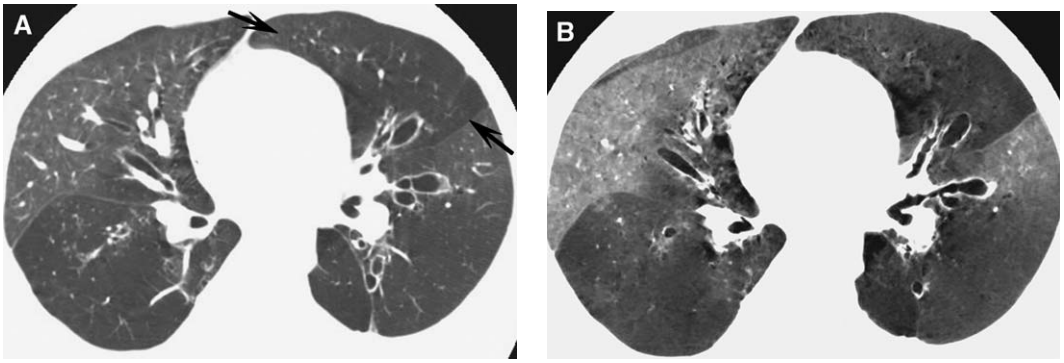

Fig. 37. Inhomogeneous lung opacity: mosaic perfusion in a patient with bronchiectasis. (*A*) Axial HRCT image shows central bronchiectasis with multifocal, bilateral inhomogeneous lung opacity, particularly in the left upper lobe (*arrows*), left lower lobe, and right lower lobe. Note how the vessels within the areas of abnormally low attenuation are smaller than their counterparts in areas of normal lung attenuation. (*B*) Axial minimum intensity projected image shows the multifocal mosaic perfusion to advantage.

[54]. The diagnosis of usual interstitial pneumonia cannot be confidently offered on HRCT imaging when honeycomb cysts are not seen. Some patients without HRCT evidence of honeycombing subsequently have usual interstitial pneumonia diagnosed on surgical lung biopsy (see Fig. 17) [52].

Mosaic perfusion and inhomogeneous lung opacity

Pulmonary tissue density is in part determined by the blood volume present within lung tissue. Any pathologic process that disturbs the distribution of pulmonary blood volume may alter pulmonary parenchymal attenuation. Alterations in pulmonary parenchymal attenuation that are seen on HRCT imaging that either result from infiltration of the lung parenchyma or from disturbances in pulmonary blood volume may be collectively referred to as ''inhomogeneous lung opacity.'' When infiltrative pathology is the cause of inhomogeneous lung opacity, either ground-glass opacity or consolidation is seen; when alterations in pulmonary blood distribution are the cause of inhomogeneous lung opacity, decreased lung opacity is encountered and the term ''mosaic perfusion'' may be used. The alterations in lung parenchymal perfusion that result in mosaic perfusion produce both areas of relatively increased attenuation (hyperperfused lung) and areas of relatively decreased attenuation (hypoperfused lung), although the latter are more striking on HRCT imaging.

Two major categories of pathologies producing mosaic perfusion are recognized: airway obstruction and vascular occlusion. Obstructive airway lesions that may produce mosaic perfusion include large airway diseases, such as bronchiectasis, and the various forms of bronchiolitis (particularly chronic bronchiolitis with hypersensitivity pneumonitis and constrictive bronchiolitis). Vascular occlusion is commonly the result of chronic thromboembolic dis-

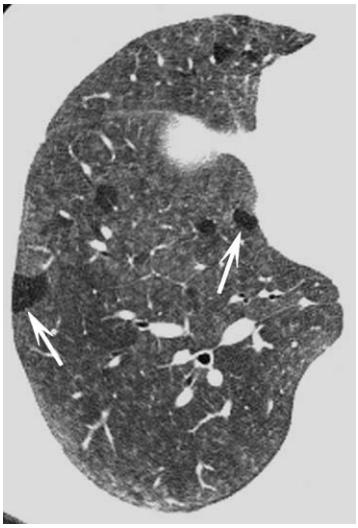

Fig. 38. Inhomogeneous lung opacity: lobular low attenuation indicating presence of mosaic perfusion. Coned axial HRCT image in a patient with hypersensitivity pneumonitis shows areas of decreased attenuation in the shape and size of secondary lobules (*arrows*). This pattern of lobular low attenuation, in the presence of physiologic evidence for airflow obstruction or when extensive, suggests mosaic perfusion caused by an airway etiology, most commonly bronchiolitis.

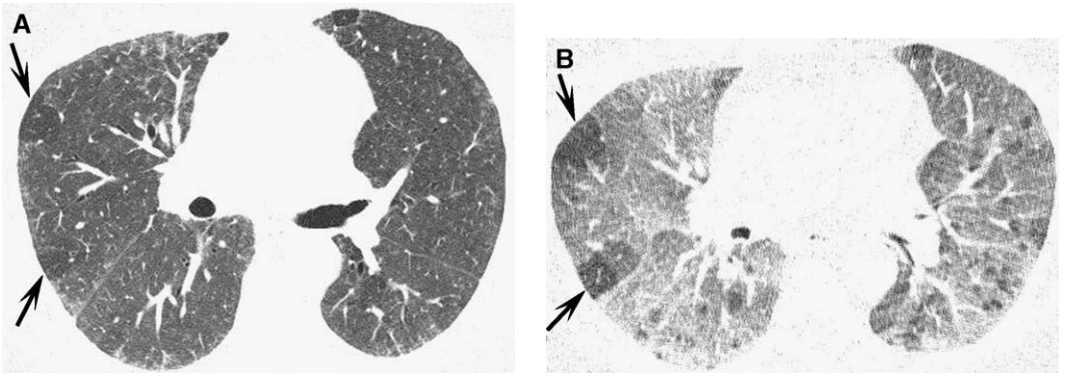

Fig. 39. Mosaic perfusion caused by airway obstruction: value of expiratory imaging with HRCT in a patient with hypersensitivity pneumonitis. (*A*) Axial HRCT image through the lower lobes shows bilateral inhomogeneous lung opacity consistent with a combination of increased lung attenuation, representing ground-glass opacity, and decreased lung attenuation, representing mosaic perfusion (*arrows*). (*B*) Axial low-dose expiratory HRCT image shows accentuation of the inhomogeneous lung opacity. There is failure of the low-attenuation areas seen on the inspiratory image (*arrows*) to increase in attenuation appropriately, indicating air trapping.

ease, pulmonary hypertension, or capillaritis caused by vasculitis.

Inhomogeneous lung opacity: distinguishing between ground-glass opacity and mosaic perfusion

When inhomogeneous lung opacity is encountered on HRCT, infiltrative pathology must be distinguished from obstructive pathology; occasionally both patterns may be present. An algorithmic approach to the assessment of inhomogeneous lung opacity facilities accurate diagnosis (Fig. 36). Mosaic perfusion may be differentiated from ground-glass opacity by the observation that vessels within the areas of relatively decreased lung attenuation are abnormally small (Fig. 37), whereas in the cases of ground-glass opacity, vessels are equal in size throughout all areas of inhomogeneous lung opacity

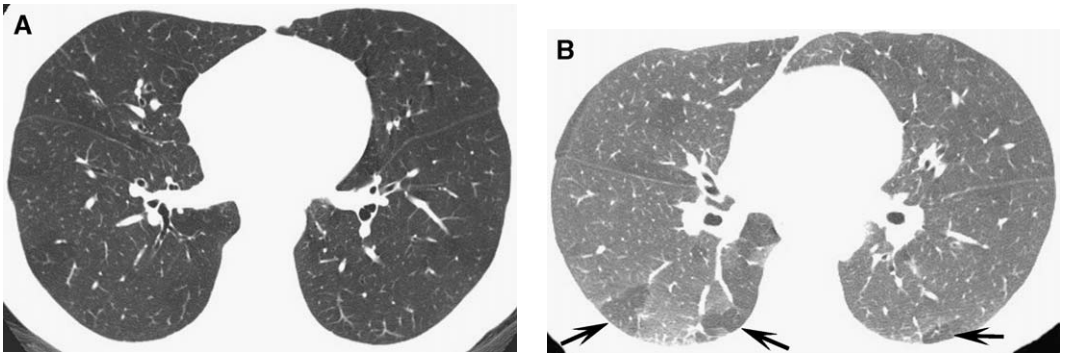

Fig. 40. Air trapping on expiratory imaging in the absence of inspiratory scan findings in a patient with bronchiolitis obliterans. (*A*) Axial inspiratory image through the lower lobes shows no clear evidence of inhomogeneous lung opacity. (*B*) Axial expiratory image shows abnormal low attenuation (*arrows*) caused by air trapping, representing failure of the expected increase in lung attenuation that should normally occur with expiratory imaging.

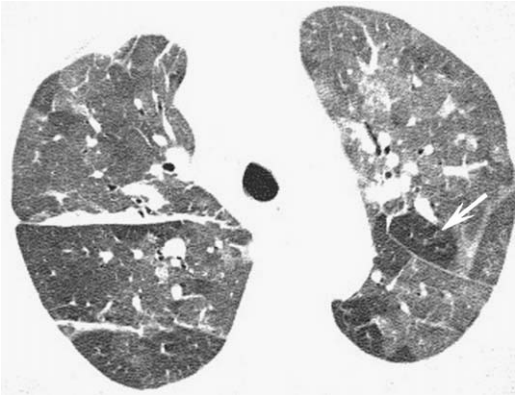

Fig. 41. Mixed infiltrative and obstructive pathology affecting the lung: the head-cheese sign. Axial HRCT image in a patient with hypersensitivity pneumonitis shows a combination of ground-glass opacity, normal lung, and mosaic perfusion (*arrow*) on the same inspiratory image.

[55]. The small size of the vessels within areas of mosaic perfusion reflects the diminished blood flow within these areas of lung. The presence of lobular low attenuation, in which the outlines of individual secondary pulmonary lobules may be recognized, also favors the presence of mosaic perfusion over ground-glass opacity (Fig. 38) [56]. Lobular low attenuation is encountered when the small lobular bronchioles are diseased.

Once mosaic perfusion is diagnosed, airway and vascular pathologies must then be distinguished; this may be accomplished with expiratory imaging [55,57]. When the cause of mosaic perfusion is vascular, the inhomogeneous opacity seen on the inspiratory image remains roughly similar on the expiratory image. When the cause of the mosaic perfusion on the inspiratory image is related to bronchiolitis, however, the appearance of the inhomogeneous lung opacity is accentuated (Fig. 39) [55,58]. This occurs because lung parenchymal attenuation increases with expiratory imaging as air within the lung is exhaled. For vascular causes of mosaic perfusion, air trapping is not present and all areas of lung increase in attenuation in a similar fashion. With airway causes of inhomogeneous opacity, however, air trapping impedes the escape of air from some areas of lung, whereas other areas decompress normally. This results in an accentuation of the inhomogeneous opacity with expiratory imaging. As a general rule, small airway causes of mosaic perfusion are far more common than vascular etiologies [57,58].

Normal inspiratory scans with air trapping on expiratory imaging

Most patients with air trapping seen on expiratory scans have inspiratory scan abnormalities, such as bronchiectasis, mosaic perfusion, airway thickening, or nodules with or without tree-in-bud that suggest the proper differential diagnosis. Occasionally, air

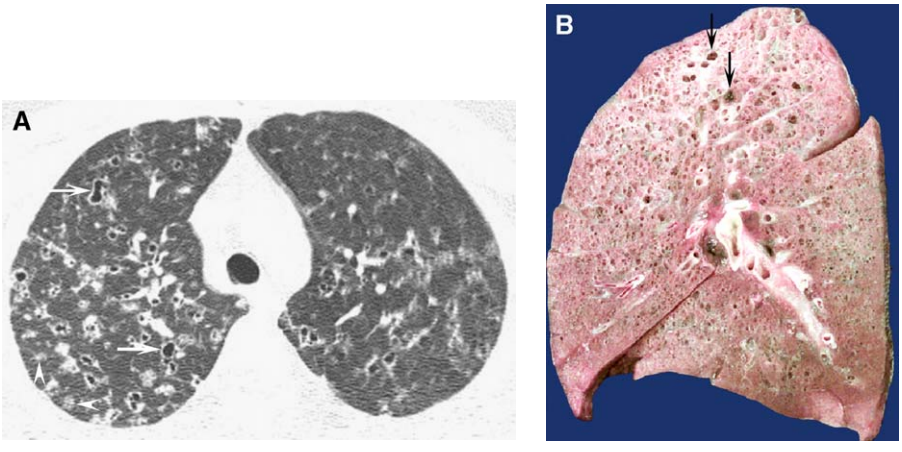

Fig. 42. Cystic pulmonary disease: Langerhans' cell histiocytosis. (*A*) Axial HRCT image through the upper lobes shows multiple bilateral bizarre-shaped cysts (*arrows*) and small centrilobular nodules (*arrowheads*) in a smoker with Langerhans' cell histiocytosis. (*B*) Gross pathologic specimen demonstrating the cysts (*arrows*). Note the upper lobe predominance of the cysts.

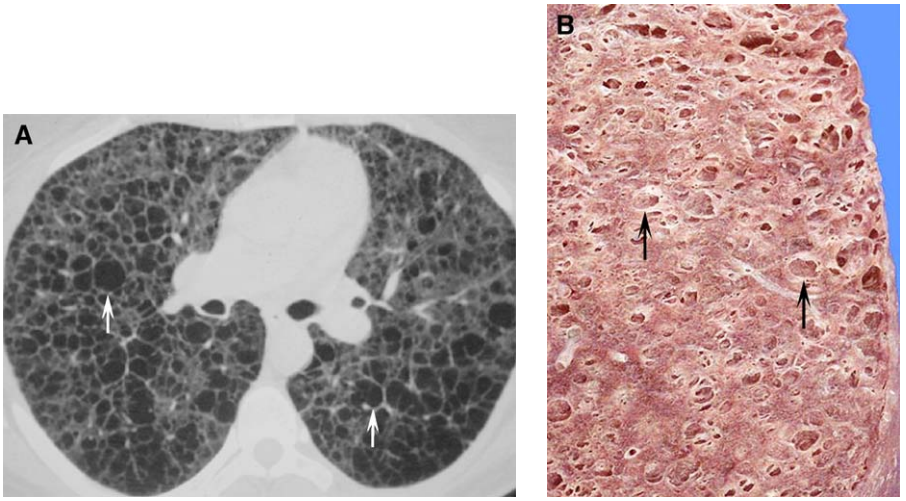

Fig. 43. Cystic pulmonary disease: lymphangioleiomyomatosis. (*A*) Axial HRCT image through the upper lobes shows multiple bilateral uniform, thin-walled cysts (*arrows*). (*B*) Gross pathologic specimen demonstrating the cysts (*arrows*).

trapping may be the sole abnormal finding on an HRCT study; the inspiratory scan is normal (Fig. 40) [57]. In this situation, expiratory HRCT techniques are valuable for demonstrating the presence of an underlying airway abnormality. This circumstance may reflect less extensive physiologic derangements than conditions in which abnormalities are visible on the inspiratory images. The differential diagnosis of this air trapping on expiratory imaging in the presence of normal inspiratory scan findings includes constrictive bronchiolitis (bronchiolitis obliterans); asthma; chronic bronchitis; and hypersensitivity pneumonitis [57].

The "head-cheese" sign

The head-cheese sign represents the simultaneous presence of ground-glass opacity, normal lung, and mosaic perfusion on inspiratory HRCT images (Fig. 41). This finding is produced by mixed infiltrative and obstructive diseases, and carries the name "head-cheese sign" because of its resemblance to the variegated appearance of sausage made from the parts of the head of a hog [59]. The differential diagnosis of this observation includes hypersensitivity pneumonitis (especially chronic disease); sarcoidosis; and atypical infections (eg, *Mycoplasma pneumoniae*). Respiratory bronchiolitis–interstitial lung disease may also produce this sign.

Cystic lung diseases

Lung diseases characterized by cysts include Langerhans' cell histiocytosis (Fig. 42), lymphangioleiomyomatosis (Fig. 43), lymphocytic interstitial pneumonia (Fig. 44), postinfectious pneumatoceles, and amyloidosis (Table 8). Recently, lung cysts have

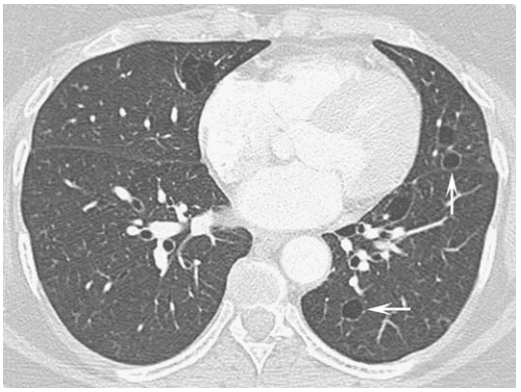

Fig. 44. Cystic pulmonary disease: lymphocytic interstitial pneumonia. Axial HRCT image through the lower lobes shows multiple thin-walled cysts (*arrows*) in a patient with Sjögren's syndrome.

Table 8
Cystic lung diseases: distinguishing features on high-resolution CT

Disease	Clinical	HRCT features
Langerhans' cell histiocytosis	Smoker	Upper lobe predominance Centrilobular nodules Bizarre-shaped cysts
Lymphangioleiomyomatosis	Women of childbearing age	Diffuse distribution Pleural effusion Uniformly shaped cysts
Lymphocytic interstitial pneumonia	Connective tissue disorders (especially Sjögren's syndrome)	Cyst size range: 1–30 mm Septal thickening Centrilobular nodules
Postinfectious pneumatoceles	Children with *Staphylococcus aureus* pneumonia Severely immunocompromised patients (AIDS, *Pneumocystis jiroveci* pneumonia Infection in endemic region (coccidioidomycosis)	Cyst evolves with bronchopneumonia Multifocal ground-glass opacity, pneumothorax Cyst evolves from a nodule

been reported in association with hypersensitivity pneumonitis [60]. The various features on HRCT that allow these disorders to be distinguished are outlined in Table 8.

Summary

HRCT is a very powerful tool in the assessment of patients with diffuse lung disease. Complete appreciation of the diagnostic capabilities of HRCT requires a firm understanding of pulmonary anatomy, particularly the anatomic arrangement of the secondary pulmonary nodule, and the technical factors required for optimal HRCT imaging. With such knowledge, abnormalities on HRCT may be effectively approached by using an organized, algorithmic method. Rigorous application of an ordered, pattern approach to HRCT abnormalities allows for reproducible and accurate interpretation.

References

[1] Webb WR, Müller NL, Naidich DP. High-resolution CT of the lung. Philadelphia: Lippincott Williams and Wilkins; 2001.
[2] Webb WR, Stein MG, Finkbeiner WE, et al. Normal and diseased isolated lungs: high-resolution CT. Radiology 1988;166:81–7.
[3] Murata K, Itoh H, Todo G, et al. Centrilobular lesions of the lung: demonstration by high-resolution CT and pathologic correlation. Radiology 1986;161:641–5.
[4] Mayo JR, Webb WR, Gould R, et al. High-resolution CT of the lungs: an optimal approach. Radiology 1987; 163:507–10.
[5] Majurin ML, Varpula M, Kurki T, et al. High-resolution CT of the lung in asbestos-exposed subjects: comparison of low-dose and high-dose HRCT. Acta Radiol 1994;35:473–7.
[6] Lucaya J, Piqueras J, Garcia-Pena P, et al. Low-dose high-resolution CT of the chest in children and young adults: dose, cooperation, artifact incidence, and image quality. AJR Am J Roentgenol 2000;175: 985–92.
[7] Cassese JA, Brody AS, Thomas SR. Utility of simple radiation dose measurements in the evaluation of different CT scanners used for high-resolution CT. J Thorac Imaging 2003;18:242–5.
[8] Mayo JR, Jackson SA, Muller NL. High-resolution CT of the chest: radiation dose. AJR Am J Roentgenol 1993;160:479–81.
[9] Mayo JR, Aldrich J, Muller NL. Radiation exposure at chest CT: a statement of the Fleischner Society. Radiology 2003;228:15–21.
[10] Naidich DP, Marshall CH, Gribbin C, et al. Low-dose CT of the lungs: preliminary observations. Radiology 1990;175:729–31.
[11] Zwirewich CV, Mayo JR, Muller NL. Low-dose high-resolution CT of lung parenchyma. Radiology 1991; 180:413–7.
[12] Volpe J, Storto ML, Lee K, et al. High-resolution CT of the lung: determination of the usefulness of CT scans obtained with the patient prone based on plain radiographic findings. AJR Am J Roentgenol 1997;169: 369–74.
[13] Aberle DR, Gamsu G, Ray CS, et al. Asbestos-related pleural and parenchymal fibrosis: detection with high-resolution CT. Radiology 1988;166:729–34.

[14] Aberle DR, Gamsu G, Ray CS. High-resolution CT of benign asbestos-related diseases: clinical and radiographic correlation. AJR Am J Roentgenol 1988;151: 883–91.
[15] Stern EJ, Frank MS. Small-airway diseases of the lungs: findings at expiratory CT. AJR Am J Roentgenol 1994;163:37–41.
[16] Franquet T, Stern EJ, Gimenez A, et al. Lateral decubitus CT: a useful adjunct to standard inspiratory-expiratory CT for the detection of air-trapping. AJR Am J Roentgenol 2000;174:528–30.
[17] Stern EJ, Webb WR, Gamsu G. Dynamic quantitative computed tomography: a predictor of pulmonary function in obstructive lung diseases. Invest Radiol 1994;29:564–9.
[18] Stern EJ, Webb WR. Dynamic imaging of lung morphology with ultrafast high-resolution computed tomography. J Thorac Imaging 1993;8:273–82.
[19] Gotway MB, Lee ES, Reddy GP, et al. Low-dose, dynamic, expiratory thin-section CT of the lungs using a spiral CT scanner. J Thorac Imaging 2000;15:168–72.
[20] Engeler CE, Tashjian JH, Engeler CM, et al. Volumetric high-resolution CT in the diagnosis of interstitial lung disease and bronchiectasis: diagnostic accuracy and radiation dose. AJR Am J Roentgenol 1994;163:31–5.
[21] Vock P, Soucek M. Spiral computed tomography in the assessment of focal and diffuse lung disease. J Thorac Imaging 1993;8:283–90.
[22] Kalender WA, Seissler W, Klotz E, et al. Spiral volumetric CT with single-breath-hold technique, continuous transport, and continuous scanner rotation. Radiology 1990;176:181–3.
[23] Yi CA, Lee KS, Kim TS, et al. Multidetector CT of bronchiectasis: effect of radiation dose on image quality. AJR Am J Roentgenol 2003;181:501–5.
[24] Johkoh T, Muller NL, Nakamura H. Multidetector spiral high-resolution computed tomography of the lungs: distribution of findings on coronal image reconstructions. J Thorac Imaging 2002;17:291–305.
[25] Nishino M, Kuroki M, Boiselle PM, et al. Coronal reformations of volumetric expiratory high-resolution CT of the lung. AJR Am J Roentgenol 2004;182: 979–82.
[26] Nishino M, Boiselle PM, Copeland JF, et al. Value of volumetric data acquisition in expiratory high-resolution computed tomography of the lung. J Comput Assist Tomogr 2004;28:209–14.
[27] Kelly DM, Hasegawa I, Borders R, et al. High-resolution CT using MDCT: comparison of degree of motion artifact between volumetric and axial methods. AJR Am J Roentgenol 2004;182:757–9.
[28] Chooi WK, Morcos SK. High resolution volume imaging of airways and lung parenchyma with multislice CT. Br J Radiol 2004;77(Suppl 1):S98–105.
[29] Grenier P, Valeyre D, Cluzel P, et al. Chronic diffuse interstitial lung disease: diagnostic value of chest radiography and high-resolution CT. Radiology 1991; 179:123–32.
[30] Colby TV, Swensen SJ. Anatomic distribution and histopathologic patterns in diffuse lung disease: correlation with HRCT. J Thorac Imaging 1996;11:1–26.
[31] Collins J, Blankenbaker D, Stern EJ. CT patterns of bronchiolar disease: what is "tree-in-bud"? AJR Am J Roentgenol 1998;171:365–70.
[32] Akira M, Kitatani F, Lee YS, et al. Diffuse panbronchiolitis: evaluation with high-resolution CT. Radiology 1988;168:433–8.
[33] Im JG, Itoh H, Shim YS, et al. Pulmonary tuberculosis: CT findings—early active disease and sequential change with antituberculous therapy. Radiology 1993; 186:653–60.
[34] Gruden JF, Webb WR, Naidich DP, et al. Multinodular disease: anatomic localization at thin-section CT—multireader evaluation of a simple algorithm. Radiology 1999;210:711–20.
[35] Nishimura K, Kitaichi M, Izumi T, et al. Usual interstitial pneumonia: histologic correlation with high-resolution CT. Radiology 1992;182:337–42.
[36] Park JS, Lee KS, Kim JS, et al. Nonspecific interstitial pneumonia with fibrosis: radiographic and CT findings in seven patients. Radiology 1995;195: 645–8.
[37] Johkoh T, Muller NL, Colby TV, et al. Nonspecific interstitial pneumonia: correlation between thin-section CT findings and pathologic subgroups in 55 patients. Radiology 2002;225:199–204.
[38] Kim TS, Lee KS, Chung MP, et al. Nonspecific interstitial pneumonia with fibrosis: high-resolution CT and pathologic findings. AJR Am J Roentgenol 1998;171:1645–50.
[39] Kim E, Lee KS, Chung MP, et al. Nonspecific interstitial pneumonia with fibrosis: serial high-resolution CT findings with functional correlation. Am J Roentgenol 1999;173:949–53.
[40] Remy-Jardin M, Giraud F, Remy J, et al. Importance of ground-glass attenuation in chronic diffuse infiltrative lung disease: pathologic-CT correlation. Radiology 1993;189:693–8.
[41] Leung AN, Miller RR, Muller NL. Parenchymal opacification in chronic infiltrative lung diseases: CT-pathologic correlation. Radiology 1993;188:209–14.
[42] Lynch DA. Ground glass attenuation on CT in patients with idiopathic pulmonary fibrosis [editorial, comment]. Chest 1996;110:312–3.
[43] Lynch DA, Newell J, Hale V, et al. Correlation of CT findings with clinical evaluations in 261 patients with symptomatic bronchiectasis. AJR Am J Roentgenol 1999;173:53–8.
[44] Reiff DB, Wells AU, Carr DH, et al. CT findings in bronchiectasis: limited value in distinguishing between idiopathic and specific types. AJR Am J Roentgenol 1995;165:261–7.
[45] Ward S, Heyneman L, Lee MJ, et al. Accuracy of CT in the diagnosis of allergic bronchopulmonary aspergillosis in asthmatic patients. AJR Am J Roentgenol 1999;173:937–42.
[46] Lee PH, Carr DH, Rubens MB, et al. Accuracy of CT

in predicting the cause of bronchiectasis. Clin Radiol 1995;50:839–41.
[47] Cartier Y, Kavanagh PV, Johkoh T, et al. Bronchiectasis: accuracy of high-resolution CT in the differentiation of specific diseases. AJR Am J Roentgenol 1999;173:47–52.
[48] Snider GL. Pathogenesis and terminology of emphysema. Am J Respir Crit Care Med 1994;149:1382–3.
[49] Thurlbeck WM, Muller NL. Emphysema: definition, imaging, and quantification. AJR Am J Roentgenol 1994;163:1017–25.
[50] King MA, Stone JA, Diaz PT, et al. Alpha 1-antitrypsin deficiency: evaluation of bronchiectasis with CT. Radiology 1996;199:137–41.
[51] Thurlbeck WM. Chronic airflow obstruction in lung disease. Philadelphia: WB Saunders; 1978.
[52] Hunninghake GW, Zimmerman MB, Schwartz DA, et al. Utility of a lung biopsy for the diagnosis of idiopathic pulmonary fibrosis. Am J Respir Crit Care Med 2001;164:193–6.
[53] Hunninghake GW, Lynch DA, Galvin JR, et al. Radiologic findings are strongly associated with a pathologic diagnosis of usual interstitial pneumonia. Chest 2003;124:1215–23.
[54] Flaherty KR, Toews GB, Travis WD, et al. Clinical significance of histological classification of idiopathic interstitial pneumonia. Eur Respir J 2002;19:275–83.
[55] Worthy SA, Muller NL, Hartman TE, et al. Mosaic attenuation pattern on thin-section CT scans of the lung: differentiation among infiltrative lung, airway, and vascular diseases as a cause. Radiology 1997;205:465–70.
[56] Im JG, Kim SH, Chung MJ, et al. Lobular low attenuation of the lung parenchyma on CT: evaluation of forty-eight patients. J Comput Assist Tomogr 1996;20:756–62.
[57] Arakawa H, Webb WR. Air trapping on expiratory high-resolution CT scans in the absence of inspiratory scan abnormalities: correlation with pulmonary function tests and differential diagnosis. AJR Am J Roentgenol 1998;170:1349–53.
[58] Arakawa H, Webb WR, McCowin M, et al. Inhomogeneous lung attenuation at thin-section CT: diagnostic value of expiratory scans. Radiology 1998;206:89–94.
[59] Chung MH, Edinburgh KJ, Webb EM, et al. Mixed infiltrative and obstructive disease on high-resolution CT: differential diagnosis and functional correlates in a consecutive series. J Thorac Imaging 2001;16:69–75.
[60] Franquet T, Hansell DM, Senbanjo T, et al. Lung cysts in subacute hypersensitivity pneumonitis. J Comput Assist Tomogr 2003;27:475–8.
[61] Johkoh T, Muller NL, Taniguchi H, et al. Acute interstitial pneumonia: thin-section CT findings in 36 patients. Radiology 1999;211:859–63.
[62] Johkoh T, Muller NL, Cartier Y, et al. Idiopathic interstitial pneumonias: diagnostic accuracy of thin-section CT in 129 patients. Radiology 1999;211:555–60.
[63] Lynch DA, Newell JD, Logan PM, et al. Can CT distinguish hypersensitivity pneumonitis from idiopathic pulmonary fibrosis? AJR Am J Roentgenol 1995;165:807–11.
[64] Desai SR, Wells AU, Rubens MB, et al. Acute respiratory distress syndrome: CT abnormalities at long-term follow-up. Radiology 1999;210:29–35.

ELSEVIER
SAUNDERS

Radiol Clin N Am 43 (2005) 571 – 588

RADIOLOGIC
CLINICS
of North America

Radionuclide Imaging of Thoracic Malignancies

Stanley J. Goldsmith, MD[a,b,*], Lale A. Kostakoglu, MD[a,b],
Serge Somrov, MD[b], Christopher J. Palestro, MD[c,d]

[a]*Weill Medical College, Cornell University, 1300 York Avenue, New York, NY 10021, USA*
[b]*Division of Nuclear Medicine, New York Presbyterian Hospital–Weill Cornell Medical Center, 525 East 68th Street, New York, NY 10021, USA*
[c]*Albert Einstein College of Medicine, Yeshiva University, 1300 Morris Park Avenue, Bronx, NY 10461, USA*
[d]*Division of Nuclear Medicine, Long Island Jewish Medical Center, 270-05 76th Avenue, New Hyde Park, NY 11040, USA*

Thoracic masses are usually detected by chest radiograph or CT during a screening procedure, as part of a routine physical examination, or in the evaluation of some symptom or sign referable to the thoracic structures such as chest pain, cough, hemoptysis, wheezing, or dyspnea. The most common malignant tumor of the thorax is carcinoma of the lung, specifically the non–small-cell type, which includes adenocarcinoma and squamous cell carcinoma. Other masses requiring different management are also encountered, including small-cell lung carcinoma; bronchial carcinoid (benign and malignant); mediastinal masses, including thymoma, teratomas, lymphomas, and mestastases from carcinomas such as breast, colon, head and neck tumors, thyroid carcinoma, and choriocarcinoma. In addition, carcinoma of the lung might be present as a second primary in patients known to have one of these other malignancies.

Traditionally, when a pulmonary mass has been identified a decision must be made regarding whether to perform a biopsy or surgical resection to characterize the lesion as a neoplasm versus granuloma or other inflammatory lesion and to determine a suitable course of management. In some instances surgical intervention is deferred and the lesion is reevaluated over time. Both approaches carry the risk of performing unnecessary surgery with the potential attendant morbidity or delaying evaluation with the associated risk of disease progression. This approach to management of the patient who has a thoracic lesion is rapidly changing with the development of nuclear medical imaging procedures that are capable of characterizing lesions according to their molecular biology. Radionuclide imaging is based on tissue or tumor function, metabolism, or other biochemical characteristics that provide information that is complementary to traditional diagnostic imaging techniques in terms of assessing if a lesion is malignant or not, and if malignant, determining the extent of disease.

In recent years radionuclide imaging has made great progress as a consequence of the development of novel radiolabeled compounds, which identify specific molecular processes and remarkable advances in the instrumentation used for acquisition and display. Nuclear medicine imaging has progressed to the point where it can provide crucial information about lesion biology and can thus play an integral part in the evaluation and management of the patient who has a suspected or known pulmonary malignancy, including noninvasive characterization of the solitary pulmonary nodule, assessment of the extent of disease in the patient who has a known malignancy, planning and optimizing radiation therapy, monitoring the response to treatment, and even

This article originally published in *Thoracic Surgery Clinics* 2004;14(1):95–112.

* Corresponding author. Division of Nuclear Medicine, New York Presbyterian Hospital, Weill Cornell Medical Center, 525 East 68th Street, New York, NY 10021.

E-mail address: sjg2002@med.cornell.edu (S.J. Goldsmith).

0033-8389/05/$ – see front matter © 2005 Elsevier Inc. All rights reserved.
doi:10.1016/j.rcl.2005.03.003

predicting prognosis. State-of-the-art nuclear medicine imaging is clinically efficacious and cost-effective, leading to more accurate diagnoses at less risk and lower cost to the patient and to society.

Technical advances

Nuclear medicine instrumentation

Nuclear medicine images, or scintigraphs, are generated by the external detection of emissions from radioactive isotopes that localize in certain tissues, organs, physiologic or pathophysiologic processes, or lesions. In the past, conventional nuclear medicine images were so-called planar images; data were recorded in multiple views: anterior, posterior, lateral, and oblique. Each image compressed the data obtained from the volume image into two dimensions, resulting in the loss of object contrast caused by the presence of background radioactivity (ie, radioactivity surrounding the object of interest). More recently, nuclear medicine has evolved toward tomographic imaging. In recent years clinicians and radiologists have become familiar with tomographic images as a result of the broad application of CT and, more recently, MRI (ie, transaxial slice images derived from reconstructed transmission data). Data are recorded in 360° geometry around the patient. Initially, backprojection techniques were used to create transverse, or transaxial, images (slices) that revealed the distribution of radioactivity, or, in the case of CT, absorption coefficient maps. Tomographic imaging is a more accurate representation of the actual distribution of radioactivity in a patient and results in improved image detail. Tomographic radionuclide imaging can be performed with single-photon or positron-emitting radionuclides.

Single-photon emission CT (SPECT) is the tomographic imaging technology employed with traditional radionuclides such as technetium-99m (^{99}Tc), gallium-67 (^{67}Ga), and thallium-201 (^{201}Tl). SPECT uses traditional collimated gamma camera positioning logic. Data are obtained at small angular intervals as the camera revolves around the patient. A gamma camera with a single detector must acquire data over 360°, whereas a device with two or three detector units requires that each head orbit only a fraction of the full circumference. Multihead systems permit greater data acquisition over a shorter period of time with a resultant improvement in image quality. Data acquired by the gamma camera are reconstructed into transaxial planes using sophisticated processing algorithms such as filtered backprojection and iterative reconstruction. In addition to the transaxial images, images from the coronal and sagittal planes are reconstructed readily. Modern computer capacity also makes it feasible to view three-dimensional, or volume, images.

Positron emission tomography (PET) is based upon the unique decay characteristics of positrons. A positron undergoes annihilation by combining with a negatively charged electron. As a result of this annihilation, two 511 keV gamma rays are emitted 180° apart. Special electronics determine if two recorded events are coincident, thus identifying the axis along which the two photons were emitted, which provides a significant advantage in terms of reconstructing the position of an event and allowing for the elimination of cumbersome lead collimators. In contrast to SPECT, in which single events are detected, PET makes use of two detector elements on opposite sides of the subject to detect coincident photons arising from the annihilation of a positron and electron. Most PET radiopharmaceuticals have short half-lives; consequently, until just a few years ago PET imaging was limited to centers that had cyclotron production facilities. After numerous investigational studies confirmed the value and cost-effectiveness of PET imaging with fluorine-18-fluorodeoxyglucose ([^{18}F]-FDG) in the management of patients who have tumors, third-party insurers and eventually governmental agencies approved the technique for reimbursement. Despite its short (2-hour) half-life, [^{18}F]-FDG is now available from commercial sources in most of the United States.

Until recently, PET imaging devices cost more than $1 million and were available only at larger centers. The contribution of this technology to patient management, however, has been so significant that this situation is changing rapidly. The increased clinical demand for these studies has stimulated development of less costly instrumentation, and a spectrum of devices is now available including a $250,000 to $350,000 upgrade of conventional dual detector gamma camera systems, a 360° simultaneous acquisition imaging system that uses six large curvilinear sodium iodide crystals (costing approximately $1.3–$1.5 million), and bismuth germanate multicrystal, multiring systems (costing $1.7–$2.3 million).

Using a phantom in an experimental comparison of a gamma camera-based coincidence imaging system with a dedicated ring detector PET system, the dedicated PET system identified nodules as small as 6 mm in diameter, whereas the camera-based system resolved 1 cm and larger lesions [1]. There has been no direct comparison between imaging with the dedicated ring system and the less expensive

devices in the clinical milieu. A meta-analysis published in 2001 found that the performance of the camera-based system was comparable to that of dedicated PET in the evaluation of lung nodules in patients who had lesions greater than 1 cm in diameter [2]. Lesions as small as 7 mm in diameter can be detected on the dual detector coincident camera system, but overall image quality and lesion detection on a dedicated high-end system are significantly better. The ability to detect a lesion based upon the resolution and sensitivity of the systems. In this regard the dedicated ring systems will regularly outperform (ie, show improved detection) dual detector systems even though coincident dual detector camera-based systems' imaging of [^{18}F]-FDG are frequently useful to characterize lesions greater than 1 cm.

In summary, the dedicated ring detector systems represent the state-of-the-art in PET imaging with greater sensitivity for lesion detection. Nevertheless, dual detector camera-based systems provide access to [^{18}F]-FDG imaging, and the positive predictive value is probably equivalent to that of the more expensive system. The negative predictive value of the dual detector system is likely to be somewhat less than that of the dedicated system because small lesions will not be detected as a result of volume averaging and reduced sensitivity.

As with most nuclear studies, PET images suffer from a paucity of anatomic detail. To maximize the accuracy of their interpretation, they should be read together with anatomic cross-sectional studies such as CT and MR, which has been accomplished by viewing the studies side-by-side on viewboxes or computer monitors or through the use of fusion software that allows direct superimposition of the images. Recently, instruments have been engineered that acquire PET and CT images. Patients undergo sequential PET and CT studies on the same instrument during the same imaging session. Fused PET and CT images and PET and CT images alone can be viewed on a slice-by-slice basis. Though costly and still new, these devices have already demonstrated that they have advantages in terms of accuracy and confidence in interpretation, and they are likely to eventually replace PET-only and CT-only devices [3].

Radionuclides

In the past, nuclear medicine assessed thoracic masses with ^{67}Ga citrate and, more recently, with ^{201}Tl and ^{99m}Tc-MIBI [4,5]. ^{67}Ga scintigraphy is positive in inflammatory and neoplastic lesions. Despite this degree of nonspecificity, the technique was useful but limited in application because of the comparatively poor resolution achieved with this radionuclide. Tumor localization of ^{201}Tl and ^{99m}Tc-MIBI is a consequence of perfusion and rapid extraction of these tracers from tumor tissue. ^{99m}Tc-MIBI has the advantage of greater photon flux than ^{201}Tl because a larger dose can be given because of the shorter (6-hour) half-life. The 140 keV photon energy is more suitable for imaging than the lower energy photons of ^{201}Tl. Furthermore, ^{99m}Tc-MIBI binds to intracellular elements, providing improved target to background ratios.

These techniques, however, provide limited improvement over CT or MR imaging in terms of detection of disease. ^{99m}Tc-MIBI could also be used to characterize tumor multiple-drug resistance by examining the retention or washout of ^{99m}Tc-MIBI over time because ^{99m}Tc-MIBI is eliminated from tissue by the same p51 glycoprotein multiple drug resistance (MDR) mechanism [6].

Any historical review should include iodine-13I (^{131}I), which is used to detect metastases from thyroid carcinoma—even in patients who have a negative chest radiograph or CT examination (Fig. 1). Thyroid carcinoma frequently has a subtle micronodular appearance, although it might occasionally appear as single or multiple nodules. It is important to correctly identify lung metastases from thyroid carcinoma because they respond to radionuclide therapy with ^{131}I.

Radiolabeled peptides

Radiolabeled compounds that bind to receptors present in normal and abnormal tissues form the basis of receptor imaging. Tumor expressing receptors can be visualized with radiolabeled antibodies or radiolabeled messenger molecules. To date, the most successful of these agents has been radiolabeled analogs of regulatory peptides. Regulatory peptides are small, easily diffuseable, naturally occurring substances that possess a wide spectrum of receptor-mediated actions. High-affinity receptors for these peptides are present on many neoplasms. These receptors offer molecular targets for diagnosis and therapy [7]. Currently, two radiolabeled peptides, Octreoscan (Mallinkrodt, St. Louis, Missouri) and Neotect (Diatide, Londonderry, New Hampshire), both of which are somatostatin analogs, are approved for diagnostic use in the United States.

Somatostatin is an endogenous neuropeptide that exists in two forms: a 14 amino acid form and a 28 amino acid form. It is synthesized in the central nervous system, the hypothalamopituitary axis, the gastrointestinal tract, the pancreas, and the immune system. Somatostatin receptors, of which there are

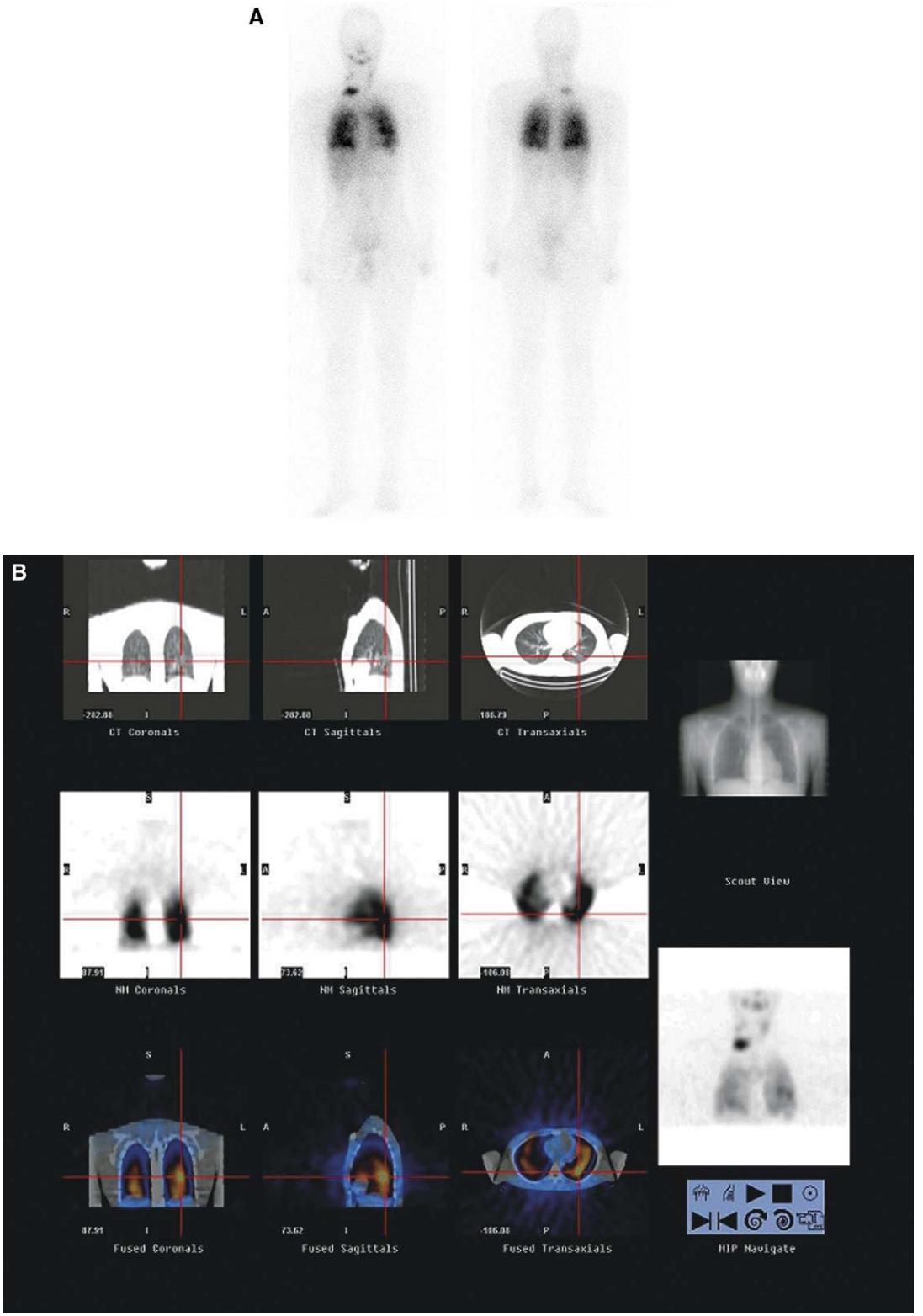
A
B
CT Coronals
CT Sagittals
CT Transaxials
Scout View
NM Coronals
NM Sagittals
NM Transaxials
Fused Coronals
Fused Sagittals
Fused Transaxials
MIP Navigate

five subtypes, are present on many cells, particularly those of neuroendocrine origin. These receptors have also been identified on activated lymphocytes and the vasa recta of the kidney. All five receptor subtypes bind to naturally occurring somatostatin with nearly identical affinity [8,9].

In addition to their presence on normal tissues, somatostatin receptors are expressed on a wide variety of human tumors. Three main groups of tumors have been identified as having the highest density of somatostatin receptors. Neuroendocrine tumors, including islet cell tumors, gastrinomas, pheochromocytomas, paragangliomas, and carcinoid tumors are one group. Central nervous system tumors such as astrocytomas and meningiomas represent another group. The third group of tumors that possess somatostatin receptors consists of lung carcinoma (small-cell and non–small-cell), breast tumors, lymphomas, and renal cell carcinoma.

The short biologic half-life of somatostatin (~1 min) precludes its use for diagnostic or therapeutic purposes, which led to the development of synthetic somatostatin analogs that had longer biologic half-lives. Octreotide is an eight amino acid analog with a high affinity for somatostatin subtype receptors 2 and 5 but a decreased affinity for subtype 3 and no affinity for subtypes 1 and 4 [7]. Octreoscan is produced by radiolabeling diethylene tetra amine penta acetic acid (DTPA)-pentetreotide (a derivative of octreotide) with indium-111 (^{111}In) and is used to image somatostatin receptor-bearing tumors. Extensive studies in large numbers of patients have shown that somatostatin receptor scintigraphy (SRS) with ^{111}In DTPA-pentetreotide is most useful in detecting and staging neuroendocrine tumors [8–10].

In the thorax, SRS is especially useful in small-cell lung carcinoma and bronchial carcinoid. In small-cell lung carcinoma, the sensitivity of SRS is more than 90% for the primary lesion. More than half of metastatic lesions, however, lose their somatostatin receptor expression as a consequence of dedifferentiation and increasing malignancy [11]. Visualization of metastatic small-cell lung carcinoma lesions indicates that the tumor is relatively well differentiated, whereas nonvisualization is associated with dedifferentiation and a poorer prognosis. Thus, it is possible, using scintigraphic imaging, to not only localize lesions but also to determine prognosis through in vivo tissue characterization.

Bronchial carcinoid is an uncommon neoplasm, accounting for less than 5% of all lung tumors. Thought at one time to be benign, this entity is, in fact, a low-grade, slow-growing, malignant neoplasm that has the potential for local invasion and distant metastatic spread (Fig. 2). Several investigators have reported on the role of SRS in bronchial carcinoid [12–14]. In a series of 21 patients, SRS revealed all eight primary lesions at the time of diagnosis, demonstrated disease in all five patients who had recurrent or metastatic disease (including two patients who were asymptomatic at the time of imaging), and identified an increase in tumor size in two patients who had unresectable disease [13]. In a series of 31 patients who had bronchial carcinoid, six patients (nearly 20%) had lesions that were identified only on SRS. Lesions identified only with SRS included pulmonary, hepatic, and osseous. In two patients who had inconclusive CT studies, SRS correctly excluded recurrent disease. Only two pulmonary lesions, both in the same patient, which were detected with other modalities were not detected with SRS [12].

The implications of the findings in these investigations are important. Although sensitive for the detection of neuroendocrine tumors, SRS cannot be used for diagnosis because other lung tumors also express somatostatin receptors. SRS is used to guide patient management. For example, the exquisite sensitivity of SRS can determine whether or not, at the time of diagnosis, curative surgery is possible. In patients who have recurrent disease, localized surgical resection has met with some success. The ability to identify recurrent disease in asymptomatic patients suggests that SRS might be useful for identifying individuals who have recurrent disease when they are

Fig. 1. Twenty-year-old man postthyroidectomy for differentiated thyroid carcinoma was found to have a palpable mass in the right supraclavicular region. The mass was positive on diagnostic ^{131}I imaging. Following dosimetry to determine the bone marrow radiation absorbed dose, the patient received 300 mCi of ^{131}I. (*A*) Whole-body scan 1 week post ^{131}I therapy confirming ^{131}I uptake in the right supraclavicular mass and demonstrating unexpected diffuse uptake throughout both lung fields. Uptake had not been recognized on diagnostic imaging with a lower dose of ^{131}I. (*B*) SPECT images of the same patient's thorax using a dual detector system with a low-output CT device (GE Millenium Hawkeye, General Electric Medical Systems, Milwaukee, Wisconsin, USA). (*Top row*) CT images in the coronal, sagittal, and transaxial plane. (*Middle row*) ^{131}I tomographic images corresponding to CT slices. (*Bottom row*) Fused CT plus ^{131}I images. On the upper right, the scout radiograph of the chest is negative; on the lower right is the anterior rendering of the ^{131}I volume (all images summed) display. (Courtesy of Division of Nuclear Medicine, Department of Radiology, New York Presbyterian Hospital, Weill Cornell Medical Center, New York, NY.)

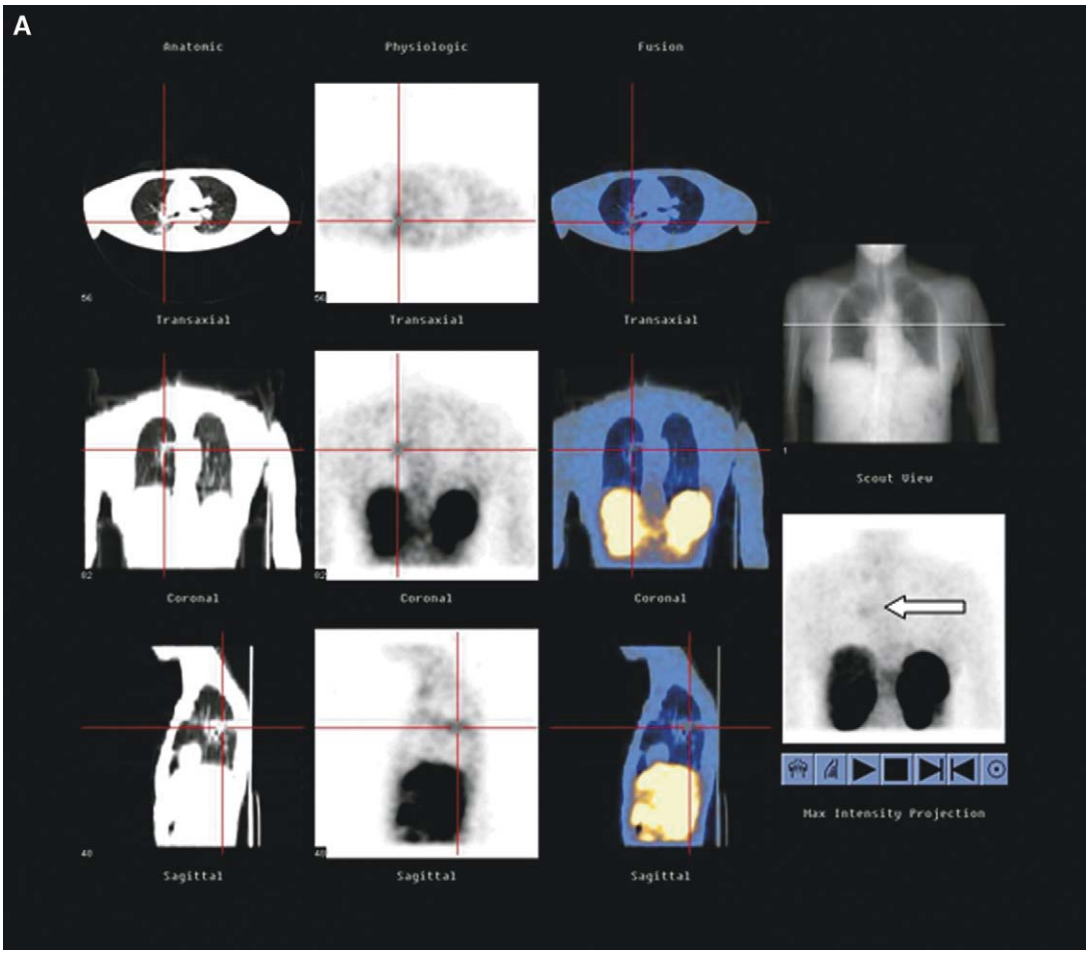
A
Anatomic
Physiologic
Fusion
Transaxial
Transaxial
Transaxial
Scout View
Coronal
Coronal
Coronal
Sagittal
Sagittal
Sagittal
Max Intensity Projection

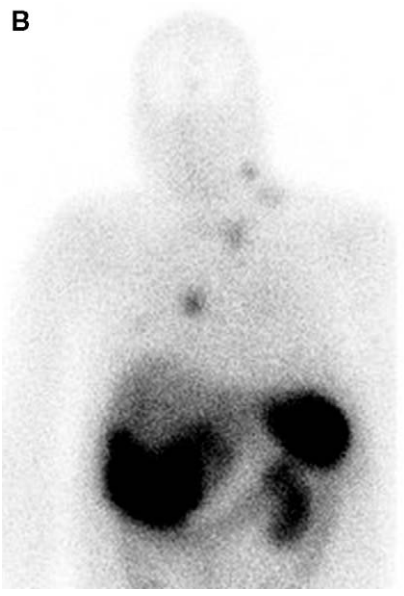
B

still amenable to surgery. This is of value to determining if metastatic disease is limited to the liver, because in some cases current surgical practice makes it possible to consider liver transplantation. Extrahepatic metastatic disease is a contraindication, however, and SRS is useful for identifying or excluding patients for this procedure. Finally, determining the presence or absence of somatostatin receptors with SRS identifies patients who are likely to respond to medical therapy.

Another radiolabeled somatostatin analog, ^{99m}Tc-depreotide (Neotect), has been developed. ^{99m}Tc-depreotide is a synthetic cyclic six amino acid peptide labeled with ^{99m}Tc is approved for the differential diagnosis of the solitary pulmonary nodule. This agent is a high-affinity ligand for human somatostatin receptor subtype 3, with in vitro characteristics that suggest it should also be useful for imaging the extent of disease in patients who have non–small-cell and small-cell lung carcinoma. In a series of 30 patients who had solitary pulmonary nodules at least 1 cm in diameter who were at high risk for lung carcinoma but had indeterminate CT criteria, the sensitivity of ^{99m}Tc-depreotide for detecting malignancy was 93% (12/13), the specificity was 88% (15/17), and the accuracy was 90% (27/30). The study was falsely negative in one patient who had squamous cell carcinoma and falsely positive in two patients who had necrotizing granulomas [15]. In a 114-patient multicenter trial, the sensitivity, specificity, and accuracy of ^{99m}Tc-depreotide was 97% (85/88), 73% (19/26), and 91% (104/114), respectively. The three false-negative lesions were adenocarcinomas; two were primary lung lesions and one was thought to be metastatic colon carcinoma. Six false-positive results were granulomatas; the seventh was a hamartoma. The data suggest that ^{99m}Tc-depreotide scintigraphy is a sensitive and accurate method for the noninvasive evaluation of the solitary lung nodule that is at least 1 cm in diameter [16].

An analysis of the cost-effectiveness of ^{99m}Tc-depreotide imaging in 114 patients who had indeterminate lung nodules found that in individuals who had a 50% probability of having a malignancy, CT alone and CT followed by ^{99m}Tc-depreotide scintigraphy showed an incremental cost-effectiveness ratio of approximately $11,200 and $8600, respectively, per year of life saved. Radiograph follow-up is only cost-effective when the probability of malignancy is less than 0.14, whereas CT alone is cost-effective when the probability of malignancy is 0.71 to 0.90. When the probability of malignancy is greater than 0.90, thoracotomy is the best choice. CT plus ^{99m}Tc-depreotide is the most cost-effective strategy, resulting in a savings of $68 to $1800 for the majority of patients, depending on the risk, when the probability of malignancy is between 0.14 and 0.71. Based on a Medicare reimbursement of approximately $900, ^{99m}Tc-depreotide imaging of pulmonary nodules that are indeterminate by CT criteria would result in an annual savings of up to $54 million compared with selecting patients for thoracotomy based on CT results alone [17]. Another beneficial aspect of this approach would be a decrease in the cost and complications of unnecessary needle biopsies.

Currently, no data are available on the accuracy of ^{99m}Tc-depreotide imaging for evaluating lesions smaller than 1 cm in diameter, nor on its role in the staging of lung carcinoma, monitoring response to therapy, or detecting recurrent disease.

Fluorodeoxyglucose

FDG is a structural analog of 2-deoxyglucose, which, like glucose, is transported into cells and phosphorylated by a hexokinase to FDG-6 phosphate. FDG accumulates intracellularly in proportion to the glycolytic rate of the cell. FDG uptake by tumor cells is also related to the presence of increased glucose transporter molecule expression at the tumor cell surface and to increased levels of hexokinase in these cells. Labeled with the positron emitter ^{18}F, FDG is useful for detecting areas of normal and abnormal glucose metabolism. Although it is filtered by the glomerulus, FDG is not reabsorbed in the proxima1 renal tubules, and the blood concentration of this compound falls quickly, providing high contrast be-

Fig. 2. (*A*) ^{111}In-DTPA-pentetreotide (Octreoscan) SPECT scintigraphy in a 67-year-old woman who had a history of pulmonary carcinoid; status right upper lobe (RUL) resection 30 months earlier with negative follow-up scans. (*Left column*) CT acquired on GE Millennium dual detector camera system with Hawkeye configuration (transaxial, coronal, and sagittal slices). (*Middle column*) Corresponding ^{111}In images. (*Right column*) Fused images. *Extreme right*: Scout radiograph and ^{111}In volume display. Note ^{111}In-DTPA-pentetreotide-positive mass in region of right hilum superimposed on superior portion of CT density. (Courtesy of Division of Nuclear Medicine, Department of Radiology, New York Presbyterian Hospital, Weill Cornell Medical Center, New York, NY.) (*B*) ^{111}In-DTPA-pentetreotide (Octreoscan) planar scintigraphy of the thorax and abdomen in a 44-year-old man who had small-cell lung carcinoma. Tumor foci are identified in the right hilar area, the left paratracheal area, and the left anterior cervical triangle. (Courtesy of Division of Nuclear Medicine, Department of Radiology, Long Island Jewish–Hillside Medical Center, New Hyde Park, NY.)

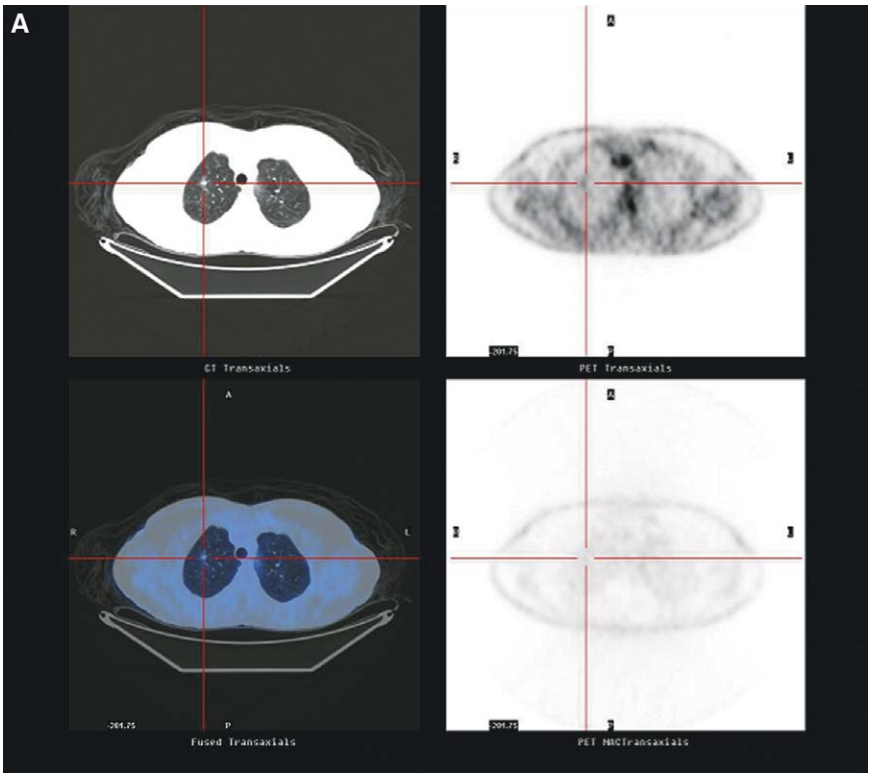
A
CT Transaxials
PET Transaxials
Fused Transaxials
PET NACTransaxials

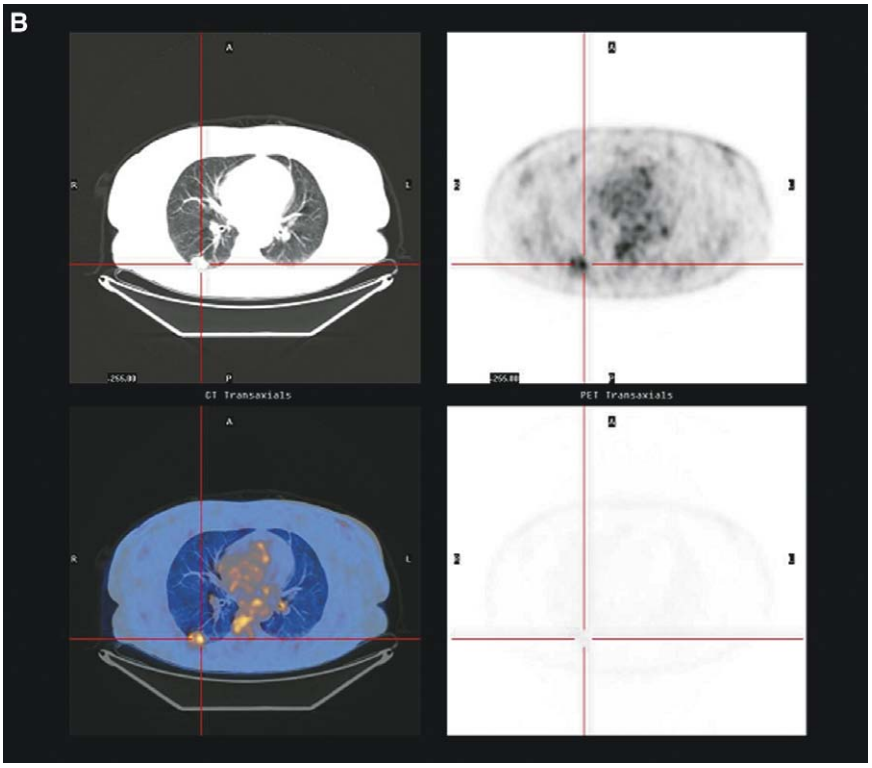
B
CT Transaxials
PET Transaxials

tween foci of increased glucose metabolism and background activity within 1 hour of injection. Many tumors are characterized by increased anaerobic glucose metabolism, and [^{18}F]-FDG provides a sensitive tool for their detection. In lung cancer, [^{18}F]-FDG-PET imaging provides important information about the diagnosis, pretreatment staging, and assessment of the effects of treatment in this entity. Its potential role in predicting prognosis is currently being assessed.

Fluorine-18-fluorodeoxyglucose–positron emission tomography and lung carcinoma

Nearly 1 million new cases of lung cancer are diagnosed annually, principally in developed nations. At the time of diagnosis, the disease has already spread to adjacent hilar or mediastinal lymph nodes in about 25% of patients, and 35% to 45% of patients have distant metastases [18,19]. A systematic approach to the diagnosis, staging, and treatment of lung cancer optimizes therapy for each individual patient.

Diagnosis

The diagnosis of lung carcinoma, as for any other tumor, is the first challenge with which the clinician is faced when presented with a patient suspected of having this entity. While morphologic imaging studies such as planar radiographs, CT, and MRI can detect a pulmonary lesion, they often cannot determine whether it is benign or malignant. Only about one third of pulmonary nodules can be diagnosed as benign or malignant on the basis of CT criteria alone. In the other two thirds, diagnosis depends on more invasive procedures such as bronchoscopy and percutaneous CT-guided transthoracic needle aspiration [20,21]. The overall sensitivity of bronchoscopy in detecting malignancy is about 65%. If transbronchial biopsy is performed, the sensitivity approaches 80% [22,23]. The sensitivity of the CT-guided procedure is greater than 90% if an adequate sample is obtained. The frequency of sampling errors depends on the size and location of the lesion and on operator expertise. The most common complication of needle biopsy is pneumothorax, which occurs in up to 10% of patients [24].

The characterization of a pulmonary nodule as benign or malignant with [^{18}F]-FDG-PET was one of the earliest oncologic applications investigated, and its value for this purpose is now well established (Fig. 3). The sensitivity and specificity of [^{18}F]-FDG-PET imaging in the evaluation of solitary lung nodules ranges from 82% to 100% and 63% to 90%, respectively [25–34]. A meta-analysis of 1474 pulmonary lesions found that the mean sensitivity and specificity of [^{18}F]-FDG-PET was 96% and 74%, respectively [2].

Several factors affect the sensitivity of [^{18}F]-FDG-PET imaging for the diagnosis of malignancy. Lesion visualization depends on the amount of [^{18}F]-FDG incorporated into the tumor. Abnormalities typically present as areas of focally increased activity, colloquially referred to as hotspots. Images can be analyzed visually and semiquantitatively. In the chest, mediastinal blood pool activity is often used as the reference point. Uptake in a lesion that is more intense than mediastinal blood pool activity is likely to be malignant, whereas activity equal to or less than mediastinal blood activity is likely to be benign. It is also possible to quantify activity by calculating the standardized uptake value (SUV), which reflects the ratio of activity per estimated tumor volume to the total activity administered to the patient, corrected for the lean body mass. Although not absolutely diagnostic, SUVs greater than 2.5 are often associated with malignancy, and malignant lesions generally have SUVs greater than 2.5. Fractional [^{18}F]-FDG uptake is affected by specific tumor metabolic activity. Consequently, tumors such as bronchioalveolar cell carcinoma and bronchial carcinoid with relatively low metabolic activity might not concentrate sufficient [^{18}F]-FDG to be identified as malignant. Nevertheless, subsets of these tumor types (bronchioalveolar carcinoma and carcinoid or other neuroendocrine tumors) might be metabolically active and identifiable as malignant on [^{18}F]-FDG imaging. Metastatic differentiated thyroid carcinoma can be positive or negative on [^{18}F]-FDG imaging

Fig. 3. (*A*) Fifty-three-year-old woman who had a recently diagnosed RUL pulmonary nodule. Patient had a 30 pack-year history of cigarette smoking. The [^{18}F]-FDG-PET images are entirely normal. The patient will continue to be followed. (*B*) Sixty-five-year-old man who had a history of an right lower lobe (RLL) solitary pulmonary nodule that had been followed since 2000. The nodule had increased in size recently. [^{18}F]-FDG-PET images demonstrate a hypermetabolic focus consistent with a malignant process. There is no evidence of regional lymph node involvement, indicating that the patient is an appropriate surgical candidate. (Courtesy of Division of Nuclear Medicine, Department of Radiology, New York Presbyterian Hospital, Weill Cornell Medical Center, New York, NY.)

depending, apparently, on the degree of biologic aggressiveness at the time of imaging. The degree of tumor aggressiveness is reflected in the metabolic rate. Although some well-differentiated adenocarcinomas might demonstrate only modest accumulation of [^{18}F]-FDG, their SUVs are nevertheless typically in the malignant range [35]. Sensitivity is also affected by lesion size. Lesions below the limits of resolution of PET scanners (currently about 4–8 mm depending upon the system hardware configuration) might not be detected [36,37]. The lesion intensity and the measured SUV will be blunted by the phenomenon known as volume averaging, in which the absolute uptake in a lesion below the spatial resolution of the system is distributed over the minimal resolution area, resulting in an apparent lowering of the activity per pixel. Sensitivity is also adversely affected by hyperglycemia. Presumably, competitive inhibition results from elevated serum glucose levels, reducing [^{18}F]-FDG uptake. In addition to this direct competitive effect, the insulin response to the glucose level is greatest in acute hyperglycemia. This response promotes muscle and hepatic uptake of glucose and [^{18}F]-FDG. Chronic hyperglycemia has a lesser effect on FDG uptake by tumors [38]. In patients who are diabetic, control of the disease should be optimized and serum glucose levels checked before injecting [^{18}F]-FDG. In general, patients who have serum glucose levels above 250 mg/dL should probably not undergo [^{18}F]-FDG imaging until serum glucose levels have been controlled.

Increased glycolysis is not unique to tumors, however; it occurs in benign conditions such as granulomas, histoplasmosis, coccidioidomycosis, and pneumonia, in which false-positive findings are observed [39–42]. Some data suggest that the specificity of the overall results can be improved by performing dual time point imaging. [^{18}F]-FDG uptake in tumor tends to increase over time, whereas inflammation tends to remain constant or decrease over time [43]. By acquiring a second set of images about 1 hour after the first set, it might be possible to distinguish [^{18}F]-FDG uptake in benign inflammatory conditions from that in tumors.

[^{18}F]-FDG-PET obviates the need for invasive biopsy in many patients who have lung nodules. To be used for this purpose, the test must have a high negative predictive value, which depends not only on sensitivity and specificity but also on the pretest likelihood of malignancy. Using decision analysis modeling, it has been shown that only patients who have a 50% or lower pretest likelihood of cancer should undergo [^{18}F]-FDG-PET imaging. If the pretest likelihood of malignancy is more than 50%, the posttest probability of disease will exceed 10% even if the [^{18}F]-FDG images are negative for one reason or another (ie, size, metabolic activity, blood glucose), and histopathologic evaluation will be necessary regardless of the [^{18}F]-FDG-PET results [44]. Because there is always the risk of a false-negative result even when the negative predictive value is high (eg, a negative [^{18}F]-FDG-PET study in a patient who has $< 50\%$ pretest probability), patients who have lung nodules and negative [^{18}F]-FDG-PET studies should undergo routine clinical and imaging follow-up every 6 to 12 months (as with other potentially malignant lesions) to monitor for any increase in the lesion size.

Staging

Pretreatment staging of non-small cell lung carcinoma (NSCLC) is necessary to assess prognosis and to determine appropriate therapy (Figs. 4–6). For example, patients who do not have mediastinal lymph node or distant metastatic disease usually undergo surgical resection of the tumor, whereas patients who have mediastinal or distant disease can undergo induction chemotherapy or radiotherapy before surgery. CT imaging is used to anatomically define the extent of the primary tumor and pleural or chest wall involvement and is superior to FDG-PET for these purposes because of its inherently better spatial resolution and delineation of normal structures and anatomic detail. CT identification of hilar and mediastinal lymph node involvement is less than optimal, however, because it depends upon lesion size. Using a size criterion of 1 cm as the threshold for identification of malignant disease leads to under- and overstaging. Normal-sized lymph nodes that are infiltrated by tumor will not be recognized, whereas lymph nodes that are enlarged secondary to benign processes will be incorrectly interpreted as containing tumor. The sensitivity, specificity, and accuracy of mediastinal staging by CT, as reported in a meta-analysis, is approximately 60%, 77%, and 65%, respectively [45]. In a prospective study, the sensitivity and specificity of CT was 52% and 69%, respectively [46]. Mediastinoscopy has, consequently, been the reference technique for mediastinal lymph node staging.

The accuracy of [^{18}F]-FDG-PET for assessment of mediastinal nodal involvement has been investigated extensively. The sensitivity and specificity of the procedure, when reported as positive or negative for the ipsilateral or contralateral side, have ranged from 67% to 92% and 86% to 97%, respectively [47–52]. When analyzed by nodal stations, the reported results

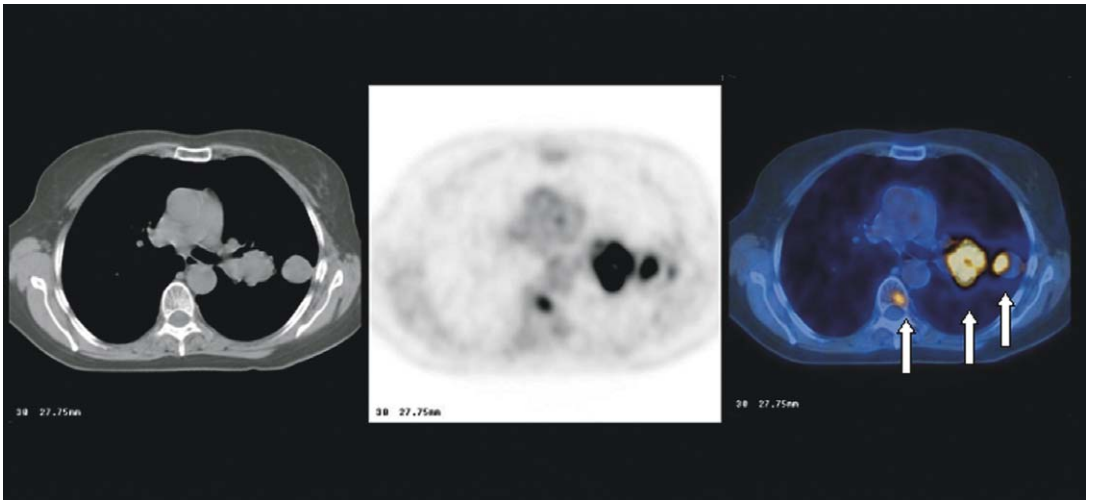

Fig. 4. Selected transaxial slice demonstrating [^{18}F]-FDG-PET images in a 68-year-old woman who smoked 1 pack of cigarettes per day for many years. She presented to her primary care physician with complaints of back pain but was otherwise in good health. A chest radiograph revealed a hilar mass and lung nodules. Transbronchial biopsy was positive for poorly differentiated non–small-cell lung carcinoma. The patient was referred for evaluation of the extent of disease. The so-called hilar mass was actually the primary lung tumor adjacent to hilar structures with a nearby second and third focus. A metastatic lesion in the vertebral body was also demonstrated. The accompanying CT image shows multiple tumor masses and evidence of a sclerotic lesion in the vertebral body (lung CT window). [^{18}F]-FDG-PET indicates the extent of viable tumor. Recently, radiation treatment plans using intensity modulated radiation therapy (IMRT) were designed to provide booster radiation doses to the well-circumscribed viable tumor defined by [^{18}F]-FDG-PET as opposed to simply delivering the prescribed dose to the entire CT defined tumor volume. (Courtesy of Jacqueline Brunetti, MD, Department of Radiology, Holy Name Hospital, Teaneck, NJ.)

are similar. A study published in 1999 compared [^{18}F]-FDG-PET and CT in 75 patients prospectively [53]. [^{18}F]-FDG-PET imaging and CT were concordant in 39 patients, correctly in 35 of the 39 patients but overstaging in two patients and understaging in two patients. The results of the two studies were discordant in 36 patients; [^{18}F]-FDG-PET was correct in 28 of these patients. Hence, [^{18}F]-FDG-PET was correct in 63 of 75 patients, whereas CT was correct in only 43 of 75 patients. In a meta-analysis of staging, the mean sensitivity and specificity of [^{18}F]-FDG-PET was 79% (± 3%) and 91% (± 2%) respectively, versus 60% (± 2%) and 77% (± 2%), respectively, for CT [45].

The anatomic–functional correlation of [^{18}F]-FDG-PET and CT images using fusion imaging (in which the two studies are obtained sequentially on the same instrument) will undoubtedly further refine the classification of patients who have nodal or mediastinal disease by separating the primary tumor from adjacent lymph nodes, differentiating hilar from adjacent mediastinal nodes, and precisely identifying the mediastinal lymph node groups involved. It is especially important to differentiate between N1 and N2 disease because the former is directly operable and the latter is not. These conclusions are based upon traditional methods of staging. The identification of N1 disease by [^{18}F]-FDG-PET at an earlier time than would have been possible with CT provides a basis for modifying surgical resection to include these positive nodes rather than to conclude that there is no nodal involvement based upon CT imaging alone.

Patients who have distant, or systemic, metastases at the time of diagnosis cannot be cured by surgery and are not likely to achieve a long-term remission. Despite the fact that the incidence of distant recurrence after complete removal of the primary tumor is at least 20%, conventional staging procedures performed at the time of diagnosis are generally unrewarding [54]. Because the diagnostic yield of anatomic imaging is low, [^{18}F]-FDG-PET offers a rapid method for whole-body imaging that identifies systemic metastatic disease effectively. [^{18}F]-FDG-PET detects distant disease in up to 15% of patients who have negative conventional staging procedures [52,55,56]. In addition to improving the detection of disease, a negative study can also exclude disease in patients who have false-positive or equivocal conventional imaging results.

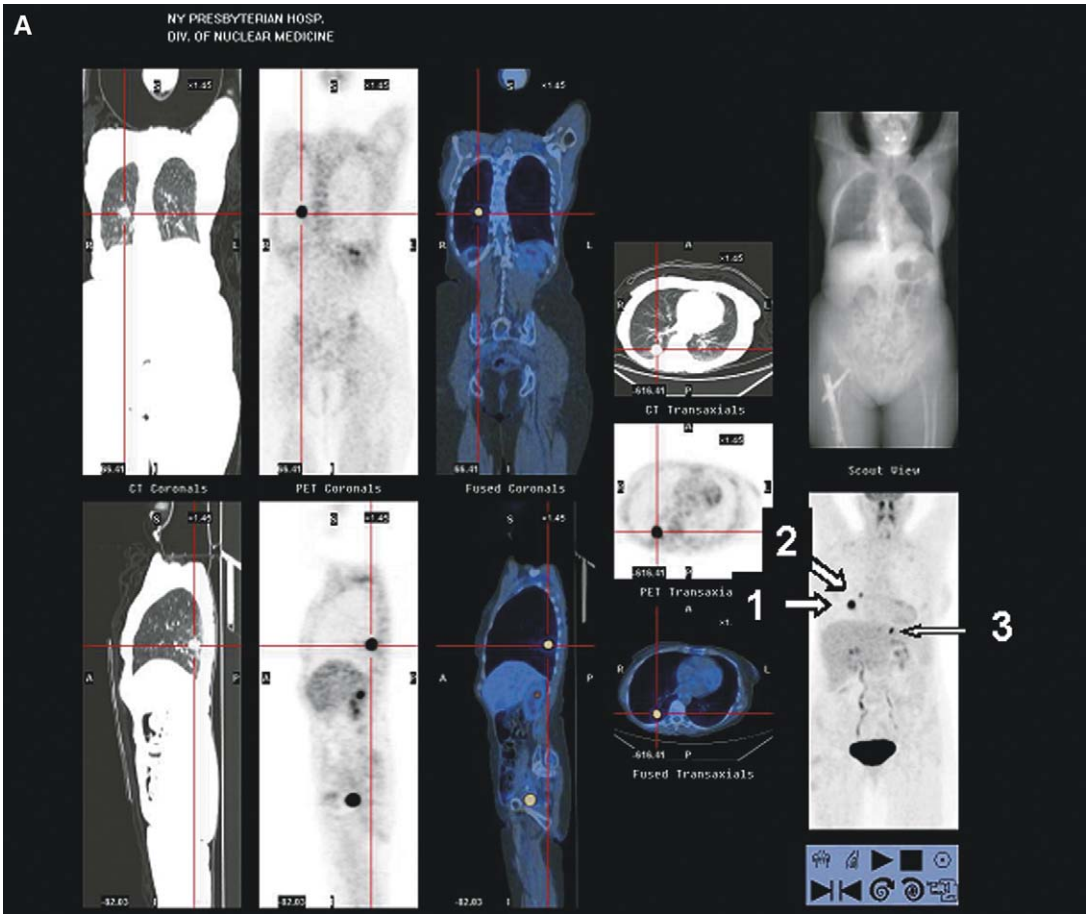

Fig. 5. (*A*) [^{18}F]-FDG-PET images from a 62-year-old woman admitted with confusion who was a cigarette smoker, 1 pack/day for 50 years. A solitary pulmonary nodule on the chest radiograph was subsequently confirmed as adenocarcinoma on biopsy. Brain metastases were present on MRI. A CT of the chest and abdomen to the kidneys was interpreted as normal except for the primary pulmonary lesion. Coronal, sagittal, and transaxial [^{18}F]-FDG-PET images are triangulated (*crosshairs*) on the primary lesion (*arrow 1*). A metastatic ipsilateral hilar lymph node is identified (*arrow 2*), and a metastasis to the left adrenal is also seen (*arrow 3*), although the right hilar node and left adrenal are normal on CT. (*B*) Transaxial slices (CT, PET, and fusion images) demonstrating adrenal metastasis in a normal left adrenal gland on CT examination. (Courtesy of Division of Nuclear Medicine, Department of Radiology, New York Presbyterian Hospital, Weill Cornell Medical Center, New York, NY).

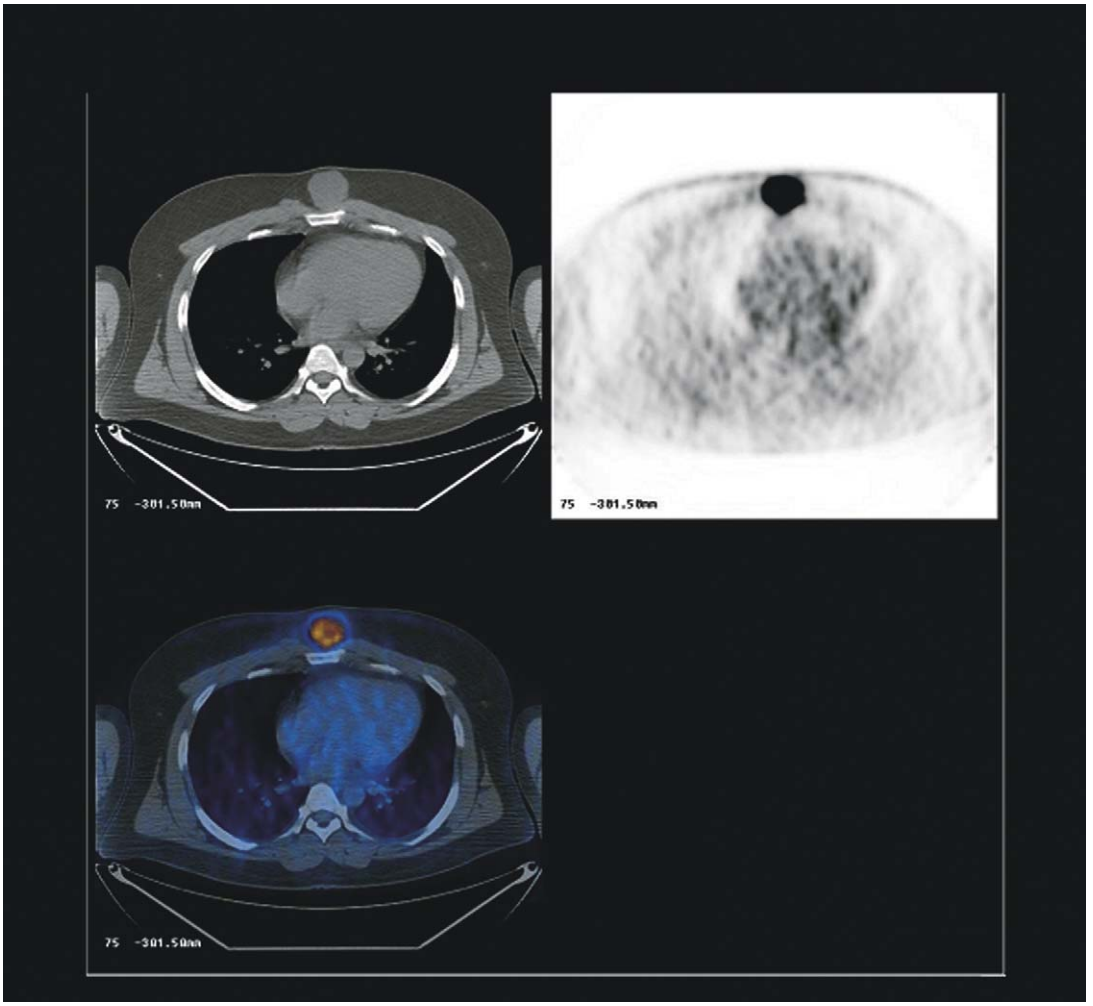

Fig. 6. [^{18}F]-FDG-PET, CT, and fusion transaxial images in a patient presenting with a chest wall mass. No satellite lesions or lymph node involvement was demonstrated; biopsy demonstrated chondrosarcoma. (Courtesy of Division of Nuclear Medicine, Department of Radiology, New York Presbyterian Hospital, Weill Cornell Medical Center, New York, NY).

Adrenal masses are identified on CT in up to 20% of patients who have NSCLC, and [^{18}F]-FDG-PET can accurately characterize the lesion as benign or malignant (Fig. 5). In one series of 27 patients, [^{18}F]-FDG-PET was 100% sensitive and 80% specific for adrenal metastases [57]. The high negative predictive value of this technique can reduce the need for routine biopsy of adrenal masses.

Lung carcinoma frequently metastasizes to bone (Fig. 5). Radionuclide bone scintigraphy using ^{99m}Tc-methylene diphosphonate (MDP) had been considered to be the procedure of choice for the clinical assessment of possible skeletal involvement. Bone metastases from NSCLC are often osteolytic, and [^{18}F]-FDG is reportedly more sensitive than conventional radionuclide bone imaging for this type of bone lesion. In addition, [^{18}F]-FDG-PET produces fewer false-positive results in degenerative, inflammatory, and posttraumatic bone disease [58,59]. False-positive [^{18}F]-FDG-PET results have been reported with acute fractures [60].

Liver metastases are readily detected by conventional imaging studies. [^{18}F]-FDG-PET is most useful for resolving abnormalities that are indeterminate on conventional studies [61]. Although [^{18}F]-FDG-PET can detect lung metastases, CT has higher resolution and is less affected by respiratory motion than [^{18}F]-FDG-PET images. For optimal detection of brain

metastases, a dedicated brain acquisition should be performed. This additional study is probably not routinely warranted in light of the low incidence of brain metastases in asymptomatic patients and because of the excellent results obtained with contrast-enhanced CT and MRI.

The effectiveness of [^{18}F]-FDG-PET in the staging of NSCLC is a direct result of its ability to detect metastases that are not apparent on conventional imaging modalities and to clarify the etiology of indeterminate lesions found on CT. It has been estimated that [^{18}F]-FDG-PET imaging results in changes in patient management in 20% to 40% of patients. Perhaps most important is the exclusion of surgery in up to 15% of patients as a result of the detection of distant metastases [56,62–64].

Treatment and prognosis

In addition to assisting in the identification of individuals who are suitable for curative surgery, [^{18}F]-FDG-PET is also used for radiotherapy planning by defining functional tumor volume and providing an outline of the radiotherapy volume for inclusion of tumor and sparing of adjacent, uninvolved structures. In one series, changes in staging were made in 33% of patients and changes in radia-

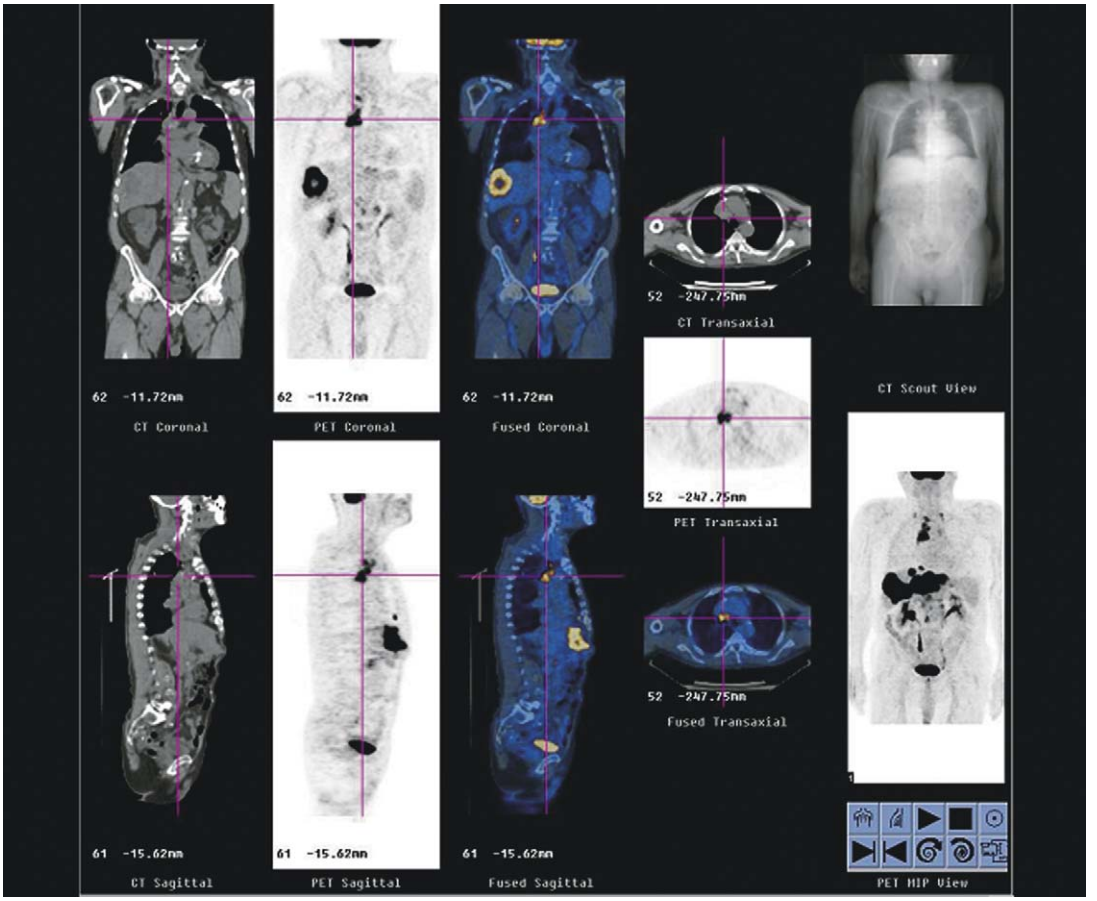

Fig. 7. [^{18}F]-FDG-PET, CT, and fusion images from a 73-year-old man who had a history of colon carcinoma that was resected 4 years earlier followed by a course of chemotherapy. The patient now has an elevated serum carcino embryonic antigen (CEA) value and suspicion of a mediastinal mass. A hypermetabolic (increased [^{18}F]-FDG) mass is seen in the right anterior mediastinum and a large mass is seen in the liver. These findings are metastatic colon carcinoma. The chest mass is indistinguishable from a second primary neoplasm. (Courtesy of Division of Nuclear Medicine, Department of Radiology, New York Presbyterian Hospital, Weill Cornell Medical Center, New York, NY.)

tion treatment volumes were made in 25% of patients as a direct result of [^{18}F]-FDG-PET imaging [65]. In addition, [^{18}F]-FDG-PET differentiates scarring from residual or recurrent disease accurately. In one study it was more sensitive than, and as specific as, other modalities employed for this purpose. In a study of 63 patients suspected of NSCLC relapse, results of [^{18}F]-FDG-PET and conventional evaluation methods were discordant in 43 patients. In 39 patients (91%), [^{18}F]-FDG-PET was correct, resulting in major changes in the diagnosis in 25 patients (59%) [66]. To maximize the accuracy of the study, [^{18}F]-FDG-PET should be performed 2 months after surgery and 4 to 6 months after radiotherapy [67].

Although prognosis in NSCLC is determined primarily by disease stage, tumor aggressiveness and invasiveness—and even metabolic activity—might also be important factors. Some data indicate that patients who have more intense uptake of ^{18}FDG have a shorter survival time. Other data have shown that patients who have persistent or recurrent abnormalities have shorter survival times than patients who have negative follow-up studies [66,68].

Fluorine-18-fluorodeoxyglucose–positron emission tomography and other thoracic tumors

Increased anaerobic glucose metabolism, which is the basis for [^{18}F]-FDG identification of carcinoma of the lung, is a feature of other malignant tumors of the thorax (Figs. 6–8). Accordingly, identification of an

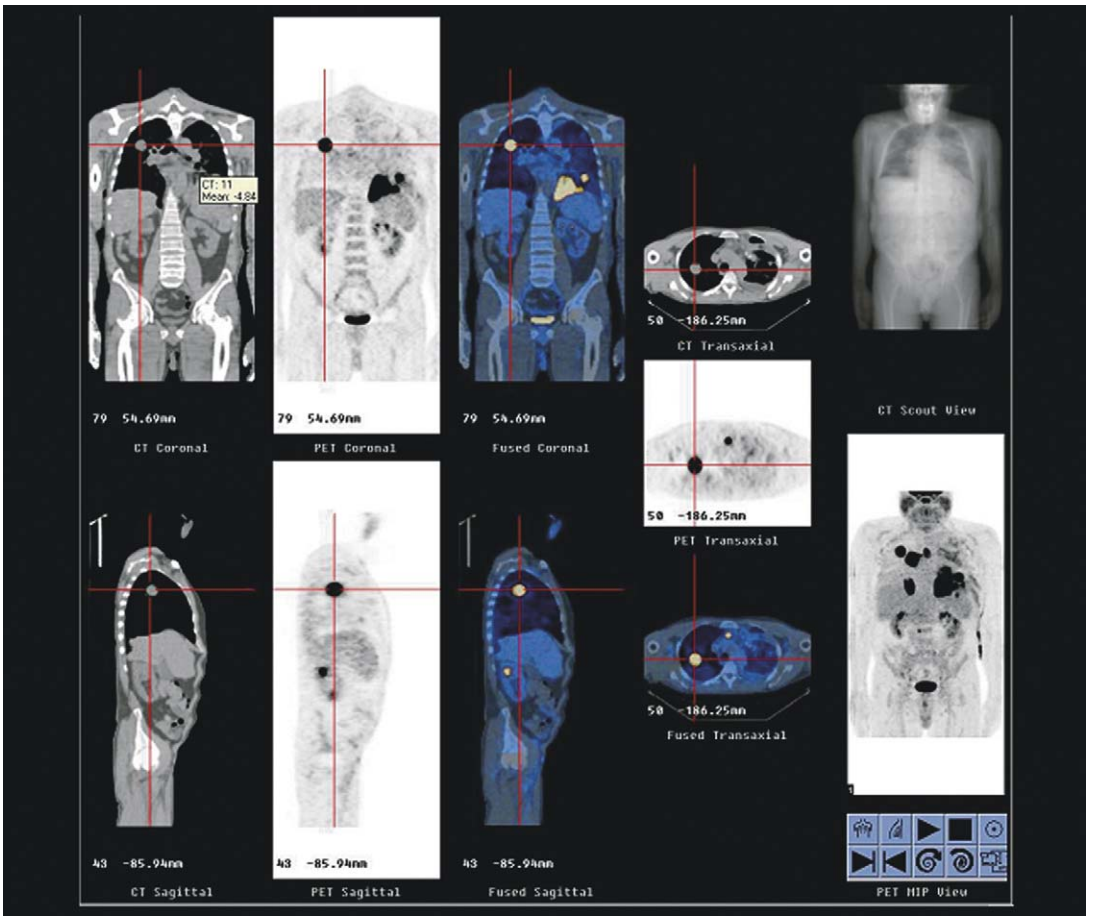

Fig. 8. [^{18}F]-FDG-PET, CT, and fusion images from a 50-year-old HIV-positive man demonstrating a hypermetabolic mass in the right lung and mediastinal lymphadenopathy and infradiaphragmatic disease. Diagnosis: non-Hodgkin's lymphoma. (Courtesy of Division of Nuclear Medicine, Department of Radiology, New York Presbyterian Hospital, Weill Cornell Medical Center, New York, NY.)

[^{18}F]-FDG-avid mass does not exclude metastatic foci from other adenocarcinomas, lymphoma, thyroid carcinomas, or even active necrotizing granulomas. The nuclear medicine physician should be provided with pertinent patient clinical history to be able to fully assess the likely etiology of the findings on the PET images. Likewise, the nuclear medicine physician should evaluate the [^{18}F]-FDG images from the neck to the mid-thigh to fully assess the extent of disease and to identify other clinical conditions that might be present.

Summary

Over the past decade a variety nuclear medicine imaging studies have become available that are of considerable value to patients who have pulmonary malignancies. By far the greatest impact on the management of patients who have thoracic malignancy has been the availability of [^{18}F]-FDG-PET imaging. In the patient who has newly diagnosed lung carcinoma, [^{18}F]-FDG-PET improves the accuracy of staging the disease by identifying or excluding mediastinal disease and distant metastatic foci. [^{18}F]-FDG-PET is superior to anatomic methods for evaluating the response to therapy and for distinguishing recurrent disease from posttreatment changes. Studies are in progress to evaluate the role of [^{18}F]-FDG-PET imaging in assessing prognosis.

In patients who have bronchial carcinoid, somatostatin receptor imaging with ^{111}In-DTPA-pentetreotide (Octreoscan) can help identify patients who are candidates for curative surgery, detect unsuspected metastatic spread, and identify patients who might benefit from certain types of medical therapy. Although it was initially speculated that [^{18}F]-FDG-PET imaging would not be sensitive for tumor detection in patients who have neuroendocrine tumors because of the usual slow metabolism and biology of these tumors many neuroendocrine tumors are positive on [^{18}F]-FDG-PET imaging. Nevertheless, there has been no direct comparison of [^{18}F]-FDG-PET imaging and somatostatin receptor imaging, nor does a positive or negative [^{18}F]-FDG-PET image exclude neuroendocrine tumor.

[^{18}F]-FDG-PET imaging and somatostatin receptor imaging with ^{99m}Tc-depreotide (Neotect) are safe, cost-effective methods that are valuable in the diagnosis and management of patients who have suspected or known lung cancer. [^{18}F]-FDG-PET and ^{99m}Tc-depreotide imaging have a high degree of sensitivity, specificity, overall accuracy, and positive and negative predictive values in the evaluation of the solitary pulmonary nodule. These agents provide noninvasive, cost-effective methods for selecting patients for aggressive intervention without contributing to increased morbidity. Both methods have incremental value over CT imaging in selecting patients who have solitary pulmonary nodules for invasive biopsy or for thoracotomy.

References

[1] Coleman RE, Laymon CM, Turkington TG. FDG imaging of lung nodules: a phantom study comparing SPECT, camera-based PET, and dedicated PET. Radiology 1999;210:823–8.

[2] Gould MK, Maclean CC, Kuschner WG, et al. Accuracy of positron emission tomography for diagnosis of pulmonary nodules and mass lesions: a meta-analysis. JAMA 2001;285:914–24.

[3] Lardinois D, Weder W, Hany TF, et al. Staging of non-small-cell lung cancer with integrated positron-emission tomography and computed tomography. NEJM 2003;348:2500–7.

[4] Goldsmith SJ, Bar-Shalom R, Kostakoglu L, Weiner R, Neumann R. Gallium-67 scintigraphy in tumor detection. In: Sandler M, Coleman R, et al, editors. Diagnostic nuclear medicine. Philadelphia: Lippincott Williams & Wilkins; 2002. p. 911–9.

[5] Waxman AD. Thallium-201 and technetium-99m methixyisobutyl isonitrile (MIBI) in nuclear oncology. In: Sandler M, Coleman R, et al, editors. Diagnostic nuclear medicine. Philadelphia: Lippincott Williams & Wilkins; 2002. p. 931–47.

[6] Kostakoglu L, Goldsmith SJ. Imaging multidrug resistance in hematological malignancies. Hematology 2001;6:111–24.

[7] Behr TM, Gotthardt M, Barth A, Behe M. Imaging tumors with peptide-based radioligands. Q J Nucl Med 2001;45:189–200.

[8] Reubi JC. Regulatory peptide receptors as molecular targets for cancer diagnosis and therapy. Q J Nucl Med 1997;41:63–70.

[9] Krenning EP, Kwekkeboom DJ, Pauwels S, Kvols LK, Reubi JC. Somatostain receptor scintigraphy. In: Freeman LM, editor. Nuclear medicine annual 1995. New York: Raven Press; 1995. p. 1–50.

[10] Krenning EP, Kwekkeboom DJ, Bakker WH. Somatostatin receptor scintigraphy with [^{111}In-DTPA-*D*-Phel]- and [^{123}I-Tyr3]-octreotide: the Rotterdam experience with more than 1000 patients. Eur J Nucl Med 1993; 20:716–31.

[11] Bohuslavizki KH, Brenner W, Gunther M, et al. Somatostatin receotor scintigraphy in the staging of small cell lung cancer. Nucl Med Coomun 1996;17: 191–6.

[12] Fanti S, Farsard M, Battista G, et al. Somatostatin receptor scintigraphy for bronchial carcinoid follow-up. Clin Nucl Med 2003;28:548–52.

[13] O'Byrne KJ, O'Hare NJ, Freyne PJ, et al. Imaging of bronchial carcinoid tumors with indium-111 pentetreotide. Thorax 1994;49:284–6.
[14] Musi M, Carbone RG, Bertocchi C, et al. Bronchial carcinoid tumors: astudy on clinicopathological features and role of octreotide scintigraphy. Lung Cancer 1998;22:97–102.
[15] Blum JE, Handmaker H, Rinne NA. The utility of a somatostatin-type receptor binding peptide in the evaluation of solitary pulmonary nodules. Chest 1999;115:224–32.
[16] Blum JE, Handmaker H, Lister-James J, et al. A multicenter trial with a somatostatin analog ^{99m}Tc-depreotide in the evaluation of solitary pulmonary nodules. Chest 2000;117:1232–8.
[17] Gambhir SS, Shephard JE, Handmaker H, Blum J. Analysis of the cost effectiveness of a somatostatin analog-Tc99m-Depreotide (Neotect) in the scintigraphic evaluation of solitary pulmonary nodules (SPN). J Nucl Med 1999;40(Suppl):57P.
[18] Boring CC, Squires TS, Tong T. Cancer statistics, 1992. CA Cancer J Clin 1992;42:19–38.
[19] Parker SL, Tong T, Bolden S, Wingo PA. Cancer statistics, 1997. CA Cancer J Clin 1997;47:5–27.
[20] Ost D, Fein A. Evaluation and management of the solitary pulmonary nodule. Am J Respir Crit Care Med 2000;162:782–7.
[21] Ward HB, Pliego M, Diefenthal HC, Humphrey EW. The impact of phantom CT scanning on surgery for the solitary pulmonary nodule. Surgery 1989;106:734–8.
[22] Salathe M, Soler M, Bolliger CT, et al. Transbronchial needle aspiration in routine fiberoptic bronchoscopy. Respiration (Herrlisheim) 1992;59:5–8.
[23] Schenk DA, Bower JH, Bryan CL, et al. Transbronchial needle aspiration staging of bronchogenic carcinoma. Am Rev Respir Dis 1986;134:146–8.
[24] Santambrogio L, Nosotti M, Bellaviti N, Pavoni G, Radice F, Caputo V. CT-guided fine- needle aspiration cytology of solitary pulmonary nodules: a prospective, randomized study of immediate cytologic evaluation. Chest 1997;112:423–5.
[25] Patz EJ, Lowe VJ, Hoffman JM, et al. Focal pulmonary abnormalities: evaluation with F-18 fluorodeoxyglucose PET scanning. Radiology 1993;188:487–90.
[26] Lowe VJ, Fletcher JW, Gobar L, et al. Prospective Investigation of positron emission tomography in lung nodules. J Clin Oncol 1998;16:1075–84.
[27] Kubota K, Matsuzawa T, Fijiwara T, et al. Differential diagnosis of lung tumor with positron emission tomography: a prospective study. J Nucl Med 1990; 31:1927–32.
[28] Gupta NC, Maloof J, Gunel E. Probability of malignancy in solitary pulmonary nodules using fluorine-18-FDG and PET. J Nucl Med 1996;37: 943–8.
[29] Patz Jr EF, Lowe VJ, Hoffman JM, et al. Persistent or recurrent bronchogenic carcinoma: detection with PET and 2-[F-18]-deoxy-D-glucose. Radiology 1994;191: 379–82.
[30] Duhaylongsod FG, Lowe VJ, Patz Jr EF, et al. Detection of primary and recurrent lung cancer by means of F-18 fluorodeoxyglucose positron emission tomography (FDG PET). J Thorac Cardiovasc Surg 1995;110:130–9.
[31] Bury T, Dowlati A, Paulus P, et al. Evaluation of the solitary pulmonary nodule by positron emission tomography imaging. Eur Respir J 1996;9:410–4.
[32] Sazon DA, Santiago SM, Soo Hoo GW, et al. Fluorodeoxyglucose-positron emission tomography in the detection and staging of lung cancer. Am J Respir Crit Care Med 1996;153:417–21.
[33] Prauer HW, Weber WA, Romer W, et al. Controlled prospective study of positron emission tomography using the glucose analogue [18f] fluorodeoxyglucose in the evaluation of pulmonary nodules. Br J Surg 1998;85:1506–11.
[34] Bury T, Rigo P. Contribution of positron emission tomography for the management of lung cancer. Rev Pneumol Clin 2000;56:1506–11.
[35] Higashi K, Ueda Y, Seki H, et al. Fluorine-18-FDG PET imaging is negative in bronchiolo-alveolar lung carcinoma. J Nucl Med 1998;39:1016–20.
[36] Farquar TH, Llacer J, Sayre J, et al. ROC and LROC analyses of the effects of lesion contrast, size, and signal-to-noise ratio on detectability in PET images. J Nucl Med 2000;41:745–54.
[37] Hoffman EJ, Huang SC, Phelps ME. Quantitation in positron emission computed tomography: I. Effect of object size. J Comput Assist Tomogr 1979;3:299–308.
[38] Wahl RL. Targeting glucose transporters for tumor imaging: "sweet" idea, "sour" result [editorial]. J Nucl Med 1996;37:1038–41.
[39] Roberts PF, Follette DM, von Haag D, et al. Factors associated with false positive staging of lung cancer by positron emission tomography. Ann Thorac Surg 2000;70:1154–9.
[40] Kapucu LO, Meltzer CC, Townsend DW, et al. Fluorine-18-fluorodeoxyglucose uptake in pneumonia. J Nucl Med 1998;39:1267–9.
[41] Brudin LH, Valind SO, Rhodes CG, et al. Fluorine-18-deoxyglucose uptake in sacroidosis measured with positron emission tomography. Eur J Nucl Med 1994; 21:297–305.
[42] Bakheet SM, Saleem M, Powe J, et al. F-18 fluorodeoxyglucose chest uptake in lung inflammation and infection. Clin Nucl Med 2000;25:273–8.
[43] Matthies A, Hickeson M, Cuchiara A, Alavi A. Dual time point ^{18}F-FDG PET for the evaluation of pulmonary nodules. J Nucl Med 2002;43:871–5.
[44] Gambhir SS, Sheperd JE, Shah BD, et al. Analytical decision model for the cost-effective management of solitary pulmonary nodules. J Clin Oncol 1998;16: 2113–25.
[45] Dwamena BA, Sonnad SS, Angobaldo JO, et al. Metastases from non-small cell lung carcinoma: mediastinal staging in the 1990s—meta-analytic comparison of PET and CT. Radiology 1999;213:530–6.
[46] Webb WR, Gatsonis C, Zerhouni EA, et al. CT and

MR imaging in staging non-small cell carcinoma bronchogenic: report of the Radiologic Diagnostic Oncology Group. Radiology 1991;178:705–13.

[47] Steinert HC, Hauser M, Allemann F, et al. Non-small cell lung cancer: nodal staging with FDG PET versus CT with correlative lymph node mapping and sampling. Radiology 1997;202:441–6.

[48] Vansteenkiste JF, Stoobants SG, De Leyn PR, et al. Mediastinal lymph node staging with FDG PET scan in patients with potentially operable non-small cell lung cancer: a prospective analysis of 50 cases. Leuven Lung Cancer Group. Chest 1997;112:1480–6.

[49] Saunders CA, Dussek JE, O'Doherty MJ, et al. Evaluation of fluorine-18 fluorodeoxyglucose whole body positron emission tomography imaging in the staging of lung cancer. Ann Thorac Surg 1999;67: 790–7.

[50] Kerstine KH, Stanford W, Mullan BF, et al. PET, CT, and MRI with Combidex for mediastinal staging in non-small cell lung cancinoma. Ann Thorac Surg 1999;68:1022–8.

[51] Weng E, Tran L, Rege S, et al. Accuracy and clinical impact of mediastinal lymph node staging with FDG PET imaging in potentially resectable lung cancer. Am J Clin Oncol 2000;23:47–52.

[52] Pieterman RM, van Putten JW, Meuzelaar JJ, et al. Preoperative staging of non-small cell lung cancer with positron-emission tomography. N Engl J Med 2000; 343:254–6.

[53] Bury T, Paulus P, Dowlati A, et al. Staging of the mediastinum: value of positron emission tomography imaging in non-small cell lung cancer. Eur Respir J 1996;9:2560–4.

[54] Martini N, Bains MS, Burt ME, et al. Incidence of local recurrence and second primary tumors in resected stage 1 lung cancer. J Thorac Cardiovasc Surg 1995; 109:120–9.

[55] Weder W, Schmid RA, Bruchhaus H, et al. detection of extrathoracic metastases by positron emission tomography in lung cancer. Ann Thorac Surg 1998; 66:886–92.

[56] Bury T, Dowlati A, Paulus P, et al. Staging of non-small cell lung cancer by whole- body fluorine-18 deoxyglucose positron emission tomography. Eur J Nucl Med 1996;23:204–6.

[57] Erasmus JJ, Patz Jr EF, McAdams HP, et al. Evaluation of adrenal masses in patients with bronchogenic carcinoma using ^{18}F-fluorodeoxyglucose positron emission tomography. Am J Roentgenol 1997;168:1357–60.

[58] Bury T, Barreto A, Daenen F, et al. Fluorine-18 deoxyglucose positron emission tomography for the detection of bone metastases in patients with non-small cell lung cancer. Eur J Nucl Med 1998;25:1244–7.

[59] Schmirreister H, Guhlmann A, Eisner K, et al. Sensitivity in detecting osseous lesions depends on anatomic localization: planar bone scintigraphy versus ^{18}F PET. J Nucl Med 1999;40:1623–9.

[60] Meyer M, Gast T, Raja S, Hubner K. Increased F-18-FDG accumulation in an acute fracture. Clin Nucl Med 1994;19(1):13–4.

[61] Hustinx R, Paulus P, Jacquet N, et al. Clinical evaluation of whole-body ^{18}F-fluorodeoxyglucose positron emission tomography in the detection of liver metastases. Ann Oncol 1998;9:397–401.

[62] Valk PE, Pounds TR, Hopkins DM, et al. Staging non-small cell lung cancer by whole-body positron tomographic imaging. Ann Thorac Surg 1995;60:1573–81.

[63] Marom EM, McAdams HP, Erasmus JJ, et al. Staging non-small cell lung cancer with whole-body PET. Radiology 1999;212:803–9.

[64] Lewis P, Griffin S, Marsden P, et al. Whole-body ^{18}F-fluorodeoxyglucose positron emission tomography in preoperative evaluation of lung cancer. Lancet 1994;334:1265–6.

[65] Hicks RJ, Kalff V, MacManus MP, et al. ^{18}F-FDG PET provides high-impact and powerful prognostic stratification in staging newly diagnosed non-small cell lung cancer. J Nucl Med 2001;42:1596–604.

[66] Hicks RJ, Kalff V, MacManus MP, et al. The utility of ^{18}F-FDG PET for suspected recurrent non-small cell lung cancer after potentially curative therapy: impact on management and prognostic stratification. J Nucl Med 2001;42:1605–13.

[67] Erasmus JJ, Patz Jr EF. Positron emission tomography imaging in the thorax. Clin Chest Med 1999;20: 715–24.

[68] Patz Jr EF, Connolly J, Herndon J. Prognostic value of thoracic FDG PET imaging after treatment for non-small cell lung cancer. Am J Roentgenol 2000;174: 769–74.

ELSEVIER
SAUNDERS

Radiol Clin N Am 43 (2005) 481 – 495

RADIOLOGIC
CLINICS
of North America

Imaging of Metastatic Disease to the Thorax

Suzanne L. Aquino, MD

Department of Radiology (FND 202), Massachusetts General Hospital, 55 Fruit Street, Boston, MA 02114, USA

Tumor imaging is at the forefront of radiology technology and is the focus of most cutting edge research and clinical applications. Radiologic applications for imaging of metastases are applied to initial staging, restaging after neoadjuvant therapy before planned definitive surgical treatment, and follow-up surveillance after therapy for tumor recurrence.

CT has evolved as the routine choice in staging, restaging, and detection of recurrence. Studies have shown that CT is superior to the chest radiograph for the detection of pulmonary metastases. Its sensitivity in detecting small nodules, however, can also be a limitation. Because of its excellent spatial resolution, CT detects small lesions that resemble metastatic foci but are frequently benign. Such limitations especially come into play in the initial diagnosis of patients with extrathoracic malignancies and no prior radiographic studies to document pre-existing parenchymal disease [1]. For instance, a study by Chalmers [2] showed pulmonary nodules in 20% of patients with extrathoracic malignancies who had normal chest radiographs; however, 80% of these nodules were benign. Similar results were found by Kronawitter et al [3]. They found that most nodules on chest CT scans were benign in patients with colon cancer undergoing routine preoperative imaging for liver metastasectomy. Only 5% of patients had true metastases. Povoski et al [4] reported that CT detected pulmonary metastases in 4 of 100 patients with colon cancer who had normal preoperative chest radiographs before hepatectomy. Picci et al [5] reported that in 51 children with osteosarcoma, CT was sensitive but not specific in detecting pulmonary metastases. They found, however, that the likelihood of a patient having metastases was proportional to the number of nodules detected. Four out of 13 patients with a single nodule had a true metastasis. All patients with more than seven nodules had metastases.

Debate has arisen as to whether a thoracic CT scan is necessary in all patients initially diagnosed with cancer. Reports have demonstrated that the stage of an extrathoracic malignancy should be taken into consideration when determining if a thoracic CT should be included in the work-up [6–8]. Lim and Carter [7] found that the incidence of metastases from small renal cell carcinomas detected by CT was low. With more advanced tumor stage or the detection of a nodule on radiograph, however, they found CT very useful in detecting pulmonary metastases. Similarly, Heaston et al [9] reported that CT improved the detection of metastases in patients with locally advanced melanoma and helped identify extrapulmonary metastases.

Reiner et al [10] found that thoracic CT was essential in the management of patients with newly diagnosed squamous cell carcinoma of the head and neck. Sixty-six of 189 patients had significant abnormalities on CT of which only 23% were detected by chest radiograph. Thirty-six patients had 41 tumors of which 13 were synchronous primary lung cancers and 28 were metastases. Plain film detected only 12 (29%) of these tumors. The authors recommended routine pretreatment thoracic CT for this patient population, which has a significant cigarette smoking history and greater risk for bronchogenic carcinoma.

In the follow-up management of patients treated with cancer and who undergo surveillance for recurrence, CT has been shown to be very useful in the detection of new pulmonary metastases [3]. Studies have shown that the use of follow-up CT imaging to detect early metastases can improve the survival of

E-mail address: saquino@partners.org

0033-8389/05/$ – see front matter © 2005 Elsevier Inc. All rights reserved.
doi:10.1016/j.rcl.2005.02.006

patients with certain malignancies, such as sarcomas and colon cancer [5,11,12].

Morphology of pulmonary metastases

Most pulmonary metastases reach the lungs through the arterial system [13–15]. The most common manifestation of pulmonary metastases is multiple nodules [13,14,16,17] that are found in the subpleural and outer third of the lungs [18]. Although pulmonary metastases are generally multiple in numbers, some tumors are more likely to manifest with a single pulmonary metastasis. These tumors include primary tumors from the colon and kidney, melanoma, and sarcoma [9,19–21].

Metastatic nodules can range from miliary to several centimeters in size. Miliary nodules are more likely to occur in tumors from the thyroid gland, kidney, and melanoma [22,23]. Larger nodules tend to originate from sarcomas and tumors from the colon and kidney. Metastases can be characterized not only by size but also by density or composition. For instance, metastases may appear solid, ground glass, or mixed solid and ground glass. Other metastases calcify or cavitate.

Distribution is not necessarily helpful in distinguishing metastases from other causes for pulmonary nodules other than they are usually random with respect to the interstitial compartments [24,25]. Association of a nodule with a pulmonary vessel or the ‘‘mass-vessel sign’’ on high-resolution (HRCT) has been correlated with a hematogenous origin [15].

Ground glass nodules or nodules with surrounding ground glass opacities are consistent with either hemorrhage or airspace disease into the adjacent lung. Metastatic nodules with surrounding hemorrhage have been described with choriocarcinoma, mela-

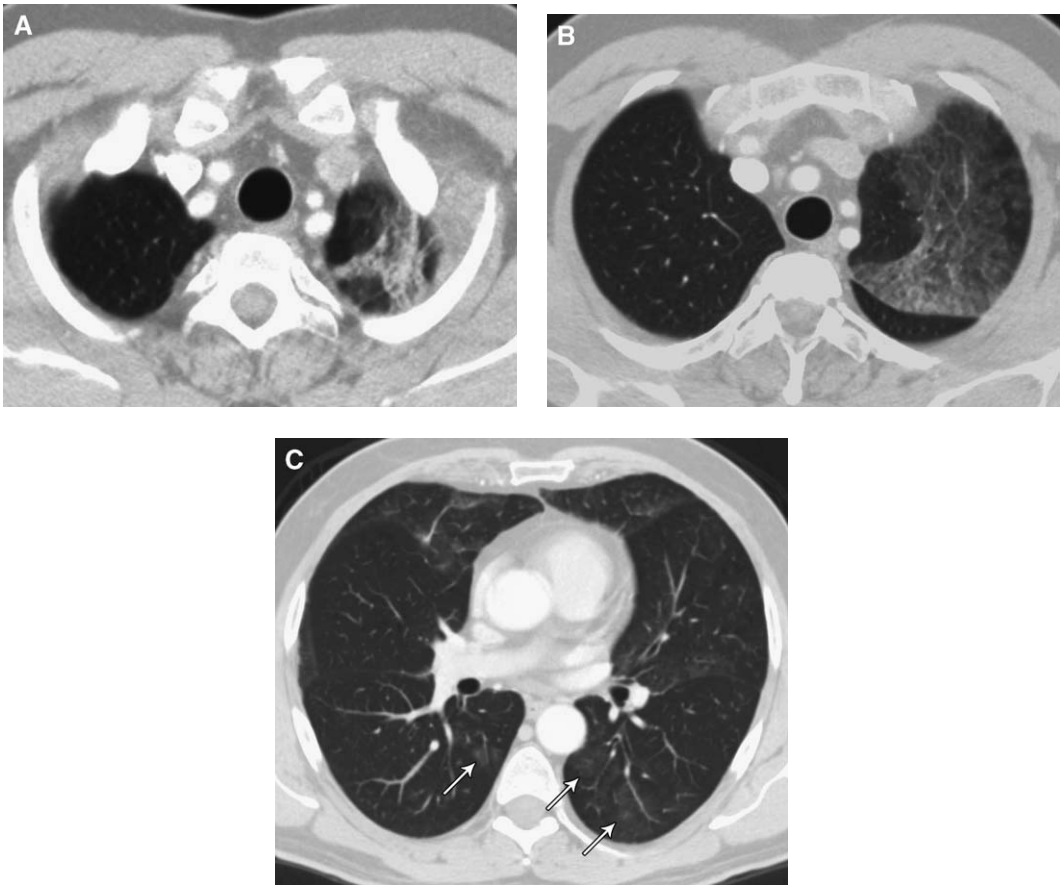

Fig. 1. A 57-year-old man with history of bronchioloalveolar cell carcinoma of the left upper lobe. (*A*) CT scan of upper lobes shows primary tumor. (*B*) CT scan shows diffuse ground glass opacification that was metastatic disease on biopsy. (*C*) Lower lobes show metastases manifesting as ground glass nodules (*arrows*).

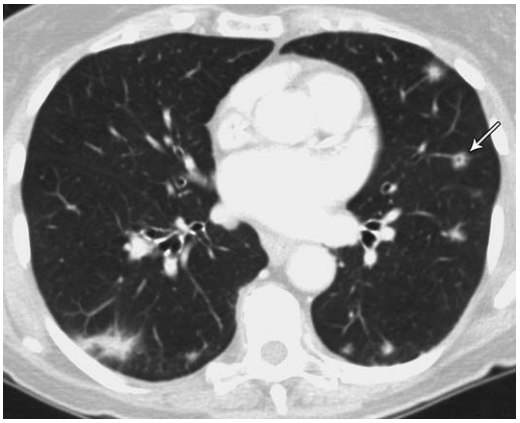

Fig. 2. An 82-year-old man with metastatic pancreatic mucinous adenocarcinoma. CT scan of the lungs shows multiple ill-defined nodules with surrounding ground glass. One of the nodules is cavitary (*arrow*).

noma, renal cell carcinoma, angiosarcoma, and Kaposi's sarcoma [26–28]. Bronchioloalveolar cell carcinoma metastases may appear as ground glass, ground glass nodules (Fig. 1), or solid nodules with surrounding ground glass [29]. The ground glass pattern has been attributed to lining of adjacent airspaces by tumor through a lipidic growth pattern or to filling of airspaces with mucinous material (Fig. 2) [30]. Nonmalignant processes may mimic metastases and should be in the differential diagnosis. Infections, such as viral pneumonias, tuberculosis, fungal infections including invasive aspergillosis, arteriovenous

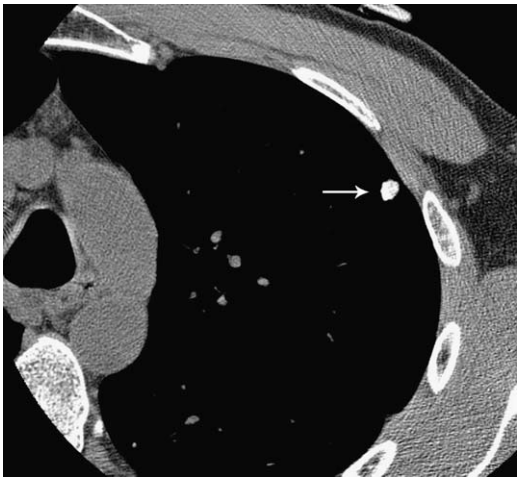

Fig. 3. A 47-year-old man with metastatic osteosarcoma. CT scan in soft tissue windows demonstrates calcification in one of multiple new pulmonary nodules that were metastases (*arrow*).

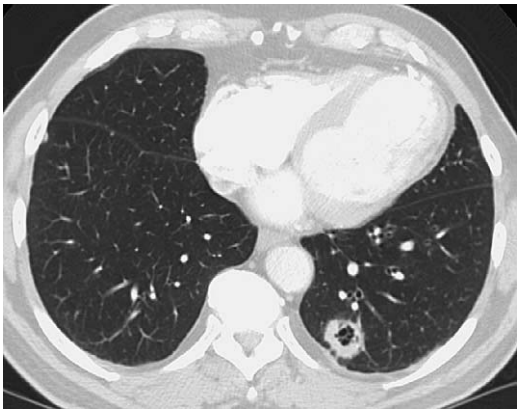

Fig. 4. A 73-year-old man with metastatic adenocarcinoma. CT scan showed multiple pulmonary nodules that were cavitary.

malformations, and Wegener's granulomatosis with local hemorrhage can also have a ground glass component [26,29].

The diagnosis of metastases can be readily identified in a patient with osteosarcoma or chondrosarcoma and new calcified nodules (Fig. 3). Without prior radiographs available to show that a nodule is new, however, other diagnoses should include granulomatous disease, amyloidosis, or a hamartoma. Metastatic mucinous adenocarcinoma originating from the pancreas, small bowel, or ovary, thyroid carcinoma, and on rare occasion sarcomas and choriocarcinoma may also contain calcifications [31–36].

Multiple cavitary metastases are more commonly associated with squamous cell carcinoma but may also be seen with transitional cell carcinoma of the bladder, adenocarcinomas (Fig. 4), sarcomas (Fig. 5), and lymphoma [37–42]. Cavitation of metastases may be seen before therapy but may also reflect

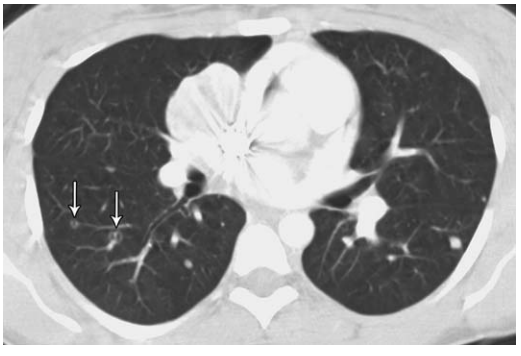

Fig. 5. A 28-year-old woman with history of metastatic soft tissue sarcoma to the lungs. CT scan of the thorax shows multiple solid and cavitary (*arrows*) nodules.

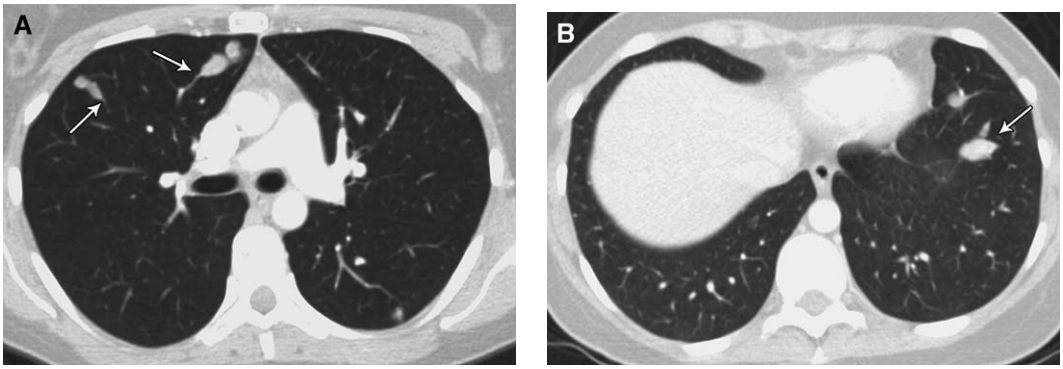

Fig. 6. A 34-year-old woman with metastatic osteosarcoma. (*A*) CT scan of the lungs shows elongated nodules extending from normal-sized vessels consistent with tumor emboli (*arrows*). (*B*) CT scan of the lower lobes shows a branching tumor embolus in an intermediate-sized vessel (*arrow*).

response following chemotherapy [39,43]. The initial finding of multiple cavitary nodules does not necessarily suggest tumor [44–46]. Inflammatory diseases, such as Wegener's granulomatosis, rheumatoid arthritis, eosinophilic granulomatosis, and amyloid may present with numerous cavitary nodules. Pulmonary infections should also be considered, such as fungal infection, mycobacterial disease, septic emboli, and tracheobronchial papillomatosis.

Tumor emboli are the result of hematogenous metastases that occlude and enlarge within the pulmonary arteries. On CT they appear as branching nodular enlargement of small- to medium-sized vessels (Fig. 6) [47]. This unusual pattern of metastases is seen with tumors that commonly reach the lungs hematogenously, such as sarcoma, renal cell carcinoma, hepatoma, and melanoma. Complete arteriole occlusion with subsequent infarction may develop and present with distal parenchymal ground glass or consolidation mimicking a Hamptom's hump [47,48]. Microscopic emboli resulting in idiopathic cor pulmonale is a rare complication associated with tumors from the breast, liver, and gastrointestinal tract. Frequently, the lungs are clear on chest radiograph and CT [25]. On rare occasion CT may show evidence of interstitial disease consistent with associated lymphangitic involvement [49]. Angiography may be normal or show delayed vessel filling [50]. Ventilation perfusion scanning may demonstrate multiple subsegmental perfusion defects [50,51].

Endobronchial metastases

The endobronchial metastases are rare with a reported incidence of 2% [52]. Renal cell carcinoma is the most common tumor to metastasize to the airways [42,53,54]. Other tumors with potential for airways involvement include melanoma; lymphoma; and tumors of the breast, larynx, thyroid, and colon [42,52–55]. Patients with tumor involvement of the airways frequently have metastases to other areas of the thorax including the lymph nodes and pulmonary parenchyma [53]. The proximal airways are most commonly involved (Fig. 7). Complete occlusion often results in poor clearance and mucus filling of the distal airways. On CT, these occluded airways give the appearance of branching opaque structures that are separate and parallel to the vasculature. Occluded branching airways have been likened to a ''finger-in-glove'' on chest radiograph. If airway plugging extends into the subpleural level a tree-in-bud pattern can be seen on CT scan (see Fig. 7).

Pulmonary lymphangitic carcinomatosis

Lymphangitic tumor involvement of the lungs predominately affects the pulmonary lymphatics; capillaries; and surrounding interstitium of the bronchovascular bundles, interlobular septa, and pleura [18,56]. The patterns most frequently found on HRCT include thickening of the interlobular septa resulting in reticular lines and polygonal structures (Fig. 8), and the bronchovascular interstitium, resulting in centrilobular nodules [18,57]. Thickened interstitial compartments can be smooth or nodular [18,58]. A smooth pattern may be the result of direct tumor infiltration in the interstitium, lymphatics, and capillaries; obstructed and dilated lymphatics; or the result of interstitial edema from more proximal tumor obstruction of lymphatics (ie, with hilar or mediastinal lymphadenopathy) [56,59]. Nodular lymphangitic disease, described as the ''beaded septum sign''

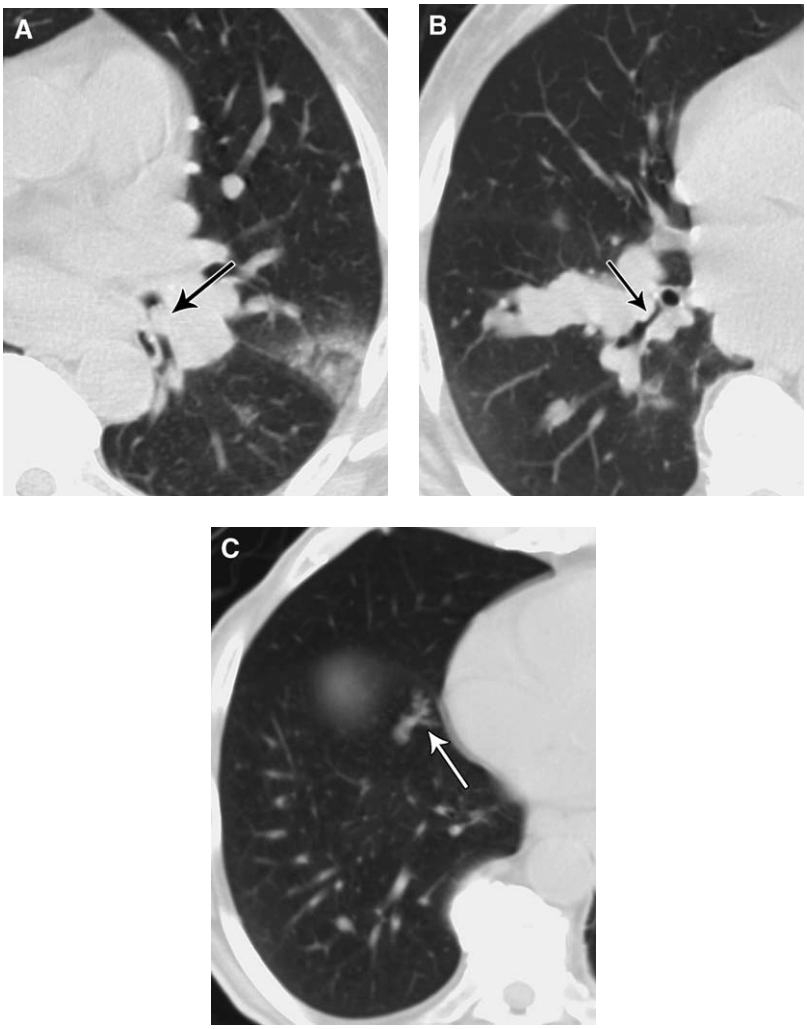

Fig. 7. A 69-year-old man with metastatic Hürthle cell carcinoma. (*A*) An endobronchial metastasis partially occludes the bronchus to the superior segment of the left lower lobe (*arrow*). (*B*) Contralateral right lower lobe segmental bronchus also shows endobronchial metastasis (*arrow*). Large lobulated branching opacity distal to endobronchial mass is consistent with tumor or debris filling the distal airways. (*C*) Subpleural branching opacity (*arrow*) corresponds to dilated and occluded bronchiole.

[18,60] on CT, is more indicative of direct tumor deposition in the interstitium and lymphatics. Malignancies commonly associated with lymphangitic carcinomatosis in the lungs include adenocarcinomas from lung, breast, and gastrointestinal tract; melanoma; lymphoma; and leukemia [25,56,59,61,62]. Disease may initially reach the lungs either by embolic spread or direct extension from hilar lymphatic disease [49,63]. On chest radiograph the pattern frequently resembles edema with thickening of the perihilar bronchovasculature and subpleural Kerley's B lines [56,59]. Frequently, however, the distribution is asymmetric, which should raise the suspicion for the presence of neoplasm.

CT and HRCT are more sensitive and specific in identifying lymphangitic involvement [56]. A study by Hirakata et al [25], however, showed that the degree of pulmonary involvement detected by HRCT is limited when compared with histopathology. Distribution of interstitial involvement can extend from the perihilar axial interstitium to the subpleural interlobular septa and also involve the subpleural interstitium leading to thickened fissures [59,64]. Johkoh et al [64] correlated HRCT findings to those on

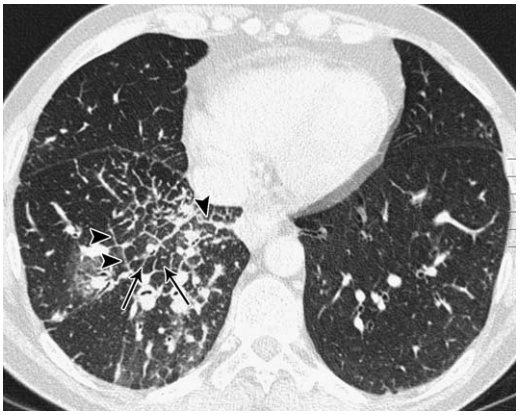

Fig. 8. A 49-year-old man with metastatic lung adenocarcinoma. High-resolution CT scan shows thickened interlobular septa (*arrowheads*) and centrilobular nodules (*arrows*) in preserved lung architecture.

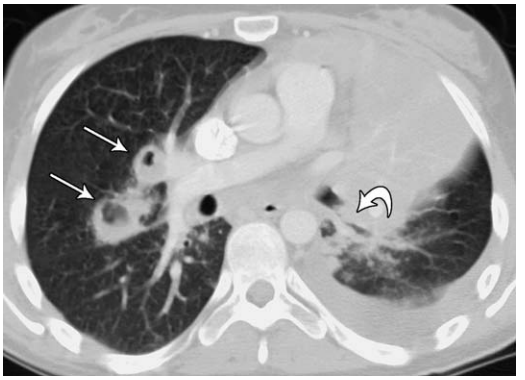

Fig. 9. A 25-year-old woman with Hodgkin's lymphoma of the lungs. CT scan of intermediate windows shows combination of consolidation in the lingula and cavitary nodules in the right lung (*arrows*). Endobronchial mass (*curved arrow*) is also present in the left lower lobe bronchus.

histopathology. They found that the distribution in most patients with lymphangitic carcinomatosis was in the perihilar axial interstitium. Other interstitial diseases may resemble lymphangitic carcinomatosis (LCA) including sarcoidosis and lymphoma. The distribution of disease and pattern of associated nodules may help distinguish one disorder from another. Honda et al [65] found that LCA had a tendency to involve the subpleural interstitial spaces more frequently than sarcoidosis, which tended to be more symmetric and in the upper lungs.

Metastases with airspace or mixed parenchymal patterns

Lymphoma involvement of the lungs may be mixed and show a combination of consolidative, nodular, or interstitial involvement (Fig. 9) [61]. The latter form commonly is seen as an extension of tumor along the axial bronchovascular interstitium from hilar lymphatic disease or from an adjacent pulmonary mass. The presence of an air bronchogram is commonly seen in both consolidative and nodular forms. Cavitation of nodules may occur (see Fig. 9). The presence of lymphadenopathy may help in the differential diagnosis, especially with Hodgkin's disease. Lymphadenopathy may not necessarily be present, however, with primary non-Hodgkin's involvement of the lungs [61,66].

The consolidative form of adenocarcinoma and its subtype, bronchoalveolar cell carcinoma, is often initially misdiagnosed as lobar pneumonia. Many patients present with fever, cough, and systemic symptoms consistent with infection (which they can have superimposed on their tumor) [67]. Coexisting pulmonary findings, such as associated subcentimeter nodules (which can be ground glass and cavitary) or scattered areas of ground glass, should raise one's suspicion for malignancy. On rare occasion cyst-like changes in the consolidation or nodules (Fig. 10) may develop [68]. This may be mistaken for bronchiectasis or cavitation from necrosis. The pattern of ground glass with septal thickening mimicking a crazy-paving is an unusual pattern for metastatic adenocarcinoma but is well described [67,69].

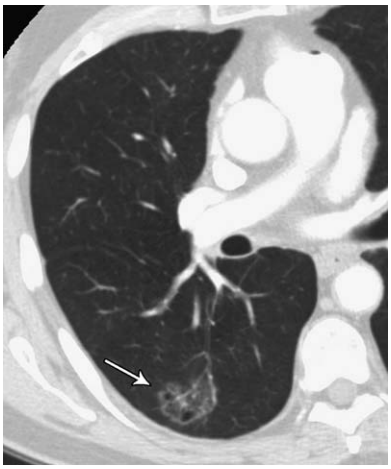

Fig. 10. A 73-year-old man with history of bronchioloalveolar cell carcinoma of the left lung. CT scan shows multiple ground glass nodules, some of which show central lucencies or cysts (*arrow*).

Kaposi's sarcoma involvement of the lungs commonly includes mediastinal and hilar lymphadenopathy. Tumor tends to extend along the bronchovasculature into the parenchyma. Multiple flame-shaped lesions or nodules with ill-defined borders or ground glass develop in the same distribution and commonly contain an air-bronchogram [27,70]. Other manifestations, however, include single pulmonary nodule, pleural effusion, or tracheal and bronchial lesions [70].

Fluorodeoxyglucose positron emission tomography and pulmonary metastases

The detection of thoracic metastases from all tumor sources has not been completely evaluated by fluorodeoxyglucose (FDG) positron emission tomography (PET) in the current literature. Results that are available, however, show that PET can be useful for the detection of thoracic metastases for tumors, such as melanoma, colon, and breast. The major weakness to the use of PET imaging is the nodule size threshold for detection. Limitations exist when metastases are less than 1 cm. PET imaging should be used with the accompaniment of imaging with excellent anatomic resolution, such as CT. For example, Majhail et al [71] evaluated the FDG-PET scans of 24 patients with renal cell carcinoma and suspected metastatic disease. Because PET was not able to detect subcentimeter nodules, the sensitivity of this modality was a mere 64%. The specificity, however, was 100%.

Imdahl et al [72] reported PET sensitivity of 100% and specificity of 98% for the detection of colon metastases. Comparison CT was 87% sensitive and 91% specific. In their study, five patients had unsuspected pulmonary metastases that were only identified on FDG-PET. In 16 patients, management was altered because of overall results from PET scans.

A similar trend in detecting metastases has been reported with metastatic melanoma. Rinne et al [73] found that FDG-PET was less sensitive than CT for detecting small pulmonary nodules. PET was only 70% sensitive compared with 87% for CT. On a per patient basis in which PET was evaluated for detecting all metastases, however, the sensitivity jumped to 100%, with 96% specificity.

FDG-PET is useful in detecting distant metastases and recurrent disease in patients with breast cancer. According to a prospective study of 117 patients by Schirrmeister et al [74], FDG-PET was compared with conventional imaging for detection and staging of breast cancer. They report a PET sensitivity of 100% for detecting distant metastases. Pulmonary metastases of seven patients were detected by PET, five of which were not identified on chest radiograph.

Other studies have shown less promising results with PET. Lucas et al [75] evaluated PET in 62 patients who were evaluated after treatment for soft tissue sarcomas. The sensitivity of PET was 87% with a specificity of 100% in detecting pulmonary metastases. This compared with CT that was 100% sensitive and 94% specific. PET, however, identified additional unsuspected metastases. The authors recommend that both modalities, PET and CT, be used as complementary imaging. Results have been mixed with the detection of carcinoid tumor. Although Marom et al [76] have shown that carcinoid can be identified as a malignant focus on FDG-PET, other studies have shown instances of false-negative results [77,78].

Lymph node metastases in the thorax

The detection of unsuspected distant lymph node disease has a significant impact on patient staging and prognosis. On chest radiograph, multiple pulmonary nodules are the most common manifestation of intrathoracic metastases followed by lymph node disease [41,79–81]. Tumors that most frequently have metastases identifiable by chest radiograph include renal and other genitourinary tumors, melanoma, breast, and head and neck tumors. Distribution of lymphadenopathy most commonly identified on radiograph is in the mediastinum, especially in the right paratracheal region [79].

Numerous studies on lung cancer imaging have demonstrated that CT is superior to chest radiographs in detecting lymph node metastases disease. Williams et al [82] demonstrated CT was superior to chest radiograph in the detection of metastatic testicular seminoma. By chest radiograph, metastases were found in 25 of 200 patients. This included mediastinal lymph nodes in 17, pulmonary metastases in 7, pleural effusions in 5, and pleural masses in 2 patients. By CT, however, metastases were found in 30 patients including 21 with mediastinal nodes, 12 with lung metastases, 6 with pleural effusions, and 2 with pleural masses. CT showed disease in five patients who had normal chest radiographs and revealed additional metastases in four patients with abnormal radiographs.

The characterization of lymph node disease by CT is limited by the use of a size threshold to detect abnormal nodes. Lymph nodes are interpreted as abnormal if the short axis diameter is greater than 1 cm. Because of this use of size criteria, enlarged

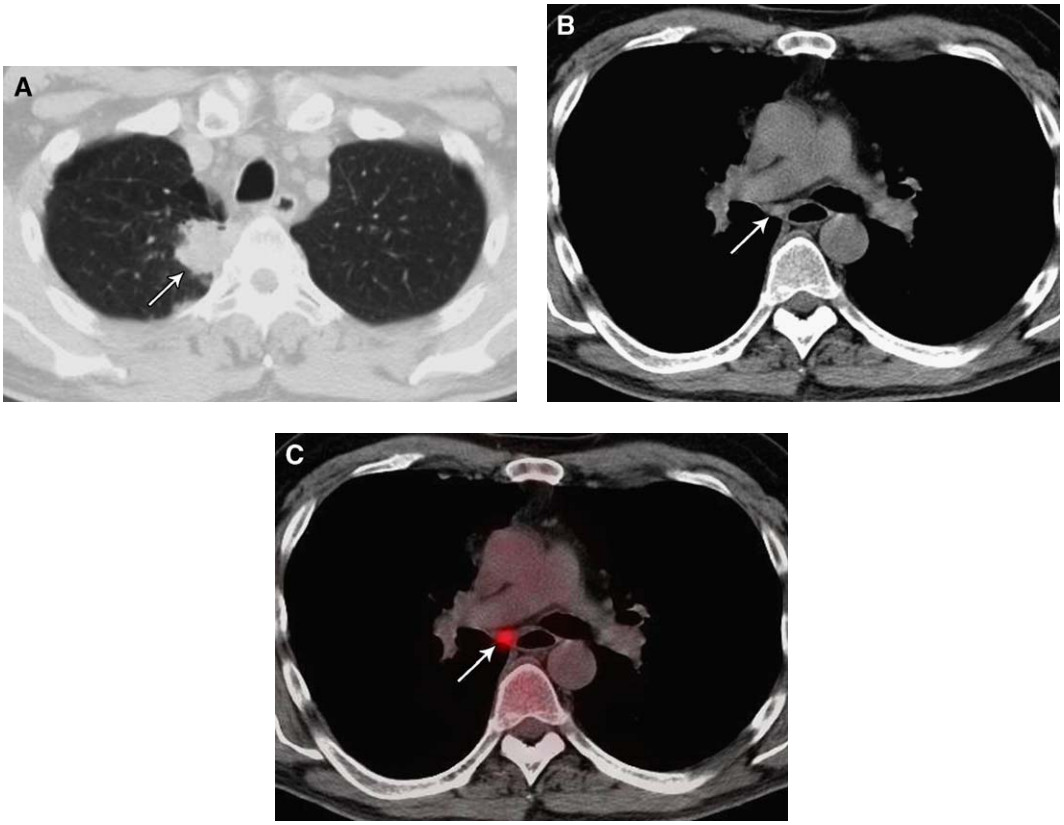

Fig. 11. A 55-year-old man with newly diagnosed right upper lobe mass. (*A*) Lung windows show primary tumor (*arrow*) in right upper lobe. (*B*) CT scan shows normal-size subcarinal lymph node (*arrow*). (*C*) Fusion CT and PET image from dual scanner demonstrates increased FDG uptake in subcarinal lymph node (*arrow*) consistent with metastatic nodal disease.

lymph nodes caused by inflammatory or infectious disease are frequently interpreted as neoplastic. Early metastases in normal-sized lymph nodes are not detected on CT. FDG-PET has improved the specificity of lymph node disease detection by better identifying lymph node involvement with tumor based on tumor glycolysis rather than using morphologic size criteria (Fig. 11). For instance, Eubank et al [83] found PET more accurate in detecting metastatic breast cancer to the mediastinum and internal mammary lymph nodes than CT. PET was 88% accurate compared with CT, which was 73% accurate. Other studies have demonstrated that PET is useful in detecting metastases from the abdomen and lung [84]. PET, however, also has size limitations. Because of limitations in camera resolution, metastatic lymph nodes that measure 5 mm or smaller may not be consistently detected [85]. For instance, although FDG-PET is useful for detecting distant metastases in patients with breast cancer, studies have shown that FDG-PET is extremely limited in detecting sentinel node involvement, and should not be the study of choice for axillary lymph node staging. Studies have shown that PET sensitivity for the detection of sentinel node disease is as low as 20% [86,87].

FDG-PET imaging has improved the radiologic staging of lung cancer because of its reliance on increased metabolism [88]. The added application of fusion imaging has shown even better sensitivity and specificity for the detection of lymph node metastases and recurrent tumor [85,89]. A study by Lardinois et al [85] has shown that the accuracy in lymph node detection and lung cancer staging significantly improved with dual CT-PET imaging in which images were fused.

Pleural metastatic disease

Twenty-two percent of newly diagnosed pleural effusions identified by chest radiograph in adults are malignant in origin [90]. The likelihood of malig-

nancy in a newly diagnosed unilateral pleural effusion increases with a patient's age and the size of the effusion [90,91]. According to Blackman and Rabin [92], 50% of patients with bilateral pleural effusions and normal heart size have malignancy. Metastatic adenocarcinoma is responsible for most (80%) malignant pleural effusions; however, in 7% to 10%, the primary site remains unknown [93–95]. Bronchogenic cancer accounts as the source in 36% to 43% of malignant pleural effusions followed by breast cancer at 9% to 25% and lymphoma at 7% to 10% [94,95].

The upright chest radiograph is the first imaging modality in the evaluation of a pleural effusion, although it is limited in detecting small volumes. According to Blackmore et al [96], the smallest amount of fluid detected is 50 mL when a meniscus sign at the costophrenic angle is identified on a lateral chest film. The approximate volume of fluid identified on a posteroanterior radiograph is 200 mL when a meniscus sign is present. At a volume of 500 mL, an effusion usually obscures the diaphragm. Other studies have shown that lateral decubitus films can detect as little as 5 mL of fluid; however, this technique is often limited if dense soft tissue, bedding, or clothing overlie the targeted dependent lateral thorax [97].

Few published reports have assessed the chest radiograph in evaluating the incidence of malignant effusions for specific tumor types outside of lymphoma. On chest radiographs, the incidence of pleural effusion in patients with primary Hodgkin's disease is 7% to 13% [98–100] and 10% in patients with primary non-Hodgkin's lymphoma [99,101]. With the use of cross-sectional CT, the sensitivity of detecting metastases in the thorax increased. For instance, Filly et al [99] reported that 80% their patients with primary Hodgkin's disease and pleural effusion also had lymphadenopathy on chest radiograph. Castellino [100] reported a 100% incidence on CT.

Ultrasound is sensitive in the detection and quantification of pleural effusions [102,103]. Yang et al [104] found ultrasound useful in characterizing the nature of pleural effusions. Transudates were usually anechoic. Although exudative effusions could also appear anechoic, fluid that was complex, homogenous echogenic, or contained complex septations was specific for an exudate. Associated findings including pleura thickening or underlying pulmonary lesions also indicated an exudate. In their study, only the presence of pleural nodules was useful in detecting malignancy in the pleural space (Fig. 12). Gorg et al [105] reported similar results on ultrasound and found that only the presence of pleural masses was specific

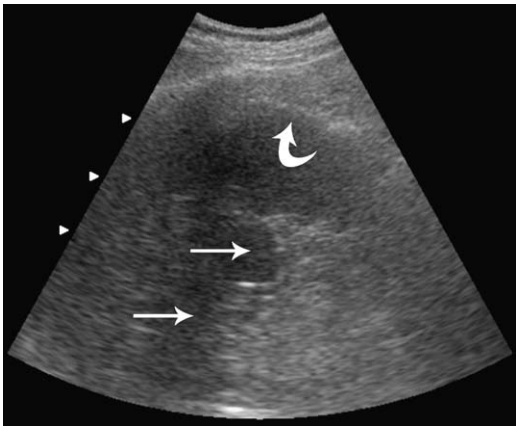

Fig. 12. A 71-year-old woman with biopsy-proved metastatic non–small cell lung carcinoma of the left pleural space. Real-time ultrasound of the pleura demonstrates parietal pleural thickening (*curved arrow*) and a soft tissue pleural mass overlying the diaphragm (*arrows*). (Courtesy of Michael Maher, MD, Boston, MA.)

for malignancy. According to a study by Bradley and Metreweli [106], ultrasound imaging of the pleura was useful in evaluating malignant effusions by both distinguishing benign from malignant pleural masses and providing real-time guidance for needle placement during percutaneous biopsy. For instance, real-time imaging assisted in detecting benign vascular abnormalities, which were readily identified as anechoic and pulsatile. Malignant tumors showed varied echogenicity indicating soft tissue consistency. Other ultrasound findings that correlated to malignancy included interruption of the pleural line (90%) and decreased motion in the mass with respiration.

Although the spatial resolution of CT is excellent, studies with surgical correlation have shown that small pleural tumor deposits can be missed [107]. According to Akaogi et al [108], the presence of small nodules in the interlobar fissures in a patient with lung cancer without an effusion may be the only indication of pleural involvement. Malignant effusions frequently do not demonstrate any pleural changes on contrast-enhanced CT. Approximately 50% of malignant effusions resemble a simple transudative effusion without pleural changes [107,109]. The absence of associated pleural thickening or nodularity does not exclude neoplasia. Several studies have evaluated the use of CT in establishing criteria for detecting malignant pleural disease [107, 109–112]. Arenas-Jimenez et al [107] found that pleural nodules and nodular pleural thickening were the most sensitive and specific findings for malignant pleural effusion (Fig. 13). The finding of mediasti-

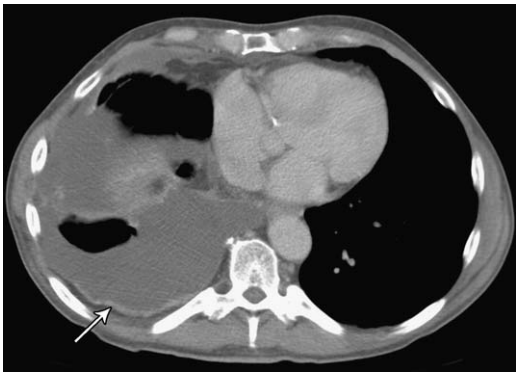

Fig. 13. A 69-year-old man with history of lung cancer. CT scan with intravenous contrast administration shows a loculated pleural effusion with pleural enhancement (*arrow*). Pleural biopsy retrieved during thoracoscopy and pleurodesis showed metastatic adenocarcinoma.

nal and circumferential pleural thickening was also more frequent in malignant disease but could be seen with an empyema. Associated findings, such as the presence of a pulmonary mass or nodules, enlarged mediastinal lymph nodes, chest wall mass, and liver nodules, helped confirm any radiologic suspicion. In patients with lymphoma, ancillary findings of extrapleural tumor or enlarged lymph nodes in the extrapleural space on CT may also help explain the source of pleural disease. A study by Aquino et al [113] found that 41% of patients with lymphoma and pleural effusion had abnormal pleural or extrapleural lymph node disease. Ninety-five percent of the patients with extrapleural tumor had adjacent paraspinal and posterior mediastinal lymph node enlargement.

MR imaging has been reported to be useful in the detection of pleural malignancy. A study by Falaschi et al [114] found that MR imaging was equal to CT in the detection of morphologic changes suggesting malignant pleural disease. The authors also found that MR imaging provided additional information because of changes in signal intensity with malignancy. In six patients, CT was equivocal, whereas MR imaging information was able to distinguish benign from malignant disease. The MR imaging findings they described as most useful were high signal intensity on proton density weighted and T2-weighted studies and the use of lesion-to-muscle ratio in each sequence. Similar results were found by Hierholzer et al [115]. Both CT and MR imaging were sensitive (93% and 96%, respectively) in detecting morphologic changes of malignant pleural disease (ie, mediastinal pleural thickening, nodularity, irregular pleural contour, and infiltration of the chest wall or diaphragm). MR imaging was able to display increase signal indicating malignancy in T2-weighted and contrast-enhanced T1-weighted series with sensitivities of 91% and 93%, respectively. No significant features were found on non–contrast enhanced T1-weighted images.

As a general imaging tool for routine pretreatment evaluation of thoracic malignancy CT is more practical and cost effective. MR imaging, however, is more sensitive in detecting tumor involvement of the chest wall and diaphragm. MR imaging is superior to CT in the assessment of chest wall and mediastinal

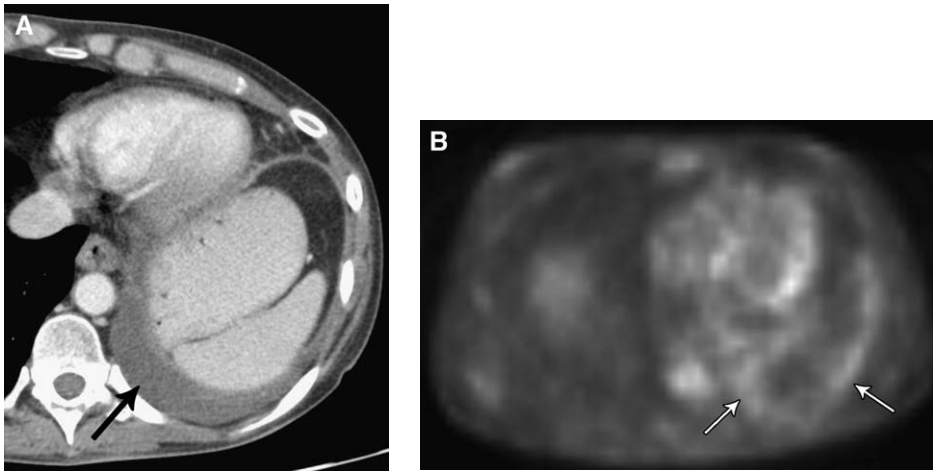

Fig. 14. A 46-year-old woman with metastatic adenocarcinoma of the lung. (*A*) CT scan shows a left pleural effusion (*arrow*) with no evidence for pleural nodularity or enhancement. (*B*) FDG-PET scan shows increase uptake in the pleural space (*arrows*). The effusion was metastatic on cytology.

involvement by superior sulcus tumors. Carlsen et al [116] also found MR imaging useful in the pretreatment assessment of patients with mediastinal lymphoma and suspected involvement of the chest wall and pleura. MR imaging detected chest wall or pleural malignancy in 22 of 57 patients compared with CT, which only detected disease in 12 patients.

Studies have shown that FDG-PET is more sensitive than CT in the detection of malignant pleural disease. Bury et al [117] describe an increase in FDG uptake in the pleura (Fig. 14) in all 16 patients with malignant pleural disease. As with most studies with FDG-PET, infection may mimic malignancy. In their study, two patients with pleural empyema also showed abnormal uptake that mimicked tumor. Gupta et al [118] reported a sensitivity and specificity of 88.8% and 94.1% of FDG-PET in correctly distinguishing benign from malignant pleural disease in patients with lung cancer. Extra care should be taken when interpreting any FDG-PET scan of a patient with malignant pleural disease who was previously treated by talc pleurodesis. Talc, which causes a chronic granulomatous response in the pleural space, appears intensely hot on FDG-PET and mimics tumor [119]. Careful correlation of PET findings with CT for detection of pleural foci of increased attenuation is necessary to distinguish these abnormal foci on PET from true neoplasm (Fig. 15).

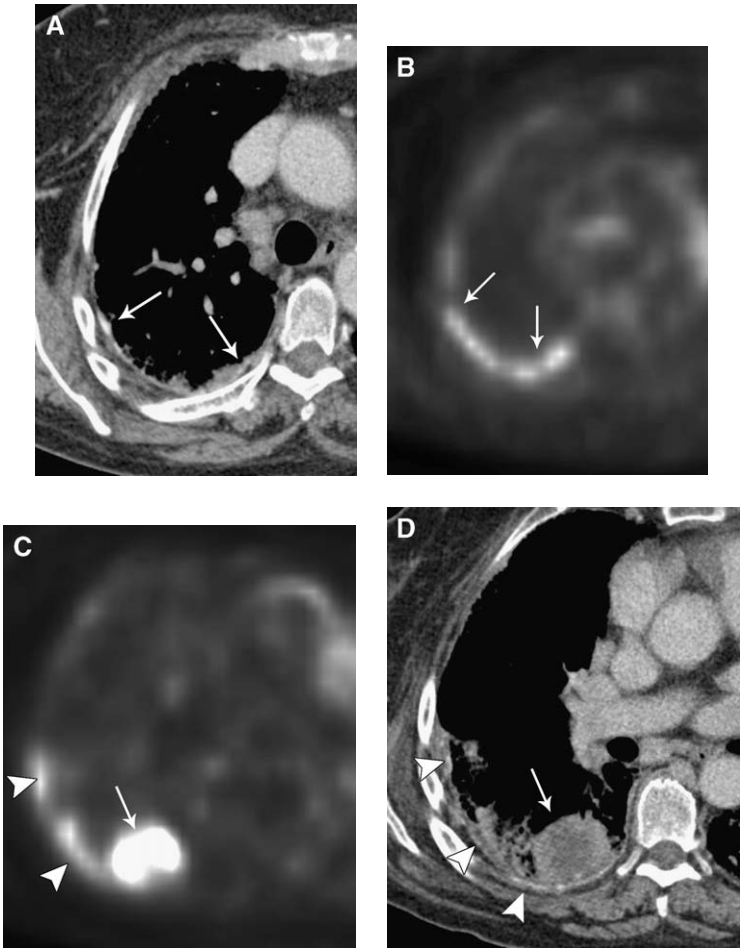

Fig. 15. A 75-year-old woman with history of metastatic pleural disease and prior talc pleurodesis in the right thorax. (*A*) CT scan shows foci of increased attenuation consistent with talc deposits (*arrows*). (*B*) FDG-PET shows intense uptake in the pleural space in the same distribution as the talc deposits (*arrows*). (*C*) In the lower thorax there is a large focus of increased FDG uptake (*arrow*) adjacent to the linear pleural talc deposits (*arrowheads*). (*D*) CT shows a metastatic focus (*arrow*) and adjacent talc in the pleura (*arrowheads*).

This abnormal uptake does not resolve over time and detection of areas of new increased FDG uptake suggests recurrent disease.

References

[1] Kim YH, Lee KS, Primack SL, et al. Small pulmonary nodules on CT accompanying surgically resectable lung cancer: likelihood of malignancy. J Thorac Imaging 2002;17:40–6.

[2] Chalmers N. The significance of pulmonary nodules detected by CT but not by chest radiography in tumour staging. Clin Radiol 1991;44:410–2.

[3] Kronawitter U, Kemeny NE, Heelan R, et al. Evaluation of chest computed tomography in the staging of patients with potentially resectable liver metastases from colorectal carcinoma. Cancer 1999; 86:229–35.

[4] Povoski SP, Fong Y, Sgouros SC, et al. Role of chest CT in patients with negative chest x-rays referred for hepatic colorectal metastases. Ann Surg Oncol 1998; 5:9–15.

[5] Picci P, Vanel D, Briccoli A, et al. Computed tomography of pulmonary metastases from osteosarcoma: the less poor technique. A study of 51 patients with histological correlation. Ann Oncol 2001;12:1601–4.

[6] Fernandez EB, Colon E, McLeod DG, et al. Efficacy of radiographic chest imaging in patients with testicular cancer. Urology 1994;44:243–8 [discussion: 8–9].

[7] Lim DJ, Carter MF. Computerized tomography in the preoperative staging for pulmonary metastases in patients with renal cell carcinoma. J Urol 1993;150: 1112–4.

[8] Warner G, Cox G. Evaluation of chest radiography versus chest computed tomography in screening for pulmonary malignancy in advanced head and neck cancer. J Otolaryngol 2003;32:107–9.

[9] Heaston DK, Putman CE, Rodan BA, et al. Solitary pulmonary metastases in high-risk melanoma patients: a prospective comparison of conventional and computed tomography. AJR Am J Roentgenol 1983; 141:169–74.

[10] Reiner B, Siegel E, Sawyer R, et al. The impact of routine CT of the chest on the diagnosis and management of newly diagnosed squamous cell carcinoma of the head and neck. AJR Am J Roentgenol 1997;169:667–71.

[11] Yamada H, Katoh H, Kondo S, et al. Surgical treatment of pulmonary recurrence after hepatectomy for colorectal liver metastases. Hepatogastroenterology 2002;49:976–9.

[12] Koong HN, Pastorino U, Ginsberg RJ. Is there a role for pneumonectomy in pulmonary metastases? Ann Thorac Surg 1999;68:2039–43.

[13] Al-Mehdi AB, Tozawa K, Fisher AB, et al. Intravascular origin of metastasis from the proliferation of endothelium-attached tumor cells: a new model for metastasis. Nat Med 2000;6:100–2.

[14] Wong CW, Song C, Grimes MM, et al. Intravascular location of breast cancer cells after spontaneous metastasis to the lung. Am J Pathol 2002;161: 749–53.

[15] Milne EN, Zerhouni EA. Blood supply of pulmonary metastases. J Thorac Imaging 1987;2:15–23.

[16] Stackpole CW. Intrapulmonary spread of established B16 melanoma lung metastases and lung colonies. Invasion Metastasis 1990;10:267–80.

[17] Alterman AL, Fornabaio DM, Stackpole CW. Metastatic dissemination of B16 melanoma: pattern and sequence of metastasis. J Natl Cancer Inst 1985;75: 691–702.

[18] Ren H, Hruban RH, Kuhlman JE, et al. Computed tomography of inflation-fixed lungs: the beaded septum sign of pulmonary metastases. J Comput Assist Tomogr 1989;13:411–6.

[19] Cahan WG, Shah JP, Castro EB. Benign solitary lung lesions in patients with cancer. Ann Surg 1978;187: 241–4.

[20] Steele JD. The Solitary Pulmonary Nodule. Report of a Cooperative Study of Resected Asymptomatic Solitary Pulmonary Nodules in Males. J Thorac Cardiovasc Surg 1963;46:21–39.

[21] Toomes H, Delphendahl A, Manke HG, et al. The coin lesion of the lung: a review of 955 resected coin lesions. Cancer 1983;51:534–7.

[22] Schlumberger M, Arcangioli O, Piekarski JD, et al. Detection and treatment of lung metastases of differentiated thyroid carcinoma in patients with normal chest X-rays. J Nucl Med 1988;29:1790–4.

[23] Piekarski JD, Schlumberger M, Leclere J, et al. Chest computed tomography (CT) in patients with micronodular lung metastases of differentiated thyroid carcinoma. Int J Radiat Oncol Biol Phys 1985;11: 1023–7.

[24] Lee K, Kim T, Han J, et al. Diffuse micronodular lung disease: HRCT and pathologic findings. J Comput Assist Tomogr 1999;23:99–106.

[25] Hirakata K, Nakata H, Haratake J. Appearance of pulmonary metastases on high-resolution CT scans: comparison with histopathologic findings from autopsy specimens. AJR Am J Roentgenol 1993;161: 37–43.

[26] Primack SL, Hartman TE, Lee KS, et al. Pulmonary nodules and the CT halo sign. Radiology 1994;190: 513–5.

[27] Patel A, Ryu J. Angiosarcoma in the lung. Chest 1993;103:1531–5.

[28] Benditt JO, Farber HW, Wright J, et al. Pulmonary hemorrhage with diffuse alveolar infiltrates in men with high-volume choriocarcinoma. Ann Intern Med 1988;109:674–5.

[29] Gaeta M, Blandino A, Scribano E, et al. Computed tomography halo sign in pulmonary nodules: frequency and diagnostic value. J Thorac Imaging 1999; 14:109–13.

[30] Sidhu GS, Wieczorek R, Cassai ND, et al. The concept of bronchioloalveolar cell adenocarcinoma: redefinition, a critique of the 1999 WHO classification, and an ultrastructural analysis of 155 cases. Int J Surg Pathol 2003;11:89–99.
[31] deSantos LA, Lindell Jr MM, Goldman AM, et al. Calcification within metastatic pulmonary nodules from synovial sarcoma. Orthopedics 1978;1:141–4.
[32] Cockshott WP, Hendrickse JP. Pulmonary calcification at the site of trophoblastic metastases. Br J Radiol 1969;42:17–20.
[33] Hall FM, Frank HA, Cohen RB, et al. Ossified pulmonary metastases from giant cell tumor of bone. AJR Am J Roentgenol 1976;127:1046–7.
[34] Jimenez JM, Casey SO, Citron M, et al. Calcified pulmonary metastases from medullary carcinoma of the thyroid. Comput Med Imaging Graph 1995;19: 325–8.
[35] Franchi M, La Fianza A, Babilonti L, et al. Serous carcinoma of the ovary: value of computed tomography in detection of calcified pleural and pulmonary metastatic implants. Gynecol Oncol 1990;39:85–8.
[36] Rosenfield AT, Sanders RC, Custer LE. Widespread calcified metastases from adenocarcinoma of the jejunum. Am J Dig Dis 1975;20:990–3.
[37] Chaudhuri MR. Cavitary pulmonary metastases. Thorax 1970;25:375–81.
[38] Dodd GD, Boyle JJ. Excavating pulmonary metastases. AJR Am J Roentgenol 1961;85:277–93.
[39] Thalinger AR, Rosenthal SN, Borg S, et al. Cavitation of pulmonary metastases as a response to chemotherapy. Cancer 1980;46:1329–32.
[40] Rovirosa A, Salud A, Felip E, et al. Cavitary pulmonary metastases in transitional cell carcinoma of the urinary bladder. Urol Int 1992;48:102–4.
[41] Shin MS, Shingleton HM, Partridge EE, et al. Squamous cell carcinoma of the uterine cervix: patterns of thoracic metastases. Invest Radiol 1995;30:724–9.
[42] Alexander PW, Sanders C, Nath H. Cavitary pulmonary metastases in transitional cell carcinoma of urinary bladder. AJR Am J Roentgenol 1990;154: 493–4.
[43] Charig MJ, Williams MP. Pulmonary lacunae: sequelae of metastases following chemotherapy. Clin Radiol 1990;42:93–6.
[44] Lee KS, Kim TS, Fujimoto K, et al. Thoracic manifestation of Wegener's granulomatosis: CT findings in 30 patients. Eur Radiol 2003;13:43–51.
[45] Ohdama S, Akagawa S, Matsubara O, et al. Primary diffuse alveolar septal amyloidosis with multiple cysts and calcification. Eur Respir J 1996;9:1569–71.
[46] Essadki O, Chartrand-Lefebvre C, Finet JF, et al. Cystic pulmonary metastasis simulating a diagnosis of histiocytosis X. J Radiol 1998;79:886–8.
[47] Shepard J, Moore E, Templeton P, et al. Pulmonary intravascular tumor emboli: dilated and beaded peripheral pulmonary arteries at CT. Radiology 1993; 187:797–801.
[48] Kang C, Choi J, Kim H, et al. Lung metastases manifesting as pulmonary infarction by mucin and tumor embolization: radiographic, high-resolution CT, and pathologic findings. J Comput Assist Tomogr 1999;23:644–6.
[49] Odeh M, Oliven A, Misselevitch I, et al. Acute cor pulmonale due to tumor cell microemboli. Respiration 1997;64:384–7.
[50] Chan CK, Hutcheon MA, Hyland RH, et al. Pulmonary tumor embolism: a critical review of clinical, imaging, and hemodynamic features. J Thorac Imaging 1987;2:4–14.
[51] Schriner RW, Ryu JH, Edwards WD. Microscopic pulmonary tumor embolism causing subacute cor pulmonale: a difficult antemortem diagnosis. Mayo Clin Proc 1991;66:143–8.
[52] Braman SS, Whitcomb ME. Endobronchial metastasis. Arch Intern Med 1975;135:543–7.
[53] Litle VR, Christie NA, Fernando HC, et al. Photodynamic therapy for endobronchial metastases from nonbronchogenic primaries. Ann Thorac Surg 2003; 76:370–5.
[54] Baumgartner WA, Mark JB. Metastatic malignancies from distant sites to the tracheobronchial tree. J Thorac Cardiovasc Surg 1980;79:499–503.
[55] Mason AC, White CS. CT appearance of endobronchial non-Hodgkin lymphoma. J Comput Assist Tomogr 1994;18:559–61.
[56] Munk PL, Muller NL, Miller RR, et al. Pulmonary lymphangitic carcinomatosis: CT and pathologic findings. Radiology 1988;166:705–9.
[57] Zerhouni EA, Naidich DP, Stitik FP, et al. Computed tomography of the pulmonary parenchyma. Part 2: Interstitial disease. J Thorac Imaging 1985;1:54–64.
[58] Ikezoe J, Godwin JD, Hunt KJ, et al. Pulmonary lymphangitic carcinomatosis: chronicity of radiographic findings in long-term survivors. AJR Am J Roentgenol 1995;165:49–52.
[59] Stein MG, Mayo J, Muller N, et al. Pulmonary lymphangitic spread of carcinoma: appearance on CT scans. Radiology 1987;162:371–5.
[60] Meziane MA, Hruban RH, Zerhouni EA, et al. High resolution CT of the lung parenchyma with pathologic correlation. Radiographics 1988;8:27–54.
[61] Berkman N, Breuer R, Kramer M, et al. Pulmonary involvement in lymphoma. Leuk Lymphoma 1996; 20:229–37.
[62] Tanaka N, Matsumoto T, Miura G, et al. CT findings of leukemic pulmonary infiltration with pathologic correlation. Eur Radiol 2002;12:166–74.
[63] Heyneman LE, Johkoh T, Ward S, et al. Pulmonary leukemic infiltrates: high-resolution CT findings in 10 patients. AJR Am J Roentgenol 2000;174: 517–21.
[64] Johkoh T, Ikezoe J, Tomiyama N, et al. CT findings in lymphangitic carcinomatosis of the lung: correlation with histologic findings and pulmonary function tests. AJR Am J Roentgenol 1992;158:1217–22.
[65] Honda O, Johkoh T, Ichikado K, et al. Comparison of high resolution CT findings of sarcoidosis, lym-

phoma, and lymphangitic carcinoma: is there any difference of involved interstitium? J Comput Assist Tomogr 1999;23:374–9.

[66] Lewis E, Caskey C, Fishman E. Lymphoma of the lung: CT findings in 31 patients. AJR Am J Roentgenol 1991;156:711–4.

[67] Aquino SL, Chiles C. Distinction of consolidative bronchioloalveolar carcinoma from pneumonia: do CT criteria work? AJR Am J Roentgenol 1998;171: 359–63.

[68] Strollo DC, Rosado-de-Christenson ML, Franks TJ. Reclassification of cystic bronchioloalveolar carcinomas to adenocarcinomas based on the revised World Health Organization Classification of Lung and Pleural Tumours. J Thorac Imaging 2003;18: 59–66.

[69] Akira M, Atagi S, Kawahara M, et al. High-resolution CT findings of diffuse bronchioloalveolar carcinoma in 38 patients. AJR Am J Roentgenol 1999;173: 1623–9.

[70] Wolff SD, Kuhlman JE, Fishman EK. Thoracic Kaposi sarcoma in AIDS: CT findings. J Comput Assist Tomogr 1993;17:60–2.

[71] Majhail NS, Urbain JL, Albani JM, et al. F-18 fluorodeoxyglucose positron emission tomography in the evaluation of distant metastases from renal cell carcinoma. J Clin Oncol 2003;21:3995–4000.

[72] Imdahl A, Reinhardt MJ, Nitzsche EU, et al. Impact of 18F-FDG-positron emission tomography for decision making in colorectal cancer recurrences. Langenbecks 2000;385:129–34.

[73] Rinne D, Baum RP, Hor G, et al. Primary staging and follow-up of high risk melanoma patients with whole-body 18F-fluorodeoxyglucose positron emission tomogrphy: results of a prospective study of 100 patients. Cancer 1998;82:1664–71.

[74] Schirrmeister H, Kuhn T, Guhmann A, et al. Fluorine-18 2-deoxy-D-glucose PET in the preoperative staging of breast cancer: comparison with the standard staging procedures. Eur J Nucl Med 2001; 28:351–8.

[75] Lucas JD, O'Doherty MJ, Wong JC, et al. Evaluation of fluorodeoxyglucose positron emission tomography in the management of soft-tissue sarcomas. J Bone Joint Surg Br 1998;80:441–7.

[76] Marom EM, Sarvis S, Herndon JE, et al. T1 lung cancers: sensitivity of diagnosis with fluorodeoxyglucose PET. Radiology 2002;223(2):453–9.

[77] Jadvar H, Segall GM. False-negative fluorine-18-FDG PET in metastatic carcinoid. J Nucl Med 1997; 38:1382–3.

[78] Erasmus JJ, McAdams HP, Patz Jr EF, et al. Evaluation of primary pulmonary carcinoid tumors using FDG PET. AJR Am J Roentgenol 1998;170: 1369–73.

[79] McLoud TC, Kalisher L, Stark P, et al. Intrathoracic lymph node metastases from extrathoracic neoplasms. AJR Am J Roentgenol 1978;131:403–7.

[80] Chen JT, Dahmash NS, Ravin CE, et al. Metastatic melanoma in the thorax: report of 130 patients. AJR Am J Roentgenol 1981;137:293–8.

[81] Kutty K, Varkey B. Incidence and distribution of intrathoracic metastases from renal cell carcinoma. Arch Intern Med 1984;144:273–6.

[82] Williams MP, Husband JE, Heron CW. Intrathoracic manifestations of metastatic testicular seminoma: a comparison of chest radiographic and CT findings. AJR Am J Roentgenol 1987;149:473–5.

[83] Eubank WB, Mankoff DA, Takasugi J, et al. 18fluorodeoxyglucose positron emission tomography to detect mediastinal or internal mammary metastases in breast cancer. J Clin Oncol 2001;19:3516–23.

[84] Schirrmeister H, Kuhn T, Guhlmann A, et al. Fluorine-18 2-deoxy-2-fluoro-D-glucose PET in the preoperative staging of breast cancer: comparison with the standard staging procedures. Eur J Nucl Med 2001;28:351–8.

[85] Lardinois D, Weder W, Hany TF, et al. Staging of non-small-cell lung cancer with integrated positron-emission tomography and computed tomography. N Engl J Med 2003;348:2500–7.

[86] Barranger E, Grahek D, Antoine M, et al. Evaluation of fluorodeoxyglucose positron emission tomography in the detection of axillary lymph node metastases in patients with early-stage breast cancer. Ann Surg Oncol 2003;10:622–7.

[87] van der Hoeven JJ, Hoekstra OS, Comans EF, et al. Determinants of diagnostic performance of [F-18] fluorodeoxyglucose positron emission tomography for axillary staging in breast cancer. Ann Surg 2002; 236:619–24.

[88] Pieterman RM, van Putten JWG, Mewuzelar JJ, et al. Preoperative staging of non-small-cell lung cancer with positron emission tomography. N Engl J Med 2000;343:254–61.

[89] Aquino SL, Asmuth JC, Moore RH, et al. Improved image interpretation with registered thoracic CT and positron emission tomography data sets. AJR Am J Roentgenol 2002;178:939–44.

[90] Marel M, Zrustova M, Stasny B, et al. The incidence of pleural effusion in a well-defined region: epidemiologic study in central Bohemia. Chest 1993;104: 1486–9.

[91] Salyer WR, Eggleston JC, Erozan YS. Efficacy of pleural needle biopsy and pleural fluid cytopathology in the diagnosis of malignant neoplasm involving the pleura. Chest 1975;67:536–9.

[92] Blackman NS, Rabin CB. Bilateral pleural effusion; its significance in association with a heart of normal size. J Mt Sinai Hosp N Y 1957;24:45–53.

[93] Monte SA, Ehya H, Lang WR. Positive effusion cytology as the initial presentation of malignancy. Acta Cytol 1987;31:448–52.

[94] Sahn SA. Malignant pleural effusions. Clin Chest Med 1985;6:113–25.

[95] O'Donovan PB, Eng P. Pleural changes in malignant pleural effusions: appearance on computed tomography. Cleve Clin J Med 1994;61:127–31 [quiz: 62].

[96] Blackmore CC, Black WC, Dallas RV, et al. Pleural fluid volume estimation: a chest radiograph prediction rule. Acad Radiol 1996;3:103–9.
[97] Moskowitz H, Platt RT, Schachar R, et al. Roentgen visualization of minute pleural effusion: an experimental study to determine the minimum amount of pleural fluid visible on a radiograph. Radiology 1973; 109:33–5.
[98] Castellino RA, Filly R, Blank N. Routine full-lung tomography in the initial staging and treatment planning of patients with Hodgkin's disease and non-Hodgkin's lymphoma. Cancer 1976;38:1130–6.
[99] Filly R, Bland N, Castellino RA. Radiographic distribution of intrathoracic disease in previously untreated patients with Hodgkin's disease and non-Hodgkin's lymphoma. Radiology 1976;120:277–81.
[100] Castellino RA. Diagnostic imaging evaluation of Hodgkin's disease and non-Hodgkin's lymphoma. Cancer 1991;67(4 Suppl):1177–80.
[101] Das DK, Gupta SK, Ayyagari S, et al. Pleural effusions in non-Hodgkin's lymphoma: a cytomorphologic, cytochemical and immunologic study. Acta Cytol 1987;31:119–24.
[102] Kocijancic I, Vidmar K, Ivanovi-Herceg Z. Chest sonography versus lateral decubitus radiography in the diagnosis of small pleural effusions. J Clin Ultrasound 2003;31:69–74.
[103] Eibenberger KL, Dock WI, Ammann ME, et al. Quantification of pleural effusions: sonography versus radiography. Radiology 1994;191:681–4.
[104] Yang PC, Luh KT, Chang DB, et al. Value of sonography in determining the nature of pleural effusion: analysis of 320 cases. AJR Am J Roentgenol 1992;159:29–33.
[105] Gorg C, Restrepo I, Schwerk WB. Sonography of malignant pleural effusion. Eur Radiol 1997;7:1195–8.
[106] Bradley MJ, Metreweli C. Ultrasound in the diagnosis of the juxta-pleural lesion. Br J Radiol 1991; 64:330–3.
[107] Arenas-Jimenez J, Alonso-Charterina S, Sanchez-Paya J, et al. Evaluation of CT findings for diagnosis of pleural effusions. Eur Radiol 2000;10:681–90.
[108] Akaogi E, Mitsui K, Onizuka M, et al. Pleural dissemination in non-small cell lung cancer: results of radiological evaluation and surgical treatment. J Surg Oncol 1994;57:33–9.
[109] Aquino SL, Webb WR, Gushiken BJ. Pleural exudates and transudates: diagnosis with contrast-enhanced CT. Radiology 1994;192:803–8.
[110] Leung AN, Muller NL, Miller RR. CT in differential diagnosis of diffuse pleural disease. AJR Am J Roentgenol 1990;154:487–92.
[111] Mori K, Hirose T, Machida S, et al. Helical computed tomography diagnosis of pleural dissemination in lung cancer: comparison of thick-section and thin-section helical computed tomography. J Thorac Imaging 1998;13:211–8.
[112] Traill ZC, Davies RJ, Gleeson FV. Thoracic computed tomography in patients with suspected malignant pleural effusions. Clin Radiol 2001;56:193–6.
[113] Aquino SL, Chen MY, Kuo WT, et al. The CT appearance of pleural and extrapleural disease in lymphoma. Clin Radiol 1999;54:647–50.
[114] Falaschi F, Battolla L, Mascalchi M, et al. Usefulness of MR signal intensity in distinguishing benign from malignant pleural disease. AJR Am J Roentgenol 1996;166:963–8.
[115] Hierholzer J, Luo L, Bittner RC, et al. MRI and CT in the differential diagnosis of pleural disease. Chest 2000;118:604–9.
[116] Carlsen SE, Bergin CJ, Hoppe RT. MR imaging to detect chest wall and pleural involvement in patients with lymphoma: effect on radiation therapy planning. AJR Am J Roentgenol 1993;160:1191–5.
[117] Bury T, Paulus P, Dowlati A, et al. Evaluation of pleural diseases with FDG-PET imaging: preliminary report. Thorax 1997;52:187–9.
[118] Gupta NC, Rogers JS, Graeber GM, et al. Clinical role of F-18 fluorodeoxyglucose positron emission tomography imaging in patients with lung cancer and suspected malignant pleural effusion. Chest 2002; 122:1918–24.
[119] Kwek B, Aquino SL, Fischman AJ. FDG-PET and computed tomography after talc pleurodesis. Chest 2004;125:2356–60.

ELSEVIER
SAUNDERS

Radiol Clin N Am 43 (2005) 497 – 512

RADIOLOGIC
CLINICS
of North America

Radiology of Community-Acquired Pneumonia

Robert D. Tarver, MD, FACR*, Shawn D. Teague, MD,
Darel E. Heitkamp, MD, Dewey J. Conces, Jr, MD

Department of Radiology, Indiana University School of Medicine, Wishard Memorial Hospital, 1001 West 10th Street, Indianapolis, IN 46202, USA

This article discusses the role of radiology in the evaluation of patients with community-acquired pneumonia. The experience the authors have gained in working more than 20 years in a large city county public hospital has helped them write this article. In addition, this article is an outgrowth of a popular course given for several years at the Radiologic Society of North America in Chicago. There are few recent scientific articles written on the radiology of community-acquired pneumonia. Much of the material contained in this article has been gathered from a few excellent textbooks on chest radiology. For further reading and a more complete discussion of community-acquired pneumonia, the reader is directed to any of the quoted articles. The best sources for information on community-acquired pneumonia are chapter 5 on "Pulmonary Infection" in the textbook by Muller et al [1], and a great article by Gharib and Stern [2].

In the United States pneumonia is the sixth leading cause of death and the number one cause of death from infection. The diagnosis of a lower respiratory infection is based on a careful clinical evaluation, plus appropriate radiographic and laboratory studies. Pulmonary infections should be thought of as occurring in various clinical subsets: community acquired, nosocomial, and immunocompromised patient populations. These clinical features should be correlated with the chest radiographic features to limit the differential diagnosis of possible causative pathogens. This approach is not foolproof because many patients are in overlap categories and many pathogens can have overlapping features, but a systematic approach can help the radiologist limit the differential diagnosis of patients with lower respiratory infections [2,3].

The basic and most used imaging tool to diagnose pneumonia is the chest radiograph. Pulmonary infections are the most common reason for obtaining a chest radiograph. The chest radiograph is often regarded as the reference standard for the diagnosis of community-acquired pneumonia. CT is used further to characterize complex pneumonias, look for complications, or detect underlying disease within the lung or mediastinum. CT can also detect some pneumonias that are not visible on chest radiograph. CT plays an important role in differentiating lung abscess from empyema [3].

The etiology of community-acquired pneumonia varies widely according to the different reviews published. It is influenced by the geographic area, the population studied, and the diagnostic methods used. The most common bacterial agents responsible for community-acquired pneumonia are *Streptococcus pneumoniae*, *Mycoplasma pneumoniae*, *Chlamydia pneumoniae*, and *Legionella pneumophila*. *Staphylococcus aureus* may complicate viral pneumonia. Community-acquired pneumonia may be caused by gram-negative organisms in elderly patients, alcoholics, patients with cardiopulmonary disease, and by the widespread use of broad-spectrum antibiotics. Other authors may list viral pneumonia as the second most common cause of community-acquired pneumonia and include *Haemophilus influenza* as the third most common organism. Most patients suspected of having pneumonia are started on an

* Corresponding author.
E-mail address: rtarver@iupui.edu (R.D. Tarver).

0033-8389/05/$ – see front matter © 2005 Elsevier Inc. All rights reserved.
doi:10.1016/j.rcl.2005.02.005

antibiotic that covers a number of common organisms and the treatment is not altered if the patient does well. In addition, most patients do not have a positive culture to guide the antibiotic treatment. Although sputum cultures and blood cultures are often obtained at the time of admission, their results are not positive or helpful in most cases. Further evaluation with bronchoscopy, pleural fluid analysis, pulmonary consultation, repeat chest radiographs, chest CT, and repeat blood cultures is usually not obtained until the patient fails initial treatment [3,4].

Patterns of pulmonary infection

Infection of the lungs can be confined to the airways or to the lung parenchyma. The patterns of infection in the lung parenchyma can be divided into radiologic patterns: lobar (nonsegmental) pneumonia; bronchopneumonia (lobular pneumonia); and interstitial pneumonia. These patterns can be recognized with sufficient frequency and are associated with different causative organisms in enough cases that their recognition is useful diagnostically. For example, lobar pneumonia is usually of bacterial origin, most commonly *S pneumoniae* or *Klebsiella pneumoniae*, whereas diffuse interstitial pneumonia most commonly results from *Pneumocystis carinii* [1–3,5].

There are, however, limitations to the pattern approach. There is variation in the radiologic manifestations of pneumonia caused by specific organisms, and sometimes it is not possible to fit an individual case into the categories of lobar pneumonia, bronchopneumonia, and interstitial pneumonia. Many factors can modify the radiologic manifestations of pulmonary infection, including the age and immunologic status of the patient and the state of the underlying lung. In addition, the radiographic pattern can be different through the time course of the infection, with opacities often becoming more confluent as the infection worsens [3].

Infection involving predominantly the airways may be limited to the trachea, bronchi, or bronchioles. Viral and mycoplasmal organisms are the most frequent pathogenic agents. Bronchiolitis may be associated with a normal radiograph or may result in accentuation of lung markings or a reticulonodular pattern. The pattern of centrilobular nodular and branching linear opacities has been referred to as ''tree-in-bud'' and is seen most commonly in infectious bronchiolitis and endobronchial spread of tuberculosis or other mycobacterial infection.

Lobar pneumonia

Lobar consolidation involving single or, less commonly, multiple lobes is the most common pattern of presentation of community-acquired pneumococcal pneumonia in patients requiring hospitalization. Lobar pneumonia can occur with other organisms. Lobar pneumonia is a result of the rapid production of edema fluid with relatively minimal cellular reaction, occurring initially and primarily in the periphery of the lung, then spreading from acinus to acinus. Radiographically, lobar pneumonia is manifested by nonsegmental, homogenous consolidation involving predominantly or exclusively one lobe (Fig. 1). The larger bronchi often remain patent and air containing, creating an air bronchogram [1,2,5].

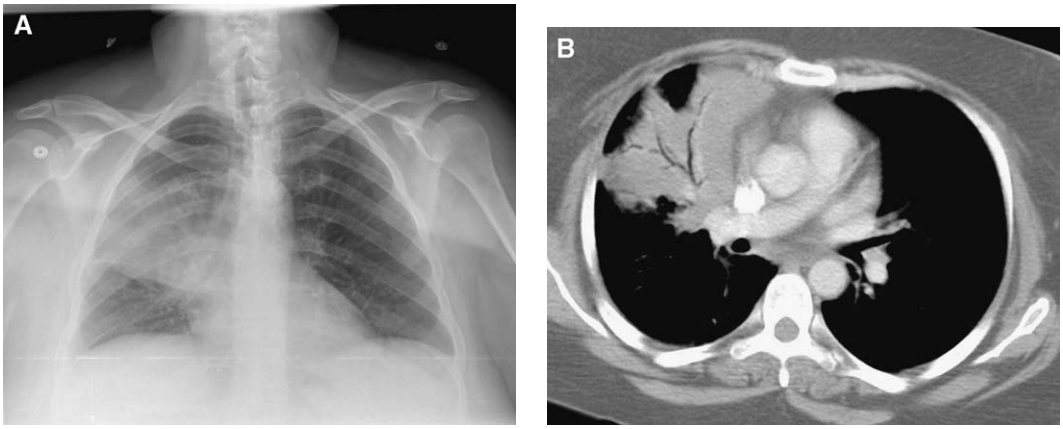

Fig. 1. Right upper lobe pneumonia caused by *S pneumoniae*. Posteroanterior (PA) chest (*A*) and CT scan (*B*) soft windows demonstrating air bronchogram.

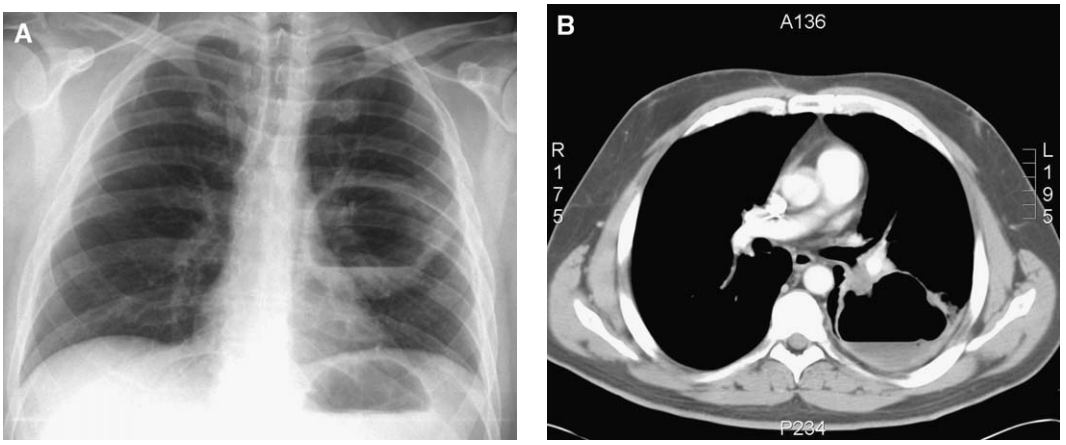

Fig. 2. Lung abscess. (*A*) PA chest. (*B*) CT scan.

Bronchopneumonia

Bronchopneumonia is exemplified by infection with *S aureus*, most gram-negative bacteria, and some fungi. Bronchopneumonia infections are centered on large inflamed airways with patchy involvement and a subsequent patchy appearance. Radiographically mild bronchopneumonia results in peribronchial thickening and poorly defined air-space opacities. More severe disease results in inhomogeneous, patchy areas of consolidation that usually involve several lobes. Consolidation involving the terminal and respiratory bronchioles and adjacent alveoli results in poorly defined centrilobular nodular opacities measuring 4 to 10 mm in diameter (air-space nodules); extension to involve the entire secondary lobule (lobular consolidation) may be seen [1,2,6].

Interstitial pneumonia

Interstitial pneumonia is caused typically by viruses, mycoplasma, or *P carinii*. The pattern is characterized by edema and an inflammatory cellular infiltrate situated predominantly in the interstitial tissue of the alveolar septa and surrounding small airways and vessels. The radiographic manifestations of interstitial pneumonia resulting from viral or mycoplasma infection consist of a reticular or reticulonodular pattern [1,2].

Pulmonary abscess

Pulmonary abscesses vary in size from those that can be seen only with the microscope to those that occupy a large area of a pulmonary lobe. The radiologic manifestations consist of single or multiple cavities that may be isolated or occur within areas of consolidation. The internal margins of the abscesses are smooth in most abscesses and irregular in approximately 10% of cases. Air-fluid levels are present in most cases, and adjacent parenchymal consolidation occurs in nearly half of the cases (Fig. 2). Anaerobic bacteria are often the cause. Other relatively common agents are *S aureus* and *Pseudomonas aeruginosa*. Pulmonary gangrene is manifest by the development of fragments of necrotic lung within an abscess cavity [7].

Empyema

Empyema is the presence of infection in the pleural space. Most pleural effusions associated with pneumonia are sterile sympathetic effusions (Fig. 3). If the course of the pneumonia is prolonged the

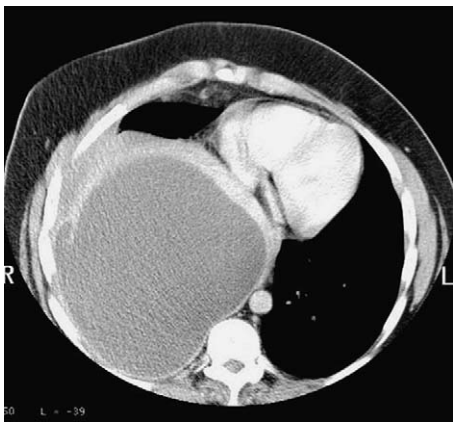

Fig. 3. CT scan of empyema.

pleural effusion is usually sampled. There are three stages in the development of empyema. In the first stage the fluid is free flowing. In the second stage the fluid develops within it fibrous strands. The third stage of an empyema is the development of more solid material within the pleural space, almost jelly-like. These stages are important to recognize because they affect what methods may be needed to remove or sample the empyema. In the first stage the empyema may be treated with repeated needle aspiration or small pleural drain if needed. The second stage may need a large-bore chest tube and fibrolytic therapy. The third stage may require surgical intervention with thoracoscopy or thoracotomy [7].

Differentiating empyema from a pulmonary abscess is often possible on the chest radiograph. An abscess usually is rounded and if it has an air-fluid level, the length of the level is equal on the postero-anterior and lateral chest radiograph. An empyema usually assumes the shape of the pleural space. If there is an air-fluid level associated with the empyema the air-fluid level is usually longer on the lateral film. CT can be used to aid in the differentiation of a lung abscess and an empyema. A lung abscess usually forms in the center of an infected portion of lung and on CT a lung abscess usually has surrounding it a rim of lung, and because it forms within the lung, the abscess usually has an acute angle versus an obtuse angle with the chest wall as with an empyema. An empyema forms outside the lung parenchyma and often there is an area of compressed lung on one side and inflamed pleura on the other. In addition, the thickened and enhancing parietal and visceral pleura are separated by the empyema giving rise to the ''split pleura sign'' of empyema. Occasionally, it can be very difficult to distinguish all components of a complex pleura-parenchymal abscess or empyema especially when an abscess is adjacent to the edge of the lung and has necrosed into the pleural space with resulting empyema. This may be a moot point because both empyema and lung abscesses can be drained if clinically needed [7].

Pneumatocele

Pneumatoceles are thin-walled, gas-filled spaces that usually develop in association with infection; characteristically, they increase in size over days to weeks and almost invariably resolve.

Pneumonia in the elderly

Community-acquired pneumonia in the elderly has a different clinical presentation than community-acquired pneumonia in other age groups. Confusion, alteration of functional physical capacity, and decompensation of underlying illnesses may appear as unique manifestations. Usually, the clinical picture is incomplete and both fever and cough can be absent. The incomplete clinical picture of community-acquired pneumonia in the elderly may be associated with a delay in establishing the diagnosis and, consequently, starting antibiotic therapy. The delay in diagnosis and treatment may contribute to the higher observed death rate in the elderly [8].

Bacterial pneumonia

Streptococcus pneumoniae

S pneumoniae is the most commonly identified pathogenic organism in patients admitted to the hospital for pneumonia, accounting for 40% of all isolated species. The clinical presentation is an abrupt onset of fever, chills, cough, and chest pain, often associated with bloody or rusty sputum. The most common radiographic pattern in pneumococcal pneumonia is a homogeneous, nonsegmental consolidation with air bronchograms. The lobar consolidation may involve single or multiple lobes. Occasionally, it may present as a round pneumonia, although this pattern is more common in children (Fig. 4). A pattern of bronchopneumonia can occur with cavitation, pulmonary gangrene, and pneumatocele formation being uncommon. Pleural effusion can be seen in at least 10% of patients and is more common in more severe pneumonia [1,2,5,6,9].

Staphylococcus aureus

S aureus is an uncommon cause of community-acquired pneumonia, accounting for only about 3% of all cases. It is an important cause of nosocomial pneumonia, especially in the intensive care unit. The parenchymal consolidation in acute staphylococcal bronchopneumonia is typically segmental in distribution. Depending on the severity the process may be patchy or homogeneous, representing confluent bronchopneumonia. Inflammatory exudate fills the airways and segmental atelectasis occurs and an air bronchogram is usually not visible. Abscesses develop in 15% to 30% of patients. Pneumatocele formation also is common, occurring in about 50% of children and 15% of adults. Pleural effusions oc-

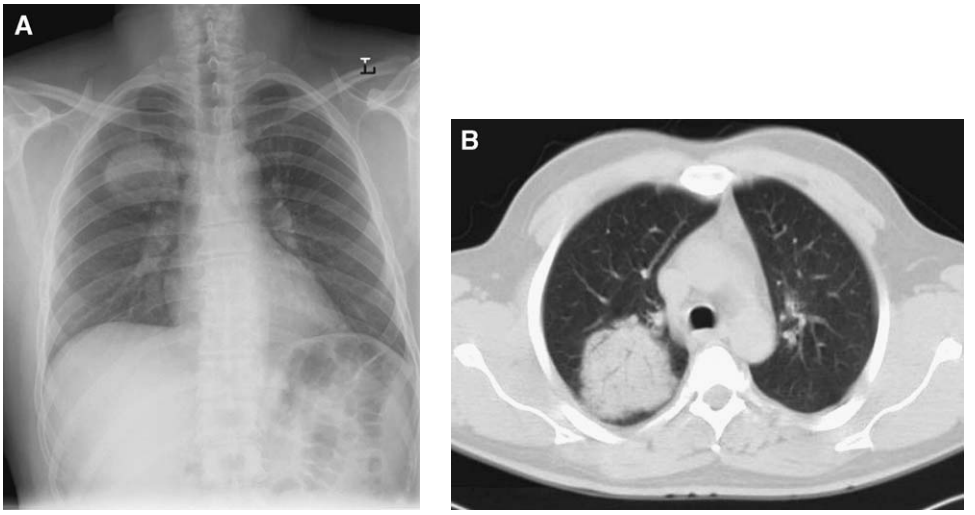

Fig. 4. Round pneumonia caused by *S pneumoniae*. (*A*) PA chest. (*B*) CT scan.

cur in 30% to 50% of patients with approximately half representing empyema [1,2,5].

Klebsiella pneumoniae

K pneumoniae is an acute air-space pneumonia that is an uncommon community-acquired pneumonia but a common nosocomial infection. Typically, *K pneumoniae* causes acute pneumonia in men in their 50s who are chronic alcoholics. *K pneumoniae* shows the same general radiographic features as pneumococcal pneumonia, a homogeneous lobar parenchymal consolidation containing an air bronchogram. Compared with pneumococcal pneumonia, acute *K pneumoniae* has a greater tendency for the formation of voluminous inflammatory exudate leading to lobar expansion with resulting bulging of interlobar fissures, a greater tendency for abscess and cavity formation, and a greater frequency of pleural effusion and empyema [1,2,5].

Haemophilus influenza

H influenza is responsible for about 5% to 20% of community-acquired pneumonias in patients in whom an organism can be identified. It is an important cause of nosocomial pneumonia. The radiologic manifestations are variable but it predominately presents as bronchopneumonia, consisting of areas of consolidation in a patchy or segmental distribution; less frequently as nonsegmental air-space consolidation similar to that of *S pneumonia*; or a combination pattern. A reticular or reticulonodular interstitial pattern, by itself or in combination with air-space consolidation, occurs in 15% to 30% of cases. Cavitation has been reported in 15% or less of cases. Pleural effusion has been reported in approximately 50%. Empyema is uncommon [1,2,5].

Legionella pneumophila

L pneumophila is found in 2% to 25% of patients hospitalized for pneumonia. Legionnaires' disease shows a propensity for older men who may have underlying disease, such as chronic obstructive pulmonary disease and malignancy. Outbreaks can result from contaminated air conditioning systems, cooling towers, hot water storage tanks, and shower heads. The characteristic radiographic pattern is one of air-space consolidation that is initially peripheral and sublobar, similar to that seen in acute *S pneumoniae* pneumonia (Fig. 5). The progression is usually rapid with complete lobar involvement within a few days. Cavitation is rare. Pleural effusion may occur in up to half of the cases [1,2,5].

Mycoplasma pneumoniae

M pneumoniae is one of the more common causes of community-acquired pneumonia, accounting for an estimated 10% to 15% of cases in the population as a whole and 50% of cases in specific groups, such as military recruits. *M pneumoniae* often is classified as an atypical pneumonia because the clinical presentation more closely resembles a systemic viral

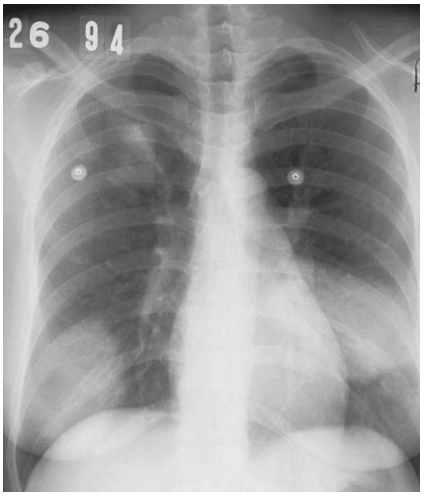

Fig. 5. Multilobar *Legionella* pneumonia.

infection than a typical community-acquired pneumonia. Infections occur throughout the year, with a peak during the autumn and early winter. The patient usually has the gradual onset of fever, nonproductive cough, headache, malaise, and occasionally chills. The radiologic pattern of acute mycoplasmal pneumonia may be indistinguishable from that of many viral or bacterial pneumonias, the manifestations consisting of interstitial or air-space opacities or a combination of both. In the early stages, the interstitial inflammation causes a fine reticular pattern, followed by signs of air-space consolidation in a patchy distribution. The radiographic findings may be unilateral or bilateral segmental or lobar air-space consolidation and less commonly a diffuse reticulonodular pattern with no evidence of air-space opacification. The high-resolution CT (HRCT) findings of mycoplasmal pneumonia consist of centrilobular nodular and branching linear opacities in a patchy distribution, thickening of the bronchovascular bundles, and areas of lobular or segmental consolidation. Pleural effusions are uncommon and small [1,2,5,10].

Chlamydia pneumoniae

C pneumoniae is a common cause of community-acquired pneumonia and a principal symptom of cough lasting longer than 2 weeks. The most frequent clinical manifestations are sore throat, nonproductive cough, and fever. The most common radiographic finding is air-space consolidation with interstitial infiltrates, combined interstitial and air-space infiltrates, pleural effusion, and a normal radiograph being much less frequent [1,2,5].

Escherichia coli

Escherichia coli accounts for about 5% to 20% of cases of pneumonia acquired in a hospital or a nursing home. The radiologic manifestations usually are those of bronchopneumonia [1,2].

Pseudomonas aeruginosa

P aeruginosa pneumonia is the most common and most lethal form of nosocomial pulmonary infection. The organism is the cause of approximately 20% of nosocomial pneumonia in adult patients in the intensive care unit. The radiologic manifestations of *P aeruginosa* pneumonia are usually those of bronchopneumonia, consisting of multifocal bilateral areas of consolidation [1,2].

Anaerobic bacteria

Anaerobic bacteria usually cause polymicrobial infections. Among all patients admitted to hospital with pneumonia, anaerobic bacteria are isolated in approximately 20% to 35%, the organisms being second only to *S pneumoniae* as a cause of community-acquired pneumonia. Anaerobes are an important cause of nosocomial infection. The radiographic pattern is that of bronchopneumonia, ranging from localized segmental areas of consolidation to bilateral, confluent consolidation. Cavitation is common, seen in as many as half the cases [1,2].

Primary tuberculosis

Mycobacterium tuberculosis

Tuberculosis is one of the most important infectious diseases. In 1996, 21,337 cases were reported in the United States (rate, 8 per 100,000). Rates are much higher in many developing countries. Between 1997 and 2020, close to 1 billion people worldwide will be infected by *Mycobacterium tuberculosis*, and 70 million will die from tuberculosis. Disease may be associated with progression of the primary focus of infection (primary tuberculosis) or with the development of new disease months or years after healing of the initial infection has occurred (post-primary tuberculosis) [1,2].

Primary pulmonary tuberculosis

Primary pulmonary tuberculosis traditionally has been thought to occur predominantly in children, and it is particularly prevalent in regions in which the annual risk of infection is high. With the reduction in the incidence of tuberculosis and the resulting increase in the number of nonsensitized individuals, the primary form of disease seems to have become more common in adults. As many as 40% of cases of adult tuberculosis in some populations are recently acquired [1,2].

The initial focus of parenchymal disease in primary tuberculosis is termed the "Ghon's focus." It either enlarges as the disease progresses or, more commonly, undergoes healing. During the early phase of infection, spread of organisms to regional lymph nodes by lymphatic channels is common and results in granulomatous inflammation adjacent to the lymphatic vessels and in the nodes themselves. The combination of a Ghon's focus and affected lymph nodes is known as the "Ranke complex" [1,2].

Progressive primary tuberculosis occurs in a small percentage of cases. Adequate cell-mediated immunity does not develop and progressive and symptomatic primary pulmonary disease develops. Local parenchymal disease spreads in a radiographic pattern similar to postprimary tuberculosis. Opacities in this form of disease can cavitate and usually affect the upper lobes. Miliary disease also can develop in these patients [1,2].

Most individuals infected with *M tuberculosis* do not have radiologic abnormalities. When radiographic abnormalities do occur the parenchyma, mediastinal and hilar nodes, the airways, and the pleura may be involved [1,2].

Parenchymal involvement

In children, air-space consolidation with no significant predilection for any particular lung region was identified in approximately 70% of patients with bilateral involvement in 15% of cases. In adults, air-space consolidation without lobar predilection was found in approximately 90% of patients. Cavitation has been reported in approximately 2% of children and 6% of adults. Miliary disease is seen in 3% of children and 6% of adults [1,2].

Lymph node involvement

Evidence of lymph node enlargement is identified on the chest radiograph in about 90% of children who have primary disease. Lymph node enlargement is seen less commonly in adults (10%–30%). The lymph node enlargement most commonly is unilateral and hilar or paratracheal and may be the only abnormality. The presence of bilateral lymph node enlargement or lymph node enlargement without parenchymal consolidation does not exclude tuberculosis but this picture is uncommon in adults. On CT scan, affected lymph nodes often have relatively low attenuation of the central region and show peripheral enhancement after intravenous administration of contrast material [1,2].

Airway involvement

Atelectasis, usually lobar and right-sided, has been reported in 10% to 30% of children who have primary tuberculosis. It usually is the result of bronchial compression by enlarged lymph nodes; less commonly, endobronchial disease is responsible. Atelectasis is less common in adults [1,2].

Pleural involvement

Pleural effusions have been reported in 5% to 10% of children and 30% to 40% of adults who have primary tuberculosis. They usually are seen in association with parenchymal abnormalities; however, in about 5% of adults, the effusion is the only radiographic manifestation of the disease [1,2].

Postprimary tuberculosis

The term "postprimary (secondary, reactivation) tuberculosis" is a clinical and radiologic form of disease that is correlated with acquired hypersensitivity and immunity. Many cases occur in adults as a result of reactivation of a focus of infection acquired earlier in life. Although previously it was believed that this mechanism was responsible for most cases of pulmonary tuberculosis, epidemiologic evidence based on DNA fingerprinting has shown that 30% to 40% of such cases are recently acquired in selected populations [1,2,5].

In contrast to primary tuberculosis, in which fibrosis and healing are the rule, postprimary tuberculosis tends to progress, foci of inflammation and necrosis enlarging to occupy ever greater portions of lung parenchyma. During this process, communication with airways is frequent, resulting in expulsion of necrotic material and cavity formation.

Radiologic manifestations

A characteristic manifestation of postprimary tuberculosis is its tendency to localize in the apical and posterior segments of the upper lobes. For example, in one study of 423 adults who had local pulmonary tuberculosis, the lesions were predominantly in the apical and posterior segments of an upper lobe in 85% and in the superior segment of one or other lower lobe in 9.5%. In about 70% to 90% of cases, the abnormalities involve more than one segment.

Air-space consolidation

Focal areas of consolidation are seen in over half of the patients who have postprimary tuberculosis. The areas of consolidation have poorly defined margins, may coalesce, and often have small satellite foci. HRCT demonstrates a lobular distribution often sparing adjacent lobules with increased bronchovascular markings leading toward the hilum. Associated hilar or mediastinal lymph node enlargement is relatively uncommon, being identified on chest radiographs in only 5% to 10% of patients.

Cavitation

Cavitation is identified on chest radiograph in 20% to 45% of patients and in a higher percentage on CT scans. Eighty percent of the cavities are located in the apical and posterior segments of the upper lobes and the remainder in the superior segments of the lower lobes. The cavities may be single, multiple, thick, or thin walled and 20% may have an air-fluid level (Fig. 6).

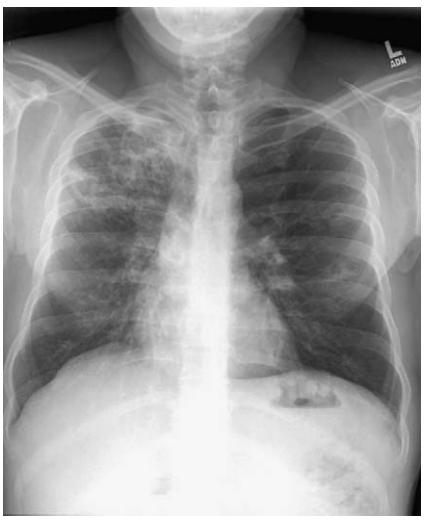

Fig. 6. Upper lobe cavities in tuberculosis.

Tuberculoma

A tuberculoma can be seen in primary or postprimary tuberculosis. The lesion is a rounded opacity usually in one of the upper lobes. They usually measure 1 to 4 cm in diameter and typically are smooth and sharply defined. Small discrete satellite lesions are common.

Focal nodular opacities

Nodular opacities measuring 2 to 10 mm in diameter and localized to one or two regions of the lungs, usually the apical or posterior segments of the upper lobes or the superior segment of the lower lobes, have been described as the main or only radiologic manifestation in 20% to 25% of patients who have postprimary tuberculosis. On HRCT scan, the opacities have been shown to be centrilobular in distribution and often associated with branching linear opacities, an appearance that has been likened to that of a tree-in-bud.

Endobronchial spread of tuberculosis

Endobronchial spread of tuberculosis can be demonstrated when multiple nodules measuring 2 to 10 mm in diameter are seen in two or more lobes or in a lobe other than the one containing a cavity or area of consolidation.

Miliary tuberculosis

The interval between dissemination and the development of radiographically discernible miliary tuberculosis is probably 6 weeks or more, during which time the foci of infection are too small for radiographic identification. When first visible, the nodules measure 1 to 2 mm in diameter; in the absence of adequate therapy, they may grow to 3 to 5 mm in diameter, a finding seen in approximately 10% of cases. Miliary nodules may be difficult to see on the radiograph at the time of diagnosis. HRCT can be helpful in the diagnosis of miliary tuberculosis in patients who have normal or nonspecific radiographic findings. Findings consist of nodules, usually sharply defined, measuring 1 to 4 mm in diameter and

having a diffuse random distribution throughout both lungs (Fig. 7).

Bronchiectasis

Bronchiectasis is seen on HRCT scan in 30% to 60% of patients who have postprimary tuberculosis. It usually affects one or two lobes and is seen most often in the upper lobes.

Pleural disease

Tuberculous pleurisy, empyema, and bronchopleural fistula can develop as a result of infection of the pleural space. When healed this results in extensive pleural fibrosis and calcification.

Extrapulmonary tuberculosis

Tuberculosis of the spine (Pott's disease) is the most common form of skeletal disease and usually affects the lower thoracic or upper lumbar vertebrae. The early radiographic manifestations consist of irregularity of the vertebral end plates, decreased height of the intervertebral disk space, and sclerosis of the adjacent bone. With progression of disease, there is a tendency to anterior wedging of the vertebral body, leading to kyphosis and development of paravertebral abscesses. CT and MR imaging are superior to the radiograph in showing the extent of the abnormalities, development of paraspinal abscesses, and involvement of the spinal canal. Paravertebral abscesses show peripheral rim enhancement and low-attenuation centers after intravenous administration of contrast material (Fig. 8).

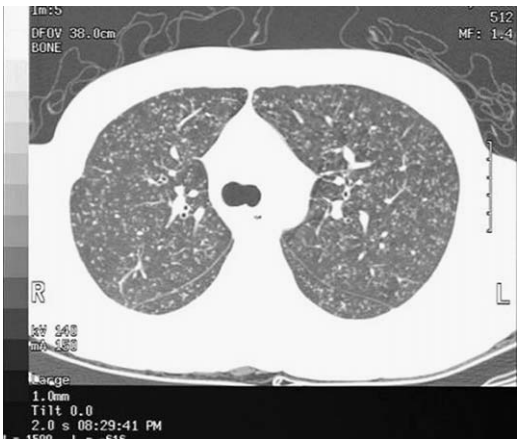

Fig. 7. CT scan of miliary tuberculosis.

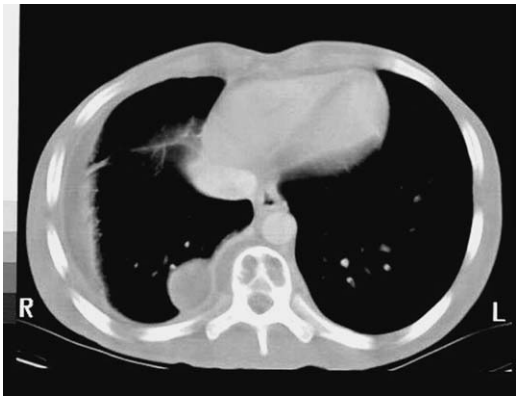

Fig. 8. CT of tuberculosis of the spine, Pott's disease.

Nontuberculous (atypical) mycobacteria

Most nontuberculous mycobacterial pulmonary infections are caused by a few species, most commonly *Mycobacterium avium-intracellulare* and *Mycobacterium kansasii*. The clinical presentation of nontuberculous mycobacterial infection of the lung is similar to that of tuberculosis. The most common findings are cough, low-grade fever, and weight loss [1,2].

M avium-intracellulare is the most common nontuberculous mycobacterium to cause human disease. As with many other nontuberculous mycobacteria, such infection often is associated with prior lung disease, such as chronic obstructive pulmonary disease, pneumoconiosis, and bronchiectasis; a dusty environment, such as seen in some mines and farms, also has been identified as a risk factor. The bacillus has become an important cause of systemic disease in patients who have AIDS, approximately 20% to 25% acquiring the infection at some point during the course of their illness.

A variety of radiologic patterns are seen with nontuberculous mycobacteria. One of the more common, in 20% to 60% of patients, consists of single or multiple cavities. Most patients have radiographic evidence of endobronchial spread. Another radiographic pattern consists of bilateral small nodular opacities that are well circumscribed; less than 1 cm in diameter; and have a centrilobular distribution more commonly in the upper lobes, middle lobe, and lingual. On HRCT these patients often have bronchiectasis. This pattern is common in women.

Fungi and actinomyces

Fungi can be divided into two major groups according to the pathogenesis of the disease they cause. Some organisms (eg, *Histoplasma capsulatum, Coccidioides immitis,* and *Blastomyces dermatitis*) are primary pathogens that most frequently infect healthy individuals. They are found in specific geographic areas (the term "endemic" often is used to describe the infection) and typically dwell in the soil as saprophytes. In appropriate climatic conditions, they germinate and produce spores, which when inhaled by a susceptible host change form and proliferate. In the individual who has an intact inflammatory response and adequate cell-mediated immunity, such proliferation almost invariably is limited, the resulting disease being subclinical or mild and evidenced only by the development of a positive skin test. In a few apparently normal individuals, however, fulminant primary infection or chronic pulmonary disease, with or without systemic dissemination, can cause significant morbidity and occasionally is fatal. Such complications are much more common and serious in patients who have an underlying immune deficiency, such as AIDS [1,2].

A second group of organisms (including *Aspergillus* and *Candida* species, and the species that cause mucormycosis) are opportunistic invaders that chiefly affect immunocompromised hosts or grow in association with underlying pulmonary disease. In contrast to members of the previous group, these organisms can be found throughout the world and usually are ubiquitous in the environment. In addition to saprophytic and invasive infection, some fungi (particularly *Aspergillus* species) can cause disease by inducing an exaggerated hypersensitivity reaction without invading tissue [1,2].

Histoplasmosis

Acute histoplasmosis

Histoplasmosis is an endemic fungal disease caused by the dimorphic fungus *H capsulatum*. The fungus grows well in soil enriched by bird and bat guano. The endemic region in the United States in the Mississippi, Ohio, and St. Lawrence River valleys [1,2].

Acute histoplasmosis is a abrupt flulike illness with fever, headache, chills, and cough. The chest radiograph is normal in most patients. The most common radiographic findings consist of single or multiple, poorly defined areas of air-space consolidation.

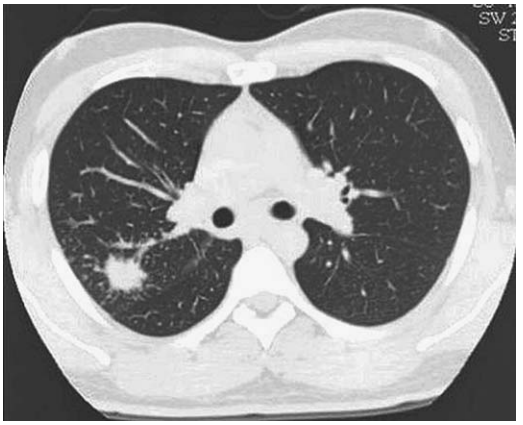

Fig. 9. CT scan of acute histoplasmosis demonstrating nonspecific nature of the parenchymal opacity.

Severe disease is characterized by homogeneous, nonsegmental, parenchymal consolidation simulating acute bacterial air-space pneumonia. Hilar lymph node enlargement is common. Pleural effusion is rare. After heavy exposure, the radiograph may show widely disseminated, fairly discrete nodular shadows, individual lesions measuring 3 or 4 mm in diameter.

Histoplasmosis also can be manifested by unilateral or bilateral enlargement of hilar or mediastinal lymph nodes in the absence of other radiographic abnormalities (Fig. 9). Calcification of lymph nodes is common and may be associated with broncholithiasis (Fig. 10).

Histoplasmoma

Histoplasmoma is a relatively common form of pulmonary histoplasmosis that may or may not be associated with a history of previous symptomatic disease. The abnormality typically appears as a sharply defined nodule 0.5 to 3 cm in diameter, in most cases in a lower lobe. Satellite lesions may be present. Hilar calcified nodes also are often present.

Chronic pulmonary histoplasmosis

The radiographic appearance simulates postprimary tuberculosis, the earliest manifestations consisting of segmental or subsegmental areas of consolidation in the apices of the lungs, frequently outlining areas of centrilobular emphysema. Thick-walled bullae sometimes contain fluid levels. Serial chest radiographs tend to show progressive loss of

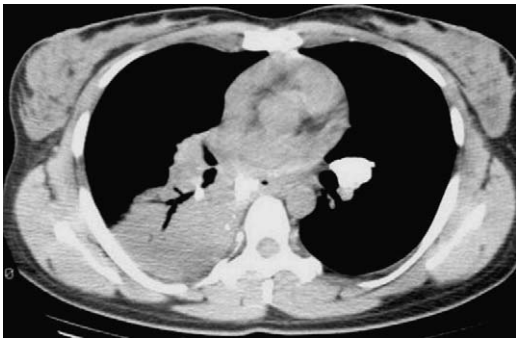

Fig. 10. CT scan of a broncholith causing postobstructive air space disease.

volume associated with increased prominence of linear opacities.

Chronic mediastinal histoplasmosis

Chronic mediastinal histoplasmosis is a process that may be secondary to an exuberant fibrous reaction caused by chronic immunologic stimulation by histoplasmin antigens. Sometimes the radiographic abnormalities are related to one or more enlarged mediastinal lymph nodes. Occasionally, there are larger masses of matted necrotic and fibrotic nodes and tissue. These nodes and fibrotic masses engulf or compress normal mediastinal and hilar structures.

The most common findings are mediastinal or hilar masses, calcification within the mediastinal mass or associated lymph nodes, superior vena cava obstruction, pulmonary artery narrowing, and bronchial narrowing. The presence of localized calcified mediastinal soft tissue mass is the most frequent of these abnormalities. In a patient with an appropriate clinical history, this finding strongly suggests a diagnosis of *H capsulatum*–induced fibrosing mediastinitis and precludes the need for biopsy. In patients without calcification or with progressive radiographic findings, a biopsy specimen should be obtained for a definitive diagnosis.

Disseminated histoplasmosis

Disseminated histoplasmosis occurs most frequently in infants and young children and in patients who are immunocompromised by such conditions as AIDS or organ transplantation. The radiographic and HRCT findings usually are similar to those of miliary tuberculosis, consisting of 1- to 3-mm-diameter nodules distributed randomly throughout both lungs (Fig. 11).

Coccidioidomycosis

Coccidioidomycosis is highly infectious and caused by the dimorphic fungus *C immitis*. It is found principally in its endemic areas in the southwestern United States and northern Mexico. In endemic areas, the incidence of infection is high [1,2].

Primary coccidioidomycosis

Most patients are asymptomatic. Symptoms that may accompany primary infection often are nonspecific and flulike, consisting of fever, nonproductive cough, chest pain, headache, and sometimes a generalized erythematous rash. The most common radiologic manifestation consists of single or multiple foci of air-space consolidation. Sometimes the foci of consolidation are transformed into thin-walled cavities that may resolve spontaneously. Lymph node enlargement occurs in approximately 20% of cases, usually with parenchymal involvement.

Chronic pulmonary coccidioidomycosis

Chronic pulmonary coccidioidomycosis is usually found in asymptomatic patients. The radiologic manifestations include lung nodules and cavities and, rarely, bronchiectasis, scarring, and calcification. The nodules are 0.5 to 5 cm in diameter and in more than 90% of cases are located in the lung periphery. Although usually single, they occasionally are multiple. Cavities have been reported to occur in 10% to 15% of patients who have pulmonary disease. They usually are single and located in the upper lobes and may be thin or thick walled. The thin-walled cavities have a tendency to change size.

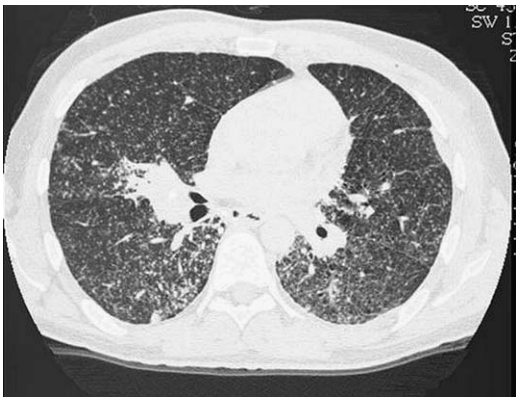

Fig. 11. CT scan of miliary histoplasmosis.

In fewer than 1% of patients who have pulmonary coccidioidomycosis, the disease is slowly progressive and may mimic reactivation tuberculosis or chronic histoplasmosis. The radiologic findings in these patients consist of upper lobe scarring, multiple nodules, and cavities.

North American blastomycosis

North American blastomycosis is caused by the dimorphic fungus *B dermatitidis.* The disease occurs most commonly in the Western Hemisphere, mainly the central and southeastern United States, Wisconsin, and southern Canada. Although infection in miniepidemics may be associated only with flulike symptoms, it is manifested more commonly by symptoms of acute pneumonia, including the abrupt onset of fever, chills, productive cough, and pleuritic chest pain [1,2].

The most common radiographic presentation, reported in over half of patients, consists of acute air-space consolidation. The next most common radiographic presentation, in 30% of cases, is a mass, either single or multiple (Fig. 12). The solitary mass can mimic primary carcinoma. Cavitation occurs in approximately 15% to 20% of cases. Overwhelming infection usually is accompanied by a radiographic pattern of miliary dissemination. Hilar and mediastinal lymph node enlargement is uncommon. Pleural effusion has been identified radiographically in 10% to 15% of cases and is associated with parenchymal disease.

Cryptococcosis

Although it can occur as pulmonary or disseminated disease in otherwise normal individuals, cryptococcosis identified most frequently in compromised hosts, particularly patients who have AIDS or lymphoma. The most common radiographic manifestation of pulmonary infection consists of single or multiple nodules, usually subpleural in location and 0.5 to 4 cm in diameter. It may also present as a localized area of less well-defined air-space consolidation, segmental or nonsegmental in distribution but usually confined to one lobe. Cavitation is uncommon except in immunocompromised patients. Hilar and mediastinal adenopathy can be seen in patients with AIDS [1,2].

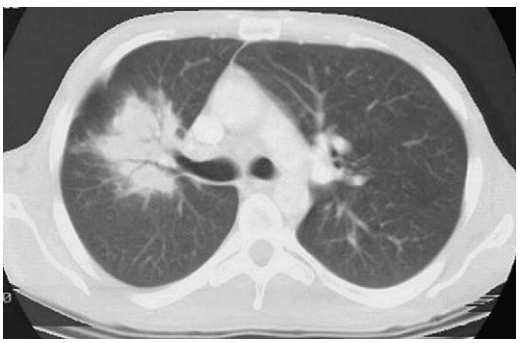

Fig. 12. CT scan of blastomycosis appearing mass-like.

Aspergillosis

Diseases caused by *Aspergillus* species can be manifested in three way, each with distinctive clinical, radiologic, and pathologic features: (1) saprophytic infestation, in which the fungus colonizes airways, cavities (aspergilloma), or necrotic tissue; (2) allergic disease, characterized by such entities as allergic bronchopulmonary aspergillosis and extrinsic allergic alveolitis; and (3) invasive disease, a form that is usually acute in onset and rapidly fatal. The pathogenesis of *Aspergillus* infection varies with the quality and virulence of the inhaled organism and the status of the host defense system [1,2].

Saprophytic aspergillosis

In a normal host, Aspergillus is characterized by mycelial growth without invasion of viable tissue. A fungus ball (mycetoma, aspergilloma) is a conglomeration of fungal hyphae admixed with mucus and cellular debris within a pulmonary cavity or ectatic bronchus. Historically, the most common underlying cause was tuberculosis, approximately 25% to 55% of patients having a history of this disease. The second most common underlying condition is sarcoidosis. Common clinical manifestations include cough and expectoration. Hemoptysis has been reported in 50% to 95% of cases. Radiographically, a fungus ball consists of a solid, rounded mass of soft tissue density within a cavity, usually in an upper lobe (Fig. 13). Typically, the fungus ball is separated from the wall of the cavity by an air space, resulting in the distinctive air crescent sign. Occasionally, the mycelial mass grows to fill a cavity completely. The fungus ball usually moves when the patient changes position. Thickening of a cavity wall may be an early sign of aspergillosis infection. Areas of increased attenuation within the fungus ball, presumably representing calcium deposits, are relatively common.

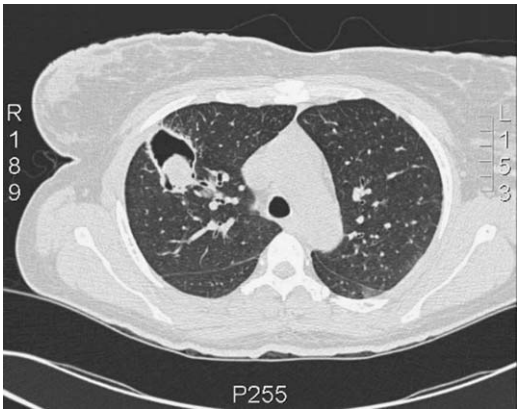

Fig. 13. CT scan of an aspergilloma or fungus ball.

Small air collections also can be seen within the fungus ball. CT may allow visualization of aspergillomas not apparent on the radiograph and multiple aspergillomas.

Angioinvasive aspergillosis

Invasive aspergillosis is characterized by extension of *Aspergillus* organisms into viable tissue, usually associated with tissue destruction. The abnormality almost invariably develops in patients whose host defenses are impaired, often as a result of cancer chemotherapy. Patients with acute myelogenous leukemia are particularly susceptible, especially if granulocytopenia is present.

The radiographic pattern consists of nodules or single or multiple areas of homogeneous consolidation. Cavitation is common and sometimes is manifested by an air crescent partly or completely surrounding a central homogeneous mass. This air crescent sign can develop 1 day to 3 weeks after the appearance of the initial radiographic abnormality (Fig. 14).

CT scan may show a characteristic finding in early angioinvasive aspergillosis, consisting of a halo of ground-glass attenuation surrounding a soft tissue nodule (the so-called ''halo sign''). This finding is related to the presence of air-space hemorrhage surrounding the nodule of necrotic lung tissue. With time, these lesions may develop air crescents or progress to frank cavitation. In the appropriate clinical setting, the presence of a soft tissue nodule with a halo sign is highly suggestive of angioinvasive aspergillosis.

Allergic aspergillosis

Allergic aspergillosis is a result of hypersensitivity reaction that produces extrinsic allergic alveolitis, a Loeffler-like syndrome, or more commonly allergic bronchopulmonary aspergillosis. Allergic bronchopulmonary aspergillosis is seen in asthmatic patients on steroid treatment. The radiographic appearance is that of mucoid impaction or ectasia of proximal bronchi. Finger-like soft tissue densities in a bronchial distribution in the upper lobes is the radiographic common appearance. On CT the findings are mucoid impaction and bronchiectasis involving the segmental and subsegmental airways.

Chronic necrotizing (semi-invasive) aspergillosis

This is uncommon and characterized by slowly progressive upper lobe disease that may spread to involve adjacent structures. Many patients have underlying chronic pulmonary disease, including inactive tuberculosis, chronic obstructive pulmonary

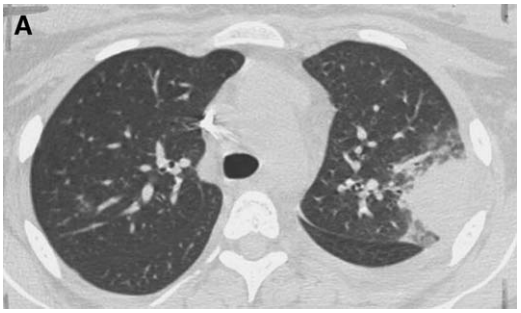

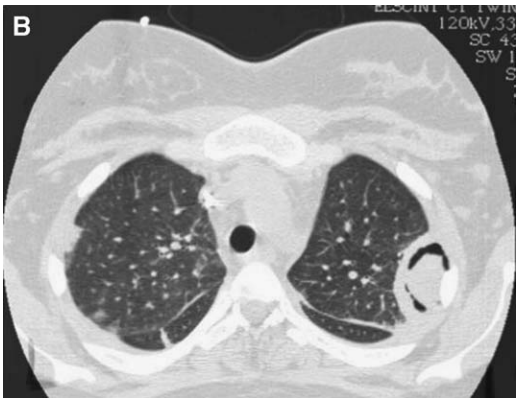

Fig. 14. CT scan of early invasive aspergillosis (*A*) and later after the air crescent has developed (*B*).

disease, fibrosis related to radiation therapy, or pneumoconiosis. There is often a mild impairment of host defense, such as diabetes, or poor nutrition. Radiographically lesions appear as an upper lobe area of consolidation, cavitation, nodules, or masses often with pleural thickening.

Pneumocystis

P carinii has now been classified as a fungi. *P carinii* results in clinically significant pneumonia in patients who have underlying disease, most commonly AIDS patients who have a CD4 count of less than 200 cells/mm^3. In patients with AIDS there is often a several week prodrome phase of fever, malaise, cough, and dyspnea [1,2].

Pneumonia caused by *P carinii* typically presents radiographically as a bilateral, symmetric, fine granular or poorly defined reticulonodular pattern. Approximately 10% to 20% of patients with AIDS and proved *P carinii* pneumonia have normal chest radiographs. With more severe infection, the findings progress to more homogeneous parenchymal opacification ranging from ground-glass opacities to consolidation. Rarely there is lobar consolidation, nodular opacities with or without cavitation, or pleural effusion. On HRCT scan, the predominant abnormality consists of extensive bilateral areas of ground-glass attenuation (Fig. 15). There may be intervening areas of normal parenchyma. Eventually interstitial opacities may occur, such as small nodules, reticular opacities, and interlobular septal thickening [1,2].

The classic radiographic pattern of *P carinii* is being encountered less frequently. Increasingly recognized patterns of *P carinii* pneumonia include cystic lung disease, spontaneous pneumothorax, and an upper lobe distribution of parenchymal opacities (Fig. 16) [11].

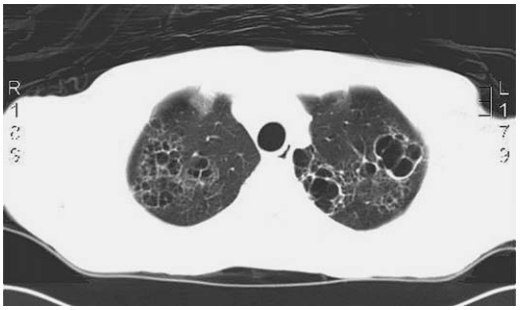

Fig. 16. CT scan of pneumatoceles caused by *P carinii* pneumonia infection.

Actinomycosis

Actinomyces israelii, a normal oropharyngeal inhabitant, is the most important cause of disease in humans. Clinically the picture is of a pneumonia that responds poorly to normal antibiotic treatment. Chest wall pain may occur as the infection spreads to the chest wall. The typical pattern of acute pulmonary actinomycosis consists of nonsegmental air-space consolidation, commonly in the periphery of the lung and with a predilection for the lower lobes. If therapy is not instituted, an abscess may develop, and the infection may extend into the pleura and into the

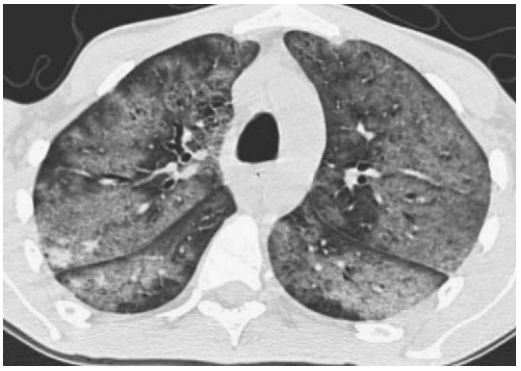

Fig. 15. CT scan of *P carinii* pneumonia demonstrating ground glass opacities.

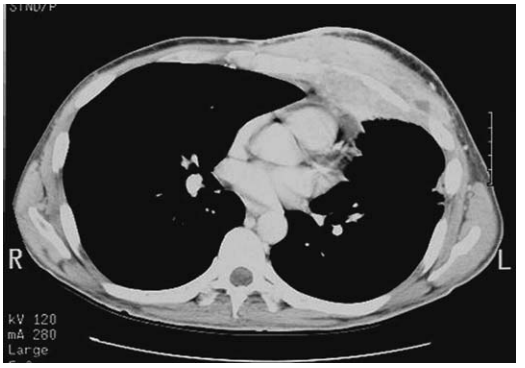

Fig. 17. CT scan of actimomycosis invading the left chest wall.

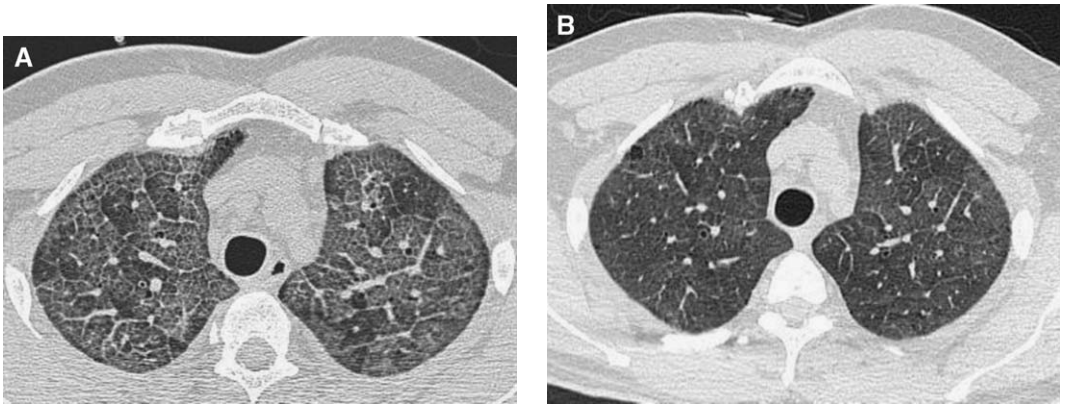

Fig. 18. CT scan of viral pneumonia before (*A*) and after (*B*) antiviral treatment.

chest wall, with abscess formation in these areas (Fig. 17). Actinomycosis may also present radiographically as a mass, which may cavitate. Chest wall involvement may include rib destruction [1,2].

Nocardia

Nocardia asteroides is an opportunistic pathogen in immunocompromised patients, especially with lymphoma, with alveolar proteinosis, and with organ transplant. Radiographically, parenchymal opacities are homogeneous and nonsegmental. There can be pleural extension with resulting empyema. Cavitation is common [1,2].

Viral pneumonia

Influenza virus

Influenza can occur in pandemics, epidemics, or sporadically in individuals or in small clusters of patients. Almost all severe epidemics and all pandemics are caused by type A viruses. Outbreaks usually occur during the winter. Pneumonia is an uncommon but serious complication of influenza infection. Bacterial superinfection is usually the cause of the pneumonia. Local involvement usually is in the form of segmental consolidation that may be homogeneous or patchy and unilateral or bilateral. Serial radiographs may show poorly defined, patchy areas of consolidation, 1 to 2 cm in diameter, which become confluent rapidly (Fig. 18). Pleural effusion is rare [1,2,12].

Varicella virus

The overall incidence of varicella-related pneumonia seems to be about 15%, although in adults admitted to the hospital the incidence has been 50%. Most cases occur in very young children or adults. In both groups, pre-existing neoplastic disease, particularly leukemia and lymphoma, other causes of immunodeficiency, and pregnancy are predisposing factors. The characteristic radiographic

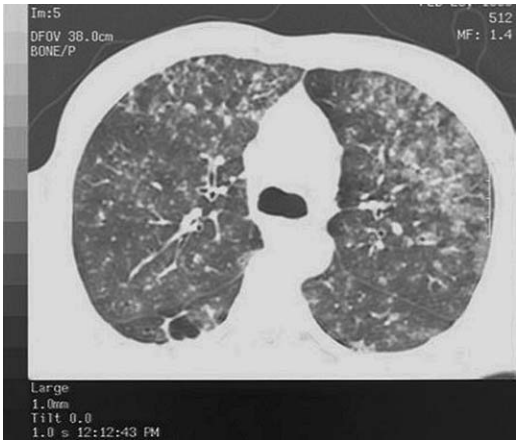

Fig. 19. CT scan of varicella pneumonia demonstrating multiple ill-defined alveolar nodules.

pattern consists of multiple 5- to 10-mm-diameter nodular opacities. The opacities usually are fairly discrete in the lung periphery but tend to coalesce near the hila and in the lung bases (Fig. 19). Progression to extensive air-space consolidation can occur rapidly. An uncommon latent manifestation of chickenpox pneumonia consists of tiny widespread foci of calcification throughout both lungs in persons who had chickenpox many years before [1,2,12].

Cytomegalovirus

Acquired cytomegalovirus infection is common; seropositivity rates vary from 40% to 100% in different adult populations around the world. Most affected individuals are asymptomatic. Pneumonia and other clinical manifestations of active infection are much more frequent in patients who have underlying disease, however, particularly immunodeficiency related to organ transplantation or AIDS. The most common radiographic findings in cytomegalovirus pneumonia are bilateral linear opacities (reticular pattern); ground-glass opacities; and parenchymal consolidation. Findings of cytomegalovirus pneumonia on CT scan include areas of ground-glass attenuation, parenchymal consolidation, and nodular or reticulonodular opacities [1,2,12].

Acknowledgments

The authors give special thanks to Dawn Wafford and Beth Ward for their clerical and technical support.

References

[1] Muller NL, Fraser RS, Colman NC, et al. Pulmonary infection. In: Muller NL, Fraser RS, Colman NC, et al, editors. Radiologic diagnosis of diseases of the chest. Philadelphia: WB Saunders; 2001. p. 141–211.
[2] Gharib AM, Stern EJ. Radiology of pneumonia. Med Clin North Am 2001;85:1461–91.
[3] Vilar J, Domingo ML, Soto C, et al. Radiology of bacterial pneumonia. Eur J Radiol 2004;51:102–13.
[4] Ruiz M, Ewig S, Angeles M, et al. Etiology of community-acquired pneumonia. Am J Respir Crit Care Med 1999;160:397–405.
[5] Katz DS, Leung AN. Radiology of pneumonia. Clin Chest Med 1999;20:549–62.
[6] Shah RM, Gupta S, Angeid-Backman E, et al. Pneumococcal pneumonia in patients requiring hospitalization. AJR Am J Roentgenol 2000;175:1533–6.
[7] Collins J, Stern EJ. Chest wall, pleura, and diaphragm. In: Collins J, Stern EJ, editors. Chest radiology the essentials. Philadelphia: Lippincott Williams and Wilkins; 1999. p. 125–49.
[8] Riquelme R, Torres A, el-Ebiary M, et al. Community-acquired pneumonia in the elderly. Clinical and nutritional aspects. Am J Respir Crit Care Med 1997;156:1908–14.
[9] Wagner AL, Szabunio M, Hazlett KS, et al. Radiologic manifestations of round pneumonia in adults. AJR Am J Roentgenol 1998;170:723–6.
[10] Reittner P, Muller NL, Heyneman L, et al. Mycoplasma pneumoniae pneumonia: radiographic and HRCT features in 28 patients. AJR Am J Roentgenol 2000;174:37–41.
[11] Boiselle PM, Crans Jr CA, Kaplan MA. The changing face of *Pneumocystis carinii* pneumonia in AIDS patients. AJR Am J Roentgenol 1999;172:1301–9.
[12] Kim EA, Lee KS, Primack SL, et al. Viral pneumonias in adults: radiographic and pathologic findings. Radiographics 2002;22:S137–49.

ELSEVIER
SAUNDERS

Radiol Clin N Am 43 (2005) 459 – 465

RADIOLOGIC
CLINICS
of North America

Radiologic Evaluation of the Solitary Pulmonary Nodule

Thomas E. Hartman, MD

Department of Radiology, Mayo Clinic, 200 First Street SW, Rochester, MN 55905, USA

Solitary pulmonary nodules (SPNs) are round or oval areas of increased opacity in the lung on chest imaging that measure less than 3 cm in diameter. It is estimated that approximately 150,000 SPNs are detected in the United States each year [1]. Many of these are discovered incidentally at chest radiography or CT. Although most SPNs are benign, up to 40% of these nodules may be malignant [2–4]. With the advent of low-dose screening for lung cancer, the detection of SPNs is likely to increase.

The imaging evaluation of an SPN can be a complex process. The primary role of radiologic evaluation is to try to differentiate benign from malignant pulmonary nodules. The chest radiograph and CT are the primary modalities in the evaluation of an SPN. When more detailed evaluation is necessary contrast-enhanced CT, positron emission tomography (PET), or PET–CT scanning are often used.

There are certain imaging criteria that can be used to predict the likelihood of a nodule being benign or malignant. The two primary criteria for the evaluation of SPNs are time and the attenuation of the nodule. Although the chest radiograph is useful in the initial evaluation of SPNs, CT is more sensitive to the attenuation differences within a pulmonary nodule. Nodules that are indeterminate on the chest radiograph can often be given a benign diagnosis based on the discovery of calcification or fat at CT [5–7]. Other criteria that may be helpful in the differentiation of benign and malignant nodules include margins of the lesion, size of the lesion, presence of cavitation, and presence of satellite nodules.

E-mail address: Hartman.thomas@mayo.edu

Time

Previous studies have shown that nodules that are stable over a 2-year period have a high incidence of benignity [8,9]. Although a more recent article [10] has shown that the original data supporting this idea are less compelling, the benefit of this evaluation has been recognized clinically over the years. The initial evaluation of an SPN should be to obtain older chest radiographs to assess whether there has been interval growth of the nodule. Lack of growth of the nodule when compared with previous studies over a 2-year interval indicates that the nodule is likely benign. Growth in and of itself does not indicate malignancy, but the presence of an enlarging nodule increases the likelihood that the nodule is malignant.

Attenuation

The attenuation of a pulmonary nodule can be classified as soft tissue, calcification, fat, and in the case of CT as ground glass. Calcification within a pulmonary nodule can take on several different forms: diffuse calcification; central calcification; lamellar calcification; chondroid (popcorn) calcification; and eccentric calcification (Fig. 1) [2,11,12]. Diffuse, central (Fig. 2), and lamellar (Fig. 3) calcifications all indicate a benign cause. In addition to chondroid calcification being a benign pattern, it also allows the specific diagnosis of a hamartoma to be made. Unlike the other types of calcification, eccentric calcification is indeterminate with regard to malignancy. Eccentric calcification can be seen in benign lesions that are calcifying eccentrically. Malignant lesions, however, which are undergoing dystrophic calcifica-

0033-8389/05/$ – see front matter © 2005 Elsevier Inc. All rights reserved.
doi:10.1016/j.rcl.2005.01.008

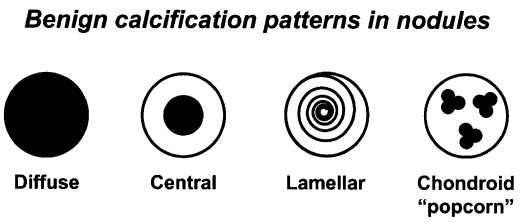

Fig. 1. (Courtesy of the Mayo Clinic Foundation, Rochester, MN; with permission.)

tion or engulfing a benign calcified lesion can also present as eccentric calcification [13].

The demonstration of fat within a pulmonary nodule is an indication of benignity. The presence of fat is virtually diagnostic of a hamartoma [14]. In addition to demonstrating calcification within a nodule better than chest radiographs, CT is also better able to detect fat within a pulmonary nodule (Fig. 4).

CT can also show nodules that do not present as solid lesions when imaged. These nodules may be entirely ground glass attenuation or may be mixed with more solid-appearing areas. Recent studies of screening CT have shown that mixed attenuation nodules have an increased likelihood of malignancy compared with solid nodules. Henschke et al [15] showed that 63% of semisolid nodules were malignant compared with only 7% malignancy in solid nodules. Studies have also shown that when malignant, ground glass attenuation nodules are typically more indolent cancers (Fig. 5). A study by Suzuki et al [16] found 69 cancers that were predominately ground glass attenuation. All these cancers were stage I and there was no evidence of recurrence

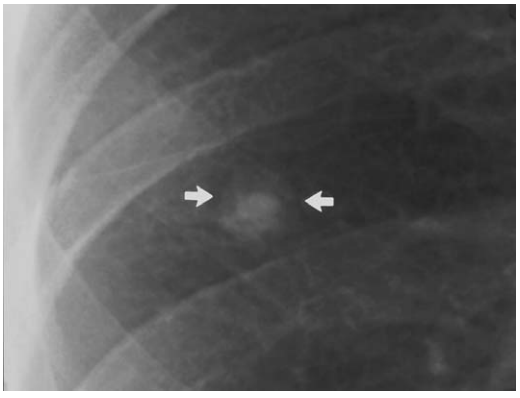

Fig. 2. Targeted view of a chest radiograph showing a nodule (*arrows*) with central calcification compatible with a benign calcified granuloma.

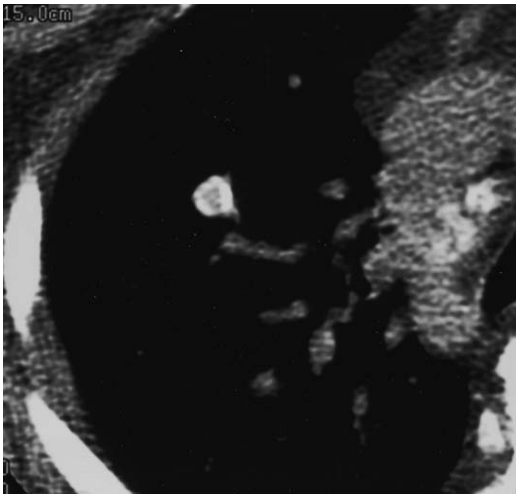

Fig. 3. Thin-section CT of the chest with soft tissue window shows a more lamellar-type calcification of a pulmonary nodule. This was a benign calcified granuloma. Note the associated calcified mediastinal nodes.

at 35 months of follow-up. Additionally, 47 (68%) of 69 of the ground glass attenuation cancers were bronchoalveolar cancers.

Margins

Margins of the nodule may be described as smooth, lobulated, irregular, or spiculated. Regardless of the descriptor, the only margin that has a significant predictive value is the spiculated margin (Fig. 6). A spiculated nodule has a predictive value

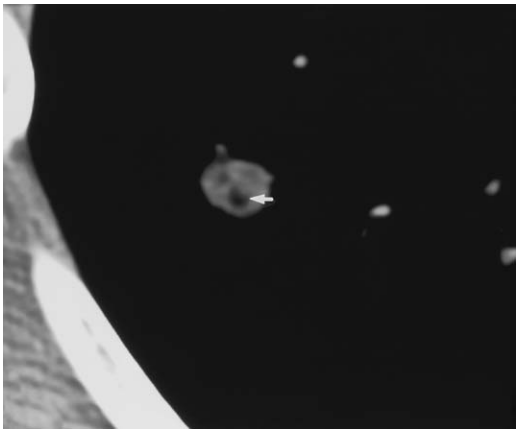

Fig. 4. Thin-section CT through a nodule in the right upper lobe shows areas of fat attenuation (*arrow*) within the nodule. This is diagnostic of a hamartoma.

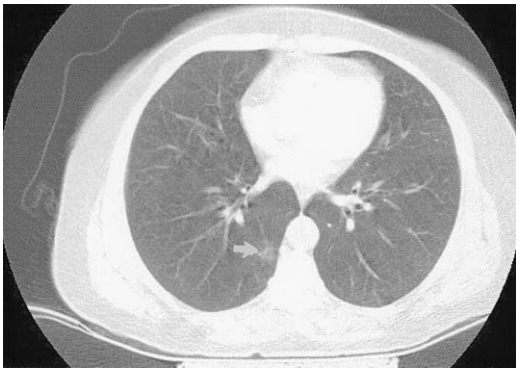

Fig. 5. CT of the chest with lung windows shows a slightly irregular ground glass attenuation nodule in the right lower lobe posteromedially (*arrow*). At resection this was shown to be an adenocarcinoma with bronchoalveolar features. This was a stage 1A lesion.

for malignancy of approximately 90% [12]. The presence of spiculation should prompt a more aggressive work-up of the pulmonary nodule [5,6,12]. Unfortunately, the converse is not true in that the presence of a smooth border does not indicate benignity. Approximately 21% of malignant nodules can have smooth borders [7]. It should also be remembered that although spiculated nodules have a 90% predictive value for malignancy, 10% of spiculated nodules are benign (Fig. 7). Spiculation by itself cannot be used as a confident discriminator between benign and malignant lesions.

Size

Most pulmonary nodules that are benign are less than 2 cm in diameter; however, lesion size below

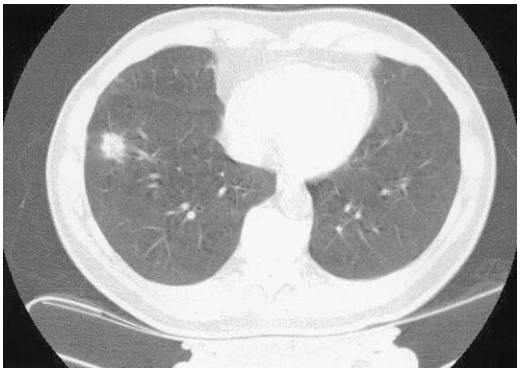

Fig. 6. Chest CT with lung windows shows a spiculated nodule in the right lower lobe laterally. At resection this was an adenocarcinoma.

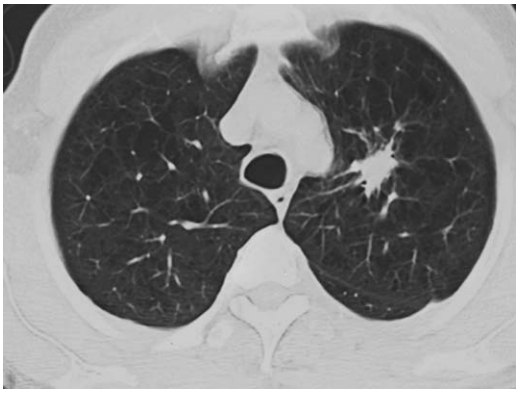

Fig. 7. Chest CT with lung windows shows a spiculated nodule in the left upper lobe centrally. Bronchoscopy revealed granulomas and fungal organisms consistent with blastomycosis. This lesion resolved over several months.

2 cm does not exclude malignancy. Over 40% of malignant nodules are less than 2 cm and 15% of malignant nodules are less than 1 cm in diameter [5,12]. Although malignant nodules are seen with diameters less than 1 cm, they make up a very small proportion of the total number of nodules in this size range. In the recently completed Mayo Clinic CT screening study there were 2832 nodules detected and 89% of these were less than 7 mm. Of this subset of small nodules less than 1% were malignant [17]. In a screening study by Henschke et al [18], no nodules less than 5 mm were malignant. Given the low likelihood of malignancy for these very small nodules even in this high-risk population, it may be possible to ignore or minimally follow-up "ditzels" in low-risk individuals.

Cavitation

Cavitation can occur in benign or malignant nodules [5,19,20]. Benign cavitary nodules often have smooth thin walls, whereas malignant cavitary nodules typically have thick irregular walls. The margins of the internal walls of cavitary nodules may also be helpful in discriminating benign from malignant cavitary nodules. The internal margins of benign cavitary nodules tend to have a smooth inner wall (Fig. 8), whereas the internal margins of malignant cavitary nodules tend to have nodularity along the inner wall of the cavity. It should be remembered, however, that there is significant overlap of these findings and the wall characteristics of cavitary

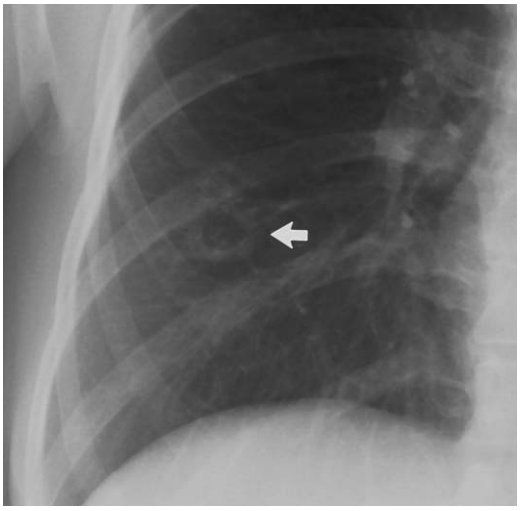

Fig. 8. Targeted view of a chest radiograph shows a cavity in the right lower lung (*arrow*). Although the walls of the cavity are thick, the internal contours of the cavity are smooth. This cavity was caused by histoplasmosis.

nodules cannot be used confidently to differentiate benign from malignant nodules.

Satellite nodules

Satellite nodules are tiny nodules associated with a dominant pulmonary nodule. The presence of satellite nodules indicates a high likelihood that the dominant nodule is benign (Fig. 9). The positive predictive value for benignity with satellite nodules is approximately 90% [12].

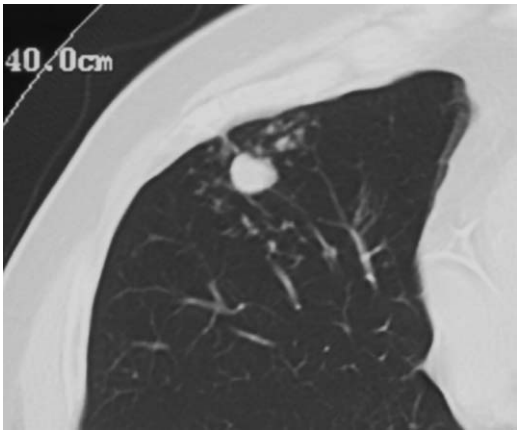

Fig. 9. Targeted CT with lung windows shows a dominate nodule in the right middle lobe. Surrounding this nodule are multiple tiny satellite nodules. At biopsy this was shown to be caused by coccidioidomycosis.

Volumetric assessment

The growth rate of a pulmonary nodule has historically been performed using diameter measurements. There are now additional measurement tools available on CT, however, that allow volumetric assessment of a nodule (Fig. 10). This may allow a more accurate determination of the doubling time of a nodule and may be possible to perform on images taken in as short a time period as 1 month apart [21]. The doubling time for most malignant nodules is between 30 and 400 days. Lack of significant growth over a 2-year period implies a doubling time of at least 730 days and is generally considered to be benign. Automated measurement of these nodules can also eliminate the human error factor.

CT nodule enhancement

CT nodule enhancement takes advantage of the fact that blood flow in malignant pulmonary nodules is increased compared with benign pulmonary nodules. The degree of enhancement is directly related to the vascularity of the nodule and this is increased in malignant nodules [22,23]. Contrast material is administered intravenously and the attenuation of the nodule is measured every 60 seconds for 4 minutes and compared with the attenuation measurement of the nodule taken before the injection of contrast (Fig. 11). Nodule enhancement of less than 15 Houns-

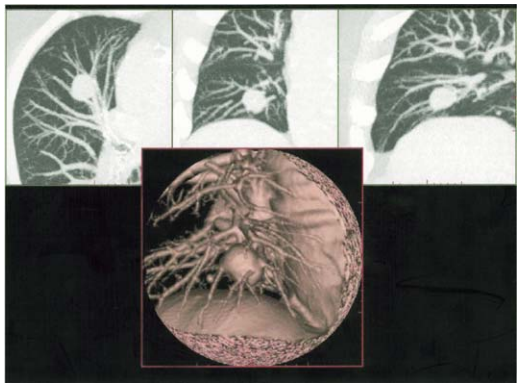

Fig. 10. Transaxial, coronal, and sagittal images of a nodule in the right middle lobe with additional shaded three-dimensional rendering of the right middle lobe nodule.

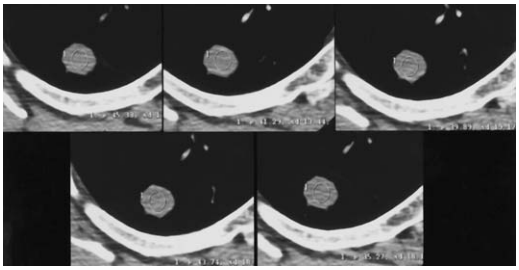

Fig. 11. CT nodule enhancement study of a nodule in the posterior segment of the right upper lobe. The top left image is the precontrast image. The other four images were obtained at 1-minute intervals following the injection of intravenous contrast. There was no significant enhancement of the nodule indicating that this nodule is most likely benign. There has been no significant change in the nodule on follow-up examinations.

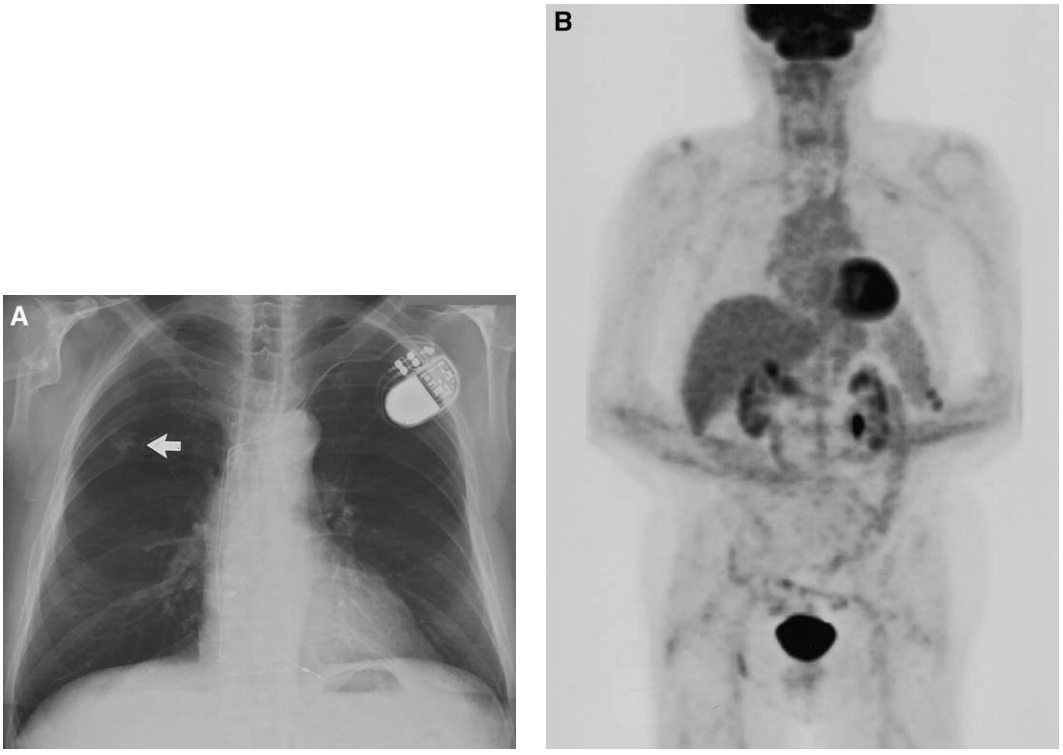

Fig. 12. (*A*) Chest radiograph shows an irregular nodule in the right upper lung (*arrow*) that had increased in size from an examination 6 months prior. (*B*) FDG PET scan with coronal maximal intensity projection image shows no evidence of a hypermetabolic focus to correspond to the pulmonary nodule. Subsequent evaluation of the nodule showed it to be caused by coccidioidomycosis.

field units after administration of contrast material is strongly predictive of benignity (positive predictive value for benignity of 99%). Only 58% of nodules with enhancement of greater than 15 Hounsfield units, however, are malignant [24]. Enhancing nodules, although more likely to be malignant, are still indeterminate and require further work-up to establish a diagnosis. CT enhancement studies have additional limitations. Lesions less than 8 mm in diameter, cavitary lesions, and lesions with central necrosis are not amenable to CT enhancement studies [22–24]. CT enhancement studies are also operator dependent, which can increase the variability of results obtained if the protocol is not adhered to strictly.

Positron emission tomography

PET is an imaging technique that uses metabolic substrates labeled with positron-emitting isotopes. The most commonly used radionuclide is a glucose analogue, 2-[fluorine-18]-fluoro-2-deoxy-D-glucose (FDG). Increased glucose metabolism in malignant relative to benign nodules results in increased uptake and accumulation of FDG, permitting differentiation of benign and malignant nodules. The sensitivity, specificity, and accuracy of PET in the diagnosis of benign nodules has been shown to be 90% or greater in several studies [25–28]. The high specificity of PET for the diagnosis of benign lesions has important clinical use in that lesions with low FDG uptake may be considered benign (Fig. 12). There are instances with slow-growing malignancies, however, such as bronchoalveolar carcinoma or carcinoid, where false-negatives can occur [29,30]. Lesions that are FDG negative should continue to be followed with other imaging modalities to ensure that there is no interval growth. The degree of uptake at PET by a nodule can also have prognostic implications if the nodule is malignant. A study by Marom et al [31] showed a correlation between increased FDG uptake in lung cancers and decreased survival. In addition to false-positive nodules, another limitation is that PET typically has difficulty accurately evaluating lesions that are less than 10 mm in diameter [29,30]. Finally, PET can yield false-positives in patients with active infectious or inflammatory processes, such as tuberculosis and histoplasmosis [28].

Bayesian analysis

Bayesian analysis can be useful in the evaluation of the indeterminate SPN. Bayesian analysis uses likelihood ratios of numerous radiologic findings and clinical features associated with SPNs to estimate the probability of malignancy [12,32]. The mathematics of bayesian analysis is beyond the scope of this article, but using these factors a likelihood ratio for malignancy can be generated. In addition to many of the radiologic findings discussed previously, age and smoking history are factors that are weighted and included in generating the likelihood ratio. It has been shown that bayesian analysis is equivalent or slightly superior to the evaluation of an experienced radiologist in the stratification of benign and malignant pulmonary nodules [12].

Cost-effectiveness analysis

Given the many avenues available for the evaluation of an indeterminate nodule some authors have done cost-effectiveness analyses looking at the different ways in which a nodule can be evaluated. A study by Gould et al [33] showed that cost effectiveness was dependent on the pretest probability of malignancy, but that CT was the recommended initial test in nearly all situations and that the selective use of PET was most cost effective. Another study by Comber et al [34] looked at CT, contrast-enhanced CT, PET, and combinations of the three modalities for the evaluation of an SPN. In this study, contrast-enhanced CT was cost effective either alone or in combination with PET.

Summary

The SPN is a common radiologic finding. The advent of low-dose screening chest CT increases the likelihood that these lesions will need to be dealt with in the future. There are different management approaches and the work-up can often require evaluation over a long period of time to establish a benign or malignant diagnosis. Comparison with old examinations and morphologic evaluation of the size, margins, and internal characteristics of a SPN should be the first step in the evaluation of these lesions. It is often necessary, however, to proceed to additional imaging techniques, such as CT or PET, and in some situations invasive tests, such as transthoracic needle aspiration or surgical biopsy, may be required.

References

[1] Lillington GA. Management of solitary pulmonary nodules. Dis Mon 1991;47:271–318.

[2] Midthun DE, Swensen SJ, Jett JR. Approach to the solitary pulmonary nodule. Mayo Clin Proc 1993;68: 378–85.
[3] Higgins G, Shield TW, Keehn RJ. The solitary pulmonary nodule. Arch Surg 1975;110:570–5.
[4] Gomstock GW, Vaughan RH, Montgomery G. Outcome of solitary pulmonary nodules discovered in an x-ray screening program. N Engl J Med 1956;254: 1018–22.
[5] Zwirewich CV, Vedal S, Miller RR, et al. Solitary pulmonary nodule: high resolution CT and radiologic/ pathologic correlation. Radiology 1991;179:469–76.
[6] Zerhouni EA, Stitik FP, Siegelman SS, et al. CT of the pulmonary nodule: a cooperative study. Radiology 1986;160:319–27.
[7] Siegelman SS, Zerhouni EA, Leo FP, et al. CT of the solitary pulmonary nodule. AJR Am J Roentgenol 1980;135:1–13.
[8] Good CA, Wilson TW. The solitary circumscribed pulmonary nodule. JAMA 1958;166:210–5.
[9] Hood RTJ, Good CA, Clagett OT, et al. Solitary circumscribed lesions of the lung: study of a 156 cases in which resection was performed. JAMA 1953;152: 1185–91.
[10] Yankelevitz D, Henschke C. Does 2-year stability imply that pulmonary nodules are benign? AJR Am J Roentgenol 1997;168:325–8.
[11] Lillington GA, Caskey CE. Evaluation and management of solitary and multiple pulmonary nodules. Clin Chest Med 1993;14:111–9.
[12] Gurney JW. Determining the likelihood of malignancy in solitary pulmonary nodules with bayesian analysis. Radiology 1993;186:405–13.
[13] Mahoney M, Shipley R, Corcoran H, et al. CT demonstration of calcification in carcinoma of the lung. AJR Am J Roentgenol 1990;154:255–8.
[14] Siegelman SS, Khouri NF, Scott WWJ, et al. Pulmonary hamartoma: CT findings. Radiology 1986;160: 313–7.
[15] Henschke CI, Yankelevitz DF, Mirtcheva R, et al. CT screening for lung cancer: frequency and significance of part-solid and nonsolid nodules. AJR Am J Roentgenol 2002;178:1053–7.
[16] Suzuki K, Asamura H, Kusumoto M, et al. Early peripheral lung cancer: prognostic significance of ground glass opacity on thin-section computed tomographic scan. Ann Thorac Surg 2002;74:1635–9.
[17] Swensen SJ, Jett JR, Hartman TE, et al. Lung cancer screening with CT. Mayo Clinic Experience. Radiology 2003;226:756–61.
[18] Henschke CI, Yankelevitz JF, Naidich JP, et al. CT screening for lung cancer: suspiciousness of nodules according to size on baseline scans. Radiology 2004; 231:164–8.
[19] Theros EG. Varying manifestations of peripheral pulmonary neoplasms: a radiologic/pathologic correlative study. AJR Am J Roentgenol 1977;128:893–914.
[20] Woodring JH, Fried AM, Chuang VP. Solitary cavities of the lung: diagnostic implications of cavitary wall thickness. AJR Am J Roentgenol 1980;135: 1269–71.
[21] Yankelevitz DF, Reeves AP, Kostis WJ, et al. Small pulmonary nodules: volumetrically determined growth rates based on CT evaluation. Radiology 2000;217: 251–6.
[22] Swensen SJ, Brown LR, Colby TV, et al. Pulmonary nodules: CT evaluation of enhancement with iodinated contrast material. Radiology 1995;194:393–8.
[23] Swensen SJ, Brown LR, Colby TV, et al. Lung nodule enhancement at CT: prospective findings. Radiology 1996;201:447–55.
[24] Swensen SJ, Vigianno RW, Midthun JE, et al. Lung nodule enhancement at CT: multicenter study. Radiology 2000;214:73–80.
[25] Patz EF, Lowe VJ, Hoffman JM, et al. Focal pulmonary abnormalities: evaluation with F-18 fluorodeoxyglucose PET scanning. Radiology 1993;188:487–90.
[26] Gupta NC, Frank AR, Dewan NA, et al. Solitary pulmonary nodules: detection of malignancy with PET with 2-[F-18]-fluoro-2-deoxy-D-glucose. Radiology 1992;184:441–4.
[27] Gupta NC, Maloof J, Gunel E. Probability of malignancy in solitary pulmonary nodules using fluorine-18-FDG and PET. J Nucl Med 1996;37:943–8.
[28] Lowe VJ, Fletcher JW, Gobar L. Prospective investigation of PET and lung nodules (PIOPILN). J Clin Oncol 1998;16:1075–84.
[29] Erasmus JJ, McAdams HP, Patz EF, et al. Evaluation of primary pulmonary carcinoid tumors using FDG PET. AJR Am J Roentgenol 1998;170:1369–73.
[30] Higashi K, Ueda Y, Seki H, et al. Fluorine 18 FDG PET imaging in negative in bronchioloalveolar lung carcinoma. J Nucl Med 1998;39:1016–20.
[31] Marom EM, Sarvis S, Herndon JE, et al. T1 lung cancers: sensitivity of diagnosis with fluorodeoxyglucose PET. Radiology 2002;223:453–9.
[32] Black WC, Armstrong P. Communicating the significance of radiologic test results: the likelihood ratio. AJR Am J Roentgenol 1986;147:1313–8.
[33] Gould MK, Sanders GD, Barnett PG, et al. Cost-effectiveness of alternative management strategies for patients with solitary pulmonary nodules. Ann Intern Med 2003;138:724–35.
[34] Comber LA, Keith CJ, Griffiths M, et al. Solitary pulmonary nodules: impact of quantitative contrast-enhanced CT on the cost-effectiveness of FDG-PET. Clin Radiol 2003;58:706–11.

ELSEVIER
SAUNDERS

Radiol Clin N Am 43 (2005) 611 – 619

RADIOLOGIC
CLINICS
of North America

Imaging for Esophageal Tumors

Robert J. Korst, MD, Nasser K. Altorki, MD*

Division of Thoracic Surgery, Department of Cardiothoracic Surgery, Weill Medical College, Cornell University, 525 East 58th Street, New York, NY 10021, USA

Carcinoma of the esophagus comprises the vast majority of malignant esophageal tumors and represents the seventh most common malignancy worldwide, with its incidence reaching endemic proportions in specific geographic locations in Asia and Africa [1]. Although esophageal cancer is presently responsible for only approximately 13,000 deaths annually in the United States [2], the incidence of adenocarcinoma of the esophagus is rising faster than any other malignant tumor in the United States [3]. Because the majority of patients present with advanced disease, only roughly 12% of patients diagnosed with this tumor will survive more than 5 years after diagnosis [2].

The treatment of carcinoma of the esophagus is stage-dependent (Table 1). While patients who have widely metastatic disease are not treated with curative intent (ie, only palliative chemotherapy or supportive care), most clinicians would agree that patients who have early (superficial, node-negative) cancers should undergo surgical resection for cure; however, the ideal treatment of locally advanced (transmural, node-positive) disease remains controversial, with some clinicians advocating surgical resection alone, others supporting preoperative neoadjuvant therapy followed by surgery, and still others backing definitive chemoradiation without surgery.

Given the stage dependency of therapeutic options for patients who have esophageal cancer, it is essential to determine the extent of disease accurately before formulating the treatment plan. Imaging plays an integral role in guiding the clinician in this staging process, with specific imaging modalities being useful for the evaluation of distant disease, locoregional disease, or both. Certain imaging techniques have proven to be useful in guiding biopsy procedures, such as fine needle aspiration (FNA) of suspicious lesions; however, the accuracy of some of these techniques seems to rely, at least in part, upon the experience of the operator [4]. Finally, individual imaging algorithms and the preference of one modality versus another varies with device availability, individual experience, and geographic location.

Imaging of distant metastatic disease

In the United States, approximately 20% to 30% of patients who have carcinoma of the esophagus have distant metastatic disease at the time of presentation [2,5]. The most common visceral metastatic sites include, in decreasing order of prevalence, liver, lung, bone, and adrenal glands [5,6]. As a result, imaging for patients who have esophageal cancer should evaluate these sites. The brain is an uncommon site of metastases from esophageal cancer, occurring in less than 2% of patients who have metastatic disease [5,6]. Further, it is uncommon for patients who have carcinoma of the esophagus to present with solitary metastatic lesions; most possess multiple numbers of metastases, albeit usually in a single organ [5,6]. In these cases of metastatic disease in a pattern consistent with esophageal cancer, oftentimes histologic confirmation by means of biopsies is not necessary; however, a second, corroborating imaging study should be performed. In the

This article was originally published in *Thoracic Surgery Clinics* 2004;14(1):61–9.

* Corresponding author.
E-mail address: naltkori@med.cornell.edu (N.K. Altorki).

0033-8389/05/$ – see front matter © 2005 Elsevier Inc. All rights reserved.
doi:10.1016/j.rcl.2005.03.002

Table 1
Staging scheme for carcinoma of the esophagus

Stage	Characteristics
Primary tumor (T)	
TX	Tumor cannot be assessed
T0	No evidence of tumor
Tis	Carcinoma in situ/high grade dysplasia
T1	Confined to mucosa or submucosa, not into muscularis proporia
T2	Invades into muscularis propria
T3	Invades through muscularis propria but not into adjacent organs
T4	Invades adjacent structures/organs
Nodal status (N)	
NX	Regional nodes cannot be assessed
N0	No regional nodal metastases
N1	Regional nodal metastases
Distant metastases (M)	
MX	Distant metastases cannot be assessed
M1a	Metastatic cervical nodes/upper thoracic esophageal tumor
	Metastatic celiac nodes/lower thoracic esophageal tumor
M1b	Any tumor location with visceral/bony metastases
	Any tumor location with nodal metastases beyond N1 or M1a
Stage groupings	
0	TisN0M0
I	T1N0M0
IIA	T2–3N0M0
IIB	T1–2N1M0
III	T3N1M0
	T4 Any N
IVA	Any T Any N M1a
IVB	Any T Any N M1b

uncommon situation in which a patient presents with a single metastatic lesion radiographically, or a pattern inconsistent with that typically seen with esophageal cancer, confirmatory biopsy should be performed more routinely to ensure that the patient does not have potentially curable (resectable) disease or another distinct disease process. Nearly all potentially metastatic foci can technically be assessed cytologically by means of image-guided FNA [4].

Because carcinoma of the esophagus is still an uncommon disease relative to other tumor types in the United States, little published data exist regarding accuracy of many imaging modalities (eg, radionuclide bone scan) exclusively for the detection of distant metastases in patients who have esophageal cancer; however, multiple published reports concerning the accuracy of these imaging techniques exist for carcinomatous tumors in general. Intravenous contrast-enhanced CT remains the workhorse for imaging patients who have carcinoma of the esophagus to rule out distant metastatic lesions because it allows assessment of the three most common sites of distant metastases. Scans should be obtained from the base of the neck (thoracic inlet) through the liver and adrenal glands in the upper abdomen. Metastatic deposits in the liver usually appear as hypodense, ill-defined lesions on contrast-enhanced CT scans (Fig. 1) [7,8]. As with any liver imaging modality, the sensitivity of the CT scan for detecting metastatic liver disease depends on the size of the lesion [7,8]. While the vast majority of lesions larger than 1 cm are detected using CT scan, the sensitivity drops precipitously for metastatic deposits less than 1 cm in diameter or if the scan is performed without intravenous contrast. Similarly, if the lesions are of adequate size (>1 cm), CT is useful for distinguishing metastases from benign entities, most notably cysts and hemangiomas, with the former possessing the density of fluid and the latter demonstrating peripheral enhancement with delayed washout of intravenous contrast [7,8].

Other imaging modalities that are useful in assessing the status of the liver include ultrasound (US) and MR imaging. Although transabdominal US is inexpensive and distinguishes between cystic and solid liver lesions accurately, its sensitivity in detect-

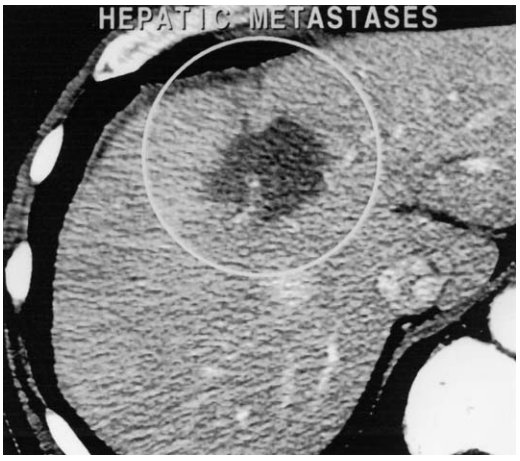

Fig. 1. Intravenous contrast-enhanced CT image of the liver of a patient who had carcinoma of the esophagus. The encircled region demonstrates a large, hypodense, irregularly bordered lesion representing the typical appearance of metastasis.

ing metastatic liver deposits in general is clearly inferior to that of CT [7,8]. Laparoscopic US is potentially more sensitive than the transcutaneous approach [9], but it is an invasive procedure that tends to be especially user-dependent, with published data suggesting only limited benefit for patients who have cancer of the esophageal body [9,10]. MR imaging can be beneficial when CT demonstrates liver lesions and further characterization is needed. Gadolinium contrast agents might enhance the sensitivity of MR imaging, which is an effective modality for distinguishing metastases from benign liver lesions, including cysts and hemangiomas [7,8].

Pulmonary metastases are also seen in patients who have esophageal carcinoma. Suspicious pulmonary nodules are usually round, smooth-bordered, and noncalcified on CT scan. Given the high prevalence of incidental, benign pulmonary nodules seen in smokers over the age of 60 [11], any suspicious lung lesion should be biopsied using FNA or a thoracoscopic approach. Further, given the role of smoking in carcinogenesis of the lung and esophagus and the concept of field cancerization, primary lung cancer also needs to be ruled out in these situations, particularly if the pulmonary lesion is solitary [12].

Because bone is a common site for metastases from carcinoma of the esophagus, routine radionuclide bone scanning can be performed in these patients. In general, in patients who have cancer, a scan showing multiple areas of uptake strongly suggests metastases; however, only 50% of solitary foci represent metastases, even in patients who have a history of cancer [13]. Tracer accumulation can occur at any skeletal site with an elevated rate of bone turnover. As a result, corroborative studies are required in the majority of cases of a positive bone scan, which include MR imaging (which is especially useful for evaluation of the spine), plain radiographs, and even a CT scan. The radiographic evaluation of adrenal lesions has been the subject of many reported studies involving the use of CT and MR imaging. While primary malignant lesions of the adrenal glands are uncommon, the prevalence of benign adrenal adenomas in the general population is significant and might approach 7% by age 70 [14]. Because of the high intracellular lipid content in adenomas, thin-cut (3 mm), noncontrast CT and MR imaging have been reported to possess specificity rivaling that of FNA with cytologic examination for distinguishing metastases from adenomas [15].

Positron emission tomography (fluorine-18-2-flouro2-deoxyglucose positron emission tomography [FDG-PET]) is a new imaging modality that is gaining popularity in staging patients who have many types of malignant disease. Based on the finding that malignant cells possess higher rates of glucose uptake compared with normal cells, several small studies have demonstrated that FDG-PET has been shown to radiographically detect occult distant metastatic disease in approximately 20% of patients who have esophageal cancer [16,17]. Given these encouraging preliminary findings, this concept is presently being evaluated in a large, multicenter, prospective study. Drawbacks of FDG-PET are related to its lack of sensitivity for detecting small (<1 cm) metastatic lesions and its relative lack of anatomic detail. The latter problem can be at least partially addressed by the advent of newer PET/CT fusion scanners, in which a composite image is generated incorporating FDG-PET and CT images. It is important to note that until larger, confirmatory studies are performed examining the utility of FDG-PET for detection of metastatic disease, FDG-PET findings in patients who have esophageal cancer should be confirmed with a second imaging technique or a biopsy depending on the individual clinical scenario. This guideline is especially true in the assessment of potentially metastatic pulmonary lesions because although the FDG-PET scan is frequently positive in pulmonary metastases, a number of benign pulmonary lesions (mainly inflammatory) can also be glucose avid [18].

Imaging of the primary tumor

Carcinoma of the esophagus originates in the epithelial lining and spreads into and through the wall of the esophagus and throughout the draining lymphatics to lymph nodes. Esophageal carcinoma readily disseminates hematogenously to distant sites. Published data have confirmed that the presence of lymph node metastases is a powerful predictor of prognosis in these patients and is a marker for systemic spread of the disease [19,20]. Similarly, the depth of penetration of the primary tumor into the esophageal wall predicts the presence or absence of lymph node metastases, with approximately 85% of T3 tumors being associated with lymphatic spread [1]. Accurate imaging of the primary tumor in patients who have esophageal carcinoma is therefore important, not only for determining resectability in patients who have locally advanced disease but also predicting prognosis in patients who have disease that appears to be limited to the esophagus.

In past decades, primary tumors of the esophagus were imaged using barium esophagography. Not only could the location and longitudinal extent of the tumor be determined, estimations of resectability could

be made based on the esophagram. In this regard, Akiyama and colleagues [21] found that 74% of transmural tumors caused distortion of the normal axis of the esophagus. This distortion is caused by tethering of the esophagus in the region of the tumor.

The two most commonly used contemporary imaging procedures for assessing the primary tumor are CT and endoscopic US (EUS). Given its lack of anatomic detail, FDG-PET is unable to provide any definition of the esophageal wall or periesophageal tissues, making it of limited utility in assessing the primary tumor (Fig. 2B). Similarly, CT does not provide adequate resolution in distinguishing the layers of the esophageal wall; however, information can be gained concerning neighboring organ involvement, or, more specifically, the lack thereof (Fig. 2A). Preservation of fat planes surrounding the tumor has been proposed and is supported as radiographic exclusion of a T4 tumor [22,23]. Conversely, loss of fat planes might indicate neighboring organ involvement. When the tumor compresses the membranous left main bronchus or trachea, bronchoscopy should be performed to definitively establish airway invasion. As with the airway, invasion of the descending thoracic aorta is difficult to predict using CT. Some published evidence suggests that the greater the circumference of the aorta abutted by the tumor, the more likely the tumor will be unresectable [24]. In summary, although T4 tumors can be excluded reliably by the preservation of peritumoral fat planes, the definitive establishment of neighboring organ invasion is difficult to predict with CT and on most occasions operative exploration is required.

EUS is an imaging modality that is gaining popularity in the preoperative assessment of patients who have esophageal tumors. The great strength of EUS lies in its ability to visualize the esophageal wall in greater detail than any other imaging modality. The esophageal wall is seen as four distinct layers using EUS: mucosa, muscularis mucosa, submucosa, and muscularis propria. A fifth layer corresponding to periesophageal fat is also readily discernable using EUS. A standard EUS examination usually involves evaluation of the tumor with 7.5 MHz and 12 MHz probes and is considered to be the most accurate means by which to estimate tumor invasion. In this regard, large review series place the accuracy of EUS in determining the depth of invasion of esophageal carcinoma at approximately 85% [25,26], with the identification of T2 tumors being the least accurate (Figs. 3 and 4) [25,26].

Drawbacks of EUS include the relatively steep learning curve [27] and the inability to pass the transducer completely through the tumor in up to 50% of

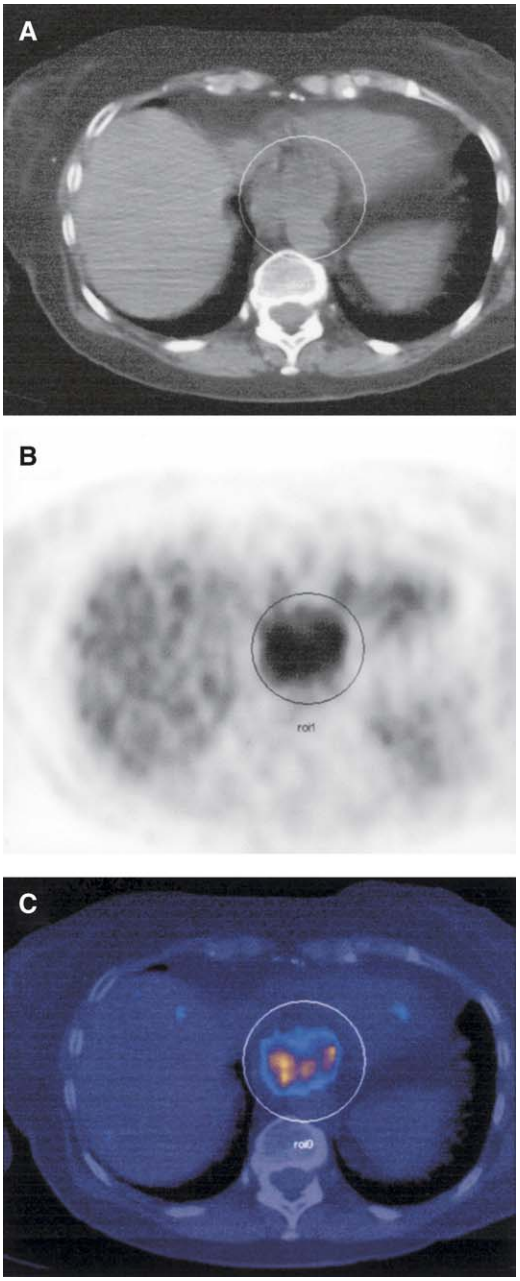

Fig. 2. CT/PET fusion study depicting esophageal carcinoma in the distal third of the esophagus. The lesion is encircled in each panel. (*A*) Noncontrast CT image. (*B*) FDG-PET image. (*C*) CT/PET fusion image.

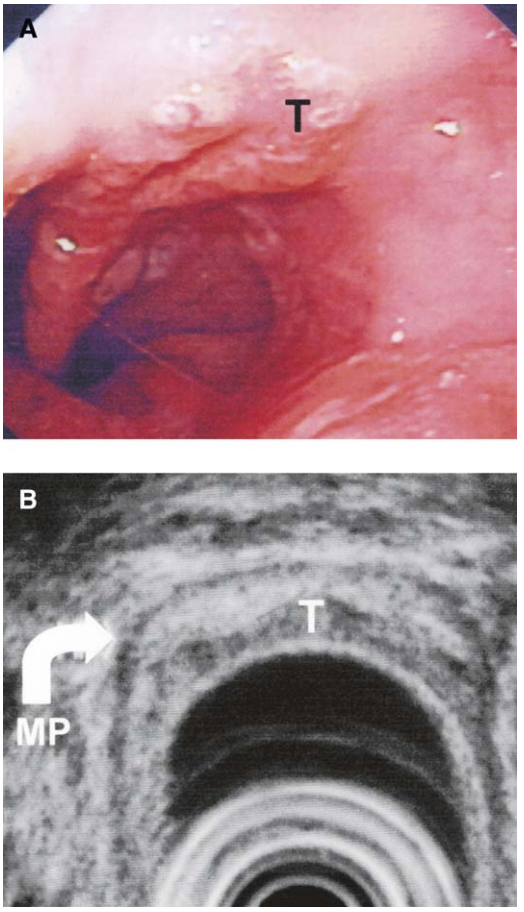

Fig. 3. Elderly patient who had T1 adenocarcinoma of the distal esophagus. (*A*) Endoscopic appearance. (*B*) EUS image demonstrating lack of penetration into the muscularis propria (MP). T, tumor.

cases [25]. Newer probes are being developed continuously to address this problem, some being thin enough to pass through the instrument channel of the endoscope [28]. Other recent developments in EUS technology include probes that allow for helical scanning with subsequent three-dimensional reconstruction of EUS images [29] and the use of high-frequency transducers. These latter probes tend to be useful in imaging superficial tumors of the esophagus by providing more detail, and they can differentiate between T1A and T1B successfully [30]. This distinction might be of importance in locations in which esophageal cancer screening is performed and lesions are detected at earlier stages more routinely.

Similar to EUS, preliminary data suggest that investigational techniques such as endoluminal MR imaging might be able to visualize the layers of the esophageal wall accurately [31]. Whether or not this technique will earn a role in the future of imaging for carcinoma of the esophagus requires further investigation.

Imaging of lymphatic metastases

It is generally agreed that the presence of lymph node metastases (N1 disease) associated with resectable carcinoma of the esophagus is the strongest known predictor of recurrence and mortality following definitive therapy for this disease [19,20]. As with some other types of malignancies, the degree of lymph node involvement might also be of prognostic value, with published studies demonstrating that patients who have less than three to five metastatic nodes survive appreciably longer than those who have more than 10 involved nodes following a potentially curative resection [19,32]. Given this information, the determination of lymph node status before definitive therapy might be of importance because patients who have more advanced locoregional disease could be enrolled in trials of novel or multi-modal therapies.

Historically, clinicians have attempted to image lymph node metastases using multiple modalities with limited success. The accuracy of the CT scan for staging this aspect of the disease has been well described in multiple literature reports. Because the detection of metastatic nodes using CT depends primarily on size criteria, its sensitivity and specificity in

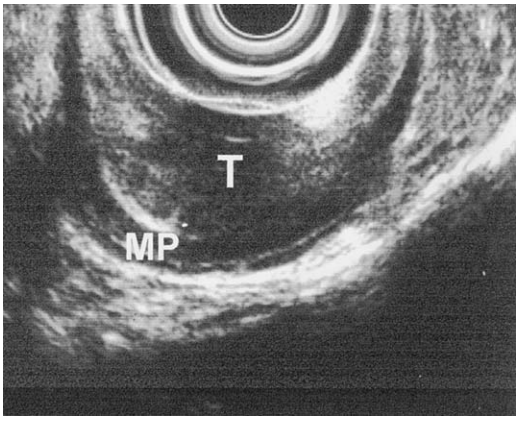

Fig. 4. EUS image of T2 squamous cell carcinoma of the esophagus. Note the tumor (T) is indistinguishable from the muscularis propria (MP).

detecting metastatic disease in the lymph nodes varies with the definition of an abnormally enlarged node. Sensitivity is enhanced if smaller size criteria are used, but specificity is sacrificed. Conversely, large lymph nodes on CT are more likely to be metastatic; however, many metastatic nodes are only minimally—if at all—enlarged, which hampers sensitivity. Using the common size criterion of 1 cm to define an enlarged node, most studies report that the sensitivity of CT is poor (30%–60%) [17,33] and does not appear to be enhanced with helical scanning [34]. In contrast, specificity tends to be somewhat better, but still suboptimal (60%–80%). In summary, if CT suggests the presence of metastatic lymph nodes, tissue confirmation should be obtained if the treatment plan will be affected.

In recent years the role of FDG-PET has been evaluated for the detection of lymph node metastases in patients who have esophageal cancer. FDG-PET is a physiologic examination that has poor anatomic definition, which severely affects its ability to predict NI disease accurately in the peritumoral location [33,35]. In this regard, most esophageal tumors are intensely FDG avid, further inhibiting the resolution of the study and making it easy to miss metastatic nodes that are adjacent to the primary tumor. In contrast, when metastatic lymph nodes are located more remotely, the accuracy of FDG-PET increases [33,35]. The differentiation of FDG-avid peritumoral nodes from the primary tumor might be aided by the development of CT/PET fusion scanners (Fig. 5), in which the anatomic detail of CT is combined with the physiologic nature of FDG-PET, but this scenario remains to be seen.

Given these spatial limitations of FDG-PET, it is not surprising that the sensitivity of this modality in detecting peritumoral metastatic lymph nodes is poor (20%–50%) in most contemporary series [17,33,35]; however, sensitivities as high as 90% have been reported in the detection of metastatic nodes in distant locations such as the abdomen and the neck [33,35]. In distinct contrast, the specificity of FDG-PET in lymph node evaluation tends to be high, exceeding 90% in many series [17,33,35].

US, transcutaneous and endoscopic, is used frequently to stage the N descriptor in patients who have esophageal carcinoma. US relies not only on size criteria to determine metastasis but also on the internal echo characteristics of individual nodes. Well-demarcated, larger, hypoechoic nodes with scattered large, internal echoes are more likely to represent metastases (Fig. 6) [36,37]. The use of transcutaneous US to image cervical and supraclavicular lymph nodes has become routine in some regions, especially in Asia, where reported accuracy is approximately 70% to 80% [36,38]; however, other reports have not been able to confirm these results [35].

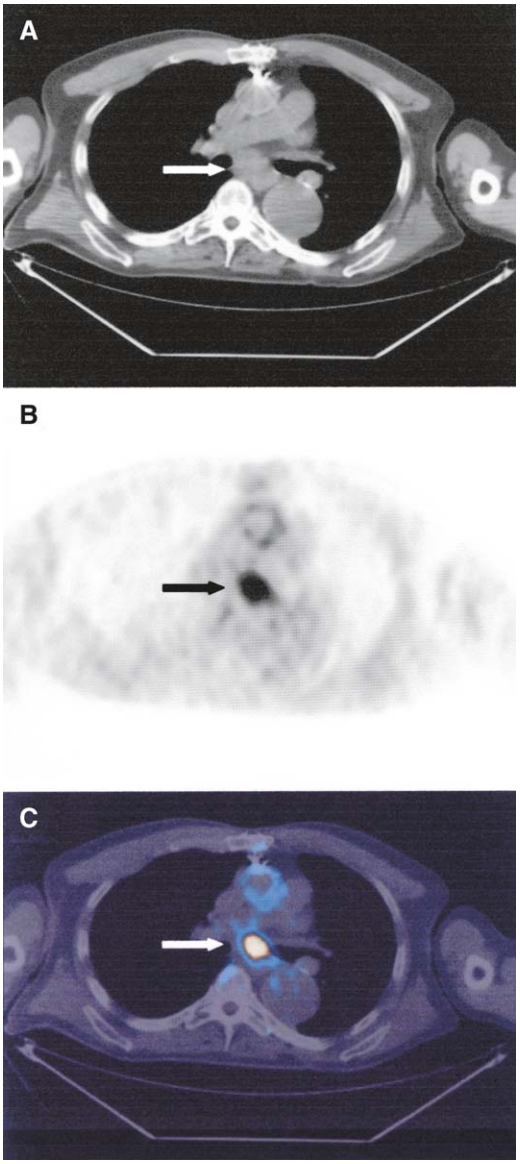

Fig. 5. CT/PET fusion study depicting malignant periesophageal lymph node. The arrow indicates the malignant node in each panel. (*A*) Noncontrast CT image. (*B*) FDG-PET image. (*C*) CT/PET fusion image.

The accuracy of EUS in detecting metastatic lymph nodes in patients who have esophageal carcinoma has also been investigated and reported in many series (Fig. 6). Wide variations of sensitivity

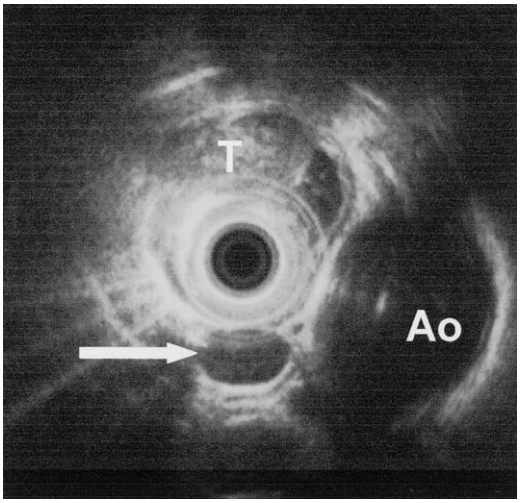

Fig. 6. EUS image of a typical metastatic lymph node in a patient who had carcinoma of the esophagus. The metastatic node is seen as a large, hypoechoic structure in the periesophageal location (*arrow*). Ao, descending thoracic aorta; T, tumor.

and specificity have been reported in these series, ranging from 40% to 100% [39]. Similar to the ability to detect T stage, the ability of EUS to stage the N descriptor effectively is highly user-dependent. Centers that perform large numbers of procedures report higher accuracy rates [37], which have not been reproducible in other studies [35], which leads one to question the accuracy of EUS in routine practice settings. To address this issue, EUS has been combined with FNA of suspicious lymph nodes. The addition of FNA to EUS has been shown by some investigators to markedly enhance the specificity of EUS alone, especially in the region of the celiac axis [40,41]. Whether or not these excellent results can be achieved and reproduced routinely remains to be determined and will influence the applicability of this technique in routine practice situations.

Assessment of response to therapy

Given the relatively poor prognosis of patients who have carcinoma of the esophagus who undergo surgical resection alone for locally advanced disease, preoperative (induction) chemotherapy or chemoradiotherapy are being investigated as means to obtain higher cure rates. Data from these clinical trials have suggested that patients who are complete pathologic responders to induction therapy seem to reap the most benefit from multimodal treatment protocols [42,43], so it might be advantageous to determine which patients would benefit most from surgery before resection. The accuracy of imaging modalities in this capacity is now being investigated, with some preliminary results published in recent literature.

Jones and colleagues [44] compared the response to preoperative chemoradiation as determined by repeat CT scanning to pathological response rates prospectively in 50 patients. Using standard radiographic response criteria, CT was found to be ineffective for determining pathologic tumor response or disease stage in this setting. Similarly, EUS was unable to stage patients accurately after induction therapy [45,46]; however, some evidence suggested that measurements of tumor size using EUS might correlate with response to chemoradiotherapy [47]. Some recent data suggest that a reduction in FDG uptake by esophageal tumors after induction chemoradiotherapy might correlate with pathologic response to therapy [48] and even improved survival in these patients [49]. The use of imaging studies to assess the response to therapy in patients who have esophageal carcinoma is an emerging field, and it requires extensive investigation in future studies.

Summary

Carcinoma of the esophagus must be staged accurately before a treatment plan is initiated, and imaging studies play a major role in this process. Imaging for esophageal carcinoma involves evaluation of the locoregional extent of the tumor and distant metastatic disease. A CT scan of the chest and upper abdomen provides the most comprehensive information about esophageal carcinoma; however, accurate assessment of the depth of primary tumor invasion and lymph node status remains limited, even with newer generation scanners. EUS is a user-dependent modality that has emerged as a highly accurate technique in experienced hands to evaluate the depth of penetration of esophageal tumors, but its ability to detect metastatic lymph nodes is less impressive, leading some investigators to perform confirmatory needle aspiration of suspicious nodes. FDG-PET is a physiologic examination that is the subject of intense investigation in patients who have esophageal carcinoma. Preliminary studies have suggested that FDG-PET can detect otherwise radiographically occult distant metastatic disease in these patients, and changes in FDG uptake might correlate

with the response to therapy. These findings need to be confirmed in larger studies. More sophisticated technology continues to be developed for imaging carcinoma of the esophagus, which will more than likely affect staging algorithms in the future.

References

[1] Korst RJ, Altorki NK. Esophageal cancer. In: Winchester DP, Daly JM, Jones RS, Murphy GP, editors. Cancer surgery for the general surgeon. Philadelphia: Lippincott-Raven; 1999. p. 155–72.

[2] Greenlee RT, Murray T, Bolden S, Wingo PA. Cancer statistics, 2000. CA 2000;50:7–33.

[3] Devesa SS, Blot WJ, Fraumeni Jr JF. Changing patterns in the incidence of esophageal and gastric carcinoma in the United States. Cancer 1998;83:2049–53.

[4] Long BW. Image-guided percutaneous needle biopsy: an overview. Radiol Technol 2000;71(4):335–59.

[5] Quint LE, Hepburn LM, Francis IR, Whyte RI, Orringer MB. Incidence and distribution of distant metastases from newly diagnosed esophageal carcinoma. Cancer 1995;76(7):1120–5.

[6] Christie NA, Rice TW, DeCamp MM, Goldblum JR, Adelstein DJ, Zuccaro Jr G, et al. M1a/M1b esophageal carcinoma: clinical relevance. J Thorac Cardiovasc Surg 1999;118(5):900–7.

[7] Paulson EK. Evaluation of the liver for metastatic disease. Semin Liver Dis 2001;21:225–36.

[8] Robinson PJA. Imaging liver metastases: current limitations and future prospects. Br J Radiol 2000;73: 234–41.

[9] Bemelman WA, van Delden OM, van Lanschot JJ, de Wit LT, Smits NJ, Fockens P, et al. Laparoscopy and laparoscopic ultrasonography in staging of carcinoma of the esophagus and gastric cardia. J Am Coll Surg 1995;181(5):421–5.

[10] van Dijkum EJ, de Wit LT, van Delden OM, Kruyt PM, van Lanschot JJ, Rauws EA, et al. Staging laparoscopy and laparoscopic ultrasonography in more than 400 patients with upper gastrointestinal carcinoma. J Am Coll Surg 1999;189(5):459–65.

[11] Henschke CI, McCauley DI, Yankelevitz DF, Naidich DP, McGuinness G, Miettinen OS, et al. Early Lung Cancer Action Project: overall design and findings from baseline screening. Lancet 1999;354(9173):99–105.

[12] Margolis ML, Howlett P, Bubanj R. Pulmonary nodules in patients with esophageal carcinoma. J Clin Gastroenterol 1998;26:245–8.

[13] Rosenthal DI. Radiologic diagnosis of bone metastases. Cancer 1997;80(8 Suppl):1595–607.

[14] Reincke M. Mutations in adrenocortical tumors. Horm Metab Res 1998;30(6–7):447–55.

[15] Lockhart ME, Smith JK, Kenney PJ. Imaging of adrenal masses. Eur J Radiol 2002;41(2):95–112.

[16] Luketich JD, Friedman DM, Weigel TL, Meehan MA, Keenan RJ, Townsend DW, et al. Evaluation of distant metastases in esophageal cancer: 100 consecutive positron emission tomography scans. Ann Thorac Surg 1999;68(4):1133–6.

[17] Block MI, Patterson GA, Sundaresan RS, Bailey MS, Flanagan FL, Dehdashti F, et al. Improvement in staging of esophageal cancer with the addition of positron emission tomography. Ann Thorac Surg 1997;64(3): 770–6.

[18] Croft DR, Trapp J, Kernstine K, Kirchner P, Mullan B, Galvin J, et al. FDG-PET imaging and the diagnosis of non-small cell lung cancer in a region of high histoplasmosis prevalence. Lung Cancer 2002;36(3): 297–301.

[19] Korst RJ, Rusch VW, Venkatraman E, Bains MS, Burt ME, Downey RJ, et al. Proposed revision of the staging classification for esophageal cancer. J Thorac Cardiovasc Surg 1998;115(3):660–9.

[20] Altorki N, Kent M, Ferrara C, Port J. Three-field lymph node dissection for squamous cell and adenocarcinoma of the esophagus. Ann Surg 2002;236(2): 177–83.

[21] Akiyama H, Kogure T, Itai Y. The esophageal axis and its relationship to the resectability of carcinoma of the esophagus. Ann Surg 1972;176:30–6.

[22] Rice TW. Clinical staging of esophageal carcinoma. CT, EUS, and PET. Chest Surg Clin N Am 2000; 10(3):471–85.

[23] Thompson WM, Halvorsen RA. Staging esophageal carcinoma II. CT and MRI. Semin Oncol 1994;21: 447–52.

[24] Picus D, Balfe DM, Koehler RE, Roper CL, Owen JW. Computed tomography in the staging of esophageal carcinoma. Radiology 1983;146(2):433–8.

[25] Lightdale CJ. Staging esophageal carcinoma I. Endoscopic ultrasonography. Semin Oncol 1994;21:438–46.

[26] Rosch T. Endosonographic staging of esophageal cancer: a review of literature results. Gastrointest Endosc Clin N Am 1995;5:537–47.

[27] Schlick T, Heintz A, Junginger T. The examiner's learning effect and its influence on the quality of endoscopic ultrasonography in carcinoma of the esophagus and gastric cardia. Surg Endosc 1999;13: 894–8.

[28] Silverstein FE, Martin RW, Kimmey MB, Jiranek GC, Franklin DW, Proctor A. Evaluation of an endoscopic ultrasound probe: in vitro and in vivo canine studies. Gastroenterology 1989;96:1058–62.

[29] Tokiyama H, Yanai H, Nakamura H, Takeo Y, Yoshida T, Okita K. Three-dimensional endoscopic ultrasonography of lesions of the upper gastrointestinal tract using a radial–linear switchable thin ultrasound probe. J Gastroenterol Hepatol 1999;14(12):1212–8.

[30] Waxman I. Endosonography in columnar-lined esophagus. Gastroenterol Clin N Am 1997;26(3):607–12.

[31] Ozawa S, Imai Y, Suwa T, Kitajima M. What's new in imaging? New magnetic resonance imaging of esophageal cancer using an endoluminal surface coil and antibody-coated magnetite particles. Recent Results Cancer Res 2000;155:73–87.

[32] Eloubeidi MA, Desmond R, Arguedas MR, Reed CE, Wilcox CM. Prognostic factors for the survival of patients with esophageal carcinoma in the US: the importance of tumor length and lymph node status. Cancer 2002;95(7):1434–43.

[33] Kato H, Kuwano H, Nakajima M, Miyazaki T, Yoshikawa M, Ojima H, et al. Comparison between positron emission tomography and computed tomography in the use of the assessment of esophageal carcinoma. Cancer 2002;94(4):921–8.

[34] Romagnuolo J, Scott J, Hawes RH, Hoffman BJ, Reed CE, Aithal GP, et al. Helical CT versus EUS with fine needle aspiration for celiac nodal assessment in patients with esophageal cancer. Gastrointest Endosc 2002;55(6):648–54.

[35] Lerut T, Flamen P, Ectors N, Van Custem E, Peeters M, Hiele M, et al. Histopathologic validation of lymph node staging with FDG-PET scan in cancer of the esophagus and gastroesophageal junction: a prospective study based on primary surgery with extensive lymphadenectomy. Ann Surg 2000;232(6): 743–52.

[36] Natsugoe S, Nakashima S, Matsumoto M, Sakita H, Sakamoto F, Okumura H, et al. Biologic and imaging diagnosis of lymph node metastasis in esophageal carcinoma. J Surg Oncol 2002;81(1):25–32.

[37] Catalano MF, Sivak Jr MV, Rice T, Gragg LA, Van Dam J. Endosonographic features predictive of lymph node metastasis. Gastrointest Endosc 1994;40(4): 442–6.

[38] Natsugoe S, Yoshinaka H, Shimada M, Shirao K, Nakano S, Kusano C, et al. Assessment of cervical lymph node metastasis in esophageal carcinoma using ultrasonography. Ann Surg 1999;229(1):62–6.

[39] Kelly S, Harris KM, Berry E, Hutton J, Roderick P, Cullingworth J, et al. A systematic review of the staging performance of endoscopic ultrasound in gastroesophageal carcinoma. Gut 2001;49(4):534–9.

[40] Eloubeidi MA, Wallace MB, Reed CE, Hadzijahic N, Lewin DN, Van Velse A, et al. The utility of EUS and EUS-guided fine needle aspiration in detecting celiac lymph node metastasis in patients with esophageal cancer: a single-center experience. Gastrointest Endosc 2001;54(6):714–9.

[41] Parmar KS, Zwischenberger JB, Reeves AL, Waxman I. Clinical impact of endoscopic ultrasound-guided fine needle aspiration of celiac axis lymph nodes (M1a disease) in esophageal cancer. Ann Thorac Surg 2002; 73(3):916–20.

[42] Urba SG, Orringer MB, Turrisi A, Iannettoni M, Forastiere A, Strawderman M. Randomized trial of preoperative chemoradiation versus surgery alone in patients with locoregional esophageal carcinoma. J Clin Oncol 2001;19(2):305–13.

[43] Bosset JF, Gignoux M, Triboulet JP, Tiret E, Mantion G, Elias D, et al. Chemoradiotherapy followed by surgery compared with surgery alone in squamous-cell cancer of the esophagus. N Engl J Med 1997;337(3): 161–7.

[44] Jones DR, Parker Jr LA, Detterbeck FC, Egan TM. Inadequacy of computed tomography in assessing patients with esophageal carcinoma after induction chemoradiotherapy. Cancer 1999;85(5):1026–32.

[45] Beseth BD, Bedford R, Isacoff WH, Holmes EC, Cameron RB. Endoscopic ultrasound does not accurately assess pathologic stage of esophageal cancer after neoadjuvant chemoradiotherapy. Am Surg 2000; 66(9):827–31.

[46] Mallery S, DeCamp M, Bueno R, Mentzer SJ, Sugarbaker DJ, Swanson SJ, et al. Pretreatment staging by endoscopic ultrasonography does not predict complete response to neoadjuvant chemoradiation in patients with esophageal carcinoma. Cancer 1999;86(5):764–9.

[47] Willis J, Cooper GS, Isenberg G, Sivak Jr MV, Levitan N, Clayman J, et al. Correlation of EUS measurement with pathologic assessment of neoadjuvant therapy response in esophageal carcinoma. Gastrointest Endosc 2002;55(6):655–61.

[48] Kato H, Kuwano H, Nakajima M, Miyazaki T, Yoshikawa M, Masuda N, et al. Usefulness of positron emission tomography for assessing the response of neoadjuvant chemoradiotherapy in patients with esophageal cancer. Am J Surg 2002;184(3):279–83.

[49] Downey RJ, Akhurst T, Ilson D, Ginsberg R, Bains MS, Gonen M, et al. Whole body 18FDG-PET and the response of esophageal cancer to induction therapy: results of a prospective trial. J Clin Oncol 2003;21(3): 428–32.